

Additive Manufacturing with Polymer Composites for Sustainable Applications

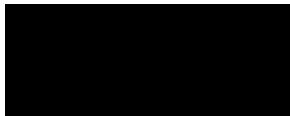
Benjamin James Cummings

**Swansea University
2023**

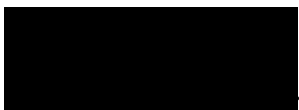
**Submitted to Swansea University
in fulfilment of the requirements for
the Degree of Engineering Doctorate**

DECLARATIONS

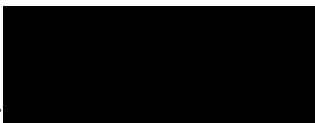
This work has not previously been accepted in substance for any degree and is not being concurrently submitted in candidature for any degree.

Signed... .....
Date..... 07/08/2023


This thesis is the result of my own investigations, except where otherwise stated. Other sources are acknowledged by footnotes giving explicit references. A bibliography is appended.

Signed... .....
Date..... 07/08/2023

I hereby give consent for my thesis, if accepted, to be available for electronic sharing.

Signed... .....
Date..... 07/08/2023

The University's ethical procedures have been followed and, where appropriate, that ethical approval has been granted.

Signed... .....
Date..... 07/08/2023

“Fantasy must be backed up by sober evaluation and calculation or you spend your life making beautiful blunders.”

– Garry Kasparov

Summary

The evolving field of digital manufacturing includes additive manufacturing (AM) that builds computationally sliced parts layer-by-layer. AM popularity continues to grow partially due to its potential to accelerate the transition to a circular economy. This thesis aims to help mitigate waste products using four novel polymer composites designed and developed for use with either fused filament fabrication (FFF) or direct writing (DW). These polymer composites are: 1) Simulation verified and AM printed triply periodic minimal surface lattice structures embedded with heat storage materials. Diamond TPMS geometry bentonite/CaCl₂ embedded prints of low packed configuration adsorb <19.1% total dry cylinder weight and reaches 38.3 °C bulk temperature when stacked in an open reactor. 2) Microporous zeolite composites for carbon capture strengthened using novel sacrificial polymer content. Zeolite 13X composite UCS increases from 4.92 (±1.22) to 7.75 (±0.75) MPa with the addition of 4 wt% CSR providing a composite BET surface area of 148 (±17) cm³/g. 3) Printer filaments made from rPP hospital blue wrap previously destined for landfill or incineration. MFI is reduced from 103 (±8) to 45 (±2) g/10mins when increasing SEBS content from 9.1 wt% to 20 wt%. The reduced MFI facilitates filament extrusion and subsequent printing of tensile and impact samples with tensile strength and impact energy absorption up to 22.5 (±1.2) MPa and 14 (±0.8) kJ/m², respectively. 4) Epoxy matrix composites for; i) weight saving applications and ii) bone-like composite manufacture to improve surgical training and patient communication. Drilled compression strength of bone-like epoxy matrix composites encompassed those of drilled bone compression strength, ranging between a 5 wt% gypsum and 20 wt% hydroxyapatite composite of 2.7 (±0.3) MPa to a 1 wt% PE, 40 wt% GY and 5wt% HA composite of 6.5 (±0.5) MPa. This thesis contributes a furthered understanding of low-cost desktop AM as utilised for local acquisition of custom engineering products that necessitates minimal lead times and transportation.

Acknowledgments

I have had the pleasure of meeting many great people throughout my time at Swansea University and will undoubtedly fail to acknowledge all of those that I am extremely grateful for working alongside and whose friendly company made my project so enjoyable. I would first like to thank Professor Matthew Davies for his sterling supervision and from whom I have learned so much. The time spent with Matthew's Photochemistry group has been a privilege and I wish everyone all the best for the future. I would like to thank Rhys Charles for his supervision and help particularly regarding my work on recycled materials. I would like to thank David Warren, Beverly Williams, Hayley McAuliffe and the team at the Materials and Manufacturing Academy (M2A) for providing financial and personable support. Thanks to the cohort of doctoral M2A students that I pulled the long straw in researching beside and I look forward to keeping up to date with your future endeavours. My gratitude extends to Jonathan Elvins, Rhodri Williams, and Eifion Jewell for accommodating and advising my research on energy storage using salt hydrates. Thanks to everyone who I worked with at the PMRC, including the teams at Murex 3D, Insight Surgery, and the Thermal Compaction Group. I am very grateful for the love and support from my wife (and cat!), this project would have been impossible without your support. Lastly, to my family, particularly my late grandad George Cummings who continues to inspire me, thank you tremendously for your unwavering support and encouragement.

Contents

Declarations.....	2
Summary.....	4
Acknowledgments	5
Contents.....	6
List of Figures	10
List of Tables.....	15
Abbreviations and Symbols.....	18
1. Chapter 1. Introduction	22
1.1. Aim of the thesis.....	23
1.2. Additive Manufacturing.....	24
1.1. Global Plastics Problem	28
1.2. End-of-Life Strategies for Plastics	30
1.3. Sustainable Innovation with Polymer Composites.....	33
1.4. Manufacture of Bone-Like Polymer Composites.....	34
1.5. Recycled Surgical Blue Wrap Polypropylene.....	35
1.6. Life Cycle Emissions from the Plastics Industry.....	38
1.7. Thermochemical Heat Storage	40
1.8. Microporous Materials for Gas Separation.....	45
1.9. Direct Writing of Heterogeneous Zeolitic Pastes.....	46
1.10. Conclusions	49
1.11. References	51
2. Chapter 2. Experimental.....	60
2.1. Chapter Summary	61
2.2. Computer Aided Design.....	61
2.3. 3D Printing Procedure and Moulding	62
2.4. Error Analysis	62
2.5. References	63
3. Chapter 3. Bentonite/CaCl ₂ Embedded Fused Deposition Modelled Lattices for Thermochemical Energy Storage.....	64

3.1. Chapter Summary	65
3.2. Aims	65
3.3. Introduction	66
3.4. Experimental.....	67
3.4.1. Lattice Matrix Geometry Selection and Modelling.....	67
3.4.2. Computed Fluid Dynamic Simulation	69
3.4.3. Printing Triply Periodic Minimal Surface Geometries	71
3.4.4. Embedding of Bentonite/CaCl ₂ Scaffolds for use in Thermochemical Energy Storage Reactor.....	73
3.4.5. Energy Storage Reactor Set-up and Use.....	75
3.4.6. Bentonite/CaCl ₂ Composite Surface Imaging.....	76
3.5. Results.....	77
3.5.1. Benchmark Flow Simulations.....	77
3.5.2. Calculated Simulation and Measured Reactor Probe Error Tables.....	85
3.5.3. Bentonite/CaCl ₂ Embedded Prints	88
3.6. Conclusions	100
3.7. References	102
4. Chapter 4. Direct Writing of a Toughened Zeolite/Binder Composite for Gas Separation.....	104
4.1. Chapter Summary	105
4.2. Introduction	105
4.3. Experimental.....	108
4.3.1. Preparation of Microporous Zeolite Composites for Gas Separation	109
4.3.2. Compression Testing.....	111
4.3.3. Direct Writing Extrusion Pressure.....	111
4.3.4. Calliper Measurements	114
4.3.5. X-Ray Diffraction Analysis	115
4.3.6. Brunauer-Emmett-Teller Nitrogen Gas Adsorption.....	115
4.3.7. Surface Tension Measurements.....	116
4.3.8. Viscometry of Zeolite Composite Pastes	116
4.3.9. Zeolitic Composite Surface Imaging	117
4.4. Results.....	118

4.4.1.	Energy Dispersive Spectroscopy of Zeolite 13X Baseline Composite and Bentonite Binder	118
4.4.2.	Mechanical Properties of Zeolite 13X Printable Composites	119
4.4.3.	X-Ray Diffraction Analysis	123
4.4.4.	Brunauer–Emmett–Teller Adsorption	126
4.4.5.	Scanning Electron Microscopy	130
4.4.6.	Calliper Measurements	132
4.4.7.	Surface Tension Analysis	133
4.4.8.	Rheology of Zeolitic Composite Pastes	134
4.5.	Conclusions	141
4.6.	References	144
5.	Chapter 5. Upcycling of Hospital Blue Wrap Waste into Fused Deposition Modelling Filament	146
5.1.	Chapter Summary	147
5.2.	Introduction	147
5.3.	Experimental.....	148
5.3.1.	Recycled Polypropylene Blended with Styrene-Ethylene-Butylene-Styrene	149
5.3.2.	Imaging of Recycled Surgical Blue Wrap Blend Morphologies	150
5.3.3.	Differential Scanning Calorimetry	151
5.3.4.	Fused Deposition Modelling of Upcycled Polypropylene from Waste Blue Wrap	152
5.3.5.	Tensile Testing	153
5.3.6.	Impact Testing	153
5.3.7.	Trouser Tear for Characterisation of Interlayer Strength	153
5.3.8.	Flexural Testing	154
5.3.9.	Melt Flow Indexing	154
5.3.10.	Cost Benefit Analysis.....	155
5.4.	Results.....	156
5.4.1.	Thermal Analysis of Recycled Polypropylene and Styrene-Ethylene-Butylene-Styrene Blends.....	156
5.4.2.	Extrudate Tolerance.....	159
5.4.3.	Micrographs and Crystallinity	161
5.4.4.	Mechanical Testing and Ligament Thickness Analysis	162

5.4.5. Cost Benefit Analysis.....	173
5.5. Conclusions	175
5.6. References	177
6. Chapter 6. Lightweight and Bone-Like Epoxy Matrix Composites Characterized using Drilling and Mechanical Testing.....	179
6.1. Chapter Summary	180
6.2. Introduction	180
6.3. Experimental.....	183
6.3.1. Epoxy Matrix Composite Preparation for the Development of Bone Phantoms	185
6.3.2. Foot and Ankle CAD Modelling and Printing.....	186
6.3.3. Optical Microscopy of Drilled Bone-like Sample Surfaces and the Drill Bits	187
6.3.4. Bone-Like Composite Density Calculation	188
6.3.5. Drilling Procedure and Data Interpretation	188
6.3.6. Compression Testing.....	190
6.4. Results.....	191
6.4.1. Drilling of Bone and Epoxy Composites	191
6.4.2. Thrust Force Profiles of Bone and Multiple Additive Composites	197
6.4.3. Density and Mechanical Testing of Epoxy Composites	201
6.4.4. Images of Machined Composites	202
6.5. Conclusions	204
6.6. References	205
7. Chapter 7. Conclusions and Future Work	208

List of Figures

FIGURE 1.1. 3D PRINTING PROCESS FROM CAD MODEL TO FINAL PART INCLUDING COMPUTED REPRESENTATION SHOWN IN GREY, SUPPORT MATERIAL SHOWN IN ORANGE, AND FINAL PART MATERIAL SHOWN IN BLUE.	25
FIGURE 1.2. HEATING AND COOLING CURVES OF PLA SHOWING GLASS TRANSITIONS AT 54 AND 50 °C, COLD CRYSTALLISATION AT 117 °C, AND MELTING PEAKS AT 152-155°C. THE VALUES DEPEND ON HEATING CYCLE NUMBER [23].	26
FIGURE 1.3. REACTIONS REQUIRED TO FORM PLA [29].	27
FIGURE 1.4. TENSILE SPECIMEN OF NON-STANDARDISED DIMENSIONS (LEFT) AND TENSILE DATA COMPARING 100% RECYCLED PP FROM HOSPITAL BLUE WRAP TO THAT OF VIRGIN PP OF UNKNOWN MFI (RIGHT) [68].	35
FIGURE 1.5. SCHEMATIC OF PRINTED LAYERS ON A HEATED PRINT BED (I.E, BUILD PLATE) WITH INTERLAYER BONDS OF TYPICAL MOLECULAR SEPARATION AND UNEVEN COOLING PROFILE. ..	36
FIGURE 1.6. SCHEMATIC OF LIGAMENT THICKNESS (LC), RUBBER PARTICLE OF DIAMETER (D), AND STRESS VOLUME SPHERE (S) [96].	38
FIGURE 1.7. 2050 ESTIMATED GHG EMISSIONS OF PLASTICS DERIVED FROM FOSSIL FUEL AND NATURAL (CORN-BASED, AND SUGARCANE-BASED) FEEDSTOCKS UNDER TWO ENERGY-MIX SCENARIOS: AN ENERGY MIX BASED ON 2019 GENERATION (A), AND A 100% RENEWABLE ENERGY SCENARIO (B) SHOWING TOTAL EMISSIONS APPROXIMATELY HALF REGARDLESS OF THE ENERGY SYSTEMS USED [117].	39
FIGURE 1.8. ILLUSTRATION OF A PACKED BED OPEN CHAMBER (1.) CONTAINING PELLETS OF POROUS STRUCTURE (YELLOW) WITH IMPREGNATED SALT HYDRATE (DARK YELLOW, 2.) FOR DISCHARGE WITH HIGH RH% INPUT FLOW. THE REVERSABLE CHARGING CYCLE REQUIRES A LOW RH% AND OFTEN HEAT IS SUPPLIED (3.) TO FULLY CHARGE THE SALT HYDRATE.	41
FIGURE 1.9. DIRECT WRITING ILLUSTRATION SHOWING A SEMI-SOLID EXTRUDATE AND 'WOOD PILE' MANUFACTURED PART VIA TWO COMMON ACTUATOR TYPES: 1. ELECTRIC MOTOR, 2. PNEUMATIC MOTOR. PRESSURE (P) IS APPLIED TO THE FEEDSTOCK HELD IN AND EXTRUDED FROM A DISPENSER – OFTEN A SYRINGE FOR SMALL PARTS – TRAVELLING AT VELOCITY (V). ..	42
FIGURE 1.10. SCHEMATIC OF BENTONITE STRUCTURE WITH EXCHANGEABLE CATIONS [158].	44
FIGURE 1.11. SEM MICROGRAPH OF 'WOOD-PILE' AM LATTICE SORBENT INTERNAL CHANNELS, LEFT [158], MOLECULAR STRUCTURE OF 13X ZEOLITE, RIGHT [177].	46
FIGURE 1.12. CONE AND PLATE VISCOMETER OF GAP HEIGHT (H) AND CONE ANGLE (θ).	48
FIGURE 2.1. INTERSECTING CAD PART SURFACES PREVENTING A WATERTIGHT FORMATION FOR FLOW SIMULATIONS.	61
FIGURE 3.1. BENCHMARK LATTICE MESHES, FIN (TOP), BAFFLES (MIDDLE), FOR THE CONSIDERATION OF TPMS DEISGNS OF INNER AND OUTER CYLINDER DESIGN (BOTTOM).	69
FIGURE 3.2. THS OPEN REACTOR DESIGN WITH CONCENTRIC AIR FLOW SHOWING UNSYMMETRICAL SIDE CUT PLOTS, ABOVE, AND INLET VORTICITY (CONTOURS) AND VELOCITY (STREAMLINES) ENTRANCE PROFILE OF AN EMPTY REACTOR VESSEL.	70
FIGURE 3.3. CHEMICAL STRUCTURE OF THE POLYCARBONATE MONOMER MADE FROM BISPHENOL A, N IS TYPICALLY 90-180.	72
FIGURE 3.4. PRINTED POLYCARBONATE CYLINDERS, FROM LEFT TO RIGHT - 15% INFILL DIAMOND, 20% INFILL DIAMOND, 15% INFILL SHWARZ, 20% INFILL SHWARZ (BOTTOM LEFT), 2.5 MM CELL HEXAGON INFILL (BOTTOM RIGHT).	72

FIGURE 3.5. STAGES OF MAKING BENTONITE/ CaCl_2 EMBEDDED PC PRINTS: PRESSING THE COMPOSITE INTO THE PRINT USING A CLAY MODELLING TOOL (1), CLEARING THE EXTERNAL AND INTERNAL LABYRINTHS (2), REMOVING LOOSE MATERIAL WITH COMPRESSED AIR (3), FINAL PART READY TO BE CHARGED FOR THS (4).	74
FIGURE 3.6. BENTONITE/ CaCl_2 EMBEDDED PRINTS. DIAMOND HIGH PACKING DENSITY (LEFT), SCHWARZ HIGH PACKING DENSITY (MIDDLE), AND DIAMOND LOW PACKING DENSITY (RIGHT).	74
FIGURE 3.7. EXPERIMENT CONFIGURATION FOR COLUMN OF EMBEDDED CYLINDERS SHOWING COPPER WRAPPED COLUMN WITH THERMOCOUPLES AND HOUSING PIPE.	76
FIGURE 3.8. REACTOR MODEL SHOWING LOAD CELL, INLET VALVE, AND REACTOR VESSEL CONTAINING PLACED SCHWARZ INNER CYLINDER LATTICE DESIGN.....	77
FIGURE 3.9. CFD TEMPERATURE AND PRESSURE BENCHMARKING OF SCHWARZ (SCHW.), GYROID, DIAMOND INNER CYLINDER (DC), SCHWARZ INNER CYLINDER (SC), AND DIAMOND LATTICE GEOMETRIES (DIA) AGAINST TYPICAL FIN (F1, F2, AND F3 WITH 8, 14, AND 28 FINS, RESPECTIVELY) AND BAFFLE (B1, B2, AND B3 WITH HORIZONTAL ALTERNATION, VERTICAL ALTERNATION, AND STAGGERED HORIZONTAL ALTERNATION, RESPECTIVELY) HEAT EXCHANGER DESIGN.	78
FIGURE 3.10. SIMULATED OUTLET TEMPERATURES OF A NON-INSULATED REACTOR CONTAINING HEATED SURFACES SHAPED AS SCHWARZ, GYROID, DIAMOND CYLINDER, SCHWARZ CYLINDER, AND DIAMOND LATTICE GEOMETRIES, WHEN COMPOSED OF EPOXY (GREY), AND ALUMINIUM (BLUE). AN INSULATED REACTOR CONTAINING AN AL LATTICE IS SHOWN IN YELLOW.	81
FIGURE 3.11. CUT PLOTS FROM SW FLOW SIMULATIONS USING A TYPICAL 20 L/MIN INLET VOLUME RATE SHOWING THE FULL LENGTH AND DIAMETER OF THE IN-HOUSE BUILT REACTOR WITH VELOCITY (TOP LEFT) AND TEMPERATURE (TOP RIGHT) CONTOUR MAPS PRESENTED. CUT PLOTS (BOTTOM) SHOW THE DEVELOPMENT OF FLUID TEMPERATURE ACROSS THE RADIUS OF THE LATTICE FROM START, CENTRE, AND UPPER REGIONS.	82
FIGURE 3.12. FLUID TEMPERATURE (TOP) AND PRESSURE (BOTTOM) AGAINST INLET VOLUME RATE: 10, 20, 30, 40, 50, AND 60 L/MINUTE (BOTTOM RIGHT). THE COLOURED POINTS SHOW FLUID HEATING AS IT MOVES THROUGH AN ALUMINIUM TPMS LATTICE CYLINDER (DEPICTED TOP LEFT) WHILE THE BLACK LINE SHOWS OUTLET TEMPERATURE AGAINST INLET FLOW RATE.	84
FIGURE 3.13. PLANE VIEW OF TPMS PC PRINTED CYLINDERS FROM LEFT TO RIGHT: 15% INFILL DIAMOND, 20% INFILL DIAMOND, 15% INFILL SCHWARZ, 20% INFILL SCHWARZ, HEX INFILL OF 2.5 MM CELL SIZE.	88
FIGURE 3.14. REACTOR BULK AND OUTLET TEMPERATURES FOR 15%, 20%, AND HEX INFILLED TPMS CYLINDER PRINTS EMBEDDED WITH BENTONITE/ CaCl_2 OF HIGH PACKED DENSITY (TOP).....	89
FIGURE 3.15. OPTICAL MICROSCOPY IMAGES OF HIGHLY PACKED DIAMOND TPMS BENTONITE/ CaCl_2 CYLINDERS BEFORE (LEFT) AND AFTER (RIGHT) EXPOSURE TO WATER VAPOUR FOR 4 HRS ACROSS TWO DISCHARGE RUNS.	90
FIGURE 3.16. TWO STACKED BENTONITE/ CaCl_2 EMBEDDED SCHWARZ TPMS CYLINDERS, A FIRST RUN WITH 70 %RH AIRFLOW AT 20 L/MIN FOR 16 HOURS MEASURED FOR BULK AND OUTLET TEMPERATURE.....	91
FIGURE 3.17. PARTIALLY BREACHED PC PRINTED LATTICE LINE COMPOSING A HIGH PACKED BENTONITE/ CaCl_2 EMBEDDED TPMS CYLINDER AFTER A FIRST OPEN REACTOR RUN EXPOSED TO 70 %RH VAPOUR AT 20 L/MIN FOR 16 HRS.....	91
FIGURE 3.18. IMAGED SURFACES CORRESPONDING TO ROUGHNESS VALUES OF DIAMOND CYLINDER BEFORE DISCHARGE (TOP LEFT), HIGHER POSITIONED (TOP MIDDLE), AND LOWER (TOP RIGHT) POSITIONED DIAMOND CYLINDERS EXPOSED TO 70 %RH AT 20 L/MIN FOR 16 HOURS. TYPICAL	

IMAGED SURFACES WITH COLOUR MAP SHOWING CHANGE IN HEIGHT OF FIRST STACKED CYLINDER AFTER SECOND RECHARGE (BOTTOM LEFT), AND SIXTH STACKED CYLINDER AFTER SECOND RECHARGE (BOTTOM RIGHT), BOTH MEASURED AT 50 %RH AT 20L/MIN FOR 3×4 HR RUNS.	92
FIGURE 3.19. STACKED PRINTED AND EMBEDDED LATTICE CYLINDERS BULK, INLET, AND OUTLET TEMPERATURE PROFILES ACROSS 4 HRS EXPOSURE TO 50% RH TRAVELING AT 20 L/MIN (TOP). R1, R2, AND R3 OUTLET ΔT PROFILES OF STACKED CYLINDER SYSTEM WITH OUTLET THEROETICAL LIMIT OF R3 (DOTTED LINE) WHEN OF THE HIGH PACKED DENSITY CONFIGURATION (BOTTOM).	93
FIGURE 3.20. SORBED WATER VAPOUR AS A PERCENT WEIGHT OF THE CYLINDER FOR EACH STACKED CYLINDER IN ORDER OF THEIR POSITION ALONG THE REACTOR LENGTH FROM INLET SIDE TO OUTLET SIDE, INCLUDING HIGH AND LOW VOLUMES OF PACKED BENTONITE/CaCl ₂ COMPOSITE.	96
FIGURE 3.21. SEM IMAGES OF BENTONITE/CaCl ₂ CYLINDER SURFACES, (A) FINE SALT DISPERSION OF LOW-DENSITY PACKED SAMPLE BEFORE R1, (B) AGGLOMERATED SURFACE SHOWING REDUCED GRANULE SIZE OF HIGH-DENSITY PACKED SAMPLE AFTER R2, (C) COATED BENTONITE/CaCl ₂ ON PC PRINTED LINES AND SURROUNDING GRANULAR LOW-DENSITY PACKED SURFACE BEFORE R1, (D) CRACKED BENTONITE/CaCl ₂ OF HIGH-DENSITY PACKED SAMPLE AFTER R3.	98
FIGURE 4.1. TYPES OF ADSORBENT ISOTHERM (LEFT) AND ISOTHERM HYSTERESIS LOOPS (RIGHT). THE ARROW MARKED 'B' INDICATES TYPICAL ONSET OF MULTILAYER FORMATION [4].	106
FIGURE 4.2. A MODEL OF THE FAUJASITE (Z- OR Y-ZEOLITE) UNIT CELL. SI AND AL ATOMS ALTERNATE AT THE TETRAHEDRAL INTERSECTIONS AS INDICATED AT THE EIGHT SOLIDATE CAVITY DEPICTED AS A FRAME FOR CLARITY. CATION EXCHANGE SITES ARE MARKED I, II OR III DEPENDING ON POSITION AT EITHER A SIX RING, B CAGE, OR A CAVITY LOCATION [11].	107
FIGURE 4.3. SUMMARY OF CHAPTER 4 EXPERIMENTAL WORKFLOW THAT IS SPLIT INTO TWO MAIN INVESTIGATIONS: COMPRESSION STRENGTH/SURFACE AREA TRADE-OFF, AND PRINTABILITY OF STRENGTHENED COMPOSITE.	109
FIGURE 4.4. PRINTED CUSTOM SYRINGE EXTRUDER HEAD.	112
FIGURE 4.5. THE DIRECT WRITING PROCESS FOR PRINTING ZEOLITE/BINDER/CSR PASTES.	113
FIGURE 4.6. SYRINGE POSITION BETWEEN TENSILE TESTER AND SUPPORT TO MEASURE RESISTANT FORCES GOVERNED BY PASTE CONTENTS.	113
FIGURE 4.7. MEASUREMENT OF ZEOLITIC WOOD-PILE DW PRINTED SAMPLES FOR GEOMETRIC DISTORTION USING CALIPERS. HEIGHT (H) IS REPRESENTED BY THE PINK LINES, WIDTH (W) BY THE BLUE LINES, AND THICKNESS (T) BY THE RED LINES WHERE THICKNESS WAS MEASURED PARALLEL (T _a) AND PERPENDICULAR (T _p) TO THE PRINTED TOP-LINES.	115
FIGURE 4.8. VISCOSITY SET-UP FOR ZEOLITE 13X PASTES WITH NO RING FORMATION PRESENT (LEFT) SUGGESTING MEASURED VISCOSITY WITHOUT PARTICLE MIGRATION THAT OCCURS WITH INEFFECTIVE GAP HEIGHT AND WATER CONTENT (RIGHT) SHOWING A RING FORMATION.	117
FIGURE 4.9. EDS SPECTRA OF SINTERED BASELINE SAMPLE (LEFT) AND NON-SINTERED BENTONITE POWDER (RIGHT). UNLABELLED PEAKS ARE NOISE (I.E., C KA).	118
FIGURE 4.10. COMPRESSION CURVES OF MEASURED BASELINE (ZERO CSR), 2, 4, 6 WT% CSR COMPOSITES AT 5 s ⁻² AND FRACTURE SURFACE OF MODULUS SPECIMEN (IMAGE).	121
FIGURE 4.11. UCS AND YIELD POINT OF BASELINE (ZERO CSR), ADDED 4 WT% MC/PVA, AND 4 WT% CSR TESTED AT 1.67 s ⁻³ AND 5 s ⁻² WHERE ERROR BARS ARE ONE SD.	122
FIGURE 4.12. XRD SPECTRUMS WITH HKL CRYSTALLOGRAPHIC PLANES FROM SINTERED AND NON-SINTERED BASELINE, 4 WT% MC/PVA, AND 4 WT% CSR.	124

FIGURE 4.13. CRYSTALLINITY AS CALCULATED FROM XRD PEAKS MEASURED FROM BASELINE, 4 WT% BINDER, AND 4 WT% CSR SAMPLES THAT WERE CAST, EXTRUDED (E), AND/OR SINTERED (S) REVEALING THE EFFECTS OF HEAT TRANSFER RATE ON CRYSTALLINITY AND FAU FORMATION. ERROR BAR HEIGHT GIVES 10% VARIANCE ERROR.	126
FIGURE 4.14. BET ANALYSIS OF POWDERED, AND EXTRUDED, BASELINE 4 WT% CSR, AND MC/PVA SAMPLES. BLACK ARROWS SHOW THE PROGRESS OF TIME.	127
FIGURE 4.15. DESKTOP SEM IMAGES OF BENTONITE (A), PRINTED ZEOLITE COMPOSITE (B), 2 WT% CSR PARTICLES AT THE PRINTED SURFACE (C), AND SINTERED 4 WT% CSR SHOWING CIRCULAR VOIDS HIGHLIGHTED BY RED AROUND (D), SINTERED COMPOSITE WITH ZERO ADDITIVE (E), SINTERED COMPOSITE WITH 4 WT% CRS ADDITION (F), NON-SINTERED FLAT SURFACE OF WITH 4 WT% ADDITION OF BINDER MIXTURE (G), AND NON-SINTERED SURFACE OF ADDED 4 WT% CSR FLAT SURFACE (H).....	131
FIGURE 4.16. BASELINE (LEFT) AND 4 WT% CSR (RIGHT) DW PRINTED SAMPLES.....	132
FIGURE 4.17. SURFACE TENSION OF 0.5, 1, 1.5, AND 2 WT% CSR IN DI WATER.	133
FIGURE 4.18. ZEOLITE COMPOSITES WITH ZERO (LEFT) AND ADDED 4 WT% CSR (RIGHT) SHOWING AN EXAMPLE OF CRACK FORMATION.....	134
FIGURE 4.19. BASELINE ZEOLITE COMPOSITE PASTES WITH WATER CONTENT 51.0, 52.5, 54.0 WT% DI WATER OF STABLE SHEAR THINNING PROFILES.	135
FIGURE 4.20. RELATIVE VISCOSITY OF BASELINE AND ADDED CSR PASTES CALCULATED USING 52.5 WT% DI WATER VISCOSITY VALUES AS A COMMON DENOMINATOR. EACH PLOTTED VALUE REPRESENTS THREE AVERAGED VISCOSITY VALUES IMPLEMENTED TO REDUCE NOISE.	136
FIGURE 4.21. LOG(H) AGAINST LOG($\dot{\gamma}$) USED TO CALCULATE POWER LAW VALUES OF BASELINE PASTES (TOP) AND ADDED CSR PASTES (BOTTOM).	137
FIGURE 4.22. EXTRUSION PRESSURE PROFILES USING A 5 ML LUER LOCK SYRINGE AT A PLUNGER SPEED OF 6 MM/S, SHOWING THE INFLUENCE OF USING 1.6, 1.8, AND 2 MM NOZZLE DIAMETERS FOR 4 WT% AND 8 WT% CRS PASTES. A PROPOSED EQUILIBRIUM/RELAXATION ZONE IS HIGHLIGHTED IN RED, AND A BLUE ARROW HIGHLIGHTS POTENTIAL CSR DECOMPRESSION.	139
FIGURE 5.1. SINGLE SCREW EXTRUDER SHOWING MAIN AND TOLERANCE DISPLAYS (1), SPOOLING OF RPP/SEBS FILAMENT (2). AND FFF PRINTING WITH RPP/SEBS FILAMENT (3).	149
FIGURE 5.2. CHEMICAL STRUCTURES OF ISOSTATIC PP WITH 'n' REPEATING UNITS TYPICALLY BETWEEN 200-2,900, AND SEBS WITH 'x', 'y', AND 'z' REPEATING UNITS TYPICAL BETWEEN 300-1,200.	150
FIGURE 5.3. TROUSER TEAR RPP/SEBS PRINTED SAMPLE SECURED IN A TENSILE MACHINE AND TORN ALONG ITS CENTRELINE FOR QUANTIFYING INTERLAYER STRENGTH.	154
FIGURE 5.4. SINGLE MELTING ENDOTHERMS INDICATING MISCIBILITY OF MOST CRYSTALLINE (9.1 WT% SEBS) AND LEAST CRYSTALLINE (20.0 WT% SEBS) SAMPLES HELD IN AIR WHEN HEATED AT 10 °C/MIN.....	157
FIGURE 5.5. MELT FLOW INDEXING OF RPP/SEBS BLEND. ERROR BARS SHOW STANDARD DEVIATION OF RESULTS.	158
FIGURE 5.6. DIAMETER OF EXTRUDED FILAMENT (LEFT) AS RECODED BY THE LASER MICROMETRE (RIGHT).....	160
FIGURE 5.7. SPOOLED 23.1 WT% SEBS FILAMENT SHOWING SIGNS OF RECYCLATE CONTAMINATION.	160
FIGURE 5.8. OPTICAL MICROGRAPHS OF RPP AND 9.1 WT% SEBS SAMPLES (TOP) AND THEIR SPHERULITE DIAMETER DISPERSIONS (BOTTOM) MEASURED USING IMAGEJ.	161

FIGURE 5.9. IMPACT ENERGY (BOTTOM) CALCULATED FOR RPP/SEBS PRINTED CHARPY SPECIMENS OF 80 MM ² CROSS-SECTION AT THE NOTCH POINT (SHOWN WITH FRACTURE SURFACE, TOP) WITH ERROR BARS GIVEN AS ± 0.8 KJ MACHINE TOLERANCE FROM A BLANK RUN.	163
FIGURE 5.10. TYPICAL BRITTLE TENSILE BEHAVIOUR OF 9.1-16.7 WT% RPP/SEBS.....	164
FIGURE 5.11. TYPICAL DUCTILE TENSILE BEHAVIOUR OF 20.0 AND 23.1 WT% RPP/SEBS.	164
FIGURE 5.12. PRINTED AND TESTED RPP/SEBS TENSILE SAMPLES (TOP) WITH STRESS WHITENED 20.0 WT% SEBS, AND THEIR MEASURED UTS AND STRAIN TO FAILURE (BOTTOM).	165
FIGURE 5.13. 20 WT% SEBS BLEND SHOWING VISIBLE PERPENDICULAR WHITENING (A), PREDOMINANTLY PARALLEL STRESS WHITENING (B), AND DUCTILE FRACTURE SURFACE (C).	166
FIGURE 5.14. PRINTED ANNEALED RPP/SEBS TENSILE UTS AND STRAIN TO FAILURE.....	167
FIGURE 5.15. TYPICAL DRAWING BEHAVIOUR OF MEASURED ANNEALED 9.1-23.1 WT% SEBS SAMPLES (I), CLOSE-UP OF 9.1 WT% SEBS FOR CLARITY (II), SAMPLES SHOWING PARALLEL INTERLAYER FAILURE OF TENSILE 16.7, 20.0, AND 23.1 WT% SEBS SAMPLES (III), AND KEY FOR GRAPHS (IV).	168
FIGURE 5.16. TROUSER TEAR FAILURE SURFACES OF THE ANNEALED 16.7, 20.0, AND 23.1 WT% G1657 SEBS SAMPLES (TOP), AND TEAR RESISTANCE OF BOTH G1657 AND SEBS GRADES (BOTTOM) WITH ERROR BAR HEIGHT GIVEN AS 1 SD.	169
FIGURE 5.17. RUBBER PARTICLES COMPOSING 20.0 WT% (TOP LEFT) AND 23.1 WT% (TOP RIGHT) NON-ANNEALED RPP/SEBS BLENDS. ANNEALED 16.7 WT.% SEBS (BOTTOM LEFT) AND ANNEALED 20.0 WT% SEBS (BOTTOM RIGHT).	170
FIGURE 5.18. PER KG COSTS OF PRODUCING RPP/SEBS FILAMENT AT A RATE OF 1 KG/HOUR.	173
FIGURE 6.1. CROSS SECTION OF CORTICAL BONE SCANNED USING SYNCHROTON RADIATION μ CT SHOWING A DISTRIBUTED PORE AND MINERAL NETWORK (A), AND A 3D RENDERING OF THE NETWORK AFTER BINARIZATION OF THE VOLUME (B) [16].	181
FIGURE 6.2. COMPRESSION STRESS/STRAIN GRAPHS OF FIVE COMMERCIAL BONE PHANTOM MATERIALS AT STRAIN RATES OF A) 10^{-3} .s ⁻¹ AND C) 10^{-1} .s ⁻¹ , CLOSE-UP PRESENTED B) AND D), RESPECTIVELY [27].	182
FIGURE 6.3. MOLECULAR STRUCTURE OF HA OF HEXAGONAL CRYSTAL STRUCTURE [31].	183
FIGURE 6.4. METHOD 1 DRILLING RIG WITH TENSILE MACHINE ACTUATOR SHOWN DRILLING PIG TIBIA BONE SECURED IN VICE (LEFT). METHOD 2 DRILLING RIG WITH LOAD CELL DRILL FORCE TRANSDUCER AND PILLAR DRILL ACTUATOR FOR DRILLING EPOXY COMPOSITES SECURED BY MACHINE SCREWS.....	184
FIGURE 6.5. ANKLE MODEL FOR SURGICAL COMMUNICATION MODIFIED IN MESHMIXER BY ADDING COLOURED TUBES FOR ENHANCED AESTHETIC AND EASE OF 3D PRINTING.	186
FIGURE 6.6. FOOT AND ANKLE MODEL PRINTED IN PLA FOR 1) MANUFACTURE OF FEMALE MOULD, AND 2) VISUAL COMPARISON WITH BONE-LIKE EPOXY COMPOSITES.	187
FIGURE 6.7. PRELIMINARY METHOD 1 DRILLING TO ESTABLISH TOUGHENING MECHANISMS AND IDENTIFY MOST AND LEAST RESISTANT MATERIALS TO DRILLING.....	189
FIGURE 6.8. METHOD 2 DRILL RIG SET-UP TO MEASURE THRUST FORCE FROM BONE-LIKE SAMPLES: DATA GATHERED (1), ARDUINO MINI MICROCONTROLLER (2), VICE USED TO HOLD THE ALUMINIUM MODULE (3), PILLAR DRILL CHUCK (4), SAMPLE ON COMPRESSION LOAD CELLS (5).	190
FIGURE 6.9. STIFFNESS AND WORK DONE REQUIRED TO DRILL EACH FIBRE OR POWDER CONTAINING EPOXY COMPOSITE PRESENTED WITH SD ERROR BARS, DRILLED AT 1750 RPM AND A 1 MM/S FEED RATE (TOP) AND 1750 RPM AT 1.5 MM/S FEED RATE (BOTTOM).	192

FIGURE 6.10. METHOD 2 DRILLED COMPOSITES OF MULTIPLE ADDITIVE CONTENT SHOWING WORK DONE AND STIFFNESS FOR EACH 3 MM THICK SAMPLE WITH CONTENT FORMATTED AS PE/GF/GY/HA WT%.....	194
FIGURE 6.11. METHOD 1 DRILLED PIG BONE THRUST FORCES AT THREE CHIP LOADINGS SHOW A POSITIVE GRADIENT AND TIME DEPENDENCE (VISCOELASTICITY), WITH FORCE BETWEEN TWO SETS OF DATA OF SIMILAR Y AXIS INTERCEPT (ZERO MACHINE RATE).....	196
FIGURE 6.12. SEM OF DRILL BIT CUTTING EDGES; OF UNUSED 3.5 MM DIAMETER BIT (LEFT) AND USED BIT HAVING DRILLED AT LEAST 25 TIMES SHOWING ROUNDED TIP (MIDDLE), AND IRREGULAR WEAR OF CUTTING EDGE (RIGHT).....	197
FIGURE 6.13. MEASURED PIG TIBIA BONE DRILLED THRUST FORCES FROM 1350-3000 RPM SPINDLE SPEED AT 1MM/S FEED RATE (TOP), AND 0.5 TO 2.5 MM/S FEED RATE (BOTTOM) AT 1750 RPM.	198
FIGURE 6.14. MEASURED DRILLING THRUST FORCE CURVES WHEN DRILLING COMPOSITE SAMPLES AT 1.3 MM/S FEED RATE AND 1750 RPM (METHOD 1, TOP) AND 1.3 MM/S AND 800 RPM (METHOD, BOTTOM).	199
FIGURE 6.15. ANKLE JOINT MEDICAL MODEL CAST USING CB1 COMPOSITE.....	200
FIGURE 6.16. METHOD 2 DRILLED MULTIPLE ADDITIVE COMPOSITES AND REFERENCE MATERIALS (FROM LEFT TO RIGHT): CLEAN EPOXY, CB2, CB4, CB1, AND BONE.....	203
FIGURE 6.17. INFINITE FOCUS MICROGRAPHS OF CB1 (TOP) AND CB4 (BOTTOM).	203

List of Tables

TABLE 1.1. DISPOSABLE PLASTIC PRODUCTS THAT PASSED THROUGH NHS SUPPLY CHAIN IN 2014/2015, RANKED BY MASS PER ANNUM AND PERCENTAGE OF TOTAL PLASTIC WASTE PRODUCED [70].....	32
TABLE 3.1. SURFACE AREA AND VOLUME OF OUTER AND INNER CYLINDER TPMS DESIGNS.....	80
TABLE 3.2. ENTHALPY CHANGE, ΔH , AND ENERGY DENSITY, E_d , CALCULATED USING LATTICE VOLUME, AND SIMULATED FLUID TEMPERATURE AND FLUID HUMIDITY AT THE OUTLET. ERROR GIVEN IN BRACKETS IS PROPAGATED ERROR.	80
TABLE 3.3. MEASURED SIMULATION RESULTS SHOWING AVERAGE, MIN, AND MAX VALUES OF GOALS ITERATED UNTIL THE CRITERIA WAS MET WITH ERROR OF DELTA. VALUES SHOW RESULTS FROM SIMULATING AN ALUMINIUM SWCHARZ TPMS GEOMETRY WITH AN INLET VOLUME OF 30L/MIN ACROSS 63 ITERATIONS.	86
TABLE 3.4. REPEATED SIMULATIONS OF REPOSITIONED AND RE-MESHED DC LATTICES, AVERAGE VALUES OF EACH ACHIEVED GOAL AS USE TO CALCULATE MEAN AVERAGE, SD, AND SD AS A % OF THE MEAN AVERAGE.	86
TABLE 3.5. MEASURED MAXIMUM INLET TEMPERATURE ($^{\circ}C$), AND HUMIDITY (%RH) VALUES FROM CLAY/SALT EMBEDDED PRINTED LATTICES OF HEX, 15, AND 20 % INFILL DENSITY.....	87
TABLE 3.6. A RECHARGED RUN WITH 6 STACKED TPMS CYLINDERS, THE THERMOCOUPLE IS EXPOSED TO AIRFLOW OUTSIDE THE RECTOR TO MEASURE ROOM TEMPERATURE AVERAGED WITH STANDARD DEVIATION CALCULATED ACROSS 4 HOURS (1200 DATA POINTS).	88
TABLE 3.7. MACROSCOPIC ROUGHNESS PARAMETERS OF IMAGED HIGH PACKED DIAMOND CYLINDER BEFORE DISCHARGE, HIGHER POSITIONED AND LOWER POSITIONED DIAMOND CYLINDERS EXPOSED TO 70 %RH AT 20 L/MIN FOR 16 HOURS. TWICE RECHARGED (RUN 3) HIGH PACKED	

MACROSCOPIC ROUGHNESS PARAMETERS FOR THE CONSIDERATION OF EFFECTS OF RECHARGING ON SWELLING AT 50 %RH. MICROSCOPIC ROUGHNESS OF TWICE RECHARGED LOW PACKED DIAMOND CYLINDERS, FIRST CYLINDER IS NEAR THE INLET AND THE SIXTH STACKED CYLINDER IS NEAR THE OUTLET WITH SD GIVEN FROM 10 MEASUREMENTS FROM BOTH SIDES OF EACH SPECIMEN.	90
TABLE 3.8. SUMMARY OF MEASURED OUTLET AND BULK TEMPERATURES TAKEN FROM CYLINDER STACK INVESTIGATION OF HIGH AND LOW PACKED DENSITY CYLINDERS FOR MULTIPLE RECHARGES (R1 TO R3).	94
TABLE 3.9. SUMMARY OF ABSORBED MASS VALUES (ΔM_{AB}) TAKEN FROM CYLINDER STACK INVESTIGATION OF HIGH AND LOW PACKED DENSITY CYLINDERS FOR MULTIPLE RECHARGES (R1 TO R3).	94
TABLE 4.1. CRUSHING STRENGTH AND ATTRITION LOSS OF NA-X ZEOLITES [5].	106
TABLE 4.2. MEASURED UCS AND COMPRESSION MODULUS OF AS-CAST AND SINTERED ZEOLITE 13X COMPOSITES AT 1.67 s – 3 AND 5 s – 2 STRAIN RATES. ‘*’ INDICATES MODULUS VALUES CALCULATED USING USC SAMPLES.	120
TABLE 4.3. DIFFRACTION ANGLES (θ) ASSOCIATED TO THE 111, 220, AND 311 PLANES COMPOSING THE FAU FRAMEWORK, AND D-SPACING (D) OF MEASURED CRYSTALS THAT SATISFY BRAGGS LAW CALCULATED USING PEAK CENTRES, AND RELATIVE INTENSITIES (IREL) CALCULATED USING PEAK AREA.	124
TABLE 4.4. MEASURED SURFACE AREA, PORE VOLUME, AND PORE SIZE OF S BASELINE, NON-SINTERED 4 WT% CRS, NON-SINTERED 4 WT% MC/PVA, 4 WT% CRS, ES, AND 4 WT% MC/PVA, ES SAMPLES.	129
TABLE 4.5. CALLIPER MEASURED BASELINE AND 4 WT% CSR SAMPLE LENGTH (L), WIDTH (W), THICKNESS PARALLEL TO PRINTED TOP LINES (T_A) AND THICKNESS PERPENDICULAR TO PRINTED TOP LINES (T_E) WITH VERTICAL DISTORTION PROVIDED AS PERCENTAGE CHANGE BETWEEN T_A AND T_E	132
TABLE 4.6. RHEOLOGY PARAMETERS FOR DW CHARACTERISATION: POWER LAW INDEX (N), SHEAR STRESS (τ), FLOW CONSISTENCY INDEX (K), VISCOSITY (H), AND PRESSURE CHANGE (P) OF BASELINE WITH 54, 52.5, AND 51 WT% DI WATER AND CSR PASTES OF 1 TO 8 WT%.	138
TABLE 5.1. SEBS ADDITION TO RPP AND WT% SEBS CONTENT IN RPP/SEBS BLENDS FOR ANALYSIS.	150
TABLE 5.2. PRINT PARAMETERS FOR PRINTING RPP/SEBS FILAMENT.	152
TABLE 5.3. UNIT COSTS USED IN COST BENEFIT ANALYSIS.	155
TABLE 5.4. DSC RESULTS: THERMAL PROPERTIES OF RPP/SEBS BLENDS.	156
TABLE 5.5. SEBS PARTICLE DIAMETERS AND CALCULATED LIGAMENT THICKNESSES OF RPP/SEBS BLENDS USING A LOWER PARTICLE DIAMETER LIMIT OF 10 μ M AND UPPER DIAMETER LIMIT OF 20 μ M FOR NOT ANNEALED SAMPLES (NA), AND A LOWER PARTICLE DIAMETER LIMIT OF 2.5 μ M FOR ANNEALED (A) SAMPLES, ERROR GIVEN IN BRACKETS IS SD.	171
TABLE 5.6. COST BREAKDOWN FOR PRODUCTION OF 15 KG PER DAY OF 1.75 MM RPP/SEBS FILAMENT AT A RATE OF 1 KG/HOUR WITH A SONGHU SHSJ-25MM EXTRUSION SYSTEM.	174
TABLE 6.1. COMPOSITION OF ITERATED BONE MIMICKING EPOXY COMPOSITES AND ASSOCIATED ABBREVIATIONS, *NUMBERS ARE WT% ADDITIONS.	185
TABLE 6.2. ADDITIVE MATERIALS WITH QUOTED DENSITY FROM SUPPLIER DATA SHEET.	188
TABLE 6.3. YIELD POINT, ULTIMATE COMPRESSION STRENGTH (UCS), AND FRACTURE POINT DATA FOR DRILLED COMPOSITES AND PIG BONE DRILLED WITH A 1750 RPM SPINDLE SPEED AND 1 MM/S AND 1.5 MM/S FEED RATES. SD ERROR IS GIVEN IN BRACKETS.	193

TABLE 6.4. YIELD, UCS, AND FRACTURE DATA OF METHOD 2 DRILLED MULTIPLE ADDITIVE CB1-CB5 SAMPLES. SD ERROR IS GIVEN IN BRACKETS.....	195
TABLE 6.5. DENSITY, POROSITY, FLEXURAL AND COMPRESSIVE PROPERTIES OF DEVELOPED COMPOSITES. STANDARD DEVIATION IS GIVEN IN BRACKETS.	202

Abbreviations and Symbols

Acrylonitrile butadiene styrene (ABS)

Additive manufacturing (AM)

Blue wrap (BW)

Brunauer-Emmett-Teller (BET)

Calcium chloride (CaCl_2)

Capital Expenditure (CAPEX)

Coefficient of performance (COP)

Computed fluid dynamics (CFD)

Computer aided design (CAD)

Compression strength (CS)

Core shell rubber (CSR)

Critical ligament thickness (L_c)

Crystallinity (X_c)

Critical particle diameter (D_c)

Crystallisation temperature (T_c)

Differential scanning calorimetry (DSC)

Direct Writing (DW)

Electron dispersive spectroscopy (EDS)

End of life (EoL)

Energy from waste (EFW)

Enthalpy change (ΔH)

Extrusion pressure (Δp)

Fused deposition manufacturing (FDM)

Fused Filament Fabrication (FFF)
Geometric coded (G-code)
Geometry creation parameter (h_{puddle})
Geometry factor close to unity (β)
Glass fibre (GF)
Glass transition temperature (T_g)
Global goal (GG)
Greenhouse gas (GHG)
Gypsum (GY)
Heating, ventilation, and air conditioning (HVAC)
Height (h)
Hydrostatic pressure (σ_{HP})
Hydroxyapatite (HA)
Layer surface energy (γ_{SE})
Life cycle assessment (LCA)
Mass (m)
Meltblown-spunwoven-meltblown (SMS)
Melting enthalpy (ΔH_m)
Melting temperature (T_m)
Melt flow index (MFI)
National Health Service (NHS)
nTopology© (nTop)
Optical microscopy (OM)
Particle loading (Φ)
Particle volume fraction (ϕ_r)

Personal protective equipment (PPE)

Polycarbonate (PC)

Polyethylene (PE)

Polylactic acid (PLA)

Polypropylene (PP)

Polyvinyl alcohol (PVA)

Power law index (n)

Pressure (P)

Recycled polypropylene (rPP)

Room humidity (RH)

Scanning electron microscopy (SEM)

Selective laser sintering (SLS)

Solidworks® (SW)

Standard deviation (SD)

Shear rate (γ)

Specific heat capacity (c)

Styrene-ethylene-butylene-styrene (SEBS)

Surface arithmetic mean height (Sa)

Surface goal (SG)

Surface kurtosis (Sku)

Surface maximum height (Sz)

Surface maximum peak height (Sp)

Surface maximum pit height (Sv)

Surface root mean square height (Sq)

Surface skewness (Ssk)

Stereolithography apparatus (SLA)

Sustainable development goals (SDG)

Thermochemical heat storage (THS)

Thickness (t)

Thickness perpendicular to top lines (t_e)

Thickness parallel to top lines (t_a)

Triply periodic minimal surface (TPMS)

Ultimate compression strength (UCS)

Ultimate tensile strength (UTS)

Viscosity (η)

Volume (V)

Volume flow rate (Q)

Width (w)

X-ray diffraction analysis (XRD)

Chapter 1. Introduction

1.1. Aim of the thesis

This thesis aims to design and develop polymer composites for sustainable applications while leveraging the benefits of additive manufacturing (AM) to identify opportunities that accelerate a transition towards a circular economy (CE). The primary AM methods used are fused filament fabrication (FFF) and direct writing (DW) for their potential to manufacture parts of diverse product functionality owed to a variety of compatible materials and printer hardware set-ups. They also enable the local manufacture of custom composite parts. In achieving local manufacture of final products, a great deal of supply chain transportation can be negated. A theme of abundant, low cost, and local acquisition of materials runs through this thesis with the aim to accommodate rapid scaling and market penetration of each sustainable product.

This thesis aims to derive methods capable of reducing unnecessary consumption of common plastics such as polypropylene (PP). Upcycling of PP from a previous single-use hospital waste stream into FFF filament aims to ultimately curb virgin PP production rates by matching its mechanical properties and printability. The non-renewable energy consumed during the production and disposal of common plastics such as PP is a significant source of global greenhouse gas (GHG) emissions. An aim of this thesis is to develop thermochemical energy storage (TCES) composites using salt hydrates embedded FFF lattices that are optimised using finite element analysis (FEA) simulations and novel triply periodic minimal surface (TPMS) geometries. This thesis aims to develop compression strengthened DW zeolites for gas separation as manufactured using proposed printing parameters as optimised using extrusion pressure and cone-plate viscometry measurements. Another aim that demonstrates the active sustainability potential of polymer composite based AM is to formulate bone-like phantom composites for medical model application, clarifying possible additives and their combinations in epoxy resin.

Each chapter aims to contribute knowledge to the field of polymer composites through the assessment of novel AM materials detailing their structural and mechanical properties. Imaging and imaging analysis aims to correlate macrostructures, microstructures, and morphologies to mechanical properties that are primarily investigated using tensile and compression testing. Discussions around each polymer composite aim to elaborate on fundamental and applied sciences to aid a transition to a CE. The design of methods aims to clarify AMs prospects in nearing zero waste and achieving a CE.

1.2. Additive Manufacturing

The recent growth of AM popularity has contributed to the increased fidelity, on-demand accessibility, and customisability of manufactured parts as applied in various sectors ranging from medical to aerospace [1–3]. Many AM options now exist capable of creating parts of superior form and function compared to those made by traditional methods [4]. Recent surveys of industrial bodies describe how the development of new AM materials and composites are considered top industrial priorities based on their potential to enable fully scalable AM manufacturing [5].

Popular AM types include FFF, stereolithography apparatus (SLA), and selective laser sintering (SLS) pioneered and applied since AMs inception in the mid-1980s [6–8]. Manufacturing via AM is not simply limited to direct manufacturing of end-use parts. In fact, it is typical for a given AM product to be post-processed or combined with traditional manufacturing methods to offer beneficial geometry and functionality [9]. Further processing of an AM part can include printed support removal, smoothening of the layered surface, or surface functionalisation by coating or spraying [10–12].

Fused filament fabrication is the most used type of AM due in part to a low cost of hardware and rapid prototyping potential [13]. FFF is a form of three-dimensional (3D) printing, a term often used synonymously with fused deposition modelling (FDM) and AM. FDM is a Stratasys trademark term whereas FFF is not, hence FFF is used throughout the thesis. 3D printing is a layer-by-layer method of AM that manufactures a computer aided design (CAD) part using slicing software (Figure 1.1). The slicing software uses complex algorithms to establish the layered formation of the part while providing a geometric coded (G-code) route that the printer nozzle travels to build each layer. Two print heads can be used to create multi-material prints with the support structures often being printed from a dissolvable polymer, e.g., polyvinyl acetate (PVA) in water. Dissolving a support material helps fully remove support from secluded areas which also reduces risks of physically damaging a print. SLA that utilises a laser to cure a vat of polymer to form typically less robust but precise parts, and a more precise method is two-photon printing capable of creating features of $<1 \mu\text{m}$ diameter [1,14,15]. Binder jetting is an AM technique that builds a 3D object using a powder-based material and adhering liquid binder using a roller, another jetting method is multijet (or polyjet) capable of printing typically challenging materials such as waxes [15,16].

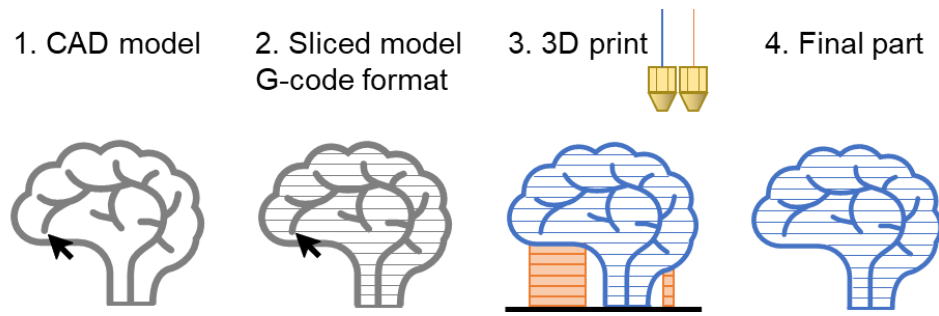


Figure 1.1. 3D printing process from CAD model to final part including computed representation shown in grey, support material shown in orange, and final part material shown in blue.

A popular material type for FFF is rigid plastics due to their suitable thermal properties and complex modelling capabilities [17]. Poly-lactic acid (PLA) is the most utilised and potentially most suitable material for FFF printed parts specifically because PLA has a glass transition temperature (T_g) of about 58 °C (Figure 1.2) and low melt flow index (MFI) of typically <10g/10mins which is ideal for extrusion and layering at room temperature [18,19]. The glass transition of a polymer is a process whereby the amorphous regions transition from a glassy state to a rubbery state upon heating [20]. PLA's chemical make-up and thermal properties yield low warping prints that do not require a heated bed, but a heated bed is often used because it smooths the cooling curve resulting in less localised stress and shrinkage of an amorphous structure that can help improve printed accuracy and mechanical properties [21]. However, PLA is limited by its mechanical properties namely low impact strength in-turn limiting its utility for engineering applications [22]. The properties of PLA can facilitate bioactivity and heat induced shape memory for printing of porous scaffolds for bone regeneration when combined with additives such as hydroxyapatite (HA) [23].

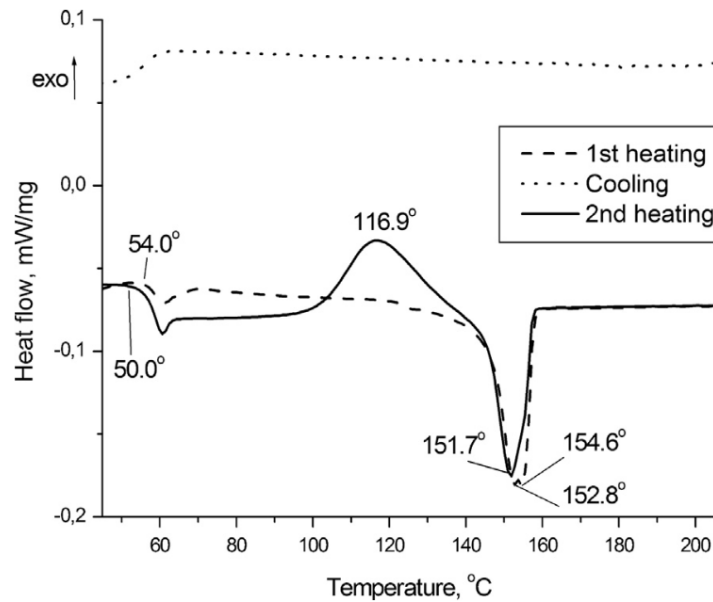


Figure 1.2. Heating and cooling curves of PLA showing glass transitions at 54 and 50 °C, cold crystallisation at 117 °C, and melting peaks at 152-155°C. The values depend on heating cycle number [23].

The heating and cooling differential scanning calorimetry (DSC) curves of PLA reveals a melting peak (T_m) that changes upon another thermal cycle due to the development of a different morphology (Figure 1.2) [23]. Melting of a thermoplastic is an endothermic process that occurs over a temperature range whereby energy is transferred to the polymer chains in crystalline formation that lose their ordered structure [20]. DSC was developed in 1962 and is now commonly utilised to provide information on physical and chemical changes with temperature, such as crystallization, melting, freezing, and oxidation [24]. The T_g and T_m represent temperature constraints of a plastic for industrial application depending on the intended environment. The term ‘plastic’ is differentiated from the term ‘polymer’ by noting that a plastic is a material that pertains some structural rigidity under load and are used in general-purpose applications as explained by Callister and Rethwisch [20]. Polymer materials such as PLA can change between semi-crystalline and more amorphous on thermal cycling to provide a cold crystallisation peak (T_c), in this case at 116.9 °C (Figure 1.2). Plastics can show T_c dependence on heating/cooling rate with greater cold crystallisation occurring at faster cooling rates, and T_c increasing with increased heating rate [25].

PLA is derived from plant starch whereby the monomer of PLA is lactic acid and is obtained by fermentation by bacterial activity [26]. PLA is polymerised by polycondensation of lactic acid which involves two reaction equilibria: (1) dehydration equilibrium for esterification, and ring-chain equilibrium

involving (2) depolymerization of PLA into lactide dimer (Figure 1.3) [27]. Fermentation of biomass has gained popularity along with the increased concerns of fossil fuels scarcity and unsustainable polymerisation of petroleum-based plastics. PLA has experienced great industrial uptake due to the prospects of renewable resources curbing environment damage caused by the plastics industry [28].

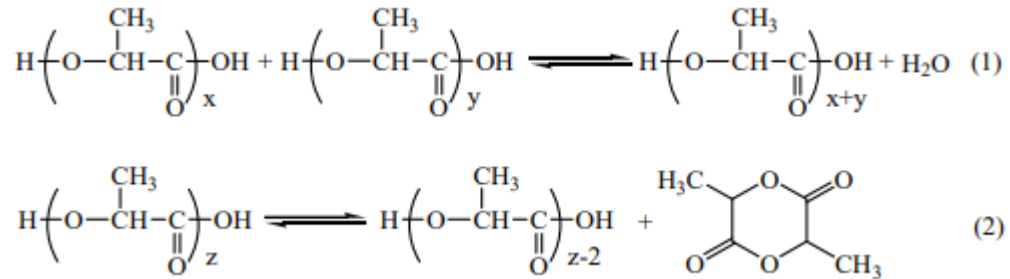


Figure 1.3. Reactions required to form PLA [29].

The biodegradable properties of PLA are of interest for medical application as bioabsorbable implants [30]. Utilising FFF for pharmaceutical drugs allows for custom drug doses, avoiding the ‘one drug fits all’ approach [31]. AM affords many medical innovations for products such as implants, prosthetics, and tissue engineering [32,33]. Later in this thesis in Section 2.4.4 the printing of medical models is described. AM enables the creation of complex lattices of porous structure that improve adherence properties to bone [34], and in Section 2.4.2 the printing of porous structures is described.

A well-known concept to polymer scientists designing biodegradable polymers of controlled contact with fluidic media is that a polymeric structure is degradable to its constituent monomer, often most effectively achieved by compounds of similar chemical composition to that of the polymer [35]. Therefore, PLA is highly susceptible to bulk hydrolysis and requires rigorous storage conditions to avoid product expiry [36]. Another popular polymeric material for printing FFF parts is acrylonitrile butadiene styrene (ABS), which has the advantages of increased toughness, higher temperature and weathering resistance compared to PLA which is of higher tensile strength, shear strength, and of lower coefficient of friction [6,37,38]. FFF parts are typically weaker than injection moulded parts due to a lower part density by 2-10%, however, FFF parameters including infill pattern, infill density, raster gap, and raster angle can be tuned to achieve flexural strength within 12% of that achieved using injection moulding [6,37]. The effects of additives, such as montmorillonite, which is discussed in Section 1.11, more greatly improve the

dimensional stability and tensile strength of printed ABS in comparison to injection moulded ABS [39].

Polycarbonate (PC) is also printable by FFF and is growing in popularity due to lightweight, tough, and heat resistant properties that finds use in pipe wall, roofing, and electronic casing manufacturing. Polycarbonate an engineering plastic for automotive and medical application including implantable scaffolds [40]. As with all common FFF polymers PC can be printed to form custom geometries for on-site and short lead time manufacture. Polypropylene is also commonly selected for low-cost production and is suitable for use as a 3D printable filament material [41].

Interest in 3D printing to grant a second life to waste plastics has increased in recent years along with research to unlock this application. Methods include modification of a recycled polymers thermal and mechanical properties to overcome polymer degradation that results from exposure to high temperatures and moisture during use which prevents extrusion of high-quality products [42]. One of the most important properties for FFF filament is melt flow index (MFI), values for which are commonly provided in product specifications because of its significant influence on printing parameters. Low MFI polymers are required for 3D printing to maintain an extrusion die cross-section and retain stability when semi-molten during printing. Wang *et al* suggested a suitable threshold value of 10 g/10mins for PLA, the most common printer filament material, stating plasticiser type and crystallinity also play important roles during the printing process and must be considered in addition to MFI [19].

1.1. Global Plastics Problem

There is a consensus on all synthetic polymer types that includes a bad reputation because they are considered environmentally damaging in part due to a carbon footprint that makes up approximately 4.5% of global GHG emissions [43]. Other condemnable factors include long decomposition times typically measured in $\mu\text{m}/\text{year}$ hence products last decades or centuries as accumulated litter in the natural environment particularly marine environments that totals approximately 125 Mt of plastic [43–46]. Anthropogenic plastic waste has recently been found in remote natural locations including the arctic sea ice, and at the bottom of oceans [47,48].

Plastic litter tends to degrade into smaller and smaller fragments. Anthropogenic macro and microplastic litter released from rivers into oceans is currently not accurately tracked and measured [49]. Proposed solutions to the global plastics litter problem can be policy or technology driven. The former is quite dependant on promoting re-use and re-manufacture of plastic products. The mechanical recycling of post-consumer plastics is complicated by the similar densities of polyethylene (PE) and polypropylene (PP) that are challenging to separate by float-sink separation [50]. Hence mixed polyolefins are widely available as recycled material but are of inferior properties to collected homogeneous plastic streams due to the immiscibility of single stream wastes. The collection and recycling of post-industrial waste plastics tends to be more readily achieved than that of post-consumer waste which consists of mixed plastic types of unknown composition and degree of contamination [50].

Considering the global plastics problem, concerns have been raised about resulting single-use plastics production and potential environmental impacts resulting from improper disposal and waste management [51]. Promising solutions to the global plastics problem are included in a directive (EU 2019/904) that prioritises re-usable products and systems, an extended producer responsibility scheme, the elimination of single-use plastic products, and a CE of closed loop plastic materials flows at end-of-life (EoL) [52]. The latter is also key to unlocking the sustainable potential of distributed manufacturing systems based on AM [53]. In 2021, the use of AM increased by 12 to 19% with a projected 24% compound annual growth rate (CAGR) for the next five-years [5]. FFF was utilised as an emergency (>2 weeks production time) in-house method for supplying hospital workers with personal protective equipment (PPE) during the global coronavirus pandemic [5,54–56]. Charlotte MEDI volunteers reached a total production of 100,000 face shields made using open-source CAD models [55].

Traditional plastic processing methods depend heavily on PP, which accounts for 27% of global thermoplastics demand [57], more than any other polymer, and so developing circular economy solutions for PP based products is perhaps more important than for any other type of plastic.

1.2. End-of-Life Strategies for Plastics

A circular economy aims to maximise value derived from products throughout their entire lifecycle and retain materials and products within the economy through consecutive product lifecycles [58]. A linear economy generates value at the point of product sale only. Conversion of waste materials into secondary raw materials facilitates a CE by valorising products at EoL, offsetting primary raw materials demand and offering synergistic environmental, economic, and societal benefits as otherwise unrealised through landfill and energy from waste (EFW) [59]. Minimising raw material demand and maximising the utility of plastics at EoL is often achieved by following the waste hierarchy which has several adaptations depending on the intended outcome but follows the general steps of reduce, reuse, recycle, recover, dispose [60].

Many industries such as aerospace, automotive, energy generation, energy storage, and medicine depend on plastics that cannot be easily recovered, reused, remanufactured, and recycled. Centres of excellence such as universities, large commercial laboratories, and authorities that contribute to online data systems such as WasteDataFlow by the Department for Environment Food and Rural Affairs (Defra) help provide guidance for waste producers on non-recyclable plastic waste management [61]. Where a lack of governing regulations exists, a key driver for reducing waste and advancing a CE is strategic partnerships between corporations and entrepreneurs that help establish viable business models [62]. Recent approaches to improving management of non-recyclable waste includes zoning which aims to reduce environmental damage caused by hazardous waste and associated collection costs by prioritising waste collection in certain geographic areas [63].

Wales is an international leader in policy for recycling and circular economy, achieving 65% recycling of municipal waste which is one of the highest rates in the world [64]. Many plastics not yet recyclable are single-use, and the Welsh Government have recently implemented strategies to tackle this issue including the ban of nine environmentally harmful single-use plastic products: plates, cotton buds, and straws [65]. Packaging compliance schemes are implemented by the UK government that aims to hold members accountable by ensuring they contribute towards the cost of recycling their packaging as tracked using packaging notes [66]. There are plans for mandatory digital waste tracking in place for the UK to help move towards a CE and extract maximum value from secondary resources [67].

Single-use plastics pertain demonstrable benefits in several applications such as health care and food packaging that necessitates their use, therefore alternative solutions to banning them is required to prevent environmental impacts at EoL. Landfill tax has been a successful policy measure to divert plastic waste from landfill to energy from waste (EFW) processes, however recycling into new products would be a more sustainable solution which increases derivable value and avoids residual waste treatment costs and emissions. The ability to valorise such materials at EoL through circular approaches creates economic incentives to collect waste plastics thereby stemming the flow of plastics into the environment. Despite national initiatives to maximise recycling, little incentive to collect single-use plastics has exists owing to a lack of economically viable recycling systems due to many low-value and low-density single-use plastics incurring large costs when transported to disposal/treatment facilities.

Interest has grown in reuse and recycling of medical waste globally to reduce natural resource use, increase availability of medical products during the global pandemic; reduce waste and financial burdens on hospitals; and reduce volumes of potentially contaminated waste which may impact public health [68]. Hospitals are a large source of unavoidable single-use plastics with one third of hospital waste arising from operating theatres, a considerable proportion of which is disposable plastic [69]. A study by Rothman and Ryan (2020) showed that in the UK, single-use protective clothing including spunbond-meltblown-spunbond (SMS) PP fabrics account for 13% of disposable plastic waste from the UK National Health Service (NHS), the greatest of 15 groups of plastic wastes considered (Table 1.1) [70]. Until recently these materials have been disposed of at cost to the NHS without viable recycling options. However, solutions to waste SMS have begun to emerge that increase derivable value, creating a revenue from these wastes. CircularBlu produces tote bags from hospital PP nonwovens that are sold to the healthcare industry [62].

Table 1.1. Disposable plastic products that passed through NHS supply chain in 2014/2015, ranked by mass per annum and percentage of total plastic waste produced [70].

Product Group Containing Plastics	Use (t/year)	% of total
Single-use theatre protective clothing (inc. drapes)	9,402	13
Examination gloves	7,952	11
Disposable wipes and cleaning cloth products	7,045	10
Catering products tableware and light equipment	5,628	8
Polymer products (aprons and bags)	5,244	7
Medical hollowware	5,044	7
Disposable continence care products	5,029	7
Blood collection systems (sample tubes & syringes)	4,851	7
General wound care	4,066	6
Suction consumables (catheters, tubing, drains)	3,823	5
Syringes, needles and associated products	3,353	5
Clinical waste containers	3,216	4
Medical packs and sterile supplemental products	3,028	4
Needle free connection systems products	2,324	3
Urology products (drainage bags, catheters)	2,296	3
Total disposable plastic containing products	72,301	

An alternative approach to recycle hospital PP curtains and single-use PP fabrics is on-site thermal compaction into dense recycled PP (rPP) blocks that improve the economics of transport and storage and can be sold for granulation and production of new PP products [71]. Recently, SMS waste has been collected from a hospitals' sterilisation and disinfection unit before on-site thermal compaction using a 'Sterimelt' machine to produce 15-20 kg PP blocks achieving an 85% volumetric reduction and thermal sterilisation rendering the material safe for use in new applications [72–74]. Handling PP in this form reduces carbon emissions associated with disposal and creates revenue for the NHS when blocks are sold to recyclers. This approach

overcomes potential recycling barriers including potential contamination, degradation, or mixed fractions, common issues for typical waste plastics which must be minimised to guarantee adequate quality for second life application as FFF printer filament [75]. The purpose of chapter 5 is to further the value of blue wrap rPP by conversion of its secondary raw material for 3D printing applications. An MFI of 118 g/10mins was measured for pelletised recycled SMS fabric by Bhat *et al.*, which suggests modification of the formulation will be necessary to reduce MFI for FFF printing [76]. Such a filament would provide a circular, short lead time supply solution for hospitals and other institutions currently relying on imports of unique products produced via conventional manufacturing.

1.3. Sustainable Innovation with Polymer Composites

Sustainability is a paradigm of generative action that can be described as passive, which is concerned with care and protection of socio-economic and environmental systems, and active, which promotes quantitative growth [77]. Sustainable innovations can be passive, active, or both and as such are unlikely to be zero waste across any given workflow line, lifecycle stage, or impact assessment step. Reinforced thermoset polymer composite are typically utilised in high force bearing applications and are energy intensive to create and dispose of therefore requiring active sustainability solutions [78]. Active sustainable innovations are decisive in providing short-term antifragility [77]. The work in chapter 6 develops medical phantoms using polymer composites, representing a sustainable innovation where options to avoid waste through remanufacturing and recycling are integrally limited. Innovations in the field of manufacturing sustainability can lead us to achieving near zero waste production across a given products lifecycle whereby processing depends only on renewable energy sources such as solar energy and offshore wind. A best-case scenario depends on transitioning to a CE as optimised through computational breakthroughs [79,80]. Currently, a continuous drive to increase global economies provides great opportunities to research and develop sustainable innovations compared to purely passive sustainability ones [81].

1.4. Manufacture of Bone-Like Polymer Composites

A popular derivative of 3D printing medical models is casting crosslinking polymer fluids into 3D printed moulds. Castable fluid chemical structures are customisable via multiple techniques that assist biomimicry of soft and hard tissues [33]. Many notable efforts include the replication of human kidney [82], liver [13], and brain tissue hardness [83] by 3D printing and casting. Hard tissue biomimicking models are less readily achieved due to the range of possible mechanical properties of patient bone. From a sustainability perspective, such properties that improve surgical capabilities develop human capital through successful procedures. Human capital is the only sustainable resource whose qualities can be developed and maintained through education and training [84].

3D printed bioglass-ceramic scaffolds have been modelled by AM for bone reconstruction [85]. Bioglass-ceramics are often silicon dioxide (SiO_2) based, with bone like properties achievable with calcium oxide (CaO) and phosphorus pentoxide (P_2O_5) addition [85]. Bone-like material can feature a sacrificial (e.g., 10 wt% PVA solution) polymer that forms a homogenous paste for printing purposes [85]. Tuneable compositions are then achievable by varying the additions during manufacture, in this case of SiO_2 :CaO powders. Glass fibre additions to epoxy matrices also enables bone-like properties as quantifiable by machining [86,87]. Additive bonding strength and wettability can influence epoxy compression strength and deformation characteristics, especially in the case of high particulate loadings [88]. Hydroxyapatite (HA) is a close approximation of the mineral content of bone and has been employed as a bone substitution material [7,89]. However, the hierarchical structure of bone composed of inhomogeneous osteons housing osteocytes that cannot be structurally mimicked by casting alone that poses a challenge to researchers aiming to mimic its mechanical properties. The time dependency of bone complicates its characterisation for patient specific applications. Bone biomimicry challenges includes patient specific mineral density, cortical wall thickness, range of biomimicking mechanical properties, and patient health and demographic (such as age, sex, weight) driven phantom customisation [90,91].

A composite of HA/PP is a feasible bone substitute material [89]. Considering bone as a composite with hydroxyapatite as the filler in a collagen matrix, the use of HA as an additive in an easily formable thermoplastic matrix is an appealing prospect. The process Bonner *et.al* used to attain a bone-like HA/PP

composite firstly cooled PP using liquid nitrogen (N₂) and then ground it into a fine powder using a centrifugal mill and compounded with the HA using a single-screw extruder [89]. Hydrostatic extrusion allowed the extruded fibres to be aligned to represent bones isotropic properties. Composite testing conditions altered bending modulus by a factor of four, and ductility by an order of magnitude, however there was no clear reference sample such as one composed of human or animal bone.

1.5. Recycled Surgical Blue Wrap Polypropylene

It was mentioned in Section 1.4 that blue wrap and other medical drapes used for surgical clothing and medical curtains account for the largest group of plastic containing products that pass through NHS hospitals. Van Straten *et al* investigated recycling of blue wrap from surgical instrument trays following sterilisation, melting and granulation before combining with virgin PP granulate for injection moulding of instrument openers [68]. They showed that melting temperature did not notably affect mechanical properties, and the inclusion of 25% virgin PP by volume compensates for degradation during the recycling process by increasing strain to failure by 50% (Figure 1.4).

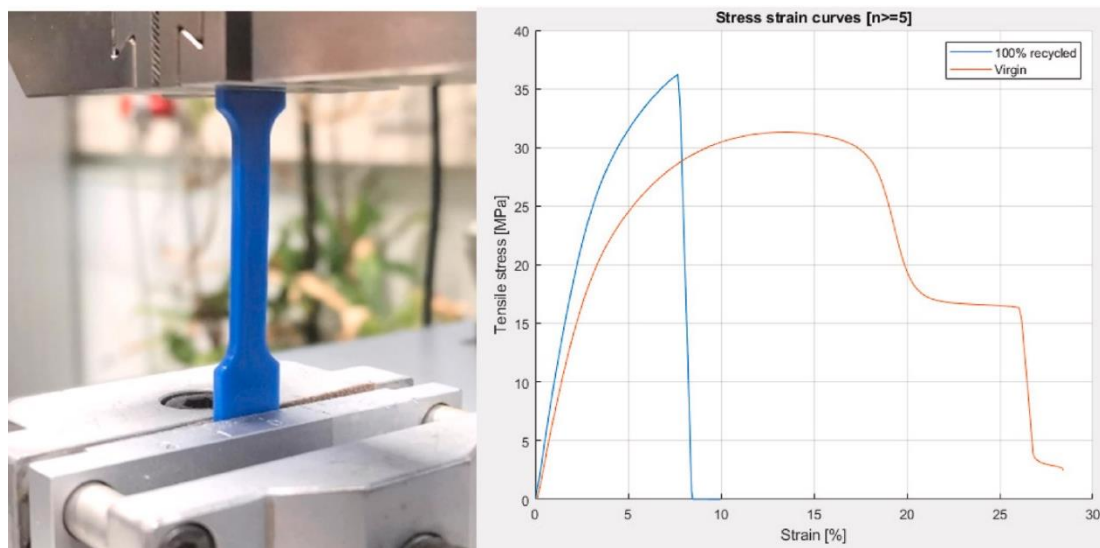


Figure 1.4. Tensile specimen of non-standardised dimensions (left) and tensile data comparing 100% recycled PP from hospital blue wrap to that of virgin PP of unknown MFI (right) [68].

Disposal of single-use PP blue wrap widely used in hospitals is currently a typical linear economic approach despite there being potential to recycle such

low-density material by thermal compaction and blending with compatible polymers for application as end-use products of tuneable mechanical properties.

Previous efforts to improve processability and mechanical properties of PP include compounding with natural rubber [92] and thermoplastic elastomers (TPEs) including ethylene-co-vinyl acetate (EVA) [93]; ethylene-propylene-diene monomer copolymer (EPDM) [94]; SEBS (styrene-ethylene-butylene-styrene) and styrene-isoprene-styrene (SIS) block co-polymers [95]; and SEBS grafted with maleic anhydride [96]. SEBS exhibits good interfacial adhesion with isotactic PP and syndiotactic PP surfaces [97]. This is particularly important for FFF where interfacial regions of printed structures represent weak zones and potential sites of structural failure (Figure 1.5). As this phenomenon is inherent to AM it requires novel materials ingenuity to overcome which to-date includes the addition of latent curing agents to thermosets and methods to reduce crystallinity rates of thermoplastics – allowing a strong bond to form by interlayer diffusion [98,99].

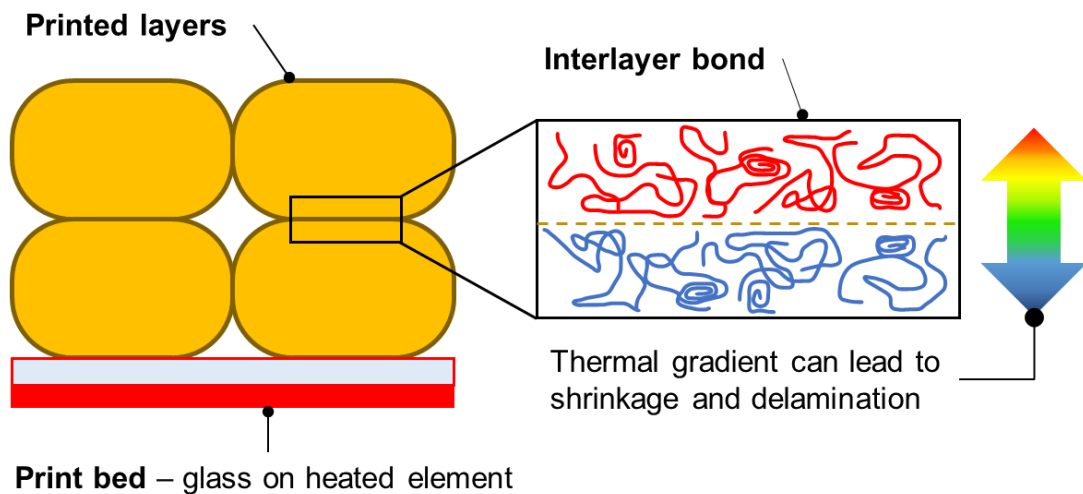


Figure 1.5. Schematic of printed layers on a heated print bed (i.e, build plate) with interlayer bonds of typical molecular separation and uneven cooling profile.

A strong molecular bond is achieved by SEBS diffusing into PP under micelle formation [100]. The blend morphology depends on the shape, size and spatial distribution of the miscible phases that result from a complex interplay between the MFI, interfacial properties, blend composition and processing conditions [101]. Blending PP with high viscosity SEBS has shown to reduce blend MFI [102]. Stable morphologies can be achieved at wide compositional ranges of SEBS in PP, and annealing when microphase-separated upon cooling has little influence on SEBS phase size [103]. Light microscopy has been used to show that polymer compounds that are initially miscible by mechanical

mixing can separate upon curing due to a step up in molecular weight [104]. Blending rPP with SEBS has been shown to increase tensile and impact strength of rPP while decreasing crystallinity, unlocking potential new applications, and compensating for any loss in thermo-mechanical properties observed in recycled materials compared to virgin raw materials [95]. Tough and miscible polymer blends are sought-after for force bearing applications and are of high economic value. This suggests that blending rPP with SEBS may significantly increase secondary material value especially if utilised as printer filament. Multiphase polymer systems can be evaluated using unified theoretical frameworks such as the Graessley equation used to predict 'self-diffusion' of layers that overcome interface activation energies [105].

Isostatic PP blended for improved mechanical performance sometimes exhibits draw-ability and mixing with strong counterpart plastics can yield high ultimate tensile strength (UTS) [106]. The crystallinity of PP can show correlations with tensile properties [107]. An increase in elastomer content such as SEBS increases elongation and reduces stiffness that can be related to increased crystallinity of the PP caused by increased matrix orientation [108]. A significant decrease in yield stress often correlates to increasing toughness, therefore the yield stress can serve as a qualitative measure of macromolecular chain mobility [109,110]. In the case of toughened PP/rubber systems, a sudden increase in ductility can be described by a mechanism of percolating stress volume spheres (Figure 1.6) [96]. This will likely occur when the interparticle distance is shorter than a critical value of matrix ligament thickness (L_c), of 0.05-0.44 μm for PP/SEBS systems that depend on SEBS particle size [111–113], where Van der Waals forces provide interparticle adhesion [114]. L_c is shown to be the single parameter determining whether a polymer/rubber blend will be tough or brittle [115]. A matrix ligament represents a blend and can help to assess optimum particle addition and dispersion for various processing methods.

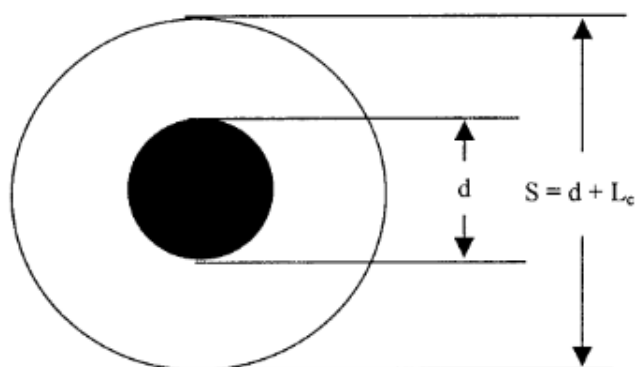


Figure 1.6. Schematic of ligament thickness (L_c), rubber particle of diameter (d), and stress volume sphere (S) [96].

The chemical composition of a blend governs re-processibility, which must be optimised to enable efficient recycling and reduce demand for virgin plastics.

1.6. Life Cycle Emissions from the Plastics Industry

There is no single approach for the plastics industry that achieves an absolute reduction of global anthropogenic greenhouse gas (GHG) emissions to below their current levels as forecasted by J. Zheng and S. Suh using a conservative 2% growth rate from 2015 to 2050. Findings suggest decarbonisation of the energy system used to produce conventional plastics is the most economically favourable and effective means of mitigating global life cycle GHG emissions by 51-62% (Figure 1.7) [116,117]. Resin production (1,085 MtCO₂e) and conversion stages (535 MtCO₂e) of a plastic's life-cycle present major GHG contributions, as too does incineration at EoL (96 MtCO₂e) [117]. In comparison the prospect of recycling 100% of plastics at EoL contributes a significant nett negative CO₂ equivalent (67 MtCO₂e) to global conventional plastic lifecycle emissions by avoiding the manufacture of virgin plastics. A transition to bio-based plastics (e.g. PLA), 100% renewable energy used for production, and complete plastics recycling (from 18 to 100%) and demand management (from 4% down to 2% growth rate) when all employed in unison can reduce projected global life-cycle GHG emissions of conventional plastics down to levels below their current level of 1,781Mt of CO₂e by 2050 [117]. The current trajectory of 4% growth rate without changes to production or EoL methods will result in 6.5 GtCO₂e global life-cycle GHG emissions from conventional plastics, and if all plastic waste is incinerated then total annual emissions reaches 8.0 GtCO₂e. Hence, ambitious strategic measures are required for the plastics industry to not further contribute to global GHG

emissions. Only at a 2%/yr growth rate, utilising a decarbonised energy mix by 2050, and producing no fossil fuel-based plastics can a reduction to zero emissions be achieved over the course of several years to decades past 2050.

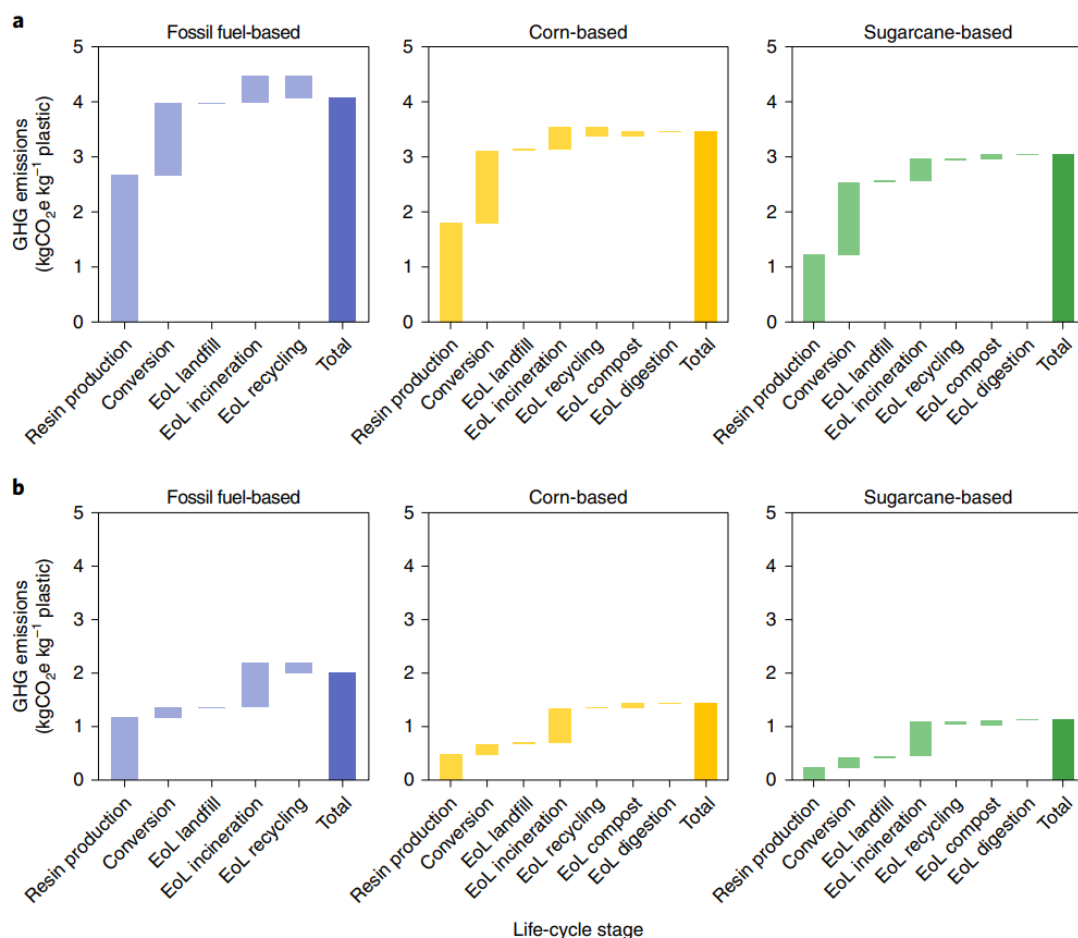


Figure 1.7. 2050 estimated GHG emissions of plastics derived from fossil fuel and natural (corn-based, and sugarcane-based) feedstocks under two energy-mix scenarios: an energy mix based on 2019 generation (a), and a 100% renewable energy scenario (b) showing total emissions approximately half regardless of the energy systems used [117].

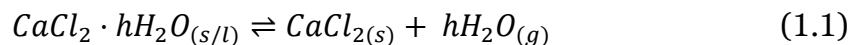
In transitioning industrial technologies that drive a linear economy towards ones that drive a circular economy a promising strategy is to prioritise improvements guided by the 17 sustainable development goals (SDG) [118]. Achieving net benefits according to strategic goals may affect other goals and ideally a holistic approach monitors impacts that certain goals have on one another [118,119]. Throughout this thesis waste plastics, gas separation for CO₂ capture, and energy storage is addressed by utilising FFF and DW that provides the potential to improve sustainability via use of secondary raw materials or abundant and reusable as starting products. The chosen applications are selected to work towards SDG 7 – affordable and clean energy,

SDG 12 – responsible consumption and production, and SDG 13 – climate action.

1.7. Thermochemical Heat Storage

Energy storage is needed to enable the transition from a fossil fuel centric economy to a renewable energy centric economy because sustainable energy generation is harnessed intermittently and is not in demand proportionally. Heat transfer plays a crucial role in managing and promoting efficiencies of a range of energy conversion devices [120]. Thermochemical heat storage (THS) has a distinct advantage over competing heat storage methods as it is of highest potential energy density compared to common sensible and latent heat storage [121].

In THS systems, heat is transferred from a source of excess heat to a storage medium which then stores and releases thermal energy depending on the demand for heat [122,123]. Effective THS depends on temperature control using materials of high storage density and thermal conductivity. Salt hydrate materials such as calcium chloride (CaCl_2), magnesium chloride (MgCl_2), and magnesium sulphate (MgSO_4) are often employed as an energy storage medium for their high energy storage density with reversible charge/discharge potential, while porous structures with high surface area are ideal hosts for salt hydrates [124]. A saline solution forms during the reversible de/hydration reaction as described by equation 1.1 for CaCl_2 .



Thermal energy is required to supply reaction enthalpy ΔRH and dissociate $\text{CaCl}_2 \cdot h\text{H}_2\text{O}$ which depends on the state of hydration, h [125]. A saline solution limits host matrix material selection and stability by inducing swelling and deliquescence [126]. Novel host matrices aim to alleviate these shortcomings via pore networks that improve vapour and solvent diffusion for complete deliquescence of the salt hydrate while containing the solution so that ΔRH can be repeatably maximised [127].

Typically, a packed bed system (Figure 1.8) is formed using beads that form a pressure drop and reduced gas velocity which is required to drive vapour to the surface of porous matrices but limits effective reactor length, which is compounded by embedded salts that swell in size [128,129]. Recent

developments have worked towards higher contact surface areas (air → absorbent) for improved vapour diffusion and lower pressure drop [130]. Poor system design with too many water molecules per compound of salt can lead to deliquesced crystal agglomeration that impedes diffusion and causes material degradation when charged.

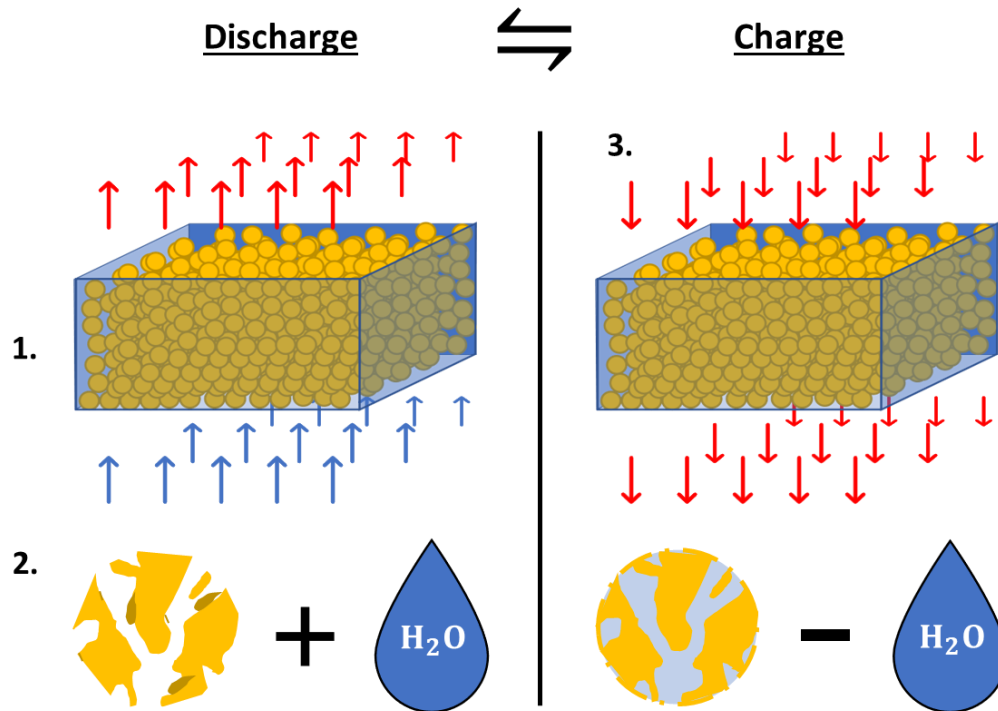


Figure 1.8. Illustration of a packed bed open chamber (1.) containing pellets of porous structure (yellow) with impregnated salt hydrate (dark yellow, 2.) for discharge with high RH% input flow. The reversible charging cycle requires a low RH% and often heat is supplied (3.) to fully charge the salt hydrate.

The energy required to charge the system is equivalent to the enthalpy of hydration. Discharge energy is the energy recovered upon dissociation. For best possible performance the system must maximise the work done from its environment during the charge cycle and minimise energy loss during discharge. For this reason, a selected THS salt hydrate must have a suitable working temperature range for the intended environment. The amount of work a system can perform when at thermodynamic equilibrium with its environment is termed exergy and is used in THS to provide a compliment to energy assessments [131]. It provides an understanding of the heat dissipated to a reactors environment by considering the first and second law of thermodynamics.

Heat transferred using host AM phase-change embedded structures, where the host matrix is mechanically and chemically compatible, can provide even

temperature profiles through a chamber for efficient storage [132]. There is a considerable opportunity to control charge/discharge cycles using AM enabled phase change designs. Examples where AM has been employed for thermal energy harvesting and storage include solar steam-generation [133], solar-evaporators [134], and solar thermal bioinspired micro-lattices [135]. Many existing and novel phase change materials, including thermoregulating core-shell salt hydrates, have the potential to be combined with AM for energy storage at a range of temperatures [136]. Tabard *et.al* directly 3D printed (by direct writing, Figure 1.9) zirconia ceramic matrices treated by partial sintering and impregnation with MgSO_4 that resulted in rechargeable prints of energy density up to $420 \text{ kWh}\cdot\text{m}^{-3}$ [137]. Vapour transport to salt surface relied on hierarchical pore sizes (from 200 nm to $200 \mu\text{m}$) controlled by a wheat starch additive, and bridged zeolite particles. A similar concept for improved mass transfer and heat transfer was employed by Middelkoop *et.al* but for use in gas sweetening units, who printed zeolite 13X AM adsorbents of highly defined lattice networks to replace standard pellet configuration [138]. Printed adsorption performances were comparable to pellets but the AM zeolite 13X structures improved potential mass transfer for on-demand and scalable pressure swing adsorption unit manufacture.

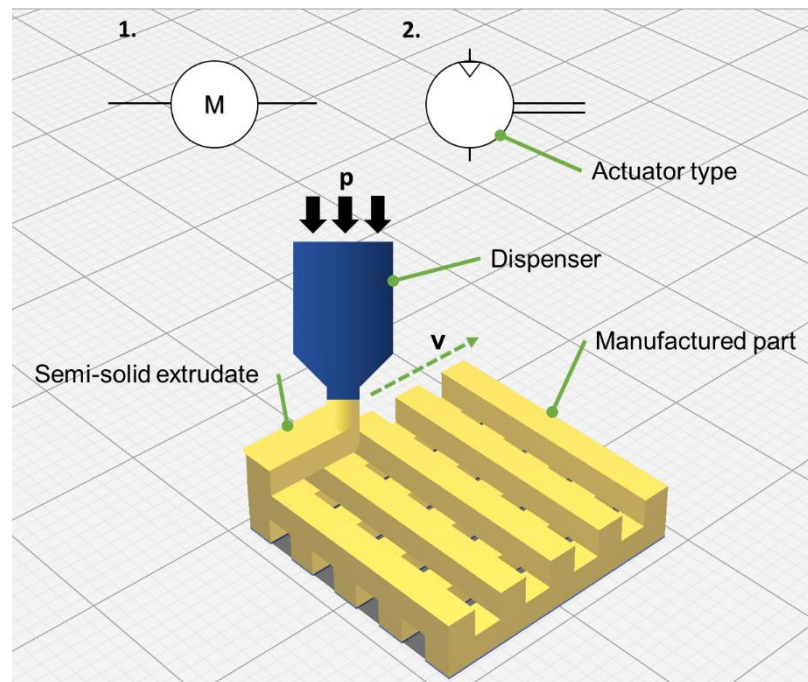


Figure 1.9. Direct writing illustration showing a semi-solid extrudate and 'wood pile' manufactured part via two common actuator types: 1. electric motor, 2. pneumatic motor. Pressure (p) is applied to the feedstock held in and extruded from a dispenser – often a syringe for small parts – travelling at velocity (v).

Electrical input is required for such forced convection systems, typically a fan provides airflow that evolves the heat and moisture profiles during packed bed discharge and recharge. An open THS system whereby gas flows through the reactor into its environment can be designed to reduce pressure drop for improved electrical coefficient of performance (COP) [130].

Advantages of controlled THS charge/discharge include host matrix fatigue resistance, efficient reactor cyclability, and comfortable temperature performance in buildings. Energy storage efficiency can be maximised for heating, ventilation, and air conditioning (HVAC) application using time saving computed fluid dynamics (CFD) [139]. Open THS systems can be combined with solar collectors that cycle between warm dry air and cold moist air each day [140].

The efficiency of an THS system depends in-part on fluid body motion around the matrix hosting salt, velocity and turbulence are key factors that affect phase change and temperature uplift (ΔT) [121,141,142]. The topology of the storage medium therefore influences temperature control [143,144]. Temperature control is important for an even temperature output and stable charge/discharge cycle. Matrix materials are typically porous ceramic beads that are mechanically brittle but chemically and thermally resistant. Often made from zeolite [145,146], bentonite [147,148], or vermiculite [149–151], they are impregnated with a salt for their low cost and high reaction enthalpy (of 11 to 384 kJ/mol depending on the salt [123]) and but are often limited to packed bed system design where beads adopt the shape of the container. Other host matrix materials employed by systems of notable heat storage efficiency include expanded graphite [152], mesoporous silica [153], and polymers [127,154]. Heat and mass transfer simulations can lead to novel matrix material selection based on energy storage per unit volume, such as ideal zeolite crystal configurations that increase heat of adsorption and reduce water mobility [155]. Vermiculite has shown significant promise for open THS systems when embedded with calcium chloride (CaCl_2), with excellent energy density, good response time to moisture, moisture uptake, and significant mass loss in the working range $30 < T < 140$ °C [130].

Bentonite is mostly composed of montmorillonite, i.e., hydrated sodium calcium aluminium magnesium silicate hydroxide, a subclass of smectite that is characterised as a 2:1 phyllosilicate mineral of octahedral charge half that of vermiculite [156]. Isomorphous substitution of cations for Al in the central alumina plane provides cation exchange capacity (Figure 1.10), hence the

exchangeable cations provide the dominant driving force for montmorillonite to swell [157].

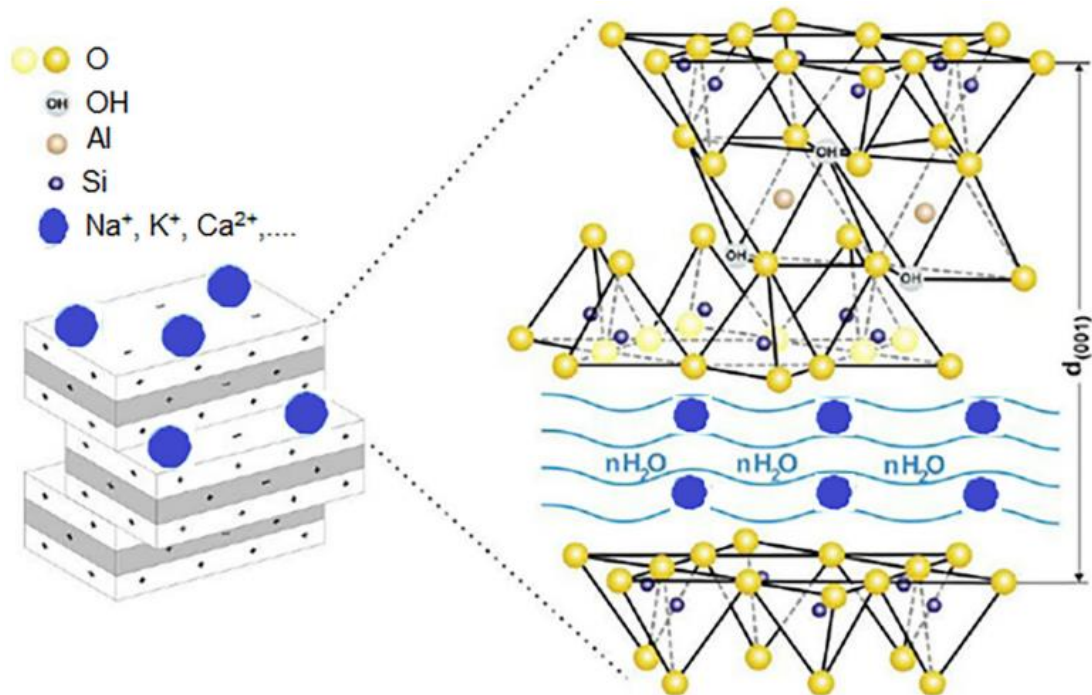


Figure 1.10. Schematic of bentonite structure with exchangeable cations [158].

Montmorillonites expand considerably more than other clays due to low pressure concomitant water adsorption. This is due to the type of exchangeable cation contained in the sample [159]. Natural bentonite when impregnated with CaCl₂ provides high THS storage density of 855 kJ/kg, and cycling stability of 93% efficiency retention after 10 cycles due to a stable shape of hydrated salts [147].

Sustainably sourcing salt hydrates and their host matrices is important when considering a THS system lifecycle. This means using non-toxic and abundant materials are beneficial while ideally being acquired locally with low energy required. The majority of bentonite is sourced from Morocco and shipped internationally; however, bentonites are abundant as they are formed from the hydrolysis of volcanic ash [89]. LCAs help to identify potential trade-offs at various stages of product development, deployment, use, and EoL. Zeolites offer higher surface area host matrices as they are more microporous than bentonites and are utilised accordingly for water treatment, catalysis, gas separations, and CO₂ capture.

1.8. Microporous Materials for Gas Separation

Microporous scaffolds provide adsorption, absorption, and transport of gasses emitted from fossil fuel burning processes in raw materials processing, internal combustion engines, and non-renewable energy generation which avoids GHG escape into the atmosphere affecting the global climate and human health [160,161]. CO₂ capture, chemical conversion, and storage are major sustainability challenges that require the continued development of economically feasible advanced materials [162].

CO₂ capture materials and configurations can be precisely controlled for rapid filtering of selected contaminants. Microporous materials can be of natural or synthetic origin and their structure and pore size, cationic charge density, and polarizability dictate the molecule that can be selectively removed from a flow of gas [163]. Structurally hierarchical design and stability of the sorbent material across multiple dimensions from angstrom to centimetre is of significance to the efficiency of CO₂ capture, where the meso- and macrostructure of a sorbent can be controlled and optimised by employing additive manufacturing [164–166].

Solid sorbents are commonly prepared as powders or porous binder-based pellets that result in limited gas permeability and sub optimal gas flow when compared to 3D printed sorbent structures [167]. Advances in material synthesis over the last few decades have enabled the development of nanoporous materials with uniform, tailormade pore structures [168]. A 3D printed gas permeable sorbent and binder composite is free of many geometric design constraints for high surface area-to-volume ratios and rapid adsorption compared to common ‘packed tower’ arrangements. Reactor housings can be fitted with complex structures printed for desirable gas flow owing to the customisation potential of robocasting [167,169]. Robocasting is a form of direct ink writing, and these terms are often used analogously with DW [170,171]. One design consideration when DW sorbent prints of zeolitic composition is filament diameter, as it has been noted that smaller filament sizes of higher surface-to-volume area absorbs CO₂ at higher rates [167,172]. Lightweight and optimally structured materials also make end-use applications more efficient and help lower the carbon footprint of the manufactured product [173].

1.9. Direct Writing of Heterogeneous Zeolitic Pastes

Additive manufacturing of microporous materials allows for complex geometry creation that can be tuned to lower pressure drop and attrition rates. Recent work on the AM scaffolds for adsorption and catalysis applications using zeolite often employs methylcellulose as a temporary binder, and bentonite that facilitates the formation of free-standing prints [174]. Methylcellulose alters the rheology of the zeolite paste, and bentonite provides rigidity to printed structures, which are heat treated as a post processing step to burn the organic binder and sinter the zeolite matrix. Thermal treatment can improve gas uptake rate and provide increased sorption by unblocking pores [175]. Lawson et.al varied the amount of methylcellulose between 2.0-3.8 wt% with 7.4 wt% kaolin binder, and zeolite 13X matrix content of 81.7-85.0 wt% to examine the effect of increasing monolith macroporosity [176]. The kaolin particles homogenised pore sizes between 13-17 and 45-60 μm , with BET surface areas measuring 550-570 m^2/g .

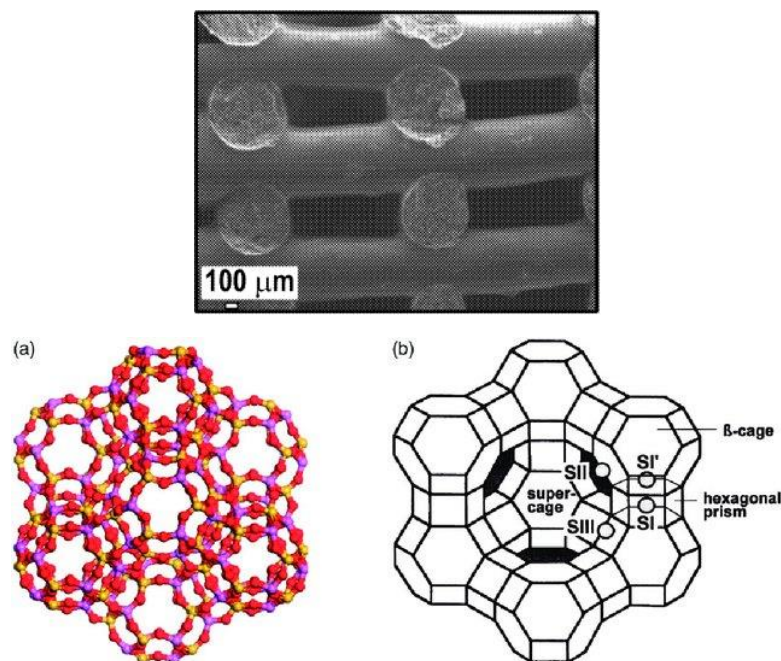


Figure 1.11. SEM micrograph of 'wood-pile' AM lattice sorbent internal channels, left [158], molecular structure of 13X zeolite, right [177].

The precise and rapid deposition of an extrudate depends on several processing parameters that include nozzle diameter, extrusion-rate, deposition temperature; while surface defects depend on binder migration, shrinkage, and drying rate [178]. Rheological properties that can be used to

predict the printability of a paste include yield stress, consistency index, and flow behaviour index [179].

Viscosity is described as a shear stress response to rotational flow that depends on shear rate. Paste viscosity can render a paste as printable or unprintable when deposited to form a curable and free-standing layer [180]. The viscosity of a zeolite suspension depends in-part on solvent absorbed by pores that increases the concentration of the polymer in the continuous phase [181]. Cone-plate viscometry of spherical particles suspended in non-Newtonian fluids have been measured for viscosity, and early work by Highgate showed that acrylate-based particles of 100 μm migrate to form circular rings by small normal stress effects in a methylcellulose and water-based fluid during shearing [182]. The cone-plate viscometer (Figure 1.12) machine surfaces are sometimes roughened to prevent slip of a suspension, but when slip occurs it tends to increase with increased particle loading (Φ) [183]. Another line of thought is concentrated dispersions are intrinsically heterogenous with wall slip depending on an abrupt transition from liquid to solid state suggesting the appropriate analogy of a jamming phase diagram [184–186]. Hence, concentrated dispersions such as colloidal pastes and granular suspensions display both solid and fluid-like flow properties due to their close-packed structures.

Particles jam and only flow past one another appreciably if a large enough shear stress that is the paste yield stress is reached [186]. This parameter is used to inform of a given pastes applicability as e.g., a film coating, screen printing, or ceramic extrusion feedstock. Compliance is shear strain per unit shear stress and paste Φ and binder molecular density alters compliance which can dictate product extrusion parameters [187]. Compliance can be used to explain how a drying pastes' mechanical strength can be compromised by shrinkage as caused by viscoelastic mechanisms [188].

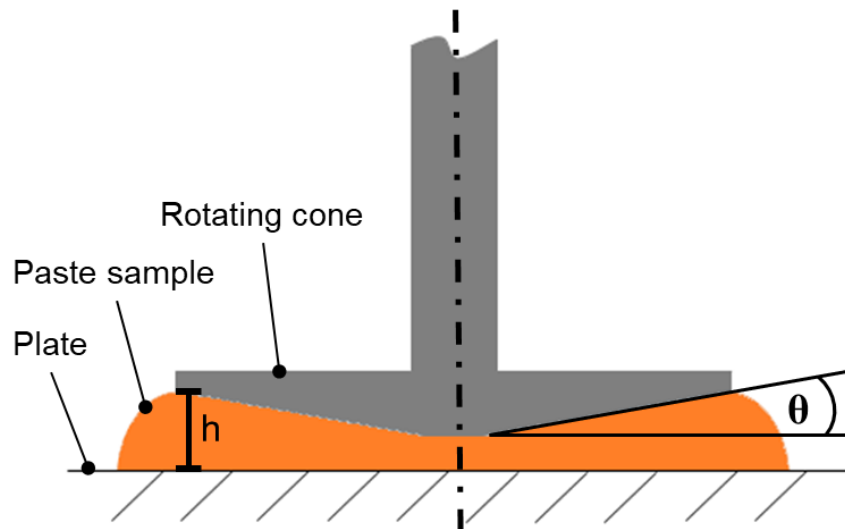


Figure 1.12. Cone and plate viscometer of gap height (h) and cone angle (θ).

A zeolite print of high compression strength ensures a low attrition of material lost during handling or adsorption [189]. A binder can prevent significant material loss before and during heat treatment by encasing zeolite particles, however, Wang et.al showed binder free zeolite structures require partial sintering that yield a 5.24 MPa compressive strength [164]. Lawson et.al showed a 2.5 wt% loading of bentonite improves mechanical strength by nearly sixfold to 10 MPa, however sacrificial biopolymers limit these compositions to 65.6 wt% of functional gas separating zeolite 13X [190]. Parallel channels shown in Figure 1.11 are often printed as an easily achieved geometry and results in uniform flow pattern, high gas throughput, low pressure drop, and low attrition [189]. Parameters such as wall thickness can fine-tune the geometry of printed zeolite CO₂ capture systems. Printed structures can be of high mechanical properties of up to 15 MPa compressive modulus and associated low attrition for industrial scalability facilitating faster breakthrough adsorption, from 40 mins in powder form to 36 mins in printed monolith form [191].

Highly crystalline filament is preferably layered during DW as fine diameters as thin as $\sim 75 \mu\text{m}$ for rapid carbon uptake rates [192]. As a result, structures are malleable when wet and fragile when dry, comparable to membranes used for chemical selectivity [193]. Drying of such fragile structures can cause cracks by the difference in component thermal expansion coefficients [194]. Zeolite adsorbent practical handling/transportation, installation, and cyclability depends in-part on elastic modulus and bending strengths that peak when fully dried or cured, providing crack arrest via polymer-inorganic strain tolerance [195]. Polymers are considered physiochemically stable and are of

low skeleton density; they can provide a sorbent system with thin-dense layers for uniform dispersion of adsorbent particles [189]. Porous polymers are used to enable membrane sub-layer inorganic fillers with high thermal, chemical and mechanical stability, and significant capture capacity [196]. Practical utility is improved by coating of tough polymers free of defects and cracks, as they offer ease of customisation compared to rigid and fragile zeolite, silica, and carbon membranes [197]. Paste materials can show time dependence (viscoelasticity) as examined for industrial processability, with preferable viscoplastic flow imparting effective extrusion processability due to negligible residual stresses [170,198]. Anticipating fluctuation-dissipation of particles in flowing elastic liquids and resulting surface effects on suspension rheology are demanding challenges [199,200].

Varying composition of many zeolitic microporous systems has been considered for sorbent structure DW, but a lack of literature addresses extrusion kinetics of zeolite pastes beyond the goal of achieving a free-standing layer. An opportunity exists to investigate zeolite composite pastes for their print accuracy, repeatability, and associated mechanical properties for further deposition control as governed by rheological characteristics. This may open pathways to increased print speeds of finer, more complex architecture using sophisticated print heads that move the field of DW towards large-scale production [171].

1.10. Conclusions

This introduction provides a background for the development of new AM materials and composites that hold great potential to increase AM utility via improved product functionality and scalability. AM materials of enhanced mechanical properties helps to offset the problem of interlayer weakness inherent to AM structures to offer improved life span of products that can be developed for sustainable industries. This thesis applies a strategy that improves the strength of printable polymeric composites by rubber toughening. Another problem that is outlined in the introduction and addressed in Chapter 5 is recycling of low-density plastics, a strategy for polymers and plastic products not currently reused, recycled, or remanufactured. The economic dilemma of recycling commodity low-density plastic waste is avoidable by banning the creation of such materials, however their use in many instances such as for hospital sterile drapes and curtains is

critical. There are several rPP products developed from recycled NHS hospital BW which is typically destined for landfill or incineration. A strategy is outlined in Chapter 5 that transforms the previous waste stream PP into a functional FFF printer filament. The introduction explores PLA as the most utilised polymer for FFF, which a developed filament from rPP can aim to replicate. Polymer crystals and rubber morphologies imaged using optical light microscopy offers a more accessible, low cost, and rapid method of quantifying failure mode for a given blend than compared to electron microscopy. In this context, a familiar brittle-to-tough behaviour change due to rubber particle diameter and distribution may be evaluated according to critical ligament thickness theory. SEBS is one of many potential rubbers that have been researched in developing toughened recycled materials. However, MFI is best managed using compatible TPEs such as SEBS in PP for improved extrusion control.

AM is capable of custom and complex geometries that finds use in bone phantom manufacture. Bone-like materials often utilise polymer composites, typically containing epoxy and glass fibre providing another prime example of a hard to remanufacture or recycle material selected out of necessity. The literature describes phantom development via drilling, standardised compression, and flexural analysis. Drilling characteristics such as thrust force and swarf formation narrows the potential range of additives that can be selected and potentially combined to provide optimum bone mimicking as referenced to baseline human or animal bone samples. In chapter 6, several novel composites are developed by drilling and mechanical testing that range between low and high drilling and mechanical strength offering a range of customisable bone phantom modelling materials.

The introduction details the importance of transitioning to a clean energy economy to curb environmental damage caused by the plastics industry. Thermochemical energy storage typically utilises salt hydrates to store heat in a reactor of packed bed configuration. The introduction details the problem that holds THS back from being more efficient and cost effective than sensible heat storage methods, in doing so being more widely adopted. It can be summarised as an inability of the ideal number of water molecules to reach and react with each compound of salt within a THS reactor. One possible direction is coated FFF scaffold composite design that is a scalable and low-cost alternative to packed bed reactor configurations. THS systems have yet to benefit from salt hydrate embedded AM structures of tunable geometry as facilitated by the plasticity and cohesivity of aluminosilicate clays. In achieving this effective open reactor design the AM production of such units can be on-

demand. Such a THS reactor design can be made to fit weight, dimensional thermal, mechanical, and other aerospace requirements for spacecraft HVAC [132]. In Chapter 3, readily available CaCl_2 is combined with natural bentonite and coated onto a PC printed lattice with the aim of increasing the occurrence of ideal $6\text{H}_2\text{O}.\text{CaCl}_2$ reactions and resulting efficiency.

Another area of research explored in the introduction is polymer composites for carbon capture technologies from anthropogenic waste fumes. A promising materials selection is zeolite 13X for its high surface area and gas separation potential. Former work shows that zeolites can be printed by DW for reducing harmful levels of CO_2 in enclosed environments such as on aircrafts. To print zeolite by DW it must be converted from a powder to a paste typically using an organic binder or combination of binders such as PVA and methylcellulose. Research into improved surface area can help to reduce health concerns associated to harmful supplies of air in enclosed environments. Chapter 4 builds on previous work by toughening a zeolite 13X composite for gas separation by adding a commercial core-shell rubber (CSR) to the DW composite and assessing any effect on final surface area.

1.11. References

- [1] Z.F. Rad et al, High-fidelity replication of thermoplastic microneedles with open microfluidic channels, *Microsyst Nanoeng.* 3 (2017)
- [2] H.K. Chan et al, The impact of 3D Printing Technology on the supply chain: Manufacturing and legal perspectives, *Int J Prod Econ.* 205 (2018)
- [3] R. Srinivasan et al, Customising with 3D printing: The role of intelligent control, *Comput Ind.* 103 (2018)
- [4] M. Attaran, The rise of 3-D printing: The advantages of additive manufacturing over traditional manufacturing, *Bus Horiz.* 60 (2017)
- [5] I. Simon, M. Gurley, 3D Printing Trend Report, Hubs - a Protolabs Company. (2022) 1–23. Available at www.hubs.com.
- [6] P. Yadav et al, Strength and Surface Characteristics of FDM-Based 3D Printed PLA Parts for Multiple Infill Design Patterns, *Journal of The Institution of Engineers (India): Series C.* 102 (2021)
- [7] F. Scalera et al, Development and characterization of UV curable epoxy/hydroxyapatite suspensions for stereolithography applied to bone tissue engineering, *Ceram Int.* 40 (2014)
- [8] M. Yampolskiy, et al, Evaluation of additive and subtractive manufacturing from the security perspective, *IFIP Adv Inf Commun Technol.* 512 (2017) 23–44.
- [9] K. v. Wong, A. Hernandez, A Review of Additive Manufacturing, *ISRN Mechanical Engineering.* (2012)
- [10] Z. Shi, et al, Renewable metal-organic-frameworks-coated 3D printing film for removal of malachite green, (2017)
- [11] S.J. Park, et al, Enhanced Solubility of the Support in an FDM-Based 3D Printed Structure Using Hydrogen Peroxide under Ultrasonication, (2018)

- [12] J.R.C. Dizon, et al, Mechanical characterization of 3D-printed polymers, *Addit Manuf.* 20 (2018)
- [13] J. Witowski, et al, Investigating accuracy of 3D printed liver models with computed tomography, *Quant Imaging Med Surg.* (2018).
- [14] B.C. Gross, et al, Evaluation of 3D printing and its potential impact on biotechnology and the chemical sciences, *Anal Chem.* 86 (2014)
- [15] J.W. Stansbury, M.J. Idacavage, 3D printing with polymers: Challenges among expanding options and opportunities, *Dental Materials.* 32 (2016)
- [16] X. Wang, et al, 3D printing of polymer matrix composites: A review and prospective, *Compos B Eng.* 110 (2017)
- [17] 3D Hubs, 3D Printing Trends Q1/2018, 3D Hubs. (2018)
- [18] 3D Hubs, Online Manufacturing Trends Q4/2018, (2018)
- [19] S. Wang, L, et al, Can the melt flow index be used to predict the success of fused deposition modelling of commercial poly(lactic acid) filaments into 3D printed materials?, *Plastics, Rubber and Composites.* 47 (2018)
- [20] W. Callister, D. Rethwisch, *Materials science and engineering: an introduction*, (2007)
- [21] Q. Sun, et al, Effect of processing conditions on the bonding quality of FDM polymer filaments, *Rapid Prototyp J.* 14 (2008)
- [22] A. Zolfagharian, et al, Fracture resistance analysis of 3D-printed polymers, *Polymers (Basel).* 12 (2020)
- [23] F.S. Senatov, et al Mechanical properties and shape memory effect of 3D-printed PLA-based porous scaffolds, *J Mech Behav Biomed Mater.* 57 (2016)
- [24] Emmett S. Watson, et al, *Differential Micrometer*, E. S. Watson Etal. 3 (1996)
- [25] R.M.R. Wellen, E, et al, Nonisothermal cold crystallization of poly(ethylene terephthalate), *J Mater Res.* 26, (2011)
- [26] L.T. Sin, et al, *Overview of Poly(lactic Acid)*, Elsevier, (2013)
- [27] J. Ren, *Biodegradable Poly(Lactic Acid): Synthesis, Modification, Processing and Applications*, Tsinghua University Press and Springer, (2010)
- [28] R.P. John, et al, Fermentative production of lactic acid from biomass: An overview on process developments and future perspectives, *Appl Microbiol Biotechnol.* 74 (2007)
- [29] E. Balla, et al, Poly(lactic acid): A versatile biobased polymer for the future with multifunctional properties-from monomer synthesis, polymerization techniques and molecular weight increase to PLA applications, *Polymers (Basel).* 13 (2021)
- [30] J.A. Ormiston, P.W.S. Serruys, Bioabsorbable coronary stents, *Circ Cardiovasc Interv.* 2 (2009)
- [31] S.J. Trenfield, et al, 3D Printing Pharmaceuticals: Drug Development to Frontline Care, *Trends Pharmacol Sci.* 39 (2018)
- [32] Y. Yang, et al, Additive manufacturing of bone scaffolds, *Int J Bioprint.* 5 (2019)
- [33] Y. He, et al, Fabrication of low-cost soft tissue prostheses with the desktop 3D printer, *Sci Rep.* (2014)
- [34] J. Norman, et al, A new chapter in pharmaceutical manufacturing: 3D-printed drug products, *Adv Drug Deliv Rev.* 108 (2017)
- [35] J.D. Gu, Microbiological deterioration and degradation of synthetic polymeric materials: Recent research advances, *Int Biodeterior Biodegradation.* 52 (2003)
- [36] W. Amass, et al, A review of biodegradable polymers: Uses, current developments in the synthesis and characterization of biodegradable polyesters, blends of biodegradable polymers and recent advances in biodegradation studies, *Polym Int.* 47 (1998)
- [37] M. Dawoud, I. et al, Mechanical behaviour of ABS: An experimental study using FDM and injection moulding techniques, *J Manuf Process.* 21 (2016)

- [38] V. Harshitha, S.S. Rao, Design and analysis of ISO standard bolt and nut in FDM 3D printer using PLA and ABS materials, *Mater Today Proc.* 19 (2019)
- [39] Z. Weng, et al, Mechanical and thermal properties of ABS/montmorillonite nanocomposites for fused deposition modeling 3D printing, *Mater Des.* 102 (2016)
- [40] A. Kausar, A review of filled and pristine polycarbonate blends and their applications, *Journal of Plastic Film and Sheeting.* 34 (2018)
- [41] D. Stoof, K. Pickering, Sustainable composite fused deposition modelling filament using recycled pre-consumer polypropylene, *Compos B Eng.* 135 (2018)
- [42] K. Mikula, et al, 3D printing filament as a second life of waste plastics—a review, *Environmental Science and Pollution Research.* 28 (2021)
- [43] L. Cabernard, et al, Growing environmental footprint of plastics driven by coal combustion, *Nat Sustain.* 5 (2022)
- [44] Glover, Ruthan, Markets for degradable plastics., *Int Biodeterior Biodegradation.* (1993)
- [45] Plastics Europe, *Plastics – the Facts,* (2017)
- [46] A. Chamas, et al, Degradation Rates of Plastics in the Environment, *ACS Sustain Chem Eng.* 8 (2020)
- [47] M.L. Mallory, et al, Anthropogenic litter in marine waters and coastlines of Arctic Canada and West Greenland, *Science of the Total Environment.* 783 (2021)
- [48] A.S. Mountford, et al, Eulerian Modeling of the Three-Dimensional Distribution of Seven Popular Microplastic Types in the Global Ocean, *J Geophys Res Oceans.* 124 (2019)
- [49] D. Barcelo, Y. Pico, Case studies of macro- and microplastics pollution in coastal waters and rivers: Is there a solution with new removal technologies and policy actions?, *Case Studies in Chemical and Environmental Engineering.* 2 (2020)
- [50] K. Ragaert, et al, Mechanical and chemical recycling of solid plastic waste, *Waste Management.* 69 (2017)
- [51] R.C. Hale, B. Song, Single-Use Plastics and COVID-19: Scientific Evidence and Environmental Regulations, *Environ Sci Technol.* 54 (2020)
- [52] European Council, Directive (Eu) 2019/904 of the European Parliament and of the Council of 5 June 2019 on the reduction of the impact of certain plastic products on the environment, (2019). Available at www.plasticseurope.org/en/resources/publications/1689-working-together-towards-more-sustainable-plastics
- [53] M. Despeisse, et al, Unlocking value for a circular economy through 3D printing: A research agenda, *Technol Forecast Soc Change.* 115 (2017)
- [54] S. Ishack, S.R. Lipner, Applications of 3D Printing Technology to Address COVID-19–Related Supply Shortages, *Am J Med.* 133 (2020)
- [55] A. Nazir, et al, The rise of 3D Printing entangled with smart computer aided design during COVID-19 era, *J Manuf Syst.* (2020)
- [56] M. Salmi, et al, 3D printing in COVID-19: Productivity estimation of the most promising open source solutions in emergency situations, *Applied Sciences (Switzerland).* 10 (2020)
- [57] PEMRG, *World Plastics Materials Demand 2015 by Types* (2015)
- [58] W.R. Stahel, The circular economy, *Nature.* 531 (2016)
- [59] R.G. Charles, et al, Platinized counter-electrodes for dye-sensitised solar cells from waste thermocouples: A case study for resource efficiency, industrial symbiosis and circular economy, *J Clean Prod.* 202 (2018)
- [60] C. Zhang, et al, An overview of the waste hierarchy framework for analyzing the circularity in construction and demolition waste management in Europe, *Science of the Total Environment.* 803 (2022)

- [61] N. Gregson, P.J. Forman, England's municipal waste regime: Challenges and prospects, *Geographical Journal*. 187 (2021)
- [62] V. Veleva, G. Bodkin, Corporate-entrepreneur collaborations to advance a circular economy, *J Clean Prod*. 188 (2018)
- [63] M. Rezaeimahmoudi, et al, Application of geographical information system in disposal site selection for hazardous wastes, *J Environ Health Sci Eng*. 12 (2014)
- [64] Welsh Government, Record year for Wales' recycling as 64% target exceeded, (2020). Available at www.gov.wales/record-year-wales-recycling-64-target-exceeded
- [65] Welsh Government, Welsh government Consultation Document - Reducing Single Use Plastics - Proposals to ban nine single use plastic products in Wales, (2020)
- [66] UK Government, Reforms to the Packaging Waste Recycling Note (PRN) and Packaging Waste Export Recycling Note (PERN) System and Operator Approval Consultation Document, (2022)
- [67] HM Government, Our Waste, Our Resources: A Strategy for England - CE Hub, (2018). Available at www.ce-hub.org/knowledge-hub/our-waste-our-resources-a-strategy-for-england
- [68] B. van Straten, et al, Surgical waste reprocessing: Injection molding using recycled blue wrapping paper from the operating room, *J Clean Prod*. 322 (2021)
- [69] H.K. Shinn, et al Segregation for reduction of regulated medical waste in the operating room: A case report, *Korean J Anesthesiol*. (2017)
- [70] R. Rothman, T. Ryan, Innovation Fund Conference Creative Circular Economy Approaches to Eliminate Plastic Waste, in: UK Circular Plastics Network, (2020) Available at www.ukcpn.co.uk/wp-content/uploads/2020/08/PRIF-Conference-Brochure-Final-1.
- [71] D.A.O. Cruz, Management and Valorization of Protective Equipment in Hospitality, Masters Thesis., Instituto Superior Técnico, (2018)
- [72] S. Buckler, NHS Sustainable Development Impact Report 2018 (2018)
- [73] IOM3, Welsh company announce plans to counter hospital waste in Europe, IOM3. (2021)
- [74] C. Castro, Cardiff company brings new hopes into the disposable face masks emergency, *The Operating Theatre Journal*. (2021)
- [75] F.A. Cruz Sanchez, et al, Plastic recycling in additive manufacturing: A systematic literature review and opportunities for the circular economy, *J Clean Prod*. 264, (2020)
- [76] G. Bhat, et al, Conversion of Recycled Polymers/Fibers Into Melt-Blown Nonwovens, *Polym Plast Technol Eng*. 38, (1999)
- [77] G. Notarstefano, Active and Passive Sustainability: Measuring the Anti-Fragility of Territories, *Pollutants*. 2, (2022)
- [78] D. Ayre, Technology advancing polymers and polymer composites towards sustainability: A review, *Curr Opin Green Sustain Chem*
- [79] L. Pokrajac, A et al, Nanotechnology for a Sustainable Future: Addressing Global Challenges with the International Network4Sustainable Nanotechnology, *ACS Nano*. 15, (2021)
- [80] A. Namboodiripad, N.C. N, Predicting the Timeline for Earth Achieving Kardashev Scale Type 1 Status, *Journal of Science and Technology*. 06, (2021)
- [81] E. Kuzma, et al, The relationship between innovation and sustainability: A meta-analytic study, *J Clean Prod*. 259 (2020)
- [82] C.L. Cheung, et al, Use of 3-dimensional printing technology and silicone modeling in surgical simulation: Development and face validation in pediatric laparoscopic pyeloplasty, *J Surg Educ*. 71 (2014)
- [83] C.C. Ploch, et al Using 3D Printing to Create Personalized Brain Models for Neurosurgical Training and Preoperative Planning, *World Neurosurg*. (2016)

- [84] Y. Moriguchi, S. Hashimoto, *Material flow analysis and waste management*, (2015)
- [85] L. Li, et al, 3D-printed ternary bioglass-ceramic scaffolds with tunable compositions and properties for bone regeneration, *Ceram Int.* 45 (2019)
- [86] A.D. Brown et al, The mechanical response of commercially available bone simulants for quasi-static and dynamic loading, *J Mech Behav Biomed Mater.* (2019)
- [87] J. Elfar, et al, Composite bone models in orthopaedic surgery research and education, *Journal of the American Academy of Orthopaedic Surgeons.* 22 (2014)
- [88] S. Harish, et al, The study of tensile and flexural strength of cattle bone particulate reinforced epoxy, *Mater Today Proc.* 5, (2018)
- [89] M. Bonner, et al, Hydroxyapatite / polypropylene composite : A novel bone, (2001)
- [90] S. Joshi, et al. Compston, Skeletal fluorosis due to excessive tea and toothpaste consumption, *Osteoporosis International.* 22 (2011)
- [91] N.J. Wachter, et al. Claes, P. Augat, Correlation of bone mineral density with strength and microstructural parameters of cortical bone in vitro, *Bone.* 31, (2002)
- [92] A.A. Phadke, S.K. De, Effect of cryo-ground rubber on melt flow and mechanical properties of polypropylene, *Polym Eng Sci.*, (1986)
- [93] X. Ying, R. et al, Study on the toughening mechanism of PP/EVA dynamically crosslinked blend, *Journal of Macromolecular Science, Part A: Pure and Applied Chemistry*, (2016)
- [94] A. van der Wal, et al, Polypropylene–rubber blends: 1. The effect of the matrix properties on the impact behaviour, *Polymer (Guildf).* 39, (1998)
- [95] E. Matei, et al, Recycled Polypropylene Improved with Thermoplastic Elastomers, *Int J Polym Sci*, (2017)
- [96] J.Z. Liang, R.K.Y. Li, Rubber toughening in polypropylene: A review, *J Appl Polym Sci.* 77 (2000)
- [97] S. Setz, et al, Morphology and mechanical properties of blends of isotactic or syndiotactic polypropylene with SEBS block copolymers, *J Appl Polym Sci.* 59, (1996)
- [98] Y. Shang, et al, Slowing crystallization to enhance interlayer strength of 3D printed poly (ether ether ketone) parts by molecular design, *Addit Manuf.* 59, (2022)
- [99] N.S. Hmeidat, et al, High-strength epoxy nanocomposites for 3D printing, *Compos Sci Technol.* 160, (2018)
- [100] S. Setz, F. et al, Morphology and mechanical properties of blends of isotactic or syndiotactic polypropylene with SEBS block copolymers, *J Appl Polym Sci.* 59, (1996)
- [101] C. Koning, M. et al, Strategies for compatibilization of polymer blends, *Progress in Polymer Science (Oxford).* 23, (1998)
- [102] S.S. Banerjee, et al, 3D-printable PP/SEBS thermoplastic elastomeric blends: Preparation and properties, *Polymers (Basel).* 11 (2019)
- [103] H. Veenstra, et al, Co-continuous morphologies in polymer blends with SEBS block copolymers, *Polymer (Guildf).* 40 (1999)
- [104] D. Ratna, A.K. Banthia, Rubber toughened epoxy, *Macromol Res.* 12, (2004)
- [105] H. Qiu, M. Bousmina, New technique allowing the quantification of diffusion at polymer/polymer interfaces using rheological analysis: Theoretical and experimental results, *J Rheol (N Y N Y).* 43, (1999)
- [106] E. Takubo, et al, Effects of poly(propylene carbonate) additive prepared from carbon dioxide on the tensile properties of polypropylene, *J Appl Polym Sci.* 134 (2017)
- [107] A.K. Gupta, S.N. Purwar, Crystallization of PP in PP/SEBS blends and its correlation with tensile properties, *J Appl Polym Sci.* 29, (1984)

- [108] F.O.M.S. Abreu, et al, SBS and SEBS block copolymers as impact modifiers for polypropylene compounds, *J Appl Polym Sci.* 95, (2005)
- [109] R.E. Cohen, Effect of Compliant Rubbery Particles, 3848, (1990)
- [110] A. Galeski, Strength and toughness of crystalline polymer systems, (2003)
- [111] F. Stricker, et al, Influence of rubber particle size on mechanical properties of polypropylene-SEBS blends, *J Appl Polym Sci.* 68, (1998)
- [112] H. Mae, et al, Material ductility and toughening mechanism of polypropylene blended with bimodal distributed particle size of styrene-ethylene-butadiene-styrene triblock copolymer at high strain rate, *J Appl Polym Sci.* 110, (2008)
- [113] H. Mae, et al, Tensile behavior of polypropylene blended with bimodal distribution of styrene-ethylene-butadiene-styrene particle size, *J Appl Polym Sci.* 107, (2008)
- [114] S. Wu, Phase structure and adhesion in polymer blends: A criterion for rubber toughening, *Polymer (Guildf.)*, (1985)
- [115] S. Wu, A generalized criterion for rubber toughening: The critical matrix ligament thickness, *J Appl Polym Sci.*, (1988).
- [116] I. Daniel Posen, et al, Greenhouse gas mitigation for U.S. plastics production: Energy first, feedstocks later, *Environmental Research Letters.* 12, (2017)
- [117] J. Zheng, S. Suh, Strategies to reduce the global carbon footprint of plastics, *Nat Clim Chang.* 9, (2019)
- [118] E. Barbier, J. Burgess, The Sustainable Development Goals and the systems approach to sustainability. *Economics Discussion Papers*, No 2017-28, *Economics-Ejournal.Org.* 11, (2017)
- [119] M. Nilsson, et al, Policy: Map the interactions between Sustainable Development Goals, *Nature.* 534, (2016)
- [120] T.L. Bergman, et al, Introduction to heat transfer, John Wiley & Sons, (2011)
- [121] J.T. Chen, et al, Topology optimization for heat transfer enhancement in thermochemical heat storage, *Int J Heat Mass Transf.* 154, (2020)
- [122] J. Lin, et al, Applications of low-temperature thermochemical energy storage systems for salt hydrates based on material classification: A review, *Solar Energy.* 214, (2021)
- [123] P.A.J. Donkers, et al, A review of salt hydrates for seasonal heat storage in domestic applications, *Appl Energy.* 199, (2017)
- [124] I. Sarbu, C. Sebarchievici, A comprehensive review of thermal energy storage, *Sustainability (Switzerland).* 10, (2018)
- [125] M. Molenda, et al, Reversible hydration behavior of CaCl₂ at high H₂O partial pressures for thermochemical energy storage, *Thermochim Acta.* 560, (2013)
- [126] P.A.J. Donkers, et al, Experimental studies for the cyclability of salt hydrates for thermochemical heat storage, *J Energy Storage.* 5, (2016)
- [127] L. Calabrese, et al, Macro-porous permeability aspects of MgSO₄ salt hydrate foams for energy storage applications, *J Appl Polym Sci.* 139, (2022)
- [128] R.J. Clark, et al, State of the art on salt hydrate thermochemical energy storage systems for use in building applications, *J Energy Storage.* 27, (2020)
- [129] H. Zondag, et al, Prototype thermochemical heat storage with open reactor system, *Appl Energy.* 109, (2013)
- [130] S.P. Casey, et al, Salt impregnated desiccant matrices for 'open' thermochemical energy conversion and storage – Improving energy density utilisation through hydrodynamic & thermodynamic reactor design, *Energy Convers Manag.* 142, (2017)
- [131] A.H. Abedin, M.A. Rosen, Closed and open thermochemical energy storage: Energy- and exergy-based comparisons, *Energy.* 41, (2012)
- [132] Y. Guo, et al, Temperature control of star sensor baffle using 3D printing and PCM thermal energy storage technology, *Int J Heat Mass Transf.* 165, (2021)

- [133] Z. Wang, et al, A three-dimensional printed biomimetic hierarchical graphene architecture for high-efficiency solar steam-generation, *J Mater Chem A Mater.* 8, (2020)
- [134] S. Chaule, J. et al, Rational Design of a High Performance and Robust Solar Evaporator via 3D-Printing Technology, *Advanced Materials.* 33, (2021)
- [135] Z. Yang, et al, Bean-Pod-Inspired 3D-Printed Phase Change Microlattices for Solar-Thermal Energy Harvesting and Storage, *Small.* 17, (2021)
- [136] M. Graham, et al, Highly Stable Energy Capsules with Nano-SiO₂Pickering Shell for Thermal Energy Storage and Release, *ACS Nano.* 14, (2020)
- [137] L. Tabard, et al, Hierarchical salt-ceramic composites for efficient thermochemical energy storage, *Appl Mater Today.* 20, (2020)
- [138] V. Middelkoop, et al, 3D printed versus spherical adsorbents for gas sweetening, (2019)
- [139] A.A. Al-Abidi, et al, CFD applications for latent heat thermal energy storage: A review, *Renewable and Sustainable Energy Reviews.* 20, (2013)
- [140] R. Sutton, et al, Discharge performance of blended salt in matrix materials for low enthalpy thermochemical storage, *Appl Therm Eng.* 145, (2018)
- [141] V. Antony Aroul Raj, R. Velraj, Heat transfer and pressure drop studies on a PCM-heat exchanger module for free cooling applications, *International Journal of Thermal Sciences.* 50, (2011)
- [142] I. Kaur, P. Singh, State-of-the-art in heat exchanger additive manufacturing, *Int J Heat Mass Transf.* 178, (2021)
- [143] A. Mirabolghasemi, et al. Therriault, Thermal conductivity of architected cellular metamaterials, *Acta Mater.* 174, (2019)
- [144] S. Catchpole-Smith, et al, Thermal conductivity of TPMS lattice structures manufactured via laser powder bed fusion, *Addit Manuf.* 30, (2019)
- [145] R.A. Shigeishi, et al, Solar energy storage using chemical potential changes associated with drying of zeolites, *Solar Energy.* 23, (1979)
- [146] B. Mette, et al, New highly efficient regeneration process for thermochemical energy storage, *Appl Energy.* 109, (2013)
- [147] H. Ait Ousaleh, et al, Enhanced inorganic salts stability using bentonite clay for high-performance and low-cost thermochemical energy storage, *J Energy Storage.* 49, (2022)
- [148] A. Sari, Thermal energy storage characteristics of bentonite-based composite PCMs with enhanced thermal conductivity as novel thermal storage building materials, *Energy Conversion and Management journal,* (2016)
- [149] R.J. Sutton, et al, Characterising the discharge cycle of CaCl₂ and LiNO₃ hydrated salts within a vermiculite composite scaffold for thermochemical storage, *Energy Build.* 162 (2018)
- [150] S.P. Casey, et al. Robinson, Salt impregnated desiccant matrices for ‘ open ’ thermochemical energy storage — Selection , synthesis and characterisation of candidate materials, *Energy Build.* 84, (2014)
- [151] Y.I. Aristov, et al, Selective water sorbents for multiple applications. 11. CaCl₂ confined to expanded vermiculite, *Reaction Kinetics and Catalysis Letters.* 71, (2000)
- [152] D. Aydin, et al, The latest advancements on thermochemical heat storage systems, *Renewable and Sustainable Energy Reviews.* 41, (2015)
- [153] P. D’Ans, et al, Humidity dependence of transport properties of composite materials used for thermochemical heat storage and thermal transformer appliances, *J Energy Storage.* 18, (2018)
- [154] P.A. Kallenberger, et al, Alginate-Derived Salt/Polymer Composites for Thermochemical Heat Storage, *Adv Sustain Syst.* 2, (2018)
- [155] M. Fasano, et al, Multiscale simulation approach to heat and mass transfer properties of nanostructured materials for sorption heat storage, *Energy Procedia.* 126, (2017)

- [156] G. Mermut, A. R. and Lagaly, Baseline Studies of the Clay Minerals Society Source Clays: Layer - Charge Determination and Characteristics of Those Minerals Containing 2 : 1 Layers, *Clays Clay Miner.* 49, (2001)
- [157] J. Peng, et al, Driving force for the swelling of montmorillonite as affected by surface charge and exchangeable cations: A molecular dynamic study, *Results Phys.* 12, (2019)
- [158] B. Bananezhad, et al, Bentonite clay as an efficient substrate for the synthesis of the super stable and recoverable magnetic nanocomposite of palladium (Fe₃O₄/Bentonite-Pd), *Polyhedron.* 162, (2019)
- [159] I.E. Odom, Smectite clay minerals: properties and uses., *Philos Trans R Soc Lond.* 409, (1984)
- [160] H. Thakkar, et al. Rownaghi, J.C. Knox, F. Rezaei, 3D-Printed Zeolite Monoliths for CO₂ Removal from Enclosed Environments, (2016)
- [161] E.T. Gall, W.W. Nazaroff, New directions: Potential climate and productivity benefits from CO₂ capture in commercial buildings, *Atmos Environ.* 103, (2015)
- [162] D.Y.C. Leung, et al, An overview of current status of carbon dioxide capture and storage technologies, *Renewable and Sustainable Energy Reviews.* 39, (2014)
- [163] S. Sircar, A. Myers, Gas Separation by Zeolites, *Handbook of Zeolite Science and Technology.* (2003)
- [164] S. Wang, et al, Fabricating Mechanically Robust Binder-Free Structured Zeolites by 3D Printing Coupled with Zeolite Soldering: A Superior Configuration for CO₂ Capture, (2019)
- [165] F. Hasan, et al, Zeolite monoliths with hierarchical designed pore network structure: Synthesis and performance, (2013)
- [166] B. Besser, et al, Hierarchical Porous Zeolite Structures for Pressure Swing Adsorption Applications., (2016)
- [167] D.T. Nguyen, (12) United States Patent - Composite 3d - Printed Reactors For Gas Absorption, Purification ,And Reaction, 2, (2019).
- [168] F.J. Sotomayor, et al, Characterization of Micro/Mesoporous Materials by Physisorption: Concepts and Case Studies, *Acc. Mater. Surf. Res.* 3, (2018)
- [169] H. Thakkar, et al, 3D-Printed Metal-Organic Framework Monoliths for Gas Adsorption Processes. (2017)
- [170] A. Corker et al, 3D printing with 2D colloids: Designing rheology protocols to predict “printability” of soft-materials, *Soft Matter.* 15, (2019)
- [171] J.A. Lewis, Direct ink writing of 3D functional materials, *Adv Funct Mater.* 16, (2006)
- [172] J. Lefevre, et al, The impact of formulation and 3D-printing on the catalytic properties of ZSM-5 zeolite, (2018)
- [173] B. He, et al, Towards low-carbon product architecture using structural optimization for lightweight, *International Journal of Advanced Manufacturing Technology.* 83, (2016)
- [174] J. Lefevre, et al, 3D-Printed Zeolitic Imidazolate Framework Structures for Adsorptive Separations, *ACS Appl Nano Mater.* 2, (2019)
- [175] S. Couck, et al, 3D-printed SAPO-34 monoliths for gas separation, (2018)
- [176] S. Lawson, et al, The Effects of Cell Density and Intrinsic Porosity on Structural Properties and Adsorption Kinetics in 3D-Printed Zeolite Monoliths, (2020)
- [177] Y. Guo, et al, Desorption characteristics and kinetic parameters determination of molecular sieve by thermogravimetric analysis/differential thermogravimetric analysis technique, *Adsorption Science and Technology.* 36, (2018)
- [178] A. Aranzabal, et al, Optimization of process parameters on the extrusion of honeycomb shaped monolith of H-ZSM-5 zeolite, *Chemical Engineering Journal.* 162, (2010)

- [179] B. Pérez, et al, Impact of macronutrients printability and 3D-printer parameters on 3D-food printing: A review, *Food Chem.* 287, (2019)
- [180] C. Duty, et al, What makes a material printable? A viscoelastic model for extrusion-based 3D printing of polymers, *J Manuf Process.* 35, (2018)
- [181] K.O. Olanrewaju, et al Breedveld, The rheology of suspensions of porous zeolite particles in polymer solutions, *Rheol Acta.* 53, (2013)
- [182] D. Highgate, Particle Migration in Cone-plate Viscometry of Suspensions, *Nature.* 211, (1966)
- [183] P. Ballesta, et al, Slip and flow of hard-sphere colloidal glasses, *Phys Rev Lett.* 101, (2008)
- [184] P. Coussot, et al, Coexistence of liquid and solid phases in flowing soft-glassy materials, *Phys Rev Lett.* 88, (2002)
- [185] A.J. Liu, S.R. Nagel, Jamming is not just cool anymore, *Nature.* 396, (1998)
- [186] S.P. Meeker, et al, Slip and flow in soft particle pastes, *Phys Rev Lett.* 92, (2004)
- [187] J. Gonzalez-Gutierrez, et al, Time-Dependent Properties of Multimodal Polyoxymethylene Based Binder for Powder Injection Molding, *Journal of Solid Mechanics and Materials Engineering.* 6, (2012)
- [188] H. Ye, et al, Drying and carbonation shrinkage of cement paste containing alkalis, *Materials and Structures/Materiaux et Constructions.* 50, (2017)
- [189] H. Thakkar, et al, Development of 3D-Printed Polymer-Zeolite Composite Monoliths for Gas Separation, (2018)
- [190] S. Lawson, et al, Binderless zeolite monoliths production with sacrificial biopolymers, (2021)
- [191] A. Rownaghi, et al, Engineering Advanced Adsorbent Materials for CO₂ Capture Applications by Harshul Vipul Thakkar Presented To The Faculty Of The Graduate School Of The Missouri University Of Science And Technology, Thesis, (2017).
- [192] F. Rezaei, et al, Zeolite Monolith Compositions And Methods For The Catalytic Cracking Of Alkanes, United States Patent, (2021)
- [193] H. Lee, P.K. Dutta, Synthesis of free-standing chabazite-type films, *Microporous and Mesoporous Materials.* 38 (2000) 151–159. [https://doi.org/10.1016/S1387-1811\(99\)00289-9](https://doi.org/10.1016/S1387-1811(99)00289-9).
- [194] M. Noack, et al, The change of the unit cell dimension of different zeolite types by heating and its influence on supported membrane layers, *Microporous and Mesoporous Materials.* 117, (2009)
- [195] S. Chakraborty, et al, Tolerance of polymer-zeolite composite membranes to mechanical strain, *J Memb Sci.* 518, (2016)
- [196] G. Ciobanu, et al, Preparation and characterization of polymer-zeolite nanocomposite membranes, *Materials Science and Engineering C.* 27, (2007)
- [197] H.B. Park, et al, Polymers with Cavities Tuned for Fast Selective Transport of Small Molecules and Ions, *Science.* 318, (2007)
- [198] R.A. Basterfield, et al, On the interpretation of orifice extrusion data for viscoplastic materials, *Chem Eng Sci.* 60, (2005)
- [199] A. Papadopoulou, et al, Effect of particle specific surface area on the rheology of non-brownian silica suspensions, *Materials.* 13, (2020)
- [200] E.S.G. Shaqfeh, On the rheology of particle suspensions in viscoelastic fluids, *AIChE Journal.* 65, (2019)

Chapter 2. Experimental

2.1. Chapter Summary

This chapter outlines the methods of CAD, 3D printing and moulding, and error analysis that are relevant to all results chapters presented in this thesis. All other methodologies are provided in each case-study chapter because they are unique to the chapter specific applications. Key chemical structures of materials and engineering standards used to evaluate them are detailed there. This project is concerned with composites that contain a continuous phase of thermoplastic or thermosetting polymer for AM; sample preparation, and viscosity (i.e., resistance to flow) techniques are of particular importance and are reported accordingly in the context of their intended sustainable application.

2.2. Computer Aided Design

There were three main CAD software used to create and modify CAD models intended for FFF printing. These were Autodesk Inventor[®], Solidworks[®] (SW), and nTopology[®] (nTop). Inventor was used to create log-pile structures that were then DW using zeolite pastes. One critical aspect to CAD modelling is to form a watertight model, which otherwise prevents the formation of a solid body required for flow simulations and slicing for printing. This is a common problem for parts of high polygon count and was avoided using mesh checking functions. An example of a surface mesh not capable of forming a solid body is shown (Figure 2.1).

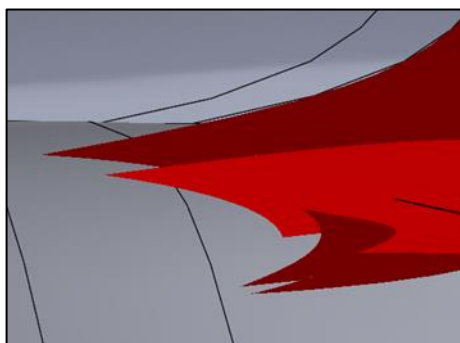


Figure 2.1. Intersecting CAD part surfaces preventing a watertight formation for flow simulations.

2.3. 3D Printing Procedure and Moulding

In this section, the 3D printing procedure is described. The object to be printed was designed in a CAD modelling software and exported as an STL file to be sliced ready for FFF. In all cases, Cura software was used to slice 3D models. A custom printer profile was needed for the Sidewinder X1 3D printer that required accommodating a Z offset for fitting a paste printing extruder head with syringe. Each CAD model was printed and post processed to add or remove material as required for the intended application.

Moulding as a final step was used throughout the project, except for the work with medical waste rPP plastic wraps (Chapter 5, where moulding is relevant in the context of injection moulding). The bentonite/CaCl₂ composite clay was hand moulded using a clay modelling tool and cocktail stick to post-impregnate the FFF printed matrix lattice. The zeolite/polymer composite paste was moulded into a tin-cured silicon mould to form the compression strength samples. The epoxy composites were cast into a platinum-cured silicone moulds. The silicone moulds were formed using FFF prints as the female part of the mould for making compression, flexural, and drilling samples.

2.4. Error Analysis

Error is quoted as standard deviation (SD, σ) throughout this thesis unless stated otherwise. Values of SD are quoted as one standard deviation and are in brackets, where average values are quoted as the arithmetic mean (\bar{x}):

$$\sigma = \sqrt{\frac{\sum(x_i - \bar{x})^2}{n-1}} \quad (2.16)$$

Where x_i is a measured data value, and n is the number of data points measured.

Propagated error (y) is quoted when a calculated data value (Y) is derived from more than one variable (A, B) with error (a, b). Equation 2.17 is used for multiplication and division while Equation 2.18 is used for addition of error:

$$\frac{y}{Y} = \sqrt{\left(\frac{a}{A}\right)^2 + \left(\frac{b}{B}\right)^2} \quad (2.17)$$

$$y = \sqrt{a^2 + b^2} \quad (2.18)$$

It should be noted that Solidworks Flow CFD simulations (Chapter 3) provide a result criterion as error for a given data point, which is $\leq 2\%$ as confirmed by a third-party software, NAFEMS Benchmarks [1]. Error from simulated reactor set-up is also considered by repeating a simulation five times with a repositioned and re-meshed TPMS lattice for calculating a representative standard deviation of velocity, fluid temperature, and absolute humidity.

2.5. References

- [1] A. Sobachkin, G. Dumnov, Numerical Basis of CAD-Embedded CFD, NAFEMS World Congress 2013. 20, (2013)

**Chapter 3. Bentonite/CaCl₂
Embedded Fused Deposition
Modelled Lattices for
Thermochemical Energy
Storage**

3.1. Chapter Summary

In this chapter, a room temperature thermochemical energy storage technique is developed using FFF with the aim to address the common bottleneck of uneven water vapour adsorption through a reactor's length. The standard approach to THS is to create salt impregnated pellets but this leads to crust formation and under-activated salt hydrate crystals by the water vapour. A range of reactor uplift values from previous literature work using the same experimental apparatus is 10 to 14 °C. Here, a bentonite/CaCl₂ composite is formed into flow simulation optimised TPMS geometries for even salt distribution and wetting of embedded THS composites held in PC printed cylinder lattices. The bulk temperatures of the low-density packed cylinder stack reach 38 °C and the temperature at the reactor outlet is stable with the potential of reaching 8 °C using 35 g of charged (dry) printed and post-print embedded composite. Modelling of lattice matrix geometries to be printed and coated with bentonite/CaCl₂ was achieved using nTop and SW software, representing the most significant CAD contributions presented in this thesis. The printed infill pattern is iterated to find effective infill density, and two recharge runs of high and low density embedded and stacked cylinders are conducted to assess the composite structure for open reactor THS and potential use with HVAC systems and low enthalpy application such as solar collectors. The novel TPMS matrix and post-print embedded bentonite/CaCl₂ is assessed for adsorbed water during discharge and mass loss between cycles, and the concept of embeddable printed TPMS matrices is discussed in the context of scale-up using previous pellet-based matrix results taken from literature works.

3.2. Aims

The primary aim of this chapter is to develop a new salt embedded matrix material that is tested in a small scale THS reactor for comparison with previous literature values of temperature uplift and water sorption. This is achieved by making an FFF supporting matrix framework that is embedded with a CaCl₂/bentonite clay composite. Fluid flow simulations of benchmark fin and baffle matrix geometries aim to validate the selection of novel TPMS geometries for use in THS open reactors. Many TPMS designs exist, selected designs for this investigation were based on nonintersecting, turbulence

invoking, and printable surfaces without the need for support material. This chapter also aims to introduce bentonite as a porous binder for free-standing and non-sintered matrices. The developed composite is made possible by FFF of polymers which is discussed in the context of traditional techniques used in the field of THS with the aim of denoting the potential of such additive manufactured scaffolds.

3.3. Introduction

The largest contributor of plastic products life cycle GHG emissions originates from the use of fossil fuels for their production and there is a resulting need for massive infrastructure adaption to transition from fossil fuels to renewable energy. AM continues to institute itself within several prominent clean energy industries such as hydrogen production and storage but is potentially entirely underutilised in the field of thermochemical energy storage. AM is a possible means to create complex lattices of salt housing matrices that aim to facilitate the best-case scenario of even salt hydrate distribution and control over deliquescence for maximum efficiency and thermal storage. The technologies in the THS literature utilise AM for patterning porous lattices by DW which requires altering existing formulations to printable ones made entirely self-standing via calcification that is energy intensive [1,2]. There has yet to be an attempt to avoid such changes to binding techniques, with printable products showing reduced energy density with little gains in efficiency to show for it. Patterning of already successful THS salt and matrix combinations via embedding of an easily fabricated polymer lattice created using desktop FFF has not been demonstrated.

CaC₂ combined with expanded vermiculite is perhaps the best option for safe and low-cost energy storage at room temperature due to its high energy density and recyclability of the system. The closest chemical formula approximation of vermiculite that offers cohesivity for embedding and coating of AM lattices is bentonite which is highly porous and stable at ≥ 120 °C, which is needed to fully dry the matrix for association and recharge of the salt hydrate. As with vermiculite, bentonite pertains a TOT structure with the storage of salt hydrates occurring on bentonite particles and in their TOT interlayers [3]. Water is attracted to these regions causing structural swelling and cationic exchange that leads to the wetting, reaction, and heat release during discharge that then redeposits during drying. The degradation of a porous structure leads

to less available salt nucleation sites, less absorption of water and often a reduction of reactor outlet temperature [4,5]. The design of a THS system that minimises degradation will be one that directs the moving air current optimally and therefore moves towards challenging the recharge efficiency of other storage methods such as sensible heat storage.

3.4. Experimental

The experimental for THS utilised a two-stage approach to optimise the temperature lift of a lab scale open THS reactor. First, novel TPMS geometries that were predicted to improve upon traditional heat transfer elements via conduction (fins) and convection (baffles) were studied using fluid flow simulations. The best performing geometries were then manufactured using FFF for the polymer matrix and post-print impregnated with the functional bentonite/CaCl₂ composite. For clarification, the FFF printed PC matrix was removed from the print bed and taken to a lab to be embedded with the wet clay and salt mixture by hand using moulding tools. This approach was selected to leverage the scalability and flexibility of 3D printing technology for potential iteration and deployment on a commercial level,

3.4.1. Lattice Matrix Geometry Selection and Modelling

TPMS's were chosen as a novel geometry for THS matrix manufacture for a few key reasons. The smooth surfaces of TPMS geometries are of interest because ideally the flow of water vapour allows for even wetting of the sample surface containing salt hydrate crystals. Another reason for the selection of smooth surfaces was to minimise loss of velocity and pressure drop through the reactor. The TPMS geometries have very high surface area/volume ratio of zero-mean curvature which was theorised for the work in this thesis to help form a uniform and high-density salt crystal distribution along the reactor length. TPMS pores are highly interconnected and non-tortuous which was considered for the purpose of high-water adsorption at typically hard-to-reach locations such as surfaces facing the reactor outlet. TPMS geometries can be precisely expressed by mathematical functions, and their repeating unit cell

structure of schwarz, gyroid, or diamond geometry are 3D printable without the need for support material.

Baffle shaped matrices were selected for benchmarking because they provide airflow turbulence and thus water vapor driving force at hard-to-reach salt crystal locations. Baffle size, shape and layout can be used to control this turbulence and therefore help improve reactor temperature uplift. Conversely, fin geometries were selected for simulation because they are commonly used for heat transfer applications while pertaining ease of manufacture. Fins were theorised to provide little resistance to the direction of vapour flow while generating a heating gradient at the outlet for comparison to baffle and TPMS matrix geometries.

Baffle and fin designs were created in SW, and TPMS geometries were generated in nTop and exported as a quadrangulated mesh. A two-part (inner/outer cylinder) TPMS lattice was created to mediate airflow towards a uniform and fast flowing vapour distribution, but also to allow for subsequent experimental results to be gathered via a one-step coating of unique salt hydrates on matrices of customisable design. A SW ring STL of 20 mm height was imported into nTop, converted into an implicit body and filled with a TPMS surface of 20 mm unit cell size before converting into a quadrangulated mesh. All final exportable meshes were simplified quadrangulated 10,000 mesh cell surfaces. A cylinder-shaped core of 10 mm height and 32 mm radius was generated in nTop, and stacked in SW to form a lattice column that fit in the outer ring column.

Three types of lattice geometry used for CFD benchmarking, fin (F1-F3), baffle (B1-B3), and TPMSs (schwarz, gyroid, diamond) are presented (Figure 3.1). All fin lattice walls run the length of the reactor chamber vessel, with an increased number of fins for the simple investigation of the effect of radiant surface area on velocity and temperature profile development. Baffle designs vary by their orientation – B1 alternates in the XY directions, B2 alternates in the Z direction, and B3 is a stagnated configuration in the XY directions.

Inner cylinder TPMS repeating cell size was 10 mm in the XYZ directions, generated to insure a inner/outer cylinder density gradient. Final nTop STLs were assembled in SW using the coordinate system, forming six stacked cylinders in three stacked outer cylinders. Care was taken to avoiding intersecting surfaces. The final lattices for benchmarking were 84.5 mm in diameter and 60 mm in length, fitted into the reactor vessel leaving a 4 mm gap for thermal expansion.

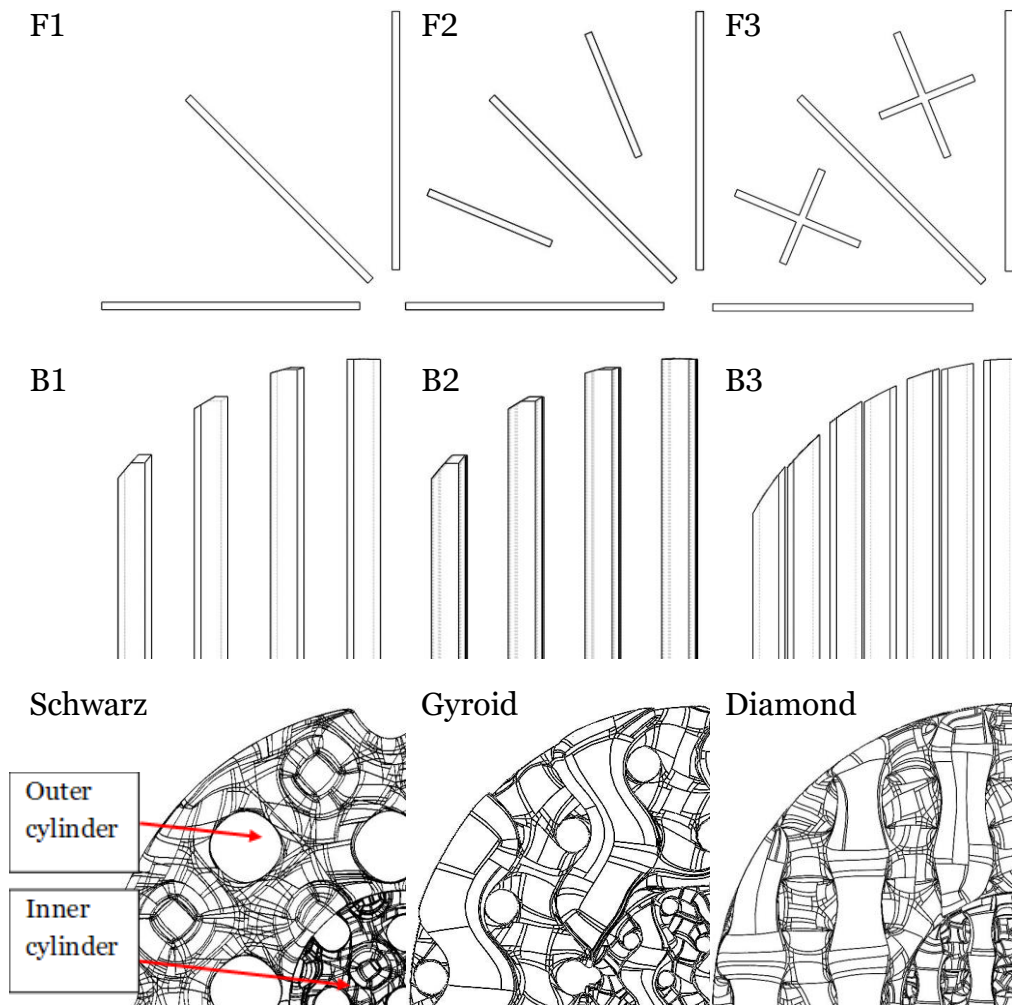


Figure 3.1. Benchmark lattice meshes, fin (top), baffles (middle), for the consideration of TPMS designs of inner and outer cylinder design (bottom).

3.4.2. Computed Fluid Dynamic Simulation

An open THS system with simulated matrix of iterative lattice geometry was investigated to maximise pressure and temperature at the reactor outlet. Simulations combined convection (gravity enabled) and radiative heat transfer. CAD models of benchmark and TPMS lattices were assembled in SW for CFD studies in Flow Simulation with a specified computational domain surrounding the reactor channel of 84.5 mm in diameter and 64 mm in length designed to house the salt hydrate (Figure 3.2). Surface goals of temperature, pressure, velocity, and moisture were iteratively calculated until the convergence criteria were met. Heat generated from salt hydrates was

mimicked using a diffusive radiative source held at 80 °C which is a typical temperature of a discharging salt hydrate [6]. Simulated airflow was set to 20 L/min, air humidity was set to 50 %RH, and outlet was set at environmental pressure. Meshing was determined by SW for simulations that ran on 16 computational cores, with initial mesh level of 3, and final mesh of approximately 18,000 cells. Reaction fronts were simulated using temperature contour plots measured from onset of heating to steady state using ImageJ software.

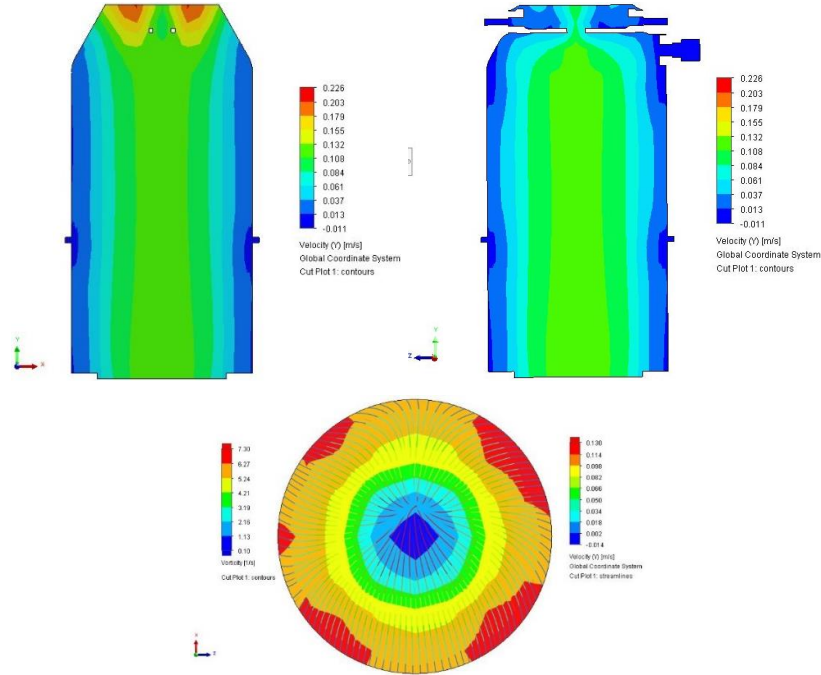


Figure 3.2. THS open reactor design with concentric air flow showing unsymmetrical side cut plots, above, and inlet vorticity (contours) and velocity (streamlines) entrance profile of an empty reactor vessel.

From the baseline and TPMS heat exchange simulations energy density (E_d) was calculated as enthalpy change (ΔH) per unit volume of heated lattice, and pressure (P) was calculated using the Bernoulli equation [7,8]:

$$Q = mc\Delta T \quad (2.1)$$

$$\Delta H = \Delta Q + V\Delta P \quad (2.2)$$

$$E_d = \Delta H/V \quad (2.3)$$

$$P = \frac{1}{2} \rho v^2 + \rho gh \quad (2.4)$$

Where Q is heat gain at the reactor outlet, m is the mass of the heated lattice, c is the specific heat of the simulated sample material selected as 1) epoxy, and 2) aluminium, ΔT is the temperature uplift between reactor inlet and outlet, V is the volume of the lattice, ρ is gas density, and ΔP is the change in pressure between inlet and outlet. SW gives density of epoxy and aluminium as 1120.0 and 2688.9 kg/m³, and specific heats of 1400 and 902 J, respectively. Q and ΔT were calculated to develop an understanding of the efficiency of lattice geometries in exchanging heat but per unit of heated volume not just according to total mass of heated solid.

3.4.3. Printing Triply Periodic Minimal Surface Geometries

Selected geometries were prepared in a cylinder shape by first modelling and printing with under extruded print lines for embeddable PC lattices that were embedded with the prepared Bentonite/CaCl₂ composite.

Lattice TPMS geometries were printed in polycarbonate (PC) for inert, low moisture absorption, and high impact toughness properties owing to a strong benzene ring and rigid carbonate ester chemical structure (Figure 3.3). Inner TPMS cylinder parts were printed at 40 mm/s using an Ultimaker 5S fitted with a 0.25 mm nozzle, programmed in Cura to a 0.23 mm line thickness, 0 wall line count, and zero top and bottom layers, with the build volume enclosed. PC lattice scaffolds were made to house embedded bentonite/CaCl₂ composite for THS. The Ultimaker 5S printer was chosen for high dimensional tolerance when printing layers of 0.1 mm height at 260 °C. The infill pattern was lines, connected infill lines was deselected, and infill densities were 15% and 20% because low infill density maximises salt hydrate density. Too low an infill density, however, and the print will not be embeddable.

One cylinder of markedly thick walls was printed with a 2.5 mm cell size patterned with hexagonal walls of 100% infill. These tests aimed to clarify effects of infill pattern and packing density on outlet temperature and establish effective infill designs that maintains geometry despite composite swelling.

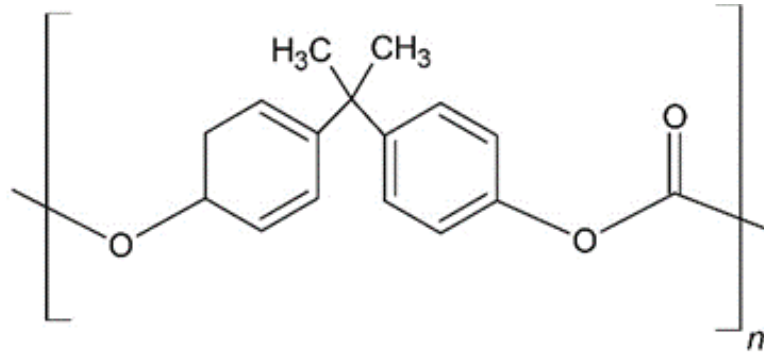


Figure 3.3. Chemical structure of the polycarbonate monomer made from bisphenol A, n is typically 90-180.

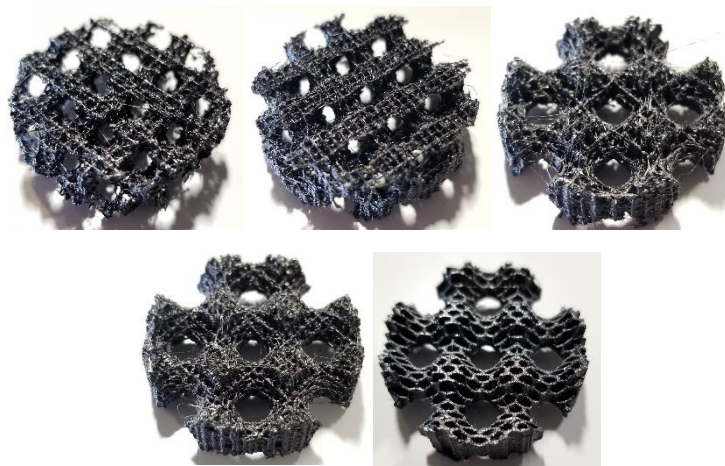


Figure 3.4. Printed polycarbonate cylinders, from left to right - 15% infill diamond, 20% infill diamond, 15% infill shwarz, 20% infill shwarz (bottom left), 2.5 mm cell hexagon infill (bottom right).

TPMS geometry lattice prints (Figure 3.4) were coated with calcium bentonite from Morocco, used as received from Intralabs. Intralabs bentonite is Fullers Earth, a soft aluminium phyllosilicate mineral formed from microscopic platy grains. The composition of Intralabs bentonite is 88% montmorillonite, 5% mica, 5% feldspars, and 2% quartz [9]. Intralabs provide a swelling volume value of 11 ml/g, and a moisture maximum of 14 wt%. Bentonite was selected for its cohesion, swelling capacity, plasticity for use as a binder, ability to absorb water, and inert properties adequate for use in open systems.

3.4.4. Embedding of Bentonite/CaCl₂ Scaffolds for use in Thermochemical Energy Storage Reactor

As mentioned in Chapter 1, there has been no clear attempt at embedding bentonite into an AM lattice acting as a scaffold of customisable geometry for THS. Developed composites for this thesis intend to improve open reactor THS energy storage efficiency by facilitating custom composite matrix thickness and associated vapour permeability.

Anhydrous CaCl₂ was supplied by Sigma-Aldrich® and employed as a salt hydrate for its high energy density and safe use in open reactors. Bentonite was supplied by Intra Laboratories and has a typical mineralogy composition of: 88% montmorillonite, 5% mica, 5% feldspars, and 2% quartz. CaCl₂ saturated water was prepared by slowly adding 54 g of CaCl₂ to 40g of deionised water while stirred with a magnetic stirrer at room temperature in a 200 ml beaker. The solution was left to sit overnight to ensure a fully dissolved salt, with the beaker opening covered in parafilm wrap to avoid evaporation and salt precipitation. Meanwhile bentonite powder was heated to 120 °C and held overnight to ensure a fully dried powder for impregnation. The CaCl₂ solution was added dropwise to the bentonite until saturation, using the insipient witness technique as reported by S. Casey *et al* [10]. Saturation occurred when 22.5 g of saturated salt water was added to 36.2 g of bentonite powder, forming a composite of 22 wt% CaCl₂.

The CaCl₂ bentonite composite was mixed by hand using a glass rod and left to soak at room temperature for 2 hrs before being embedded into a lattice using a clay modelling tool with excess material at the sample surface loosened and removed with the tool. A cocktail stick was used to excavate intended open labyrinths and compressed air removed any remaining surface. A low packing density was achieved by gently rinsing embedded material with deionised water using a wash bottle, placing the lighter part in an oven preheated to 120 °C for 45 minutes. Then excess workable composite was loosened using a moulding tool and removed via compressed air. Bentonite/CaCl₂ embedded PC printed sample preparation is shown in Figure 3.5.



Figure 3.5. Stages of making bentonite/ CaCl_2 embedded PC prints: pressing the composite into the print using a clay modelling tool (1), clearing the external and internal labyrinths (2), removing loose material with compressed air (3), final part ready to be charged for THS (4).

Two cylinder packing densities were made to observe the effect of bentonite/ CaCl_2 sample wall thickness on effective vapour diffusion into the composite. A high packing density (7.4 ± 0.15 g of dried composite including lattice) and a low packing density (5.8 ± 0.45 g of dried composite including lattice) as shown in Figure 3.6.

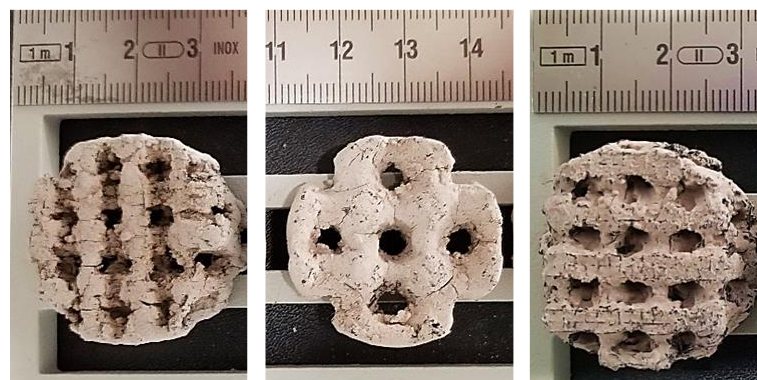


Figure 3.6. Bentonite/ CaCl_2 embedded prints. Diamond high packing density (left), schwarz high packing density (middle), and diamond low packing density (right).

A high packing density was characterised by embedding the maximum possible amount of wet bentonite/ CaCl_2 , pressed from the upper and lower surfaces of the print before removing material that only obstructed the intended open labyrinths. A lower packing density was characterised by an embedded surface that laid flat with all walls of the supporting print – showing lines of the printed lattice at its surface.

Discharged heat was measured from an open reactor using a thermocouple for inlet temperature monitoring. Six TPMS shaped cylinder parts were stacked to investigate the effect of stacking and packing density on thermal gradient and overall reactor performance. Moisture adsorbed was measured by weighing

each sample after each run using analytical scales to discuss any relationships between quantity of composite packed onto the lattice print (corresponding to wall thickness) and the wetted and thermally liberated salt hydrates. SEM images were captured, and Keyence images are captured as described in Section 2.5.8.1 to qualitatively describe salt formations and to quantitatively describe embedded cylinder part roughness respectively.

3.4.5. Energy Storage Reactor Set-up and Use

An experimental open THS reactor was used for proof of concept that featured an outer vessel length of 180 mm, and inserted PC pipe of 40 mm outer diameter that directed gas flow through housed bentonite/CaCl₂ cylinders (Figure 3.7). The pipe was modified by cutting a rectangular prism of base and height 8 × 15 mm to facilitate an inlet thermocouple, with gaps sealed using polypropylene tape. The inlet thermocouple was positioned 50 mm above the reactor entrance, and an outlet thermocouple was positioned 30 mm below the outlet. A middle thermocouple located 60 mm below the outlet was an uppermost bulk sensor positioned within 5 mm of a stacked column of bentonite/CaCl₂ cylinders but not touching it, representing an ideal outlet position.

The bentonite/CaCl₂ cylinders were numbered 1 to 6 with the 6th being closest to the outlet. Cylinders were placed in order of their dry weight between the inlet and middle thermocouples, with the heaviest cylinder of highest CaCl₂ mass placed at the inlet side. Each embedded cylinder was weighed before and after each cycle using analytical scales to measure water absorption via vapour transported along the column and observe corresponding relationships between adsorbent mass, diffusion, and bulk and outlet temperatures (ΔT).



Figure 3.7. Experiment configuration for column of embedded cylinders showing copper wrapped column with thermocouples and housing pipe.

Inter-cylinder thermocouples were positioned between each stacked cylinder with the column secured by a 0.02 mm thick copper sheet (Figure 3.7). Reactor inlet temperature was controlled at 25 °C by a heated jacket placed around a silicone tube that transported humid air set to 50 % RH travelling at 20 L/min from a Cellkraft P-50 humidifier. Data to and from the reactor inlet, outlet, and bulk thermocouple was received by an Arduino Uno microcontroller relaying to a logger on a desktop computer. Bulk temperatures from the inter-cylinder thermocouples were received by a PicoLog TC-08 data logger and relaying to PicoLog 6.2.4. software. Both loggers captured data at a rate of 1/s.

3.4.6. Bentonite/CaCl₂ Composite Surface Imaging

Images of swollen surfaces were captured using a Keyence VHX-7000 series digital microscope in transmitting light mode with samples placed on a glass stage. Imaging of 20 × magnified bentonite/CaCl₂ surfaces were captured to observe swelling severity, crack formations, and salt crystal sizes and dispersions. Samples surfaces were imaged and measured with 0.52 μm Z-step with their open labyrinths exposed by tilting the microscope 30 ° relative to the stage. Surface roughness parameters were output to quantify changes to surface roughness due to bentonite swelling: (Sa) arithmetic mean height, (Sz) maximum height, (Sq) root mean square height, (Ssk) Skewness, (Sku) Kurtosis, (Sp) Maximum peak height, (Sv) maximum pit height. A Hitachi TM4000 was acquired later in the project and replaced a TM3000 with the same backscatter detector as standard but improved software for image

analysis of dry bentonite/CaCl₂ surfaces once discharged by water vapour absorption.

3.5. Results

3.5.1. Benchmark Flow Simulations

Standard fin, baffle, and novel TPMS models were compared using simulated airflow input at 20 °C and 20 L/min through an open reactor model (Figure 3.8) to investigate the effect of matrix geometry on thermodynamics for THS. Software inaccuracy error (Table 3.3) and set-up error concerning positioning of stacked lattice cylinders (Table 3.4) is estimated as $\pm 1\%$. Reactor outlet pressure and temperature is governed by the matrix geometry (Figure 3.9); ranging between 0.63 and 0.66 (± 0.01) Pa, and 27 and 30 (± 0.3) °C, respectively.

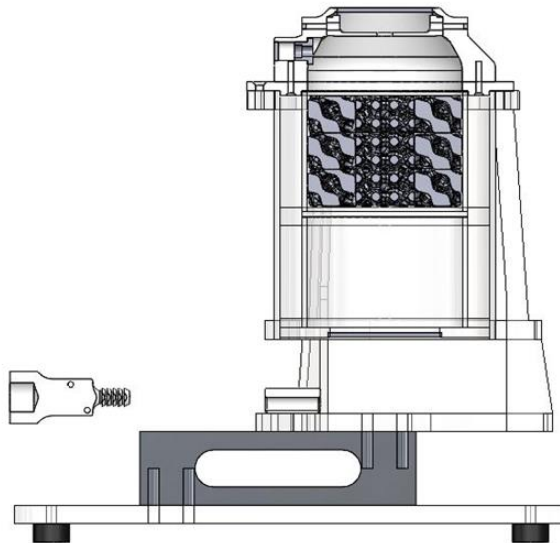


Figure 3.8. Reactor model showing load cell, inlet valve, and reactor vessel containing placed schwarz inner cylinder lattice design.

Fin designs yield low pressure and temperature values of 0.64 (± 0.01) Pa and ≤ 27.5 (± 0.3) °C, and an increase from 8 to 28 fins causes a negligible change to outlet pressure. However, an increase in outlet temperature from 26.7 (± 0.3) to 27.5 (± 0.3) °C is observed when a greater heated solid volume is present. These fins are integral to phase change heat exchangers for their ease of manufacture and means to invoke heat transfer through induction [11].

Here, fins fail to generate significant ΔT due to uneven temperature profiles through the reactor chamber (Figure 3.9). A more feasible geometric design for open reactor heat transfer is baffles, an integral element to shell and tube heat exchangers that provide vapour direction and provide here a valuable benchmark for TPMS geometries [12]. Baffles yield an outlet pressure of 0.64 (± 0.1) Pa for the three designs and a consistent outlet temperature of between 28.9 (± 0.3) and 29.4 (± 0.3) °C. Baffles outperform fins, as fin surface resistance create long viscous boundary layers that drag and slow airflow [13]. Baffles, however, mainly reduce airflow via turbulence that promotes even temperature lift with a lesser influence from drag. Turbulence could benefit salt hydrate matrices by providing water vapour to otherwise unreachable matrix surfaces further down a reactor's length [14].

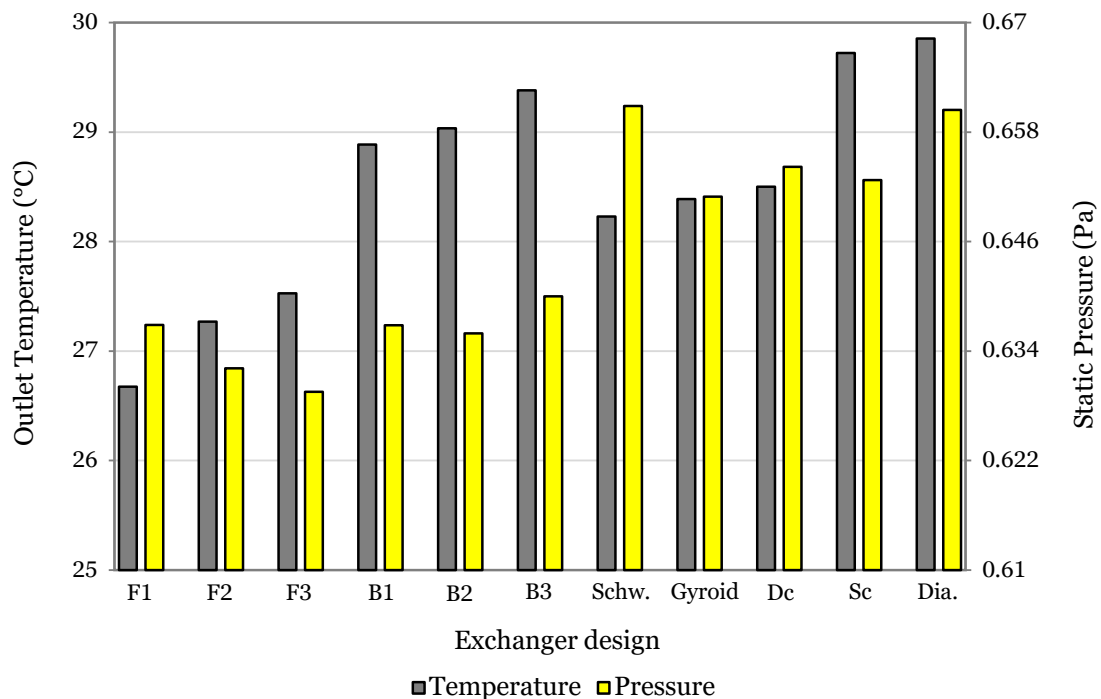


Figure 3.9. CFD temperature and pressure benchmarking of schwarz (schw.), gyroid, diamond inner cylinder (Dc), schwarz inner cylinder (Sc), and diamond lattice geometries (dia) against typical fin (F1, F2, and F3 with 8, 14, and 28 fins, respectively) and baffle (B1, B2, and B3 with horizontal alternation, vertical alternation, and staggered horizontal alternation, respectively) heat exchanger design.

Average outlet pressure of the five TPMSs is slightly higher compared to fin and baffle matrix design (Figure 3.9). The average outlet temperature of the baffle design is 29.1 (± 0.3) with variability of 0.50 °C, which is equivalent to TPMS design of 28.8 (± 0.3) °C with variability of 1.62 °C. The diamond lattice geometry is the highest performing of all designs with outlet pressure and

temperature of 0.66 (± 0.01) Pa and 29.9 (± 0.3) °C, respectively. The diamond lattice is a promising candidate for scalable hydrate embedded AM parts; however, it is also the most intricate to manufacture owing to a high TPMS surface area. Therefore, the simplest manufactured TPMS design of lowest surface area – the schwarz lattice – holds some logistic value and is also used to identify an effective print infill pattern.

The inner and outer cylinder lattice design (Section 2.3.1, Figure 3.1.) is implemented in part for greater control over airflow, and to avoid airflow stagnation. The utility of each TPMS as an inner cylinder can be determined by inner to outer cylinder TPMS surface area ratio (Table 3.1). Geometries with large cells outside and small cells inside in the radial direction allows greater radiation to penetrate a reactor to the centre/core of its porous lattice body [15]. Therefore, outer cylinders of double the cell size of inner cylinders were implemented here for heat transfer effectiveness, with the desired outcome of high inner/outer TPMS surface area ratio for uniform and rapid salt surface activation. The highest inner/outer TPMS surface area is a diamond and schwarz (Schw,c) configuration, which across three reactor set-ups yields outlet temperatures comparable to diamond. The schwarz inner cylinder in diamond outer cylinder opens potential for ease of manufacture at little trade-off in reactor performance compared to a fully diamond configuration.

Energy density values for each TPMS design as benchmarked against F3 and B3 show that reactor performance depends less on simply increasing lattice volume between 27.1-53.8 cm³ (B3 and gyroid) and more on heat transferred according to lattice geometry (Table 3.2). Aluminium composed B3 design of 27.1 cm³ volume and 22.8 (± 0.39) MJ/m³ E_d is similar in energy density to the Schwarz inner lattice of 45.8 cm³ volume and 23.6 MJ/m³ 23.6 (± 0.41) energy density despite a disparity in volume. This may be due to suitability of geometry for temperature distribution and heat exchange. The least efficient geometry, F3, is of 33.9 cm³ volume and when composed of aluminium has an E_d of 18.3 (± 0.32).

Table 3.1. Surface area and volume of outer and inner cylinder TPMS designs.

Lattice	Surface Area (cm²)	Solid volume (cm³)	Maximum inner/outer TPMS Surface Area Ratio
F3	70	33.9	-
B3	62	27.1	-
Gyroid outer	194	48.5	0.21
Gyroid inner	33	4.3	0.22
Schwarz outer	151	45.8	0.27
Schwarz inner	27	3.9	0.18
Diamond outer	251	46.6	0.16
Diamond inner	41	3.9	0.27

Table 3.2. Enthalpy change, ΔH , and energy density, E_d , calculated using lattice volume, and simulated fluid temperature and fluid humidity at the outlet. Error given in brackets is propagated error.

Lattice	ΔH, epoxy lattice (J)	ΔH, Al lattice (J)	E_d, epoxy lattice (MJ/m³)	E_d, aluminium lattice (MJ/m³)
F3	402 (± 7)	621 (± 11)	11.9 (± 0.21)	18.3 (± 0.32)
B3	400 (± 7)	618 (± 11)	14.8 (± 0.26)	22.8 (± 0.39)
Gyroid	698 (± 12)	1080 (± 19)	13.2 (± 0.23)	20.4 (± 0.35)
Schwarz	645 (± 11)	995 (± 17)	13.0 (± 0.22)	20.0 (± 0.35)
Diamond	784 (± 14)	1210 (± 21)	15.5 (± 0.27)	24.0 (± 0.42)
Diamond inner	666 (± 12)	1030 (± 18)	13.4 (± 0.23)	20.7 (± 0.36)
Schwarz inner	773 (± 13)	1190 (± 21)	15.3 (± 0.27)	23.6 (± 0.41)

Thermal conductivity and reactor insulation are key parameters to the potential efficiency of a THS system (Figure 3.10). Aluminium, simulated as a lattice material to be coated in energy storage material, increases outlet temperature by 1.16-1.68 °C compared to epoxy composed lattice geometries. Epoxy is stereolithography printable and has a low thermal conductivity of 0.188 W/m.K, unlike aluminium of 170 W/m.K which is printable by selective laser sintering, both potential materials for the intended clay/hydrate embeddable lattice design. The thermal conductivity of aluminium is closer to ideal (copper of 390 W/m.K) than epoxy but AM of metal powders increases expense, resources, post processing, and often corrosion resistant coating requirements. Installing readily available glass wool to the reactor exterior increases outlet temperatures by between 2.03-2.46 °C, providing a promising method for improved open reactor performance at relatively low-cost.

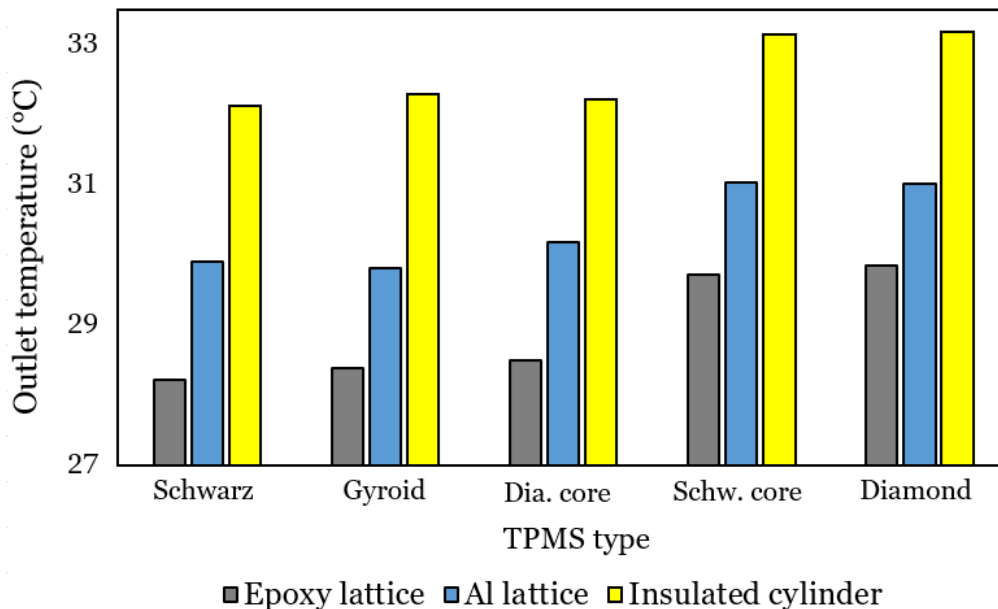


Figure 3.10. Simulated outlet temperatures of a non-insulated reactor containing heated surfaces shaped as schwarz, gyroid, diamond cylinder, schwarz cylinder, and diamond lattice geometries, when composed of epoxy (grey), and aluminium (blue). An insulated reactor containing an Al lattice is shown in yellow.

CFD simulations show airflow velocity and temperature through a schwarz cylinder lattice starts as a concentric contour due to inlet shape and drag caused by vessel walls (Figure 3.11, top). The vessel in the XY plane is not symmetrical due to an opening intended for the placement of an outlet thermocouple that creates a non-uniform back pressure, hence anisotropic airflow develops beneath the lattice. Airflow velocity through the outer cylinder reaches 0.18 (± 0.02) m/s at its centre and nears 0.07 (± 0.01) m/s at the outer

perimeter, showing faster moving air than at the vessel walls below and above the outer cylinder due to labyrinth convection. It is worth noting that the passage of air through the diamond labyrinth is less direct than through the schwarz lattice as there is no direct pathway towards the outlet (Figure 3.13). Despite this, outer cylinder diamond labyrinth air passage velocity is 4× that of air passing through the inner cylinder schwarz labyrinths at velocities of 0.18 (± 0.02) and 0.04 (± 0.01) m/s respectively.

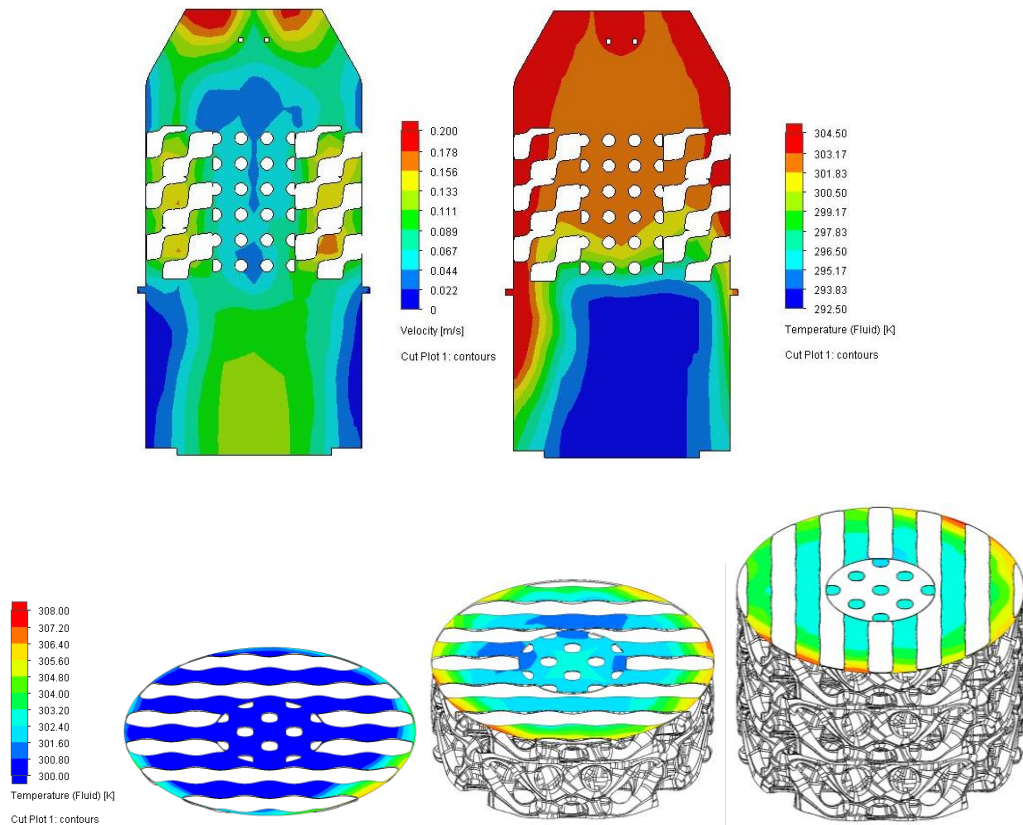


Figure 3.11. Cut plots from SW flow simulations using a typical 20 L/min inlet volume rate showing the full length and diameter of the in-house built reactor with velocity (top left) and temperature (top right) contour maps presented. Cut plots (bottom) show the development of fluid temperature across the radius of the lattice from start, centre, and upper regions.

The diamond and schwarz open labyrinths raise and homogenise air temperature (Figure 3.11). There develops a distinct influence from both cylinder geometries, with schwarz heating to 28.7 (± 0.3) °C at the same point along the reactors length where the diamond cylinder has heated to 26.0 (± 0.3) °C. However, the heated reactor walls promote higher temperatures of ≥ 30.0 (± 0.3) °C above the diamond cylinder compared to 28.9-30.0 °C above the inner cylinder. Air is heated at the inlet from 20.0 (± 0.2) °C to between 28.7 (± 0.3) and 31.4 (± 0.3) °C at the top surface of the lattice, with warm air

converging along tapered walls towards the outlet. Such a heating effect may be rationalised by the lattice geometries thermal mass distribution, as a reaction front of 24- 30 mm forms in the diamond labyrinths that accounts for 83% of all lattice volumetric heat capacity, and a shorter schwarz reaction front of 14-20 mm results from slow moving airflow through the schwarz stack providing more time to heat.

Air temperature radial distributions at the lower surface of an aluminium schwarz inner lattice vary by 6 °C with temperatures highest at the perimeter probably resulting from the conduction of heat by the reactor walls (Figure 3.11). The centre of the lattice shows similar radial distribution with the centre reaching 30 °C, which is maintained up to the top lattice surface. However, the top lattice surface radial temperature distribution is lowered and there are no stagnant zones. At the centre, the radial area of the diamond lattice surrounding the inner schwarz is up to 2 °C lower than the schwarz centre due to a halved unit cell size whereby walls of the inner cylinders are closer together. Solid volume gradients can be tuned using TPMS cell size (equivalent to baffle thickness and z-height distribution) to any reactor design made possible with the proposed AM and bentonite/salt coating method.

Airflow approaches an equilibrium temperature further from the inlet as inlet flow rates increase from 10 to 60 L/min (Figure 3.12). ΔT is highest with a 10 L/min flow rate, where the first 15 mm (from the purple to green point parameter) measures a ΔT of 8.0 °C and the remaining lattice heats the air by 0.5 °C. In comparison, the outlet temperature is lowest for a 60 L/min flow rate, whereby the first 15 mm measures a ΔT of 2.0 °C and the remaining lattice heats the air by 1.1 °C. By observing pressure and temperature gradients using CFD, optimal inlet flow rate and effective length of lattice adsorbent can be estimated, as influenced by their shape, cell size, and air flow between inner and outer cylinders. All flow rates show a residual heat convection from the preheated lattices; initial temperatures at the lattice entry are above the inlet temperature of 20 (± 0.2) °C. A stagnation cooling effect is shown only at a 10 L/min flow rate, where peak airflow temperature is not at the outlet due to thermal losses to the reactors external environment. At 10 L/min, air at the entry of the lattice is 0.4 °C hotter than at the outlet. All other flow rates show heating past the top surface of the lattice as warm air moves from the perimeter to the centreline of the vessel where the outlet is located.

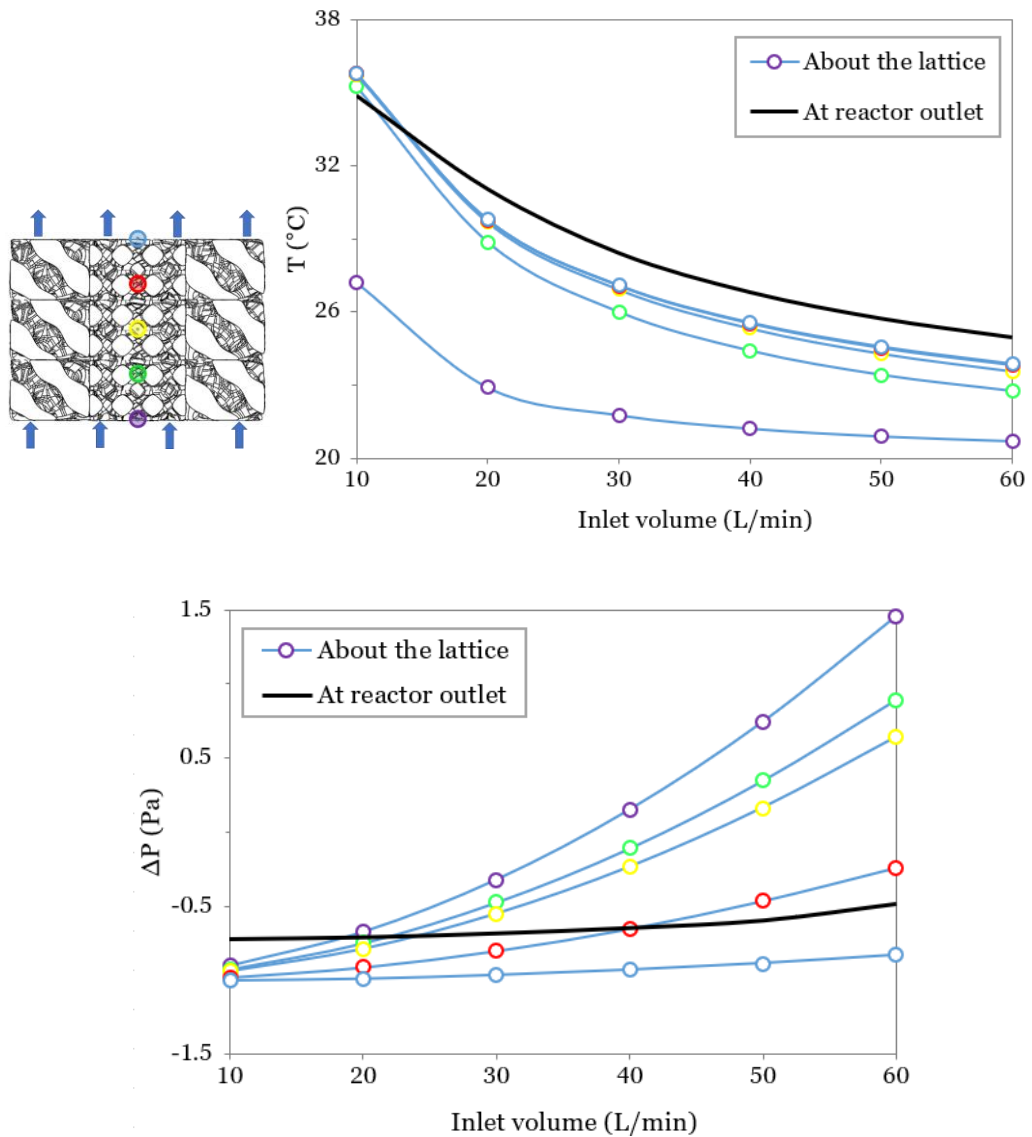


Figure 3.12. Fluid temperature (top) and pressure (bottom) against inlet volume rate: 10, 20, 30, 40, 50, and 60 L/minute (bottom right). The coloured points show fluid heating as it moves through an aluminium TPMS lattice cylinder (depicted top left) while the black line shows outlet temperature against inlet flow rate.

Outlet pressure increases by $0.24 (\pm 0.01)$ Pa with inlet rates between 10 and 60 L/min. More work is done at the lower surfaces of the lattice as shown by the higher P at lower positions in the reactor. Pressure at the outlet is 0.3 Pa higher than at the top of the lattice because air flow to the reactor environment is restricted by an outlet of 51 mm diameter compared to a reactor body of 84 mm diameter. Pressure about the lattice does not drop linearly and at higher inlet rates the pressure at the top surface of the lattice (blue point parameter, Figure 3.12) follows a relatively low gradient suggesting turbulence increases with inlet flow rate. Furthermore, pressure about the lattice alternates between

accelerating and decelerating when approaching the inlet as indicated by the point parameters. This suggests currents of air travelling through the diamond lattice labyrinths partially mix with airflow through the schwarz lattice labyrinths. The lower TPMS surface area and more direct vertical pathways of the schwarz geometry lends to greater mass transfer, hence mixed airflows can aid in dispersing moisture from inner lattices to upper reactor regions. Turbulence promotes sorption driving force at the outlet side of the reactor where driving force and mass transfer is typically low, and salt hydrate surfaces are harder to access with water vapour especially when in the bulk of the matrix. Reactor designs can be rapidly optimised for transport and drying of vapour using point parameters and CFD modelling. Future iterations could include a reduced density of the lower lattice parts as to observe lengthened reaction fronts and associated effective reactor length to promote even sorption of water and maximum ΔT . By accounting for reactor cell size, lattice density gradient, and lattice length a step towards avoiding overly deliquesced salt that prevents vapour diffusion can be taken.

3.5.2. Calculated Simulation and Measured Reactor Probe Error Tables

This section provides simulation error as calculated in SW using convergence of residuals. Steady state is achieved (100% progress) as delta error drops below criterion values for each iterated parameter (Table 3.3). Simulation set-up error analysis is given (Table 3.4) showing SD error is $\geq 1.2\%$ of the mean average. As convergence is never completed the 1.2% value of error provides a benchmark of reliability, for more rigorous simulations converging dozens of parameters of perhaps extreme values, SW error may not reach such reliable values in which case ANSYS or other fluid flow software capable of reacting, non-Newtonian, multiphase analysis could be utilised.

Thermocouples at the inlet of the experimental reactor show a temperatures range of $0.54\text{ }^{\circ}\text{C}$ and SD error of $0.18\text{ }^{\circ}\text{C}$ (Table 3.5). A room temperature range of $0.54\text{ }^{\circ}\text{C}$ was also measured across 4 hrs using a thermocouple in the environment of the reactor (Table 3.6), hence a fairly accurate measurement of similar peak temperature conditions in all cases. Measured peak inlet humidity values ranged by 3.54 RH% with the mean average at 45.18 RH% being lower than the programmed 50 RH%.

Table 3.3. Measured simulation results showing average, min, and max values of goals iterated until the criteria was met with error of delta. Values show results from simulating an aluminium swcharz TPMS geometry with an inlet volume of 30L/min across 63 iterations.

Goal Name	Unit	Value	Averaged Value	Minimum Value	Maximum Value	Progress [%]	Delta	Criteria
Global average relative humidity	[%]	38.5	38.6	38.5	39.0	100	0.5	1.2
Outlet temperature (fluid), bulk average	[K]	301.6	301.4	300.9	301.6	100	0.70	0.90

Table 3.4. Repeated simulations of repositioned and re-meshed Dc lattices, average values of each achieved goal as use to calculate mean average, SD, and SD as a % of the mean average.

Goal Name	Unit	Run 1	Run 2	Run 3	Run 4	Run 5	\bar{x}	SD	%
Surface (outlet) temperature (fluid) bulk	[K]	305.40	305.41	305.47	305.47	305.51	305.45	0.046	0.02
Surface (outlet) maximum temperature (fluid)	[K]	309.0	309.2	309.0	309.0	308.9	309.0	0.10	0.03
Surface (outlet) minimum temperature (fluid)	[K]	298	293	302	295	295	297	3.5	1.20
Surface (outlet) environment pressure velocity	[m/s]	0.1766	0.1755	0.1768	0.1765	0.1770	0.1765	0.0005	0.32
Surface (outlet) minimum velocity	[m/s]	0.011	0.003	0.016	0.004	0.009	0.009	0.005	62*
Surface (outlet) maximum velocity	[m/s]	0.297	0.302	0.301	0.301	0.302	0.301	0.002	0.59
Surface (outlet) minimum absolute humidity	[g/m ³]	8.235	8.231	8.236	8.234	8.239	8.235	0.003	0.03

Surface (outlet) maximum absolute humidity	[g/m ³]	8.5	8.7	8.4	8.6	8.6	8.6	0.1	1.20
Global average relative humidity 1	[%]	32.9	32.5	32.8	32.9	32.8	32.8	0.14	0.43

*High error of minimum velocity is due to air flowing momentarily at near zero velocity

Table 3.5. Measured maximum inlet temperature (°C), and humidity (%RH) values from clay/salt embedded printed lattices of hex, 15, and 20 % infill density.

Lattice geometry and printed infill density	Inlet temperature (°C) max	Inlet humidity (%RH) max
Schw. 15%	23.7	45.3
Schw. 20%	23.5	44.7
Schw. Hex	23.6	43.2
Dia. 15%	23.8	45.5
Dia. 20%	23.5	46.1
Recharged Schw. 15%	23.5	46.8
Recharged Schw. 20%	23.5	45.5
Recharged Schw. Hex	23.6	45.4
Recharged Dia. 15%	24.0	44.8
Recharged Dia. 20%	23.8	44.6
average	23.7	45.2
SD	0.18	0.95

Table 3.6. A recharged run with 6 stacked TPMS cylinders, the thermocouple is exposed to airflow outside the reactor to measure room temperature averaged with standard deviation calculated across 4 hours (1200 data points).

	Av. T, hour 1 (°C)	Av. T, hour 2 (°C)	Av. T, hour 3 (°C)	Av. T, hour 4 (°C)	\bar{x}	SD
Thermocouple to PicoLog	21.45	21.61	21.8	21.99	21.71	0.24

3.5.3. Bentonite/CaCl₂ Embedded Prints

Bentonite/CaCl₂ embedded lattice prints of novel schwarz and diamond geometries were compared for maximising ΔT via water adsorption. Measured bulk temperatures of the bentonite/CaCl₂ were higher than room temperature and peaked above inlet temperature in all cases (Figure 3.14). The embedded diamond lattice cylinder shows a greater temperature increase from hydrating dispersed salt crystals compared to the schwarz lattice cylinder, which agrees with the steady state CFD simulation results. In the case of schwarz lattices, bulk temperatures peaked with a 20 % print infill density, reaching 25.2 (± 0.3) °C once recharged. All embedded diamond lattice cylinders provided bulk temperatures higher than their schwarz counterpart. A peak bulk temperature of 26.8 (± 0.3) °C for diamond cylinders was provided by a 15% print infill density. The lowest diamond cylinder bulk temperature was 1.6 °C higher than the worst performing schwarz cylinder, and 0.6 °C higher than the best performing schwarz cylinder owing to larger TPMS surface areas and optimal labyrinth geometry for greater CaCl₂ crystal surface exposure.



Figure 3.13. Plane view of TPMS PC printed cylinders from left to right: 15% infill diamond, 20% infill diamond, 15% infill schwarz, 20% infill schwarz, hex infill of 2.5 mm cell size.

Reactor outlet temperatures between 22.9 (± 0.2) and 23.5 (± 0.2) °C show a marginal uplift dependence on lattice cylinder geometry, whereby temperatures from schwarz cylinders are higher than from diamond cylinders on the first run but not the recharged run. Schwarz cylinders on their first run generated average outlet temperatures of 23.5 (± 0.2) °C that dropped to 23.0 (± 0.2) °C when recharged, and average diamond cylinders reached outlet temperatures of 23.1 (± 0.2) °C on their first run and 23.5 (± 0.2) °C when recharged (Figure 3.14). The variability between measured schwarz cylinder governed outlet temperatures of 0.2 °C, and diamond cylinder variability of 0.1°C, are within the outlet thermocouple SD error of 0.2 °C. Outlet temperature could be influenced by air flowing between the part and outlet thermocouple - a large volume of slow-moving air lies between the pipe exit and the outlet thermocouple as observed using CFD simulations (Figure 3.11).

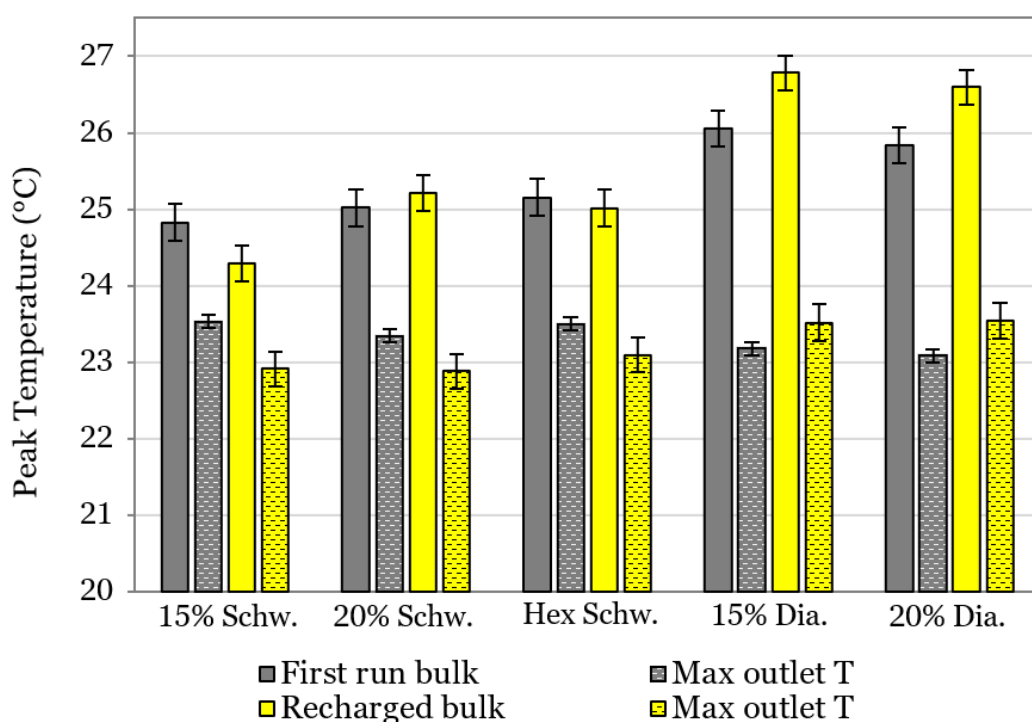


Figure 3.14. Reactor bulk and outlet temperatures for 15%, 20%, and hex infilled TPMS cylinder prints embedded with bentonite/CaCl₂ of high packed density (top).

Unlike the smooth simulated cylinder surface, the investigated clay/salt surface is an uneven particulate composition, i.e., microplatelets and crystals form a relatively rough cylinder texture that worsens with a recharge (Figure 3.15). Such bentonite swelling of cylinder parts will affect airflow velocity and ΔT across the reactor. Expansion could slow airflow, increase adsorbed water at the lower levels of a reactor compared to higher levels, and decrease overall salt surface activation.



Figure 3.15. Optical microscopy images of highly packed diamond TPMS bentonite/CaCl₂ cylinders before (left) and after (right) exposure to water vapour for 4 hrs across two discharge runs.

Hex infill is the heaviest of the infill patterned prints owing to strong PC walls that potentially confine bentonite/CaCl₂ to individual sections within its bulk to a greater extent than 15 and 20 % infills composed of pliable under-extruded lines. In the latter case, composite surfaces readily expand and roughen according to adsorbed water mass. Mean roughness, Sa, of embedded diamond parts increased upon swelling from 1400 μm to 1700 μm before and after discharging (Table 3.7).

Table 3.7. Macroscopic roughness parameters of imaged high packed diamond cylinder before discharge, higher positioned and lower positioned diamond cylinders exposed to 70 %RH at 20 L/min for 16 hours. Twice recharged (run 3) high packed macroscopic roughness parameters for the consideration of effects of recharging on swelling at 50 %RH. Microscopic roughness of twice recharged low packed diamond cylinders, first cylinder is near the inlet and the sixth stacked cylinder is near the outlet with SD given from 10 measurements from both sides of each specimen.

	Pre-run	High position (16 hrs)	Low position (16 hrs)	Run 3 (3×4 hrs)	Cylinder 1 (SD) (3×4 hrs)	Cylinder 6 (SD) (3×4 hrs)	Unit
Sa	1,400	1,700	1,700	1,900	70 (±30)	30 (±10)	μm
Sq	1,900	2,000	2,000	2,300	80 (±40)	40 (±10)	μm
Ssk	-1.0	0.5	-0.5	-0.6	-0.4 (±0.4)	-0.6 (±0.4)	
Sku	4.6	2.7	2.6	3.3	2.7 (±0.8)	3.0 (±0.7)	
Sp	3,100	3,600	4,400	4,300	150 (±80)	80 (±20)	μm
Area size	92.76	100.36	82.60	91.50	1.65	1.65	mm ²

A high exposure experiment of 70 %RH vapour for 16 hours presents a sharp peak in bulk temperature at 29.1 °C (Figure 3.16), which is 2 °C higher than previously observed with one cylinder in the reactor vessel. Bentonite/CaCl₂ surfaces roughened due to vapour exposure and swelling, whereby lower

positioned and highly exposed surfaces showed a $100 (\pm 80) \mu\text{m}$ higher S_q compared to unexposed pre-run surfaces (Table 3.7, macroscopic error is taken as 5% from Charles *et al* [16] which is coherent with microscopic roughness SD values of $<33 \mu\text{m}$). Surfaces exposed to three 4 hour runs (twice recharged) at the more application representative humidity level of 50 %RH roughened by $400 (\pm 100) \mu\text{m}$.

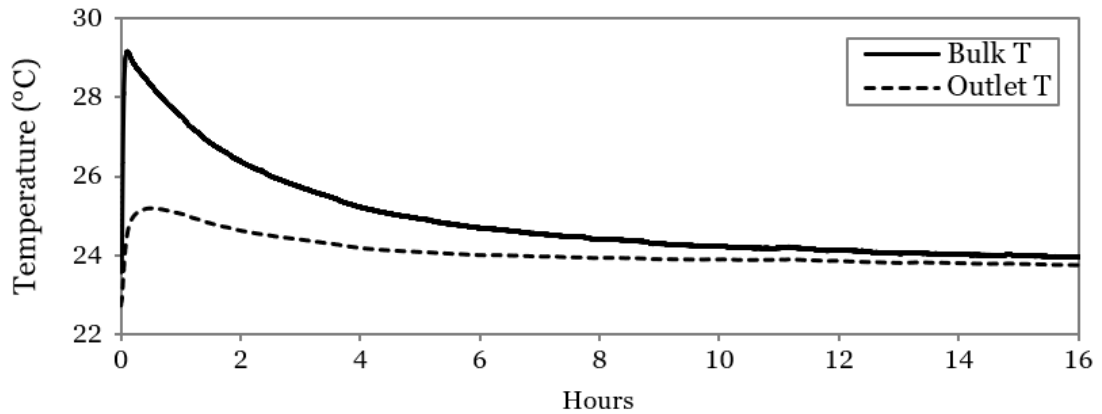


Figure 3.16. Two stacked bentonite/ CaCl_2 embedded schwarz TPMS cylinders, a first run with 70 %RH airflow at 20 L/min for 16 hours measured for bulk and outlet temperature.

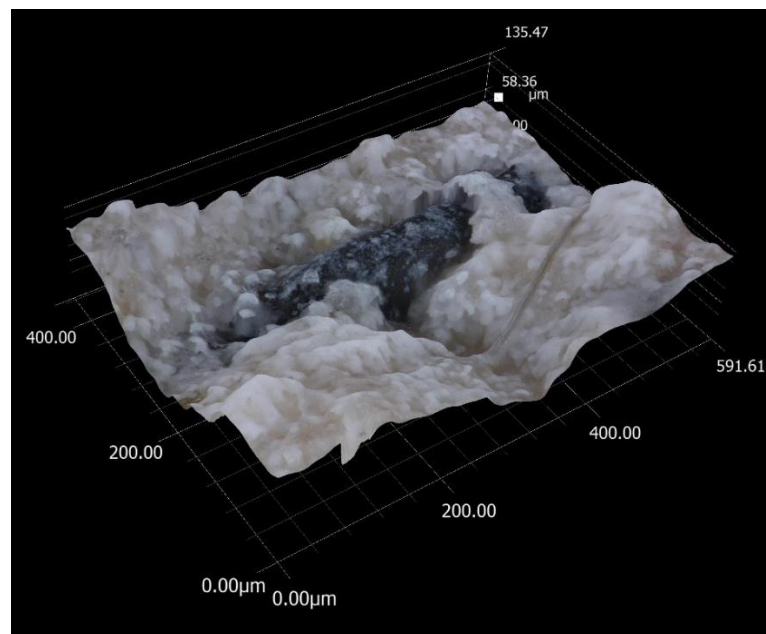


Figure 3.17. Partially breached PC printed lattice line composing a high packed bentonite/ CaCl_2 embedded TPMS cylinder after a first open reactor run exposed to 70 %RH vapour at 20 L/min for 16 hrs.

The samples are relatively rough before being tested due to the handling of malleable clay necessary for experiment set-up. Pre-run composite roughness

skew and kurtosis values of -1.02 and 4.58, respectively, indicate wetting samples significantly move pit depths towards the mean surface level. Hence, adsorption causes swelling and reduced labyrinth open volumes, and newly formed areas of inconsistent height are raised. This is clarified by maximum peak height values (S_p , i.e., amplitude) that increase from a pre-run surface of $3,100 (\pm 150) \mu\text{m}$, to the high positioned and less exposed cylinder surface of $3,600 (\pm 180) \mu\text{m}$, to low positioned and most exposed cylinder surface in the reactor of $4,400 (\pm 220) \mu\text{m}$.

Expanded and cracked bentonite matrix is a roughened surface (Figure 3.18) due to sorption causing turbulent airflow past newly exposed surfaces that can act to wet and thermally liberate otherwise under-hydrated volumes of embedded CaCl_2 . Adsorption at CaCl_2 newly exposed to vapour could explain how diamond outperforms schwarz for outlet temperature on the recharge run (Figure 3.14), based on a higher TPMS surface area and associated surface roughing of the diamond geometry.

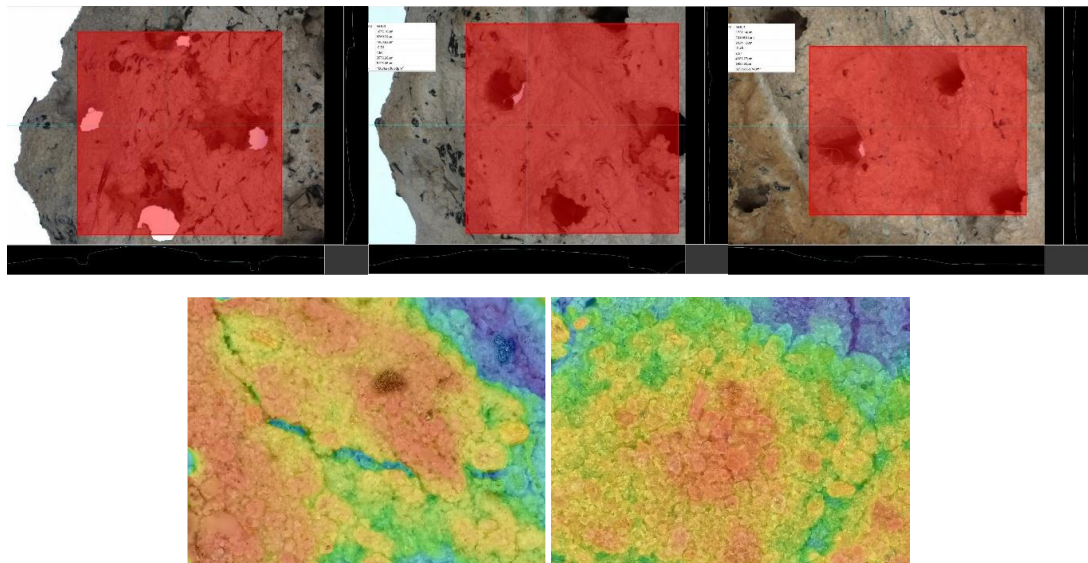


Figure 3.18. Imaged surfaces corresponding to roughness values of diamond cylinder before discharge (top left), higher positioned (top middle), and lower (top right) positioned diamond cylinders exposed to 70 %RH at 20 L/min for 16 hours. Typical imaged surfaces with colour map showing change in height of first stacked cylinder after second recharge (bottom left), and sixth stacked cylinder after second recharge (bottom right), both measured at 50 %RH at 20L/min for 3×4 hr runs.

Increased recharged bulk temperature of the diamond might offset slow airflow cooling effects from surrounding internal reactor volumes by rising at greater temperature. Hence swelling may favour the diamond lattice cylinder because of its high TPMS surface area, which is $1.5 \times$ that of schwarz, because

during swelling water does not exclusively adsorb on the external surface but can adsorb to deep structural interlayers [17]. A higher TPMS surface area of a part with thin walls such as the diamond geometry creates more opportunity for swelling induced interlayer diffusion.

The volume expansion of hydrated $\text{CaCl}_2 \cdot 6\text{H}_2\text{O}$ at its melting point (28°C) is about 11% and has been known to cause physical and thermal storage problems to pellet configurations with recent efforts to reduce expansion being focused on crystal encapsulation [18]. However, a compromise in energy storage density is subsequently made.

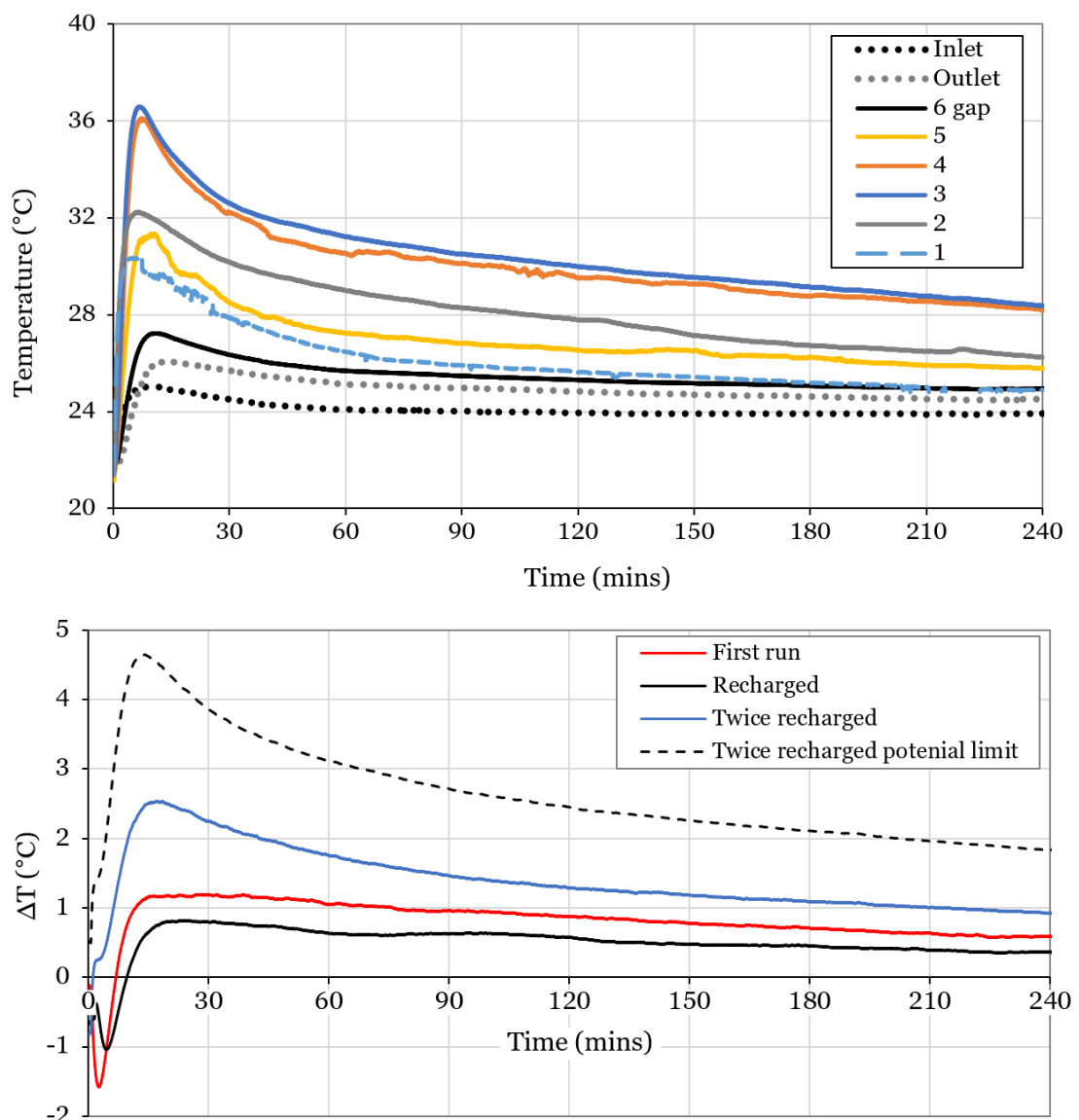


Figure 3.19. Stacked printed and embedded lattice cylinders bulk, inlet, and outlet temperature profiles across 4 hrs exposure to 50% RH traveling at 20 L/min (top). R1, R2, and R3 outlet ΔT profiles of stacked cylinder system with outlet theoretical limit of R3 (dotted line) when of the high packed density configuration (bottom).

Bentonite swells less when wetted with CaCl₂ solution as opposed to DI water [19], therefore an even coating of CaCl₂ is needed to improve matrix to wall contact. Low swelling means closer packed crystals, higher energy density, and minimised voids throughout the structure, however opened voids may create pathways for interlayer diffusion. Despite swelling, the PC printed lattice surface is visible at the bentonite/CaCl₂ cylinder surface showing a well contained salt and matrix. With a change to low packed density configuration of bentonite/CaCl₂ a further reduction of swollen matter reduces blocking of open labyrinths for promoted vapour flow.

Table 3.8. Summary of measured outlet and bulk temperatures taken from cylinder stack investigation of high and low packed density cylinders for multiple recharges (R1 to R3).

Sample, run number	Outlet ΔT max (°C)	Bulk T max, (thermo-Couple #) (°C)	Av. bulk T above stack, (SD) (°C)	Time to ΔTmax (min)	Potential ΔTmax (°C)
High packed R1	1.2	36.6 (3)	25.4 (0.6)	28	2.2
High packed R2	0.8	35.5 (5)	25.8 (0.7)	24	2.8
High packed R3	2.5	37.4 (4)	27.5 (0.8)	17	4.6
Low packed R1	3.0	38.3 (5)	31.1 (2.3)	17	7.8

Table 3.9. Summary of absorbed mass values (ΔM_{ab}) taken from cylinder stack investigation of high and low packed density cylinders for multiple recharges (R1 to R3).

Sample type and number of runs	ΔM_{ab} at 4hrs (g)	ΔM_{ab} at 4hrs (%)	ΔM_{ab} dry weight loss (g)
High packed R1	6.8	15.3	0.06
High packed R2	6.7	15.2	0.05
High packed R3	5.8	13.1	-0.10
Low packed R1	6.6	19.1	0.06

Highly packed bentonite/CaCl₂ prints were investigated for temperature uplift and sorption along the length of the vessel by stacking six diamond cylinders vertically, which also worked to strengthen the correlation between bulk and

outlet temperatures. First run bulk temperatures from 44.2 g total dry mass (incl. PC printed lattice) successfully heated airflow travelling from the inlet at 24.0 °C to provide the reactor system of 1521 cm³ vessel volume a stable ΔT of 0.6-1.2 °C for 4 hours (Figure 3.19, bottom). Inlet, outlet, and bulk temperatures were successfully measured from above and between each cylinder showing bulk temperatures (with inter-cylinder part thermocouple error is given as 1%, Table 3.6) peak in the centre of the stack above cylinder 3, closely followed by 4 at 36.6 (± 0.4) and 36.1 (± 0.4) °C, respectively. It was visually observed that vapour fails to maintain even adsorption to cylinder surfaces higher up the stack that likely caused the bulk peak temperature of the fifth cylinder to drop by 4 °C to 32 (± 0.3) °C, and by the last cylinder bulk peak temperature to drop to 27.2 (± 0.3) °C. However, the highest positioned cylinder thermocouple (6 gap) is placed above the cylinder stack whereas all other thermocouples touch the bentonite/CaCl₂ surfaces. If air left the open reactor at this position above the stack the exiting air would read an equivalent temperature to that of the sixth thermocouple.

Stacked bentonite/CaCl₂ cylinders, as with single cylinder experiments, show best temperature uplift when recharged which in this case peaked during a twice recharged run (Figure 3.19, bottom). However, ΔT dropped from 0.8 (± 0.1) to 0.4 (± 0.1) °C during the first recharge to then peak at 2.5 (± 0.1) to 0.9 (± 0.1) °C during the second recharge whereby water vapour uptake is 0.9 g lower (Table 3.9), indicating a notable change to diffusion kinetics. The first run and first recharged runs both show a stable outlet temperature plateau from the onset, and temperatures peak at 28 and 24 minutes, respectively. Whereas the twice recharged stack outlet temperature peak point is a spike at 17 minutes that gradually stabilises. This suggests a twice recharged stack yields increased water molecule to salt crystal surface interaction. Therefore, the cylinder surfaces improve for THS by wetting, expansion, and drying cycles. Expansion of the montmorillonite has facilitated new pathways for vapour diffusion, utilising more CaCl₂ salt hydrate that was previously bulk material inaccessible to vapour. The benefit of reorientated salt crystals by bentonite expansion that forms cleaved composite surfaces upon drying is twofold because new sub surfaces can potentially be accessed by capillary action through bentonite interlayers. Intercalation of water in these interlayers form hydrogen bonds with hydroxyl groups that release more heat, and the dissolved salt hydrate forms Ca²⁺ cations that can flow into interlayer regions by intercalation [20,21]. These exchangeable cations can revert to CaCl₂ upon evaporation of water, in doing so creating a new supply of crystals beneath the

original surface and effectively activating newly cleaved surfaces upon the second recharge.

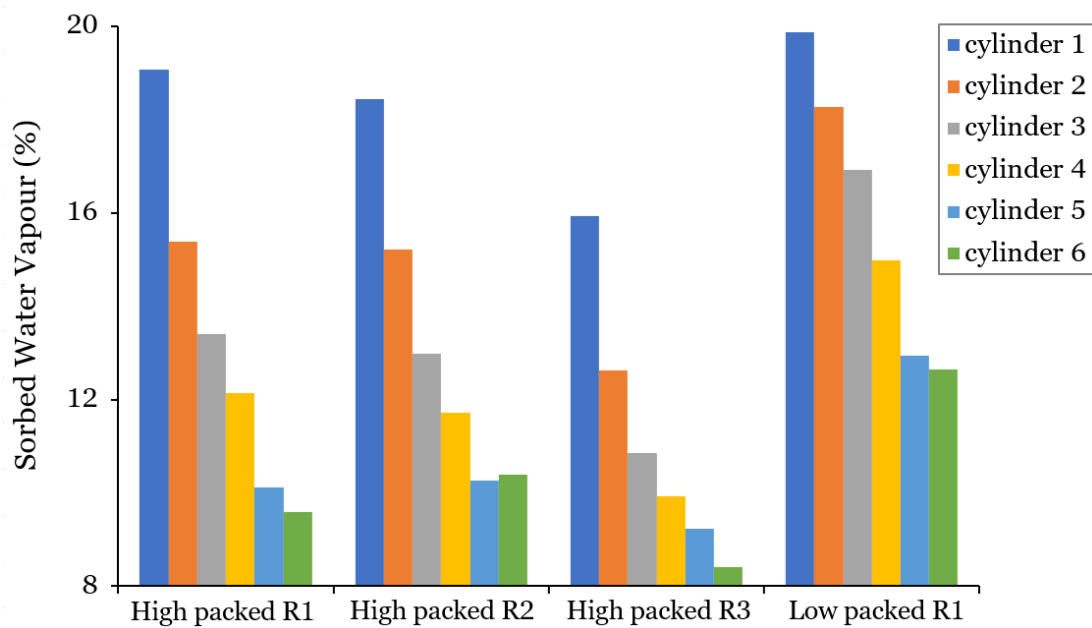


Figure 3.20. Sorbed water vapour as a percent weight of the cylinder for each stacked cylinder in order of their position along the reactor length from inlet side to outlet side, including high and low volumes of packed bentonite/CaCl₂ composite.

High water adsorption is key and helps to illustrate bentonite/CaCl₂ applicability as an embeddable THS composite. A negligible change in mass of ≤ 0.1 g across all stacked experiments (Table 3.9) confirm swelling of bentonite is accommodated by the PC of high impact toughness, which acts to avoid loss of dry composite material through mechanical wear when handled. Diamond cylinder print time was 25 minutes and weighed 0.7 g, with resulting embedded print longevity depending on volumetric stability that can deplete by attrition of the matrix via loss of plasticity [22]. Embedded diamond lattice water sorption of $<19.1\%$ total dry cylinder weight is a promising indication for commercial THS system application with recharge performance (Figure 3.20) providing system safety, cost, and robustness credentials. Matrix rotation in the reactor vessel to promote even wetting would further exploit the cohesive strength of bentonite. A limitation of the proposed system could be an increase in weight observed by post- twice recharged (R3) runs showing a less than 100% dried bentonite/CaCl₂ composite at 120 °C due to newly redistributed crystal formations (Table 3.9).

Average bulk temperatures above the stack increased from 25.4 (± 0.6) to 31.1 (± 2.3) °C (where SD is calculated using all data points from a 4 hr run) when employing lowered packed density diamond lattice cylinders, which also

increased potential ΔT (ΔT max) from 2.2-7.8 °C indicating better subsurface activation of CaCl_2 crystals. Highest ΔT of all observed configurations was provided by the low packed configuration of exposed PC printed walls - of thin composite wall thickness. Total mass of embedded high packed cylinders ranged from 7.2-7.5 g, compared to 5.3-6.2 g for low packed cylinders, which increased average bulk ΔT by 5.7 °C due to more open labyrinths.

Low packed cylinders showed an improved mass transfer and absorption of 0.8 g at the inlet side and 3.0 g at the outlet side of the reactor confirming increased salt crystal accessibility via matrix permeation that offsets energy density deficit (Figure 3.20). A drop in absorption occurred along the length of the high packed cylinder stack after each discharge cycle, however the second recharge (R3), which failed to dry entirely at 120 °C, steadily absorbed mass at the lowest rate of change between stacked cylinders. Lower absorption would suggest lower bulk temperatures, however, this sample provided ≤ 1.7 °C and ≤ 2.4 °C higher outlet ΔT max and potential ΔT max, respectively when compared to earlier runs. This likely arises by the postulated hypothesis of activated cleaved surfaces, an intercalation of interlayer Ca^{2+} cations that recombine with Cl^- to form a fine dispersion upon evaporation. Low packed first run (R1) lattice cylinders and water vapour permeated high packed lattice cylinders presented fine salt dispersions on their surfaces (Figure 3.21). Considerable morphology variations are present between each surface, where pre-run R1 samples show a uniform scatter of individual salt crystals on bentonite and R1 vapour permeated cylinder surfaces show a more agglomerated morphology composed from bentonite enveloped CaCl_2 crystals. Enveloped salt prevents a crust formation of large salt crystal agglomerations, a common pitfall of pellet design matrices that often leads to vapour impermeable layers near the reactor inlet [23], shows a fine formation of CaCl_2 crystals 1-4 μm in diameter on micro-platelet composed bentonite particles of various sizes measuring 10-45 μm in diameter (Figure 3.21, A). However, bentonite formed as ≤ 150 μm diameter agglomerates that are similar in size to the agglomerates shown in image B, being smoothed by exposure to adsorbed vapour and deliquesced salt solution. Roughened surfaces between bentonite smoothed particles are evident in image B showing cracks formed to accommodate swelling.

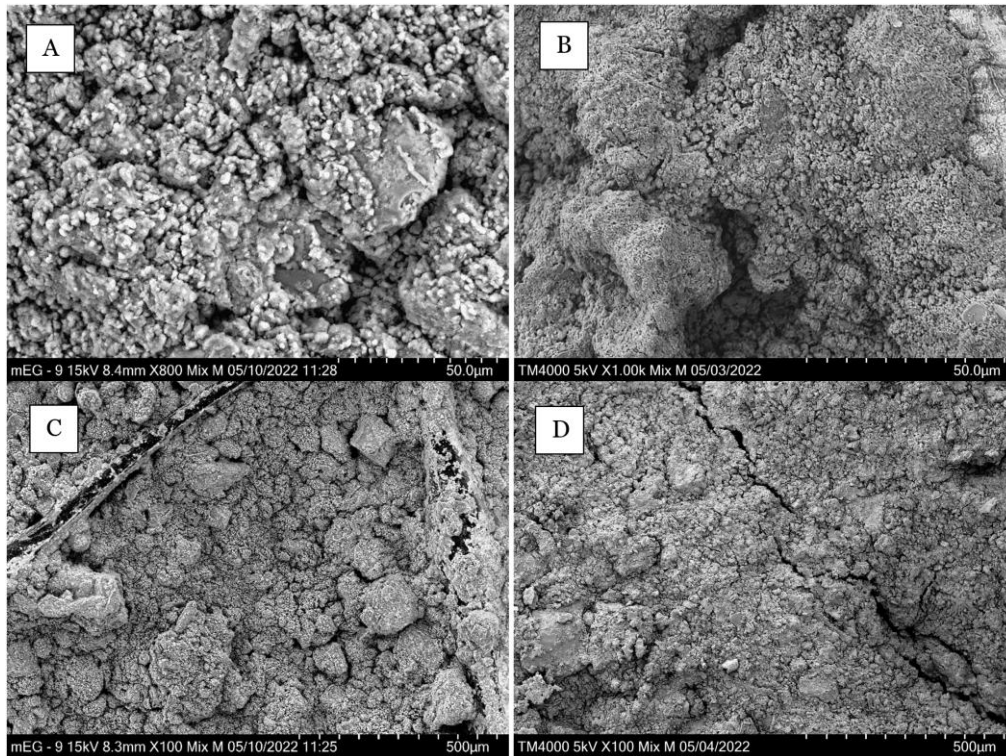


Figure 3.21. SEM images of bentonite/CaCl₂ cylinder surfaces, (A) fine salt dispersion of low-density packed sample before R1, (B) agglomerated surface showing reduced granule size of high-density packed sample after R2, (C) coated bentonite/CaCl₂ on PC printed lines and surrounding granular low-density packed surface before R1, (D) cracked bentonite/CaCl₂ of high-density packed sample after R3.

Partially coated PC lattice lines of neutral polarity and low intrinsic water absorption shows compatibility with the cohesive bentonite/CaCl₂ composite (Figure 3.21, Image C). The bentonite/CaCl₂ surface also sits beneath the printed lattice suggesting a uniformly embedded composite. The under-extruded filament (Figure 3.21, C and Figure 3.17) is approximately $\leq 50 \mu\text{m}$ in diameter, reaching $\geq 230 \mu\text{m}$ at printed perimeter walls (Figure 3.13). This is a sufficient printed profile to form strong inter-layer bonds and self-supporting and embeddable printed structures. Pre-run bentonite agglomerates are not present after R3 (Figure 3.21, D) that instead shows a more uniform dispersion of small particles and smoothed agglomerates comprising a swollen and cracked surface. Such macroscopic and microscopic cracks potentially act as diffusive routes to montmorillonite interlayers where cation exchange can occur, and subsurface activation of CaCl₂ can generate improved ΔT .

The bentonite/CaCl₂ composite forms a hierarchical structure as the embedded lattice features macropores and moisture is drawn through microscopic pores and interlayers. The composite adopts diamond lattice geometry despite the under extruded printed lines and demonstrates exceptional matrix potential with regards to vapour permeation via adsorption as capillary action moves condensed moisture through microscopic layers to finely dispersed salt. Observed ΔT peaks when bentonite/CaCl₂ is of lower packed configuration showing that packing amount influences maximum sorption and greater CaCl₂.6H₂O reactions as opposed to swelling, cracking, and roughening alone (Figure 3.20). These techniques both show similar work done by sorbed water, i.e., the ratio of total sorbed water to average bulk temperature above the stack of high-packed cylinders is 0.27 for R1, and 0.21 for R3 which is equal to 0.21 in the case of low packed cylinder R1. Such embedded lattices can help transition away from packed bed pellet design because bentonite is pliable when wet yet robust when dry which compliments possible matrix geometries customisable by AM [7]. The low-cost and naturally occurring bentonite clay combined with rapid size and shape iteration potentially offers locally sourced and FFF manufactured open THS reactors used for low enthalpy applications such as HVAC in buildings.

Using the same lab scale experimental apparatus, Jack Reynolds *et al* recently investigated the effect of CaCl₂ loading in expanded graphite and alginate pellet shaped matrices for THS [24]. A high salt loading caused instability during charge and discharge cycling. The salt loading within the matrix varied from 63.7 to 77.2 wt%, corresponding to energy density between 1052 and 1281 kJ/kg respectively. As with the results presented in this thesis, Renolds found an energy density limiting salt loading (60% of the salt bath during composite preparation) threshold for ideal salt distribution, salt swelling induced pore closure and consequent moisture transfer kinetics. The samples of 250 g just below the saturation threshold presented temperature uplift of 14 °C using 250 g of material subject to 25 °C and 50 %RH airflow. Renolds recommends considering composite size, which the work presented in this thesis aims to contribute to by introducing FFF and post-print impregnated bentonite/salt hydrate composites whereby the macropore size and composite shape can be tuned on-demand. In other work by G. L. Sullivan *et al*, CaCl₂ impregnated vermiculite pellets showed an initial increase in reactor uplift from cycle 1 to cycle 2 with reactor uplift increasing from 7.2 to 9.3 °C [25]. Sullivan showed the migration of dissolved salt into the valleys of the lamella that is presumed to be associated to stabilisation within the vermiculite, and may be comparable to the work presented in this thesis chapter where the

second discharge run is more effective due to a theorised bentonite interlayer cation exchange.

Lorena Skevi *et al* recently addressed more scaling relevant problems including the high cost, low sustainability, and limited heating power potential of CaCl₂ impregnated geopolymer, alkali-activated metakaolin [26]. The authors describe that to have a considerable thermochemical heat storage capacity at low temperatures (<200 °C), short exposure time salt-impregnation can improve the heat storage capacity of the geopolymers, while a prolonged exposure to the salt solution can have adverse effects. The scalability of the proposed approach in this thesis chapter introduces the concept of a reinforced geopolymers for stable THS using FFF, although it is possible to use metal 3D printed reinforcement. Further work should consider metal as the matrix material and the effects of interfacial properties on surface tension and composite longevity.

3.6. Conclusions

This chapter aims to develop a new salt embedded matrix composite structure using a lab scale open THS reactor for comparison with literature values of typical pellet THS temperature uplift. The use of 3D printed matrices of TPMS geometry combined with post-print bentonite/CaCl₂ composite embedding is a new approach to improving salt distribution for vapour accessibility. The main problem with a typical approach is that a crust forms on the pellets that lowers the recharge performance, and the technology in general is limited by the imprecise placement of salt crystals. The concept introduced here is that the smooth and zero mean curvature surfaces of the TPMS combined with 3D printing allows for control of the position of the salt hydrate and turbulence of fluid flow generated during discharge.

Bentonite clay was investigated as a host matrix to CaCl₂ salt hydrate for THS with the binding properties of bentonite utilised to embed a FFF printed lattice. Natural bentonite has sufficient mechanical, thermal, and chemical properties for this application as shown by repeated charge and discharge cycles when exposed to 50 %RH vapour. Embedded PC scaffold prints were stacked to successfully increase ΔT and temperatures peaked before or at the top surface of the stack to suggest that development of the thermal conductivity of the parts is needed for future work. Low packed, 5.8 (± 0.4) g of

composite, and recharged high packed, 7.4 (± 0.15) g of composite bulk temperatures peaked at the uppermost cylinder in a reactor of stacked bentonite/CaCl₂ embedded prints, peaking at 38.3 °C for low packed cylinders.

Preheated solid body CFD evaluated reactor design predicted highest heating affects from a diamond TPMS geometry that gave a computed maximum outlet temperature of 29.9 (± 0.3) °C and a stronger dependence on insulating the reactor vessel (ΔT of ≥ 2.5 °C) over conductive aluminium matrix selection (ΔT of ≥ 1.7 °C). Simulations used convection (as gravity was enabled) and radiation, presenting the three most efficient geometries for heat transfer were diamond, diamond with schwarz inner cylinder, and stagnated baffles as used for benchmarking. Cut plots present the capability of the diamond with inner schwarz lattice to evenly distribute temperature with a radial change of $\leq 3^\circ$ C. Pressure at the outlet is highest with schwarz and diamond TPMS solid body geometry, improving over benchmark results by 5% from 0.63-0.66 Pa. Measured experimental results in a laboratory of 21.7 (± 0.2) °C room temperature show diamond TPMS shaped cylinders generate between 2.7-10.4% more heat than schwarz shaped cylinders – of single cylinder bulk T of ≥ 25.2 °C for schwarz and ≥ 26.8 °C for diamond.

Recharged samples show water absorbed swollen surfaces and average bulk temperature increase from 25.4 (± 0.6)-27.5 (± 0.8) °C likely by activation of bentonite interlayers due to exposure of new surfaces and intercalation cation exchange in montmorillonite. Roughness also increases with exposure to moisture; root mean square height, Sq, increased from the sixth stacked and least exposed cylinder of 40 (± 10) μm to the first stacked and most exposed cylinder of 80 (± 40) μm .

It is shown that surface area of a porous hydrate storing matrix is not as influential as the permeability of the matrix that can be customised in thickness and geometry when embedding clay/salt composites on an FFF printed polymer lattice. The conceptualised strategy of bentonite embedded lattice prints of tuneable unit cell size and density gradient specific to a given reactor's inlet humidity and flow rate is a new prospect for local, low-cost, and sustainable development and deployment of efficient THS open reactors. A limitation may be encountered during scale-up where the cost of 3D printing the matrix may off-set energy saving costs. Another may be achieving a dried material between runs because if the composite structure is large or tall then the system will encounter oven size limitations. Further work on 3D printing THS matrices for post-print embedding can potentially reduce the cost of

electricity in households, or be investigated for industrial utility by using high temperature formulations for economic and environmental benefit.

3.7. References

- [1] L. Tabard *et al*, Hierarchical salt-ceramic composites for efficient thermochemical energy storage, *Appl Mater Today*. 20, (2020)
- [2] O.H. Laguna *et al*, A review on additive manufacturing and materials for catalytic applications: Milestones, key concepts, advances and perspectives, *Mater Des*. 208, (2021)
- [3] A.R. Mermut and G. Lagaly, Baseline Studies of the Clay Minerals Society Source Clays: Layer - Charge Determination and Characteristics of Those Minerals Containing 2 : 1 Layers, *Clays Clay Miner*. 49, (2001)
- [4] S.P. Casey *et al*, Salt impregnated desiccant matrices for ‘open’ thermochemical energy storage – Selection , synthesis and characterisation of candidate materials, *Energy Build*. 84, (2014)
- [5] L. Calabrese *et al*, Macro-porous permeability aspects of MgSO₄ salt hydrate foams for energy storage applications, *J Appl Polym Sci*. 139, (2022)
- [6] F. Agyenim *et al*, A review of materials, heat transfer and phase change problem formulation for latent heat thermal energy storage systems (LHTESS), *Renewable and Sustainable Energy Reviews*. 14, (2010)
- [7] A.A.A. Arani and R. Morradi, Shell and tube heat exchanger optimization using new baffle and tube configuration, *Appl Therm Eng*. 157, (2019)
- [8] B. Watel *et al*, Influence of Flow Velocity and Fin Spacing on the Forced Convective Heat Transfer from an Annular-Finned Tube, *JSME International Journal Series B*. 42, (1999)
- [9] A. Tandiroglu, Effect of flow geometry parameters on transient heat transfer for turbulent flow in a circular tube with baffle inserts, *Int J Heat Mass Transf*. 49, (2006)
- [10] M. Pelanconi *et al*, Thermal design, optimization and additive manufacturing of ceramic regular structures to maximize the radiative heat transfer, *Mater Des*. 163, (2019)
- [11] F. Agyenim *et al*, A review of materials, heat transfer and phase change problem formulation for latent heat thermal energy storage systems (LHTESS), *Ren and Sust En Revs*. 14, (2010)
- [12] A.A.A. Arani and R. Morradi, Shell and tube heat exchanger optimization using new baffle and tube configuration, *Appl Therm Eng*. 157, (2019)
- [13] B. Watel *et al*, Influence of Flow Velocity and Fin Spacing on the Forced Convective Heat Transfer from an Annular-Finned Tube, *JSME International Journal Series B*. 42, (1999)
- [14] A. Tandiroglu, Effect of flow geometry parameters on transient heat transfer for turbulent flow in a circular tube with baffle inserts, *Int J Heat Mass Transf*. 49, (2006)
- [15] M. Pelanconi *et al*, Thermal design, optimization and additive manufacturing of ceramic regular structures to maximize the radiative heat transfer, *Mater Des*. 163, (2019)
- [16] A. Charles *et al*, Down-facing surfaces in laser powder bed fusion of Ti6Al4V: Effect of dross formation on dimensional accuracy and surface texture, *Addit Manuf*. 46, (2021)
- [17] P. Wersin *et al*, Modelling bentonite-water interactions at high solid/liquid ratios: Swelling and diffuse double layer effects, *Appl Clay Sci*. 26, (2004)

- [18] K.E. N'Tsoukpoe *et al*, A review on the use of calcium chloride in applied thermal engineering, *Appl Therm Eng.* 75, (2015)
- [19] N. Shariatmadari *et al*, Effect of inorganic salt solutions on some geotechnical properties of soil-bentonite mixtures as barriers, *Int Journ of Civ Eng.* 9, (2011)
- [20] L. Lian *et al*, Use of CaCl₂ modified bentonite for removal of Congo red dye from aqueous solutions, *Desalination.* 249, (2009)
- [21] E. Ferrage *et al*, Experimental evidence for Ca-Chloride ion pairs in the interlayer of montmorillonite. An XRD profile modeling approach, *Clays Clay Miner.* 53, (2005)
- [22] A.S. Al-Homoud *et al*, Cyclic Swelling Behavior of Clays, *Journal of Geotechnical Engineering.* 121, (1995)
- [23] K. Linnow *et al*, Experimental studies of the mechanism and kinetics of hydration reactions, *Energy Procedia.* 48, (2014)
- [24] J. Reynolds *et al*, Optimisation of CaCl₂ impregnated expanded graphite and alginate matrices – Targeted salt loading, *Energy Con Man* 302, (2024)
- [25] G. Sullivan *et al*, Cycling Stability of Calcium-Impregnated Vermiculite in Open Reactor Used as a Thermochemical Storage Material, *Energies.* 16, (2023)
- [26] L. Skevi *et al*, The Effect of Salt-Impregnation on Thermochemical Properties of a Metakaolin Geopolymer Composite for Thermal Energy Storage BT - Int RILEM Con on Syner Exp Tow Sust and Rob of Cement-based Mat and con struc, pp. 1232–1242, (2023)

**Chapter 4. Direct Writing
of a Toughened
Zeolite/Binder Composite
for Gas Separation**

4.1. Chapter Summary

Here, zeolite 13X composites are developed for improved scale-up and commercial deployment potential by increasing compression strength (which reduces attrition and increases adsorbent structure longevity) and improving the printing performance of the pastes. The pastes are assessed for AM extrusion parameters including viscosity (η). This chapter is concerned with low-cost binder and CSR additions noting the effects of CSR addition on gas separation potential and extrusion pressure. A baseline paste composition of 90 wt% zeolite 13X is identified from the literature and benchmarked against 2, 4, 6, and 8 wt% CSR composites to improve the formulation for printed structure manufacture and reliability. Log-pile shaped gas separation scaffolds are DW printed to be used in enclosed spaces such as for pressure swing adsorbent systems. XRD analysis indicates the presence of the FAU structures that capture CO₂ and the FAU content is observed having calcinated the structure under moulded, extruded, annealed and non-annealed conditions. BET analysis using N₂ as the adsorbate shows a 447 m²/g surface area for the 4 wt% CSR composite which is strongest of the assessed material in compression. By identifying optimum printing parameters and toughening the printable zeolite composite it may be possible to enhance the size and complexity of scaffold production for large and complex geometries that better manage gas flow, pressure gradients, thermal gradients, and hence improve system efficiency (i.e. reduce electricity costs).

4.2. Introduction

Zeolites are microporous aluminosilicates that find application in industries ranging from medicine (e.g. bone regeneration) to energy production (e.g. catalyst for biomass conversion) [1]. The utility of zeolites owes to gas separation achieved via physisorption or chemisorption of molecules to microporous surfaces. Synthetic zeolites can be made from a range of raw materials such as natural clay (bentonite), fly ash, or halloysite [2]. Their types include A, X, Y and ZSM, and offer hundreds of possible pore geometries depending on the synthesis methods. Pore synthesis for gas separation can be by hydrothermal, sol-gel, inert templates, alkali fusion, alkali leaching, microwave-assisted, ultrasound-assisted, and iono-thermal means [3]. The BET and Langmuir models calculate surface area from an adsorbed multilayer

or monolayer respectively, and observed isotherms are classified as Type I to Type VI with hysteresis loops classified as H1 to H4 (Figure 4.1).

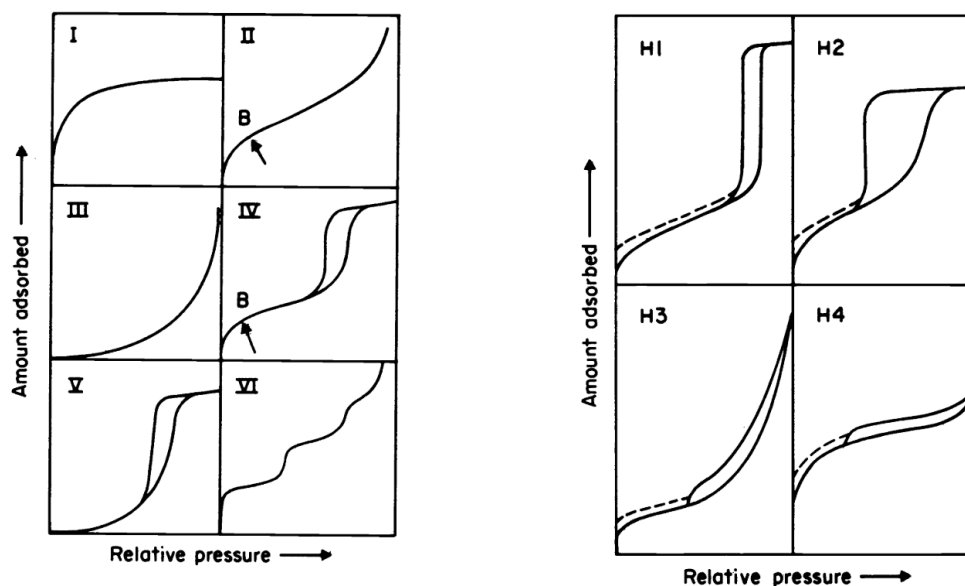


Figure 4.1. Types of adsorbent isotherm (left) and isotherm hysteresis loops (right). The arrow marked 'B' indicates typical onset of multilayer formation [4].

The compression strength of a microporous zeolite is of interest as to avoid structural damage to the zeolitic crystallographic pore structure and manufactured adsorbent layer or monolith under applied pressure. Mechanical properties such as elasticity and rigidity influence the structures stability, separation efficiency and long-term performance. Measures taken to avoid attrition of a structures surface include synthesis conditions, particle size control, and binder selection that when applied as a thin continuous layer can prevent particles contacting and damaging each other [5,6]. Research has shown viable methods to improve the mechanical properties (and attrition, Table 4.1) of zeolite monoliths include steel beams coated with zeolite 13X, organic/inorganic coated binders, halloysite nanotubes reinforcement, and soldering of printed structures [7].

Table 4.1. Crushing strength and attrition loss of Na-X zeolites [5].

Samples	NZL-400	NZL-500	NZH-400	NZH-500	MZ
Crushing strength	3.46	7.12	4.11	8.94	8.54
Attrition loss (%)	24.28	11.24	20.87	9.12	9.61

Zeolite 13X is relatively strong in compression (54.3 MPa) owing to a faujasite (FAU) pore framework (Figure 4.2) that affords a surface area of <876 m²/g and gas regeneration [8]. Zeolite 13X synthesis method generally uses sodium aluminosilicate gels and a hydrothermal reaction. Micropore volumes can achieve <6.9 mmol/g of CO₂ adsorption [2,9,10].

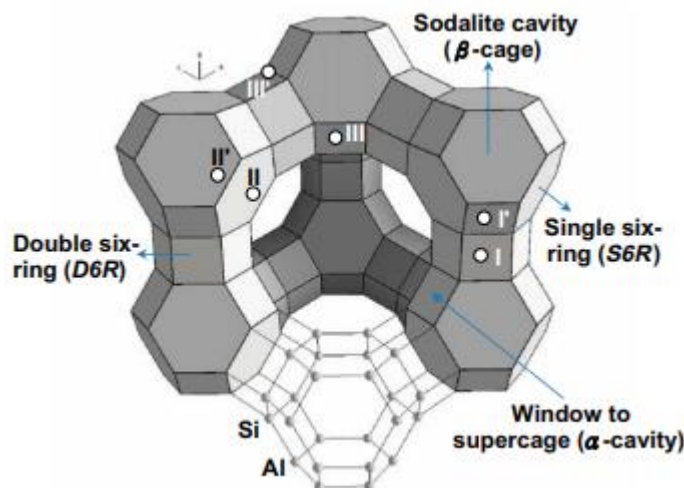


Figure 4.2. A model of the faujasite (Z- or Y-zeolite) unit cell. Si and Al atoms alternate at the tetrahedral intersections as indicated at the eight sodalite cavity depicted as a frame for clarity. Cation exchange sites are marked I, II or III depending on position at either a six ring, β cage, or α cavity location [11].

The formation of microporous frameworks such as FAU can be identified using x-ray diffraction (XRD) with parallel atomic arrangements forming diffraction patterns that correspond to crystallographic planes (denoted using miller indices, hkl) composing unit cells. The spacing between parallel planes is referred to as d-spacing and can be altered by sample preparation techniques that influence gas separation potential. Crystal planes are quantifiable using Bragg's Law which states the angle of incidence is equal to the angle of diffraction [12]:

$$n\lambda = 2d\sin\theta \quad (1)$$

Gas separation techniques include cyclic adsorption processes such as pressure or temperature swing adsorption. Zeolite 13X is the most widely studied adsorption material for commercial pressure swing operated hydrogen production via H₂/CO₂ separation [2]. Mass transfer, pressure drop, and thermal management are factors that dictate power consumption and electricity required for such gas separation. Here is where geometry of the selective media, which is typically a powder or bead that forms a 'pancake' shaped chamber bed, can play a significant role in improving process

efficiencies [13]. A drawback of using ‘pancake’ molecular sieve systems is the potential uneven distribution of gas flow and underutilisation of porous media (as was the case with packed bed reactors in Chapter 3) accompanied by a risk of fluidisation that can offset the benefits of small particle size associated with low mass transfer resistance and energy consumption.

A typical manufacturing method to create pellets for adsorption of GHG from flume gas is the compaction of zeolite with sacrificial binder by heat assisted compression. To print a zeolitic powder into a more favourable geometric structures for pressure and temperature swing the properties of the composite must not only facilitate self-standing structures but also its extrusion and subsequent 3D layering through a direct writing (DW) dispenser nozzle. Research has focussed predominantly on developing printed zeolite structures of high surface area and tunable pore structure for favourable molecular sieving [14]. Less research has focussed on the creation of robust prints that are resistant to shock, attrition, and efficiency depletion expected from handling and continuous use of such brittle materials.

4.3. Experimental

In this section, the methods for the chapter are introduced and reasoning behind the choice of analysis is given. A summary of the workflow is given (Figure 4.3). Zeolite composite pastes were printed as a preliminary measure to confirm the baseline paste and CSR containing paste compositions as printable before optimising the polymer content for high mechanical strength and printability. The optimum CSR addition for increased compression strength was identified by compression testing dried 2, 4, 6, and 8 wt% CSR compression samples. These were compared to the equivalent addition of MC/PVA binder for crystallinity, surface area, and compression strength. SEM images were captured to observe changes to surface texture and possible CSR agglomeration. Surface areas and pore characteristics were measured using BET analysis.

The CSR toughening additive was selected as commercially available Geniopearl® P52 and compounded in the zeolite/binder mix at to improve compression strength and investigate any trade-off between strength and surface area of sintered and non-sintered parts. Extruded and cast parts were sintered at 720 °C. Crystallinity and crystallographic planes were measured using XRD analysis. Both extruded and moulded samples of roughly cylinder

and prism geometry respectively were prepared under two sintering conditions where one was subject to annealing to identify changes to the crystalline FAU structure due to the printing process.

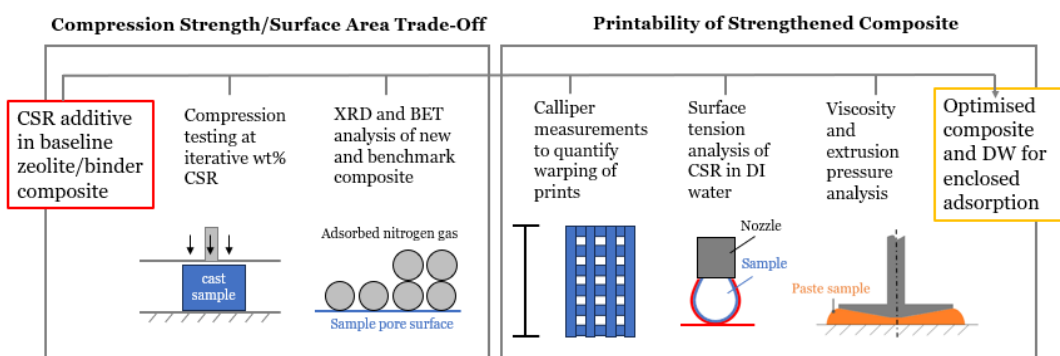


Figure 4.3. Summary of Chapter 4 experimental workflow that is split into two main investigations: compression strength/surface area trade-off, and printability of strengthened composite.

Calliper measurements were made to quantify added CSR content effect on DW print resolution. Changes to surface tension caused by CSR addition was approximated using pendant droplet testing. Samples placed in a 5 ml syringe fitted with a 1.6, 1.8, or 2.0 mm diameter nozzle were characterised for extrusion pressure using a tensile machine. Viscosity was measured using a cone and plate viscometer, and rheological parameters. Direct writing was carried out using the 5 ml syringe set-up to show a change of printed resolution owing to CSR content.

4.3.1. Preparation of Microporous Zeolite Composites for Gas Separation

Self-standing composite prints were made from zeolite 13X for the removal of CO₂ from enclosed environments. Bentonite was selected as an additive for composite paste cohesion and rigidity of dried parts, the bentonite used with zeolite is the same as was used for the THS application detailed in Section 2.2.1 Methylcellulose was selected to tune rheological properties for extrusion, and PVA as a co-binding polymer linker for reduced surface cracking. The zeolite 13X (molecular sieves) of 2 μm average particle size were supplied by Sigma-Aldrich®. The zeolite has a linear formula of Na₈₆[(AlO₂)₈₆(SiO₂)₁₀₆] · xH₂O. Methylcellulose of viscosity: 300-560 cP as 2% in water, and gel point 50-55 °C was supplied in powder form Sigma-Aldrich®. The PVA of viscosity 4 ± 0.5

mPas as 4% in water was manufactured by CTS Europe Ltd and supplied by Aurelio in powdered form.

Genioperl® P52 is a commercially available crosslinked core shell rubber (CSR) that was selected as a composite toughening agent. It was used as supplied by Wacker Chemie AG® in powder form. It is typically compounded for polymer toughening and consists of an organic acrylic (methacrylate) shell enveloping a silicone (siloxane) core [15]. The CSR has a median particle size of 29 µm which is approximately 30 times the diameter of the zeolite. The core has the lowest composite constituent melting temperature of 120 °C and an overall ignition temperature of 420 °C which is high enough to remain solid during wetting and heating of the zeolite due to heat of hydration, and low enough to be a sacrificial polymer during sintering of the zeolite. Wacker recommends processing temperatures between 50-120 °C for optimum particle dispersion, this was achieved via the zeolite 13X heats of hydration being around 80 °C [15,16].

A baseline gas separation composition was selected for benchmarking CSR composites. The baseline composite contained 90 wt% zeolite 13X as described by Harshul Thakkar *et al*, i.e., the best performing sorption and compression sample was highest in zeolite content [17]. In this thesis, the composites contain CSR to improve compression strength, with effects on DW performance and surface area also assessed.

All materials for gas separation were weighed using analytical scales, with the established composite of 90 wt% zeolite, 7 wt% bentonite clay, 2 wt% methylcellulose, and 1 wt% PVA made in batches of 20 g contained in a 250 ml reagent bottle [17]. The CSR was then added in increments of 2 wt%: 0, 2, 4, 6, 8, and 10 wt% addition CSR. Randomised mixing of the composite component powders utilised a 5 L Merris Minimix gyroscopic paint mixer for 30 seconds. A water content of 1:1 solid to liquid ratio was added (20 g of water) to form a viscous paste texture, and immediately further mixed with a glass stirrer to insure deagglomeration of the CSR at the raised temperature governed by the heat of zeolite sorption. The composite paste was then dispensed and pressed into compression specimen shaped silicone moulds and dried in an oven held at 60 °C overnight to evaporate water. The relatively low water content facilitated a highly viscous zeolite paste of high density when dried for maximum strength representation and minimum shrinkage and cracking caused by drying. Each hardened sample was then compression tested or ground into a powder using a mortar and pestle at room temperature for BET analysis.

A baseline sintered sample of the zeolite/polymer composite with no CSR content was made for BET, and sintered 0, 2, 4, 6 wt% CRS samples were prepared for mechanical testing to observe any effect of carbonated polymer on compression strength. Polymer addition pastes for XRD and BET analysis were passed through an extruder with a 1.6 mm diameter nozzle before being sintered. Sintering was achieved using a Nabertherm 3000 oven set to ramp to 720 °C in 1 hour before isothermal heating for 2 hours and 30 minutes with the oven programmed to cool to 100 °C in 1 hour. The sintering process was carried out for three samples of each composite, varying in their CSR content ready for BET analysis or compression testing. Powdered samples for XRD and BET analysis were ground for 2 minutes using a mortar and pestle.

4.3.2. Compression Testing

Dried and sintered zeolitic paste samples were measured for quasi-static compression strength. Right prism samples were cast and dried at room temperature. Test speed was set to 30 mm/minute in Horizon software with samples placed between flat parallel plates and compressed using a H5KT Tinius Olsen machine. Zero strain was interpreted as the interception between the elastic linear region and the x axis. Time dependant responses to compression of the CSR were observed by measuring compressive forces at two strain rates. Compression strength, i.e., peak force, was investigated by applying a crosshead speed of 1 mm/min, which is a typical quasi-static strain rate equivalent to 1.67 s^{-3} . A second moderate strain rate of 5 s^{-2} was used, which is equivalent to 30 mm/min crosshead speed.

4.3.3. Direct Writing Extrusion Pressure

An Artillery Sidewinder X1 FFF printer was selected to be modified for DW for its large building volume of 300 mm Z height. An open-source paste extruder by Ofer Levinger was downloaded from Instructible[©] [18], printed in PLA and assembled using plywood to fix to the printer head, and zip ties instead of screws for faster disassembling between runs and less wear to the plywood (Figure 4.4).

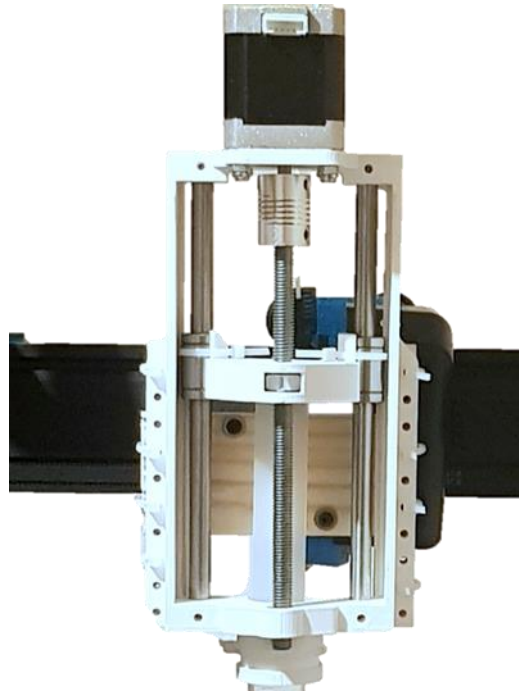


Figure 4.4. Printed custom syringe extruder head.

Printing of the zeolite pastes required a well-balanced water content once mixed to be processable by extrusion, so water additions were measured at time intervals allowing for evaporation to reduce wt% water content. Printing parameters for the zeolite pastes using a 2 mm nozzle were: 1.0 mm initial layer height, 1.8 mm layer height, 1.0 mm line width, 40% layer flow, 60 mm/s print speed, and 6.5 mm retraction distance.

Forces required to extrude pastes at two water additions were measured to represent extrusion of a soft-plastic paste and stiff-plastic paste. The syringe used was a 5 ml terumo eccentric luer lock syringe with a 12.7 mm plunger diameter filled with zeolitic paste composites using a spatula. The syringe was placed vertically on a cylindrical steel support (Figure 4.6) that was cut using a lathe and featured a through-hole designed so that the nozzle was free to extrude paste through the support.

The process for direct writing (Figure 4.5) was: 1. program the custom material Cura profile with a z-offset (300 mm), 2. set print parameters, 3. import log-pile STL file, 4. fit custom print head to the printer and fill the syringe with paste 5. print the part and let dry before removing.

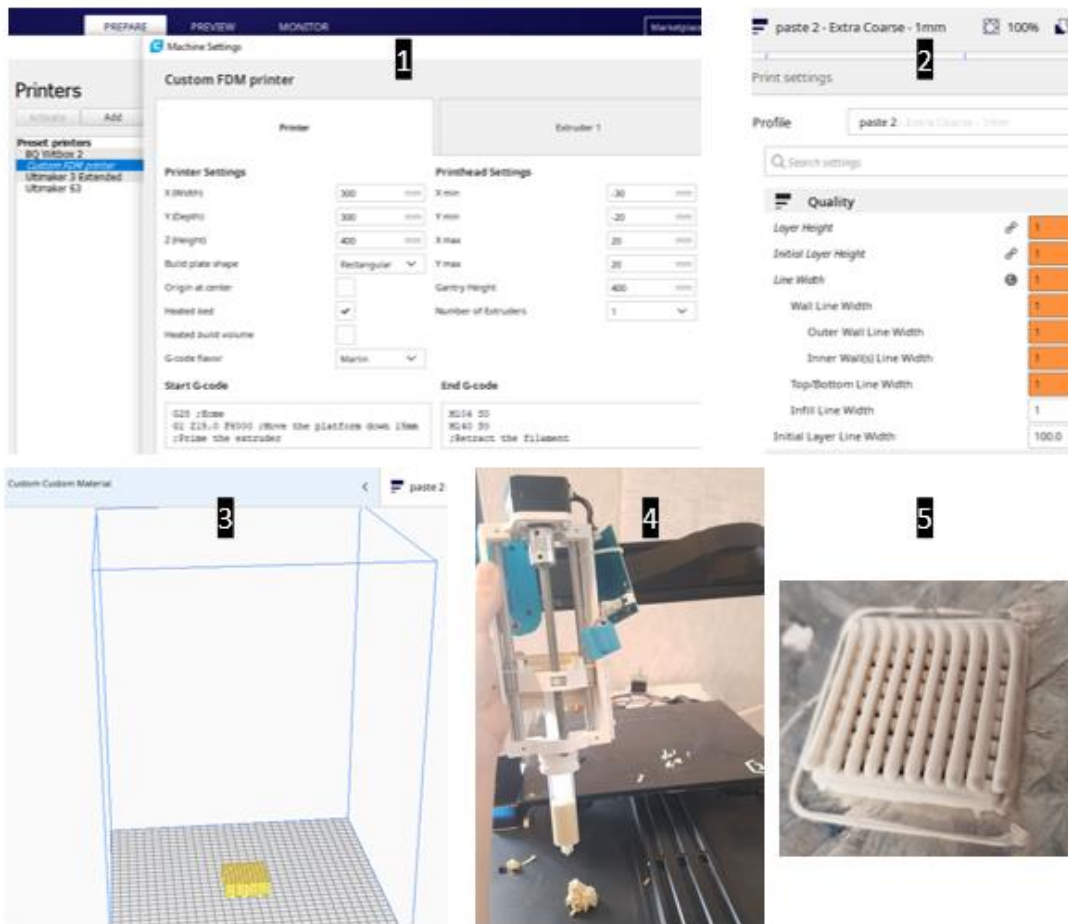


Figure 4.5. The direct writing process for printing zeolite/binder/CSR pastes.

The assembled syringe was placed in a H5KT Tinius Olsen tensile machine and the crosshead was displaced at 6 mm/s to push the plunger. Results were recorded as kg and plotted as pressure in MPa.



Figure 4.6. Syringe position between tensile tester and support to measure resistant forces governed by paste contents.

From this set-up many flow parameters can be determined, such as shear rate (γ), extrusion pressure (ΔP), and layer geometry creation (h_{puddle}). Equations (2.5) to (2.9) are used as reported by C. Duty *et.al* [19]:

$$\gamma = \frac{4Q}{\pi R^3} \left(\frac{3n+1}{4} \right) \quad (2.5)$$

Shear rate (γ) depends on Q which is the volume flow rate, through a nozzle of radius R, and n is the power law index.

$$\Delta P = \frac{8 \eta Q L}{\pi R^4} \quad (2.6)$$

The pressure (ΔP) required to extrude a shear thinning fluid through a nozzle of length L is calculated using viscosity (η).

$$h_{puddle} = 2 \sqrt{\frac{\gamma_{SE}}{g \cdot \rho}} \quad (2.7)$$

A geometry creation parameter (h_{puddle}) is used to describe the height of a stable layer, where γ_{SE} is the surface energy and ρ is the density of the candidate material respectively, and g is the gravity constant.

$$\sigma_{HP} = \rho * g * h \quad (2.8)$$

$$\sigma_{wall} = n_{layers} * \rho * g * h \quad (2.9)$$

Hydrostatic pressure (σ_{HP}) is used to indicate internal pressure of a layer, and the pressure exerted by an adjacent deposited layer that quantifies the paste for consecutive solid layering is estimated as σ_{wall} .

4.3.4. Calliper Measurements

A simple assessment of printed geometric distortion was carried out using a Kynup IP54 digital calliper tool accurate to 0.01 mm. Sample thickness (t), width (w) and height (h) of the zeolitic wood-pile structures were measured. Three measurements were taken for each value of t,w, and h to provide averages with SD error as shown in Figure 4.7. Owing to an uneven perimeter, the first and third measurements were not taken from the sample edge taken but instead taken from in-line with the first fully deposited printed layers.

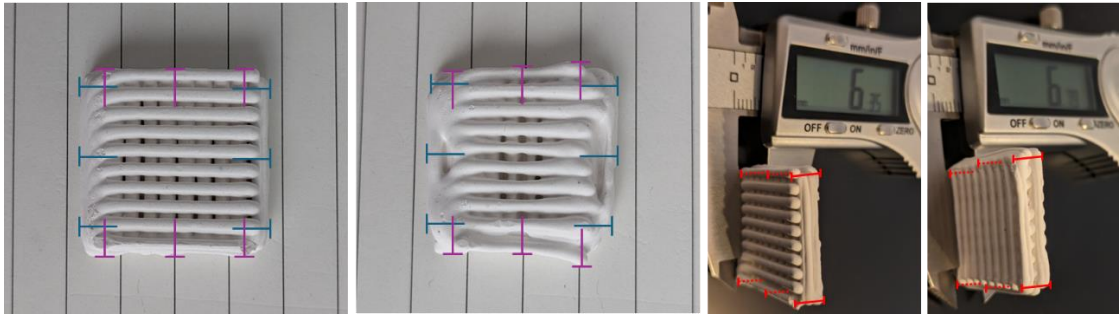


Figure 4.7. Measurement of zeolitic wood-pile DW printed samples for geometric distortion using calipers. Height (h) is represented by the pink lines, width (w) by the blue lines, and thickness (t) by the red lines where thickness was measured parallel (t_a) and perpendicular (t_e) to the printed top-lines.

4.3.5. X-Ray Diffraction Analysis

Crystallographic structural properties of zeolite composites was studied using a Bruker D8 Discover XRD machine measured 2θ ranging from 5 to 50° using a copper twist tube (40 kV, 40 mA) with a step size of 0.02° at $2^\circ/\text{min}$. XRD measurements were carried out in collaboration with Rodrigo Garcia Rodriguez at Swansea University. Origin software was used to analyse XRD curves for crystal size and for the presence of porous frameworks. Crystallinity was calculated in Origin by measuring the area of the peaks and dividing peak area by total area under the diffraction spectra.

4.3.6. Brunauer-Emmett-Teller Nitrogen Gas Adsorption

Samples of an established polymer co-binder detailed in previous research was used here for benchmark composites containing 2% methylcellulose and 1% PVA as prepared for N_2 gas adsorption [17]. Surface area and uptake rates were compared to those from CSR containing samples to indicate potential use in CO_2 capture and other separation technologies. BET measurements were carried out in collaboration with Jenny Baker at Swansea University. Powdered samples were degassed at 350°C overnight, and N_2 adsorption and desorption runs were conducted at partial pressures from 0.01 to 0.95 using a Micromeritics 3020 surface area analyser. Adsorption isotherms were measured at -196°C .

4.3.7. Surface Tension Measurements

Pendant surface tension was used to describe the attraction between CSR particle filled water droplets and help understand surface tension effect on composite paste deformation during layering. Samples weighed 5 g and were made by mixing DI water with CSR using analytical scales. Samples of 0.5, 1, 1.5, and 2 wt% CSR were prepared in a glass beaker by stirring with a glass rod and left to soak overnight. Each sample was drawn into a 5 ml syringe with 1 mm luer lock nozzle. An Ossila contact angle goniometer recorded droplet formation over 5 mins and 25 seconds at a frame rate of 2 fps. Each recording started before the syringe was pressed to form a large droplet. Greyscale videos were analysed with a droplet density of 1 g/ml and calibration diameter was set according to the nozzle diameter as a reference. Values of surface tension were calculated every 30 seconds once the droplet had formed and stopped visibly moving.

Two 5 ml samples of fluidic zeolite/bentonite/polymer samples were deposited onto glass substrates to compare the effect of CSR content on sample cracking. One sample was of zero CSR (baseline) and one of added 4 wt% CSR content prepared by pouring each paste from a glass beaker and placing the paste films in an oven held at 80 °C for 2 hours before cooling at room temperature. The print bed of a typical FFF printer is made from glass, which provides a flat and polarised surface for materials such as zeolite to closely adhere to. Images were captured with a scale bar added to observe crack formations resulting from surface energy interaction between composite and glass substrate.

4.3.8. Viscometry of Zeolite Composite Pastes

Paste viscosities were measured to identify shear thinning behaviour at room temperature using a Brookfield RST C25-1 cone and plate rheometer with Rheo 3000 software. A benchmark (baseline, zero CSR) paste was measured for viscosity at various water contents by combining as-received powders with 54, 52.5, and 51 wt% DI water. This was carried out with 6.5 g sample that contained 55 wt% water and was measured for viscosity every 15 minutes as the paste thickened due to water evaporation the sample was weighed using analytical scales. The shear rate ramped from 0.5 to 30 /s that corresponds to a rotation of 0.1 to 5 rpm of the cone of 25 mm diameter. A gap between cone and plate was 0.3 mm to allow for even shear and horizontal flow of pastes

without disruption from slip and particle migration. This was repeated for samples containing 1, 2, 4, 6 and 8 wt% CSR to observe any effects that CSR has on paste yield stress, viscosity, and shear thinning behaviour.

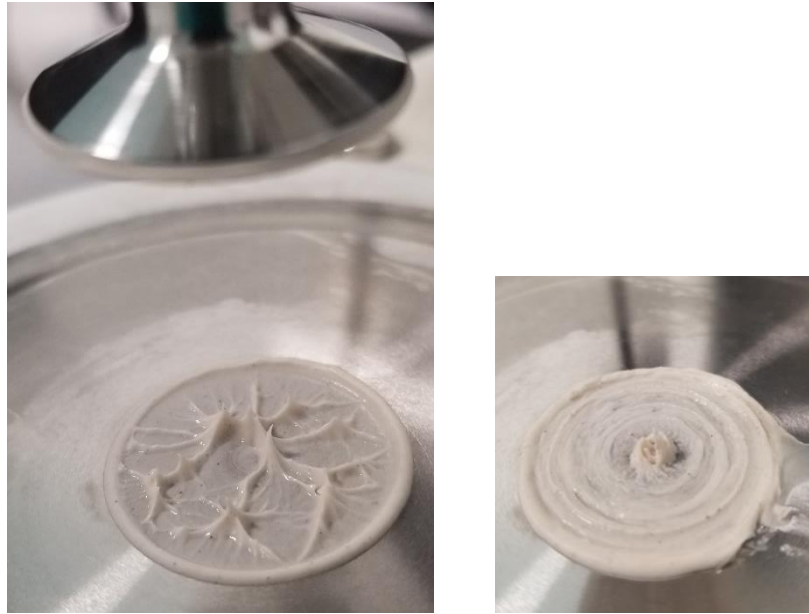


Figure 4.8. Viscosity set-up for zeolite 13X pastes with no ring formation present (left) suggesting measured viscosity without particle migration that occurs with ineffective gap height and water content (right) showing a ring formation.

4.3.9. Zeolitic Composite Surface Imaging

Zeolite and polymer additive morphologies were imaged using scanning electron microscopy (SEM) and electron dispersive spectroscopy (EDS). A Hitachi TM3000 bench top instrument was used to observe morphologies and confirm chemical composition. The SEM was set to receive and compose images using backscatter electrons at an applied voltage of 15 kV, and images were captured at 100, 600, and 1,200 × magnification.

4.4. Results

4.4.1. Energy Dispersive Spectroscopy of Zeolite 13X Baseline Composite and Bentonite Binder

The alumina-silicate elemental composition of the sintered baseline composite is mainly oxygen, sodium, aluminium, and silicon (Figure 4.9, left). The amounts of silicon and aluminium are similar by number of atoms shown by their EDS peak heights. Sodium is present in zeolite 13X during synthesis because sodium cations are utilised to balance negative charges and alkalinity which in-turn affects crystallinity of the formed zeolite. Ideally zeolite is fully crystalline so that the maximum number of Si-O-Al composed FAU frameworks form when fully synthesised. Furthermore, sodium cations dictate the formation of the final electrostatic field capable of strongly interacting with the large quadrupole moments of CO₂ molecules accommodating CO₂ capture [20].

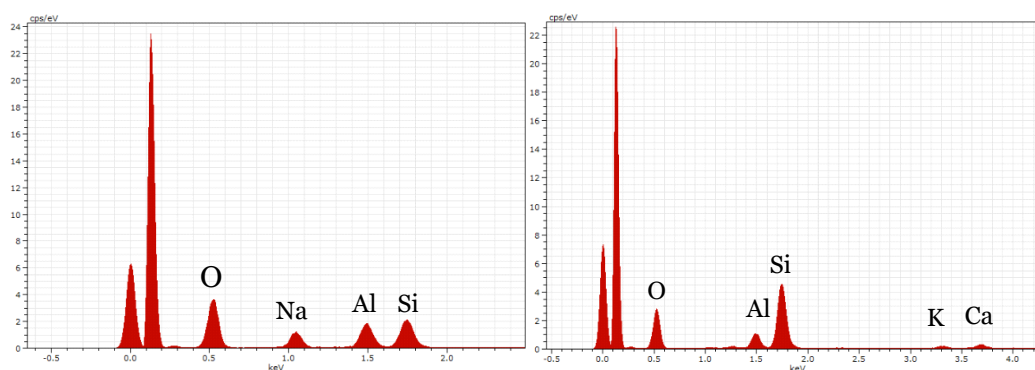


Figure 4.9. EDS spectra of sintered baseline sample (left) and non-sintered bentonite powder (right). Unlabelled peaks are noise (i.e., C K α).

Natural bentonite has a similar elemental composition to the zeolite baseline composite (Figure 4.9); however, silicon is the most dominant element composing bentonite and is approximately 4 \times the mass of aluminium. This co-existence of Al and Si provides zeolites with catalytic versatility. The EDS spectra indicate appropriate elemental compositions (approximately 12% Al and 17% Si [21]) for gas separation as used for applications such as medical oxygen, air conditioning, and CO₂ capture. Molecular selectivity can be identified using XRD and BET, however, this depends on crystallinity and spatial arrangements that are likely affected by sintering and CSR addition. Therefore, the composite was toughened with CSR and iterated to find the

ideal CSR addition to represent a final product before conducting XRD and BET analysis.

4.4.2. Mechanical Properties of Zeolite 13X Printable Composites

Zeolite 13X/binder composites of zero (baseline) to 8 wt% CSR addition in 2 wt% increments were compression tested (Table 4.2), with all CSR samples showing an increase in ultimate compression strength (UCS) compared to baseline value of 3.8 (± 0.4) MPa. UCS peaked at 7.8 (± 0.8) MPa in the case of a 4 wt% CSR composite. A decrease in UCS with increased crosshead speed from 1.67 s^{-3} to 5 s^{-2} was measured for all composites, again peaking for a 4 wt% CSR addition at 4.6 (± 1.0) MPa. A narrowing of UCS and modulus between strain rates occurs at ≥ 4 wt% CSR as the increased rubber content provides the composite with greater ductility and predictability of failure.

Polymer loadings provide brittle zeolite particles with opportunity to reconfigure and accommodate stress via molecular reorientation. A continuous interparticle layer of binder likely decreases zeolite compaction resulting in lowered localised force concentration and increased printed structure elasticity during use under pressure. This promotes absorbent longevity and efficiency which in-turn attributes active sustainability to the assembled separation system.

A significant 95 MPa increase in compression modulus occurs between the baseline and 4 wt% CSR sample tested at 5 s^{-2} , showing improved stiffness. Modulus values cannot be directly compared across strain rates because values for 1.67 s^{-3} were calculated using UTS specimens. However, modulus is highest for added 4 wt% CSR, peaking at 654 (± 54) MPa with a sudden drop of 206 MPa modulus at 6 wt% addition (Table 4.2). The 2 wt% composite shows the second highest values in all cases hence optimal CSR addition could lie between 2-4 wt% addition. The increased UCS of the 4 wt% CSR composite means increased resistance to subsequent layering, fixings such as bolts that impose compression stress, and end-part environmental forces leading to attrition when transported, installed, and used for pressure swing cyclability. Strengthening is a step towards improved printed complexity and accuracy of CAD lattice replication, granting adsorbent systems of tunable channel

architecture for mass transfer at reduced pressure drop compared to standard pellet or ‘pancake’ beds.

Table 4.2. Measured UCS and compression modulus of as-cast and sintered zeolite 13X composites at 1.67 s^{-3} and 5 s^{-2} strain rates. ‘*’ Indicates modulus values calculated using USC samples.

CSR addition	UCS 1.67 s^{-3} (SD), MPa	Modulus, 1.67 s^{-3} (SD)*	UCS, 5 s^{-2} (SD), MPa	Modulus, 5 s^{-2} (SD), MPa	CSs 5 s^{-2} (SD), MPa
Zero	4.9 (1.2)	163 (26)	3.8 (0.4)	559 (16)	1.3 (0.4)
+2 wt%	6.4 (0.9)	217 (23)	5.0 (0.8)	569 (85)	0.9 (0.1)
+4 wt%	7.8 (0.8)	223 (17)	6.4 (1.0)	654 (54)	1.1 (0.4)
+6 wt%	5.8 (0.4)	176 (7)	5.0 (0.6)	448 (35)	0.9 (0.2)
+8 wt%	5.0 (0.6)	148 (10)	4.4 (0.3)	296 (30)	-

A force damping effect provided by a CSR loading works to reduced break-up and attrition caused by pressure cycling. Once fractured, all samples stabilise at about 3 MPa due to crumbling of the composite from the top surface. The compression strength when crumbling is speculative due to an unknown surface area under compression but are nevertheless ordered according to their compressive modulus: 2 wt% CSR being the strongest, then 4 wt%, then the baseline, and then 6 wt% CSR (Figure 4.10). This may show a dependence of attrition on elastic modulus which is optimised by a 2 wt% CSR addition.

The baseline is a brittle composite compared to CSR composites and fails suddenly past its yield point potentially due to stress accumulation at locations such as voids which develop cracks along preferential planes (e.g., Figure 4.10, image). A fracture surface that features cleaved surfaces at roughly 45° indicates a well packed sample. Intracrystalline frictional forces build according to stress fields that form through a matrix which is greatest at the midline of the sample, where compaction is greatest due to physical constraint of surrounding material, and typically yields suddenly when crushed. Research into monolith zeolite failure modes has shown fracture is influenced by sample aspect ratio (sample height/width), with ratios higher than 3 yielding from the top surface [22]. Here, the investigated fracture surfaces of modulus samples originate from the top surface. Improved understandings of fracture location and plasticity can potentially reduce structural damage to zeolite printed parts

that incur particle loss (attrition) during manufacture, transportation, and in-situ gas separation.

Modulus values measured at 1.67 s^{-3} strain rate are low (Table 4.2) despite a higher measured UCS and lower yield point (Figure 4.11) because they were calculated using UCS samples, which highlights that greater aspect ratios accommodates greater force bearing.

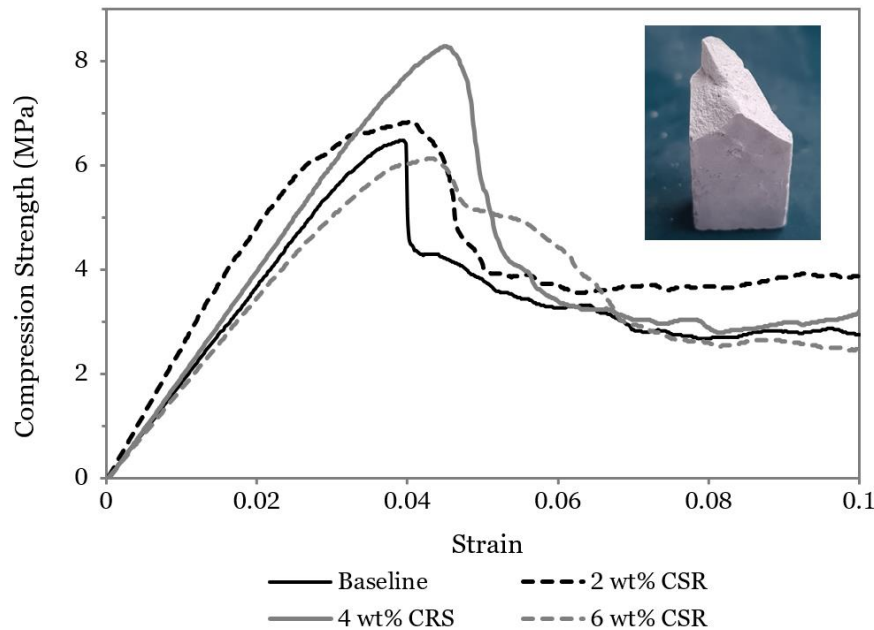


Figure 4.10. Compression curves of measured baseline (zero CSR), 2, 4, 6 wt% CSR composites at 5 s^{-2} and fracture surface of modulus specimen (image).

A 4 wt% CSR addition increases baseline compression strength more so than a 4 wt% MC/PVA addition (Figure 4.11). The 4 wt% CSR composite shows a 2.1 and 1.1 MPa increase in UCS over the 4 wt% MC/PVA composite at strain rates of 1.67 s^{-3} and 5 s^{-2} , respectively. The 4 wt% MC/PVA composite provides structural support to the baseline sample that increases baseline UCS from 4.9 (± 1.2)-5.6 (± 0.5) MPa at 1.67 s^{-3} , and from 3.8 (± 0.4) to 5.2 (± 0.4) MPa at 5 s^{-2} respectively. By observing the change of UCS measured at both strain rates it can be noted that compression properties are work softening. Time dependency of the viscoelastic contents means that more stress dispersion occurs at 5 s^{-2} strain rate at the cost of UCS.

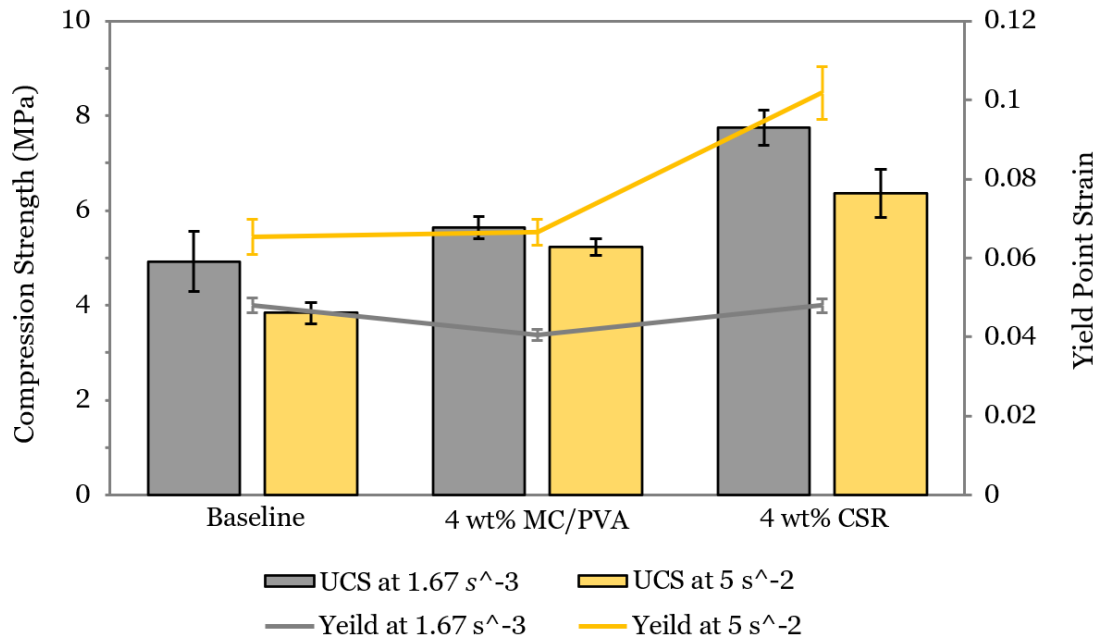


Figure 4.11. UCS and yield point of baseline (zero CSR), added 4 wt% MC/PVA, and 4 wt% CSR tested at 1.67 s⁻³ and 5 s⁻² where error bars are one SD.

A brittle baseline composite undergoes the most rapid drop-off in stress when fractured due to a highly elastic 90 wt% zeolite content, yielding a UCS SD error of ± 1.2 MPa at 1.67 s⁻³ as averaged across five samples. Added 4 wt% MC/PVA provides a more predictable failure, with lower SD error than those of a baseline and added 4 wt% CSR composition. Composite plasticity is increased by the extra binder that reduces UCS SD error likely due to greater stress dispersion during compression. UCS SD of 4 wt% MC/PVA remains at a baseline value of ± 0.4 MPa despite failing at higher applied force. In comparison, a 4 wt% CSR zeolite matrix may be less uniformly contained, and agglomeration of CSR might further randomise packing density which would explain an increase of SD error at higher strain rate.

Composites containing 4 wt% CSR withstand the highest deformation leading to failure at 0.1 (± 0.01) strain at a 5 s⁻² strain rate, while the 4 wt% MC/PVA and baseline composites fail at 0.07 (± 0.003), and 0.07 (± 0.005) strain, respectively. Ductility and strength are therefore best enhanced by the addition of 4 wt% CSR, with the imparted viscoelasticity less evident at a 1.67 s⁻³ strain rate, with a 4 wt% CSR yield point measuring 0.05. This is due to time dependant rubber particle compression that facilitates further associated alignment of polymer chains to the direction of stress at a 5 s⁻² strain rate. It is possible that a 1.67 s⁻³ strain rate deforms only the hard acrylic shell component of the CRS particles that is closer in hardness to the surrounding

zeolite matrix than the other polymers used. Perhaps increased frictional forces and particle confinement at a 5 s^{-2} strain rate is sufficient to cause the siloxane content to deform, providing a step-up in yield point by molecular reorientation in addition to deformation of the hard acrylate shell that increases UCS. In which case the CSR core acts to further reduce the rate of force transferred from the crosshead to localised zeolite lamella.

4.4.3. X-Ray Diffraction Analysis

The 4 wt% CSR and 4 wt% MC/PVA samples were benchmarked against the baseline for crystallinity content and corresponding FAU structures using XRD. Typical zeolite 13X crystallographic peaks are present for all CSR loaded composites, and peaks are higher and hence crystallinity is greater for all non-sintered samples (Figure 4.12). This can be attributed to partial degradation and collapse of FAU structures during sintering at 720 °C as reported to occur past 700 °C when isothermally heating for 2hrs [23]. This thermal degradation depends on holding time which is in turn affected by thermal mass and heat transfer rates. Powdered zeolite 13X has been reported to be thermally stable up to 800 °C at which point the zeolite becomes amorphous [24,25]. All XRD samples examined show FAU framework structure present, hence, samples crystallised with cubic symmetry as attributed by the (111), (220), and (311) crystallographic planes (Figure 4.12) and as research has shown [26,27].

Table 4.3. Diffraction angles (θ) associated to the 111, 220, and 311 planes composing the FAU framework, and d-spacing (d) of measured crystals that satisfy Braggs law calculated using peak centres, and relative intensities (I_{rel}) calculated using peak area.

Sample	$\theta = 3.05$		$\theta = 4.98$		$\theta = 5.86$	
	I_{rel}	d (Å)	I_{rel}	d (Å)	I_{rel}	d (Å)
Reference [28]	100	14.48	12.7	8.86	11.1	7.56
Baseline	100	14.53	25.1	8.87	19.1	7.56
Baseline, S	100	14.48	26.3	8.83	19.8	7.54
Baseline, ES	100	14.62	27.9	8.89	21.4	7.59
4 wt% binder, S	100	14.48	24.8	8.83	17.3	7.54
4 wt% CSR, S	100	14.48	27.2	8.85	21.6	7.54

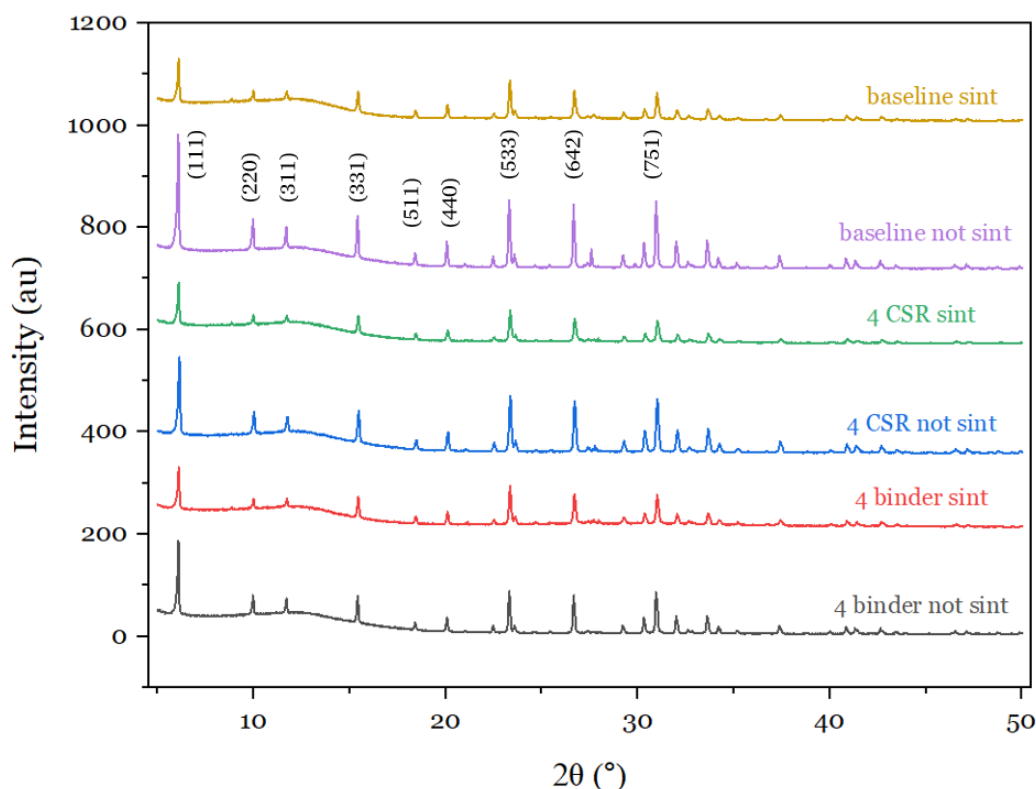


Figure 4.12. XRD spectrums with hkl crystallographic planes from sintered and non-sintered baseline, 4 wt% MC/PVA, and 4 wt% CSR.

A 2θ peak at 6.1° is indicative of the 111 plane and is the maximum intensity measured from all samples (Figure 4.12). 2θ peaks at 9.97° and 11.73° are indicative of the 220 and 311 planes respectively and compose the FAU framework of cubic lattice structure. Relative intensities of these planes are

higher than the referenced values of Na-X type zeolite (Table 4.3) potentially due to greater disorder of the heterogenous sample, overlapping of peaks (combining zeolitic beta phase intergrowths), and instrumental broadening due to sub-micron sized crystals or lattice defects formed by interfering bentonite and polymer crystallites that lower measured proportion of FAU. Furthermore, thermal expansion and shrinkage can occur during heat treatment which alters the spacing between crystalline atomic planes (d-spacing, calculated using Braggs law) of the FAU and can influence gas separation potential.

Crystallinity calculations, a measured ratio of accumulated peak area over total spectra area, show the baseline sample is of highest crystallinity, 26 (± 3)%, and hence FAU content of all XRD samples probably due to a 90 wt% zeolite 13X content (Figure 4.13). A 10% error is assumed from the baseline variance of relative intensity (I_{rel}) measured for each peak (Table 4.3). The process of sintering breaks covalent bonds and disorders the structure, hence the following most crystalline samples are the non-sintered 4 wt% CSR of 24 (± 2)%, and non-sintered 4 wt% binder of 18 (± 2)%. One explanation for a range of thermal degradation addresses the physical space occupied by polymers during the composites heat treatment. CSR particles disperse less evenly than the soluble binder causing a 10% and 2% loss in crystallinity respectively, likely due in part to differences in shrinkage rate and intercrystallite void formation upon heating. I.e., a lowered zeolite against zeolite surface area and overall bond formation during sintering of the 4 wt% binder sample due to even distribution. Zeolite against zeolite surface area is greatest in the case of the baseline which when sintered lowers by 13% crystallinity. The d-spacing of the 100% peak that represents the distance between 111 planes is expanded by 0.014 nm which is the greatest of all the measured samples and typical of crystallinity loss. It is also possible that the baseline sample absorbed the most water due to a 90 wt% zeolite content and hydrolysed before sintering, or the most guest molecules were adsorbed on the sintered zeolite as drying FAU leads to expansion of the unit cell [28]. The mismatch between expansion rates of the zeolite and support leads to thermal damage and lowered FAU content.

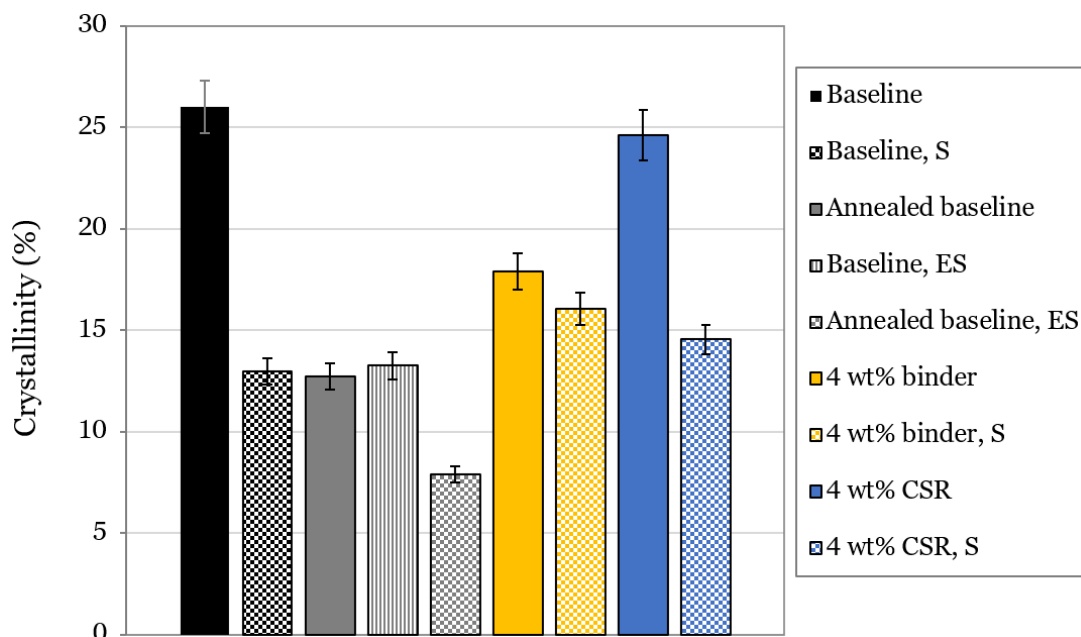


Figure 4.13. Crystallinity as calculated from XRD peaks measured from baseline, 4 wt% binder, and 4 wt% CSR samples that were cast, extruded (E), and/or sintered (S) revealing the effects of heat transfer rate on crystallinity and FAU formation. Error bar height gives 10% variance error.

Annealing of the extruded baseline paste pertains a further reduction in crystallinity compared to annealed cast baseline paste perhaps due to a difference in sintered geometry with a 1.6 mm diameter paste extrudate granting increased heat transfer rate compared to a cast 4 mm monolith wall. Thinner walls reduce time required to reach T_{max} (720 °C), with sintering time spent at high temperature significantly effecting crystallinity of such zeolites [29].

4.4.4. Brunauer–Emmett–Teller Adsorption

BET surface area was measured using N_2 to assess a sintered baseline zeolite composite for comparison with a) non-sintered cast and powdered: 4 wt% MC/PVA, and 4 wt% CSR composites; and b) sintered (S) and extruded (E): baseline, 4 wt% MC/PVA, and 4 wt% CSR. The sintered baseline sample absorbed the most gas reaching 523 m^2/g (Figure 4.14) of comparable type IV isotherm plot results to those of Thakkar et.al who measured 13X monolith BET surface areas of 498-571 m^2/g [30].

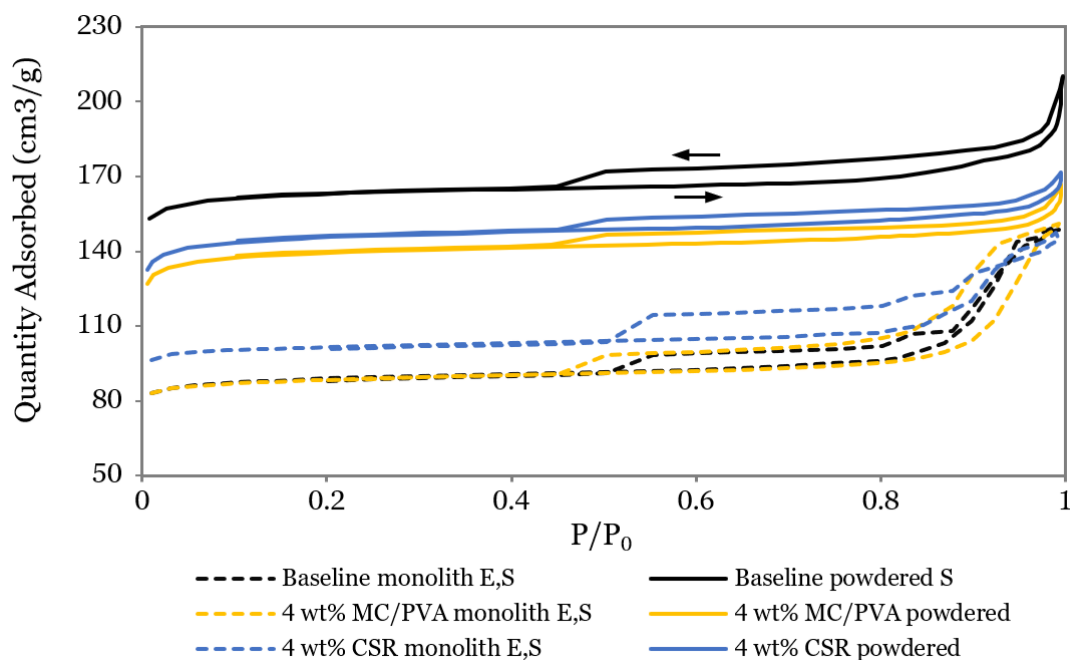


Figure 4.14. BET analysis of powdered, and extruded, baseline 4 wt% CSR, and MC/PVA samples. Black arrows show the progress of time.

Measured BET curves are typically Type IV curves of H4 hysteresis. Hysteresis shows a disparity between quantity absorbed during applied pressure and released pressure (Figure 4.14, arrows). The greater this disparity the greater the resistance to gas flowing from the pores, and the hysteresis transforms from a H4 to H5 classification.

All samples feature a similar isotherm profile type with the majority of N_2 adsorption occurring before pressure is applied, starting at near zero partial pressure (P/P_0 , where P_0 is the saturation pressure of the absorptive) at an adsorbed quantity of between 83-153 cm^3/g . After a fast initial uptake at P/P_0 below 0.05 due to micropore adsorption, the N_2 adsorption equalises which in the case of the baseline sample occurred between 162-169 cm^3/g from 0.15-0.8 P/P_0 . A 44-70 cm^3/g drop in N_2 adsorption occurs when samples are extruded with a 1.6 mm thickness instead of cast and ground (Figure 4.14) which is potentially due to the difference in sample thickness and resulting length of intracrystalline pore channels. The only variable difference between S baseline and baseline, ES is the geometric form of the sorbent sample (ground from a cast prism compared to as-extruded lines) hence geometry influences FAU accessibility during BET analysis. Uptake past about 0.8 P/P_0 is likely due to capillary condensation in the mesopores where a multilayer develops by physisorption driven by van der Waals interactions. Hysteresis is similar for

all cast samples and shows a slight delay in desorption due to the presence of flow resisting pores and metastable nitrogen multilayers.

The isotherm adsorption plateaus indicate Langmuir adsorption, a model whereby molecules reside as a single layer on a flat plane as opposed to the BET model that describes the formation of a multilayer that is characteristic of mesoporous materials with pore diameters of 2-50 nm [31]. Langmuir surface area analysis shows a cast baseline 723 m²/g surface area is reduced to 647m²/g in the case of cast 4 wt% CSR, and 620m²/g in the case of cast 4 wt% MC/PVA (Table 4.4). The average pore width of cast samples is 2.5 (±0.13) nm (where error is 5% tolerance), hence, the BET model is potentially a more accurate measure of surface area.

Adsorbed N₂ to non-sintered surfaces past 0.8 P/P₀ shows a steady uptake rate that could be due to round and consistent mesopores. The presence of macropores cause a rapid rise near P/P₀=1 with wider macropores of the sintered samples causing a sharper rise than non-sintered (Figure 4.14), as detailed by the International Union of Pure and Applied Chemistry (IUPAC) [4]. All samples are of Type IV(a) adsorption curve showing hysteresis, which is associated with capillary condensation taking place in mesopores, with less sever hysteresis of non-sintered samples indicating a more reversable ad/desorption process. Sintering facilitates condensation and desorption at lower P/P₀ due to larger and less regular pores composing highly accessible surfaces. Destroyed FAU frameworks are present in sintered monoliths having been extruded and sintered which may account for the reduced microporosity and increased macroporosity.

4 wt% MC/PVA E, S is distinct in that it shows a larger ad/desorption disparity than non-extruded samples which adsorb earlier at 0.82 P/P₀ as opposed to 0.87 for the extruded baseline and 0.95 for the non-extruded samples. The key differences that the hysteresis depicts includes damaged pores due to sintering of extruded monoliths and a corresponding lowered surface area that is confirmed by average pore widths of 2.7 to 6.7 nm for the extruded samples (Table 4.4).

Table 4.4. Measured surface area, pore volume, and pore size of S baseline, non-sintered 4 wt% CRS, non-sintered 4 wt% MC/PVA, 4 wt% CRS, ES, and 4 wt% MC/PVA, ES samples.

Sample	Single point surface area (m ² /g)	BET (m ² /g)	Langmuir (m ² /g)	V _{micro} (cm ³ /g)	Av. pore width (nm)
Baseline, S	523	466 (±16)	723 (±1)	0.24	2.4
4 wt% CRS	447	396 (±14)	647 (±2)	0.21	2.5
4 wt% MC/PVA	419	375 (±14)	620 (±1)	0.20	2.5
Baseline, ES	333	332 (±5)	390 (±1)	0.12	2.7
4 wt% CRS, ES	311	148 (±17)	447 (±1)	0.12	5.9
4 wt% MC/PVA, ES	272	131 (±15)	389 (±1)	0.14	6.7

Sintered sample surface areas show that sintering is effective at promoting N₂ adsorption, hence DW printed parts are to be sintered before use as a gas separation technique for applications such as CO₂ capture. The range between non-sintered 4 wt% CRS and 4 wt% MC/PVA zeolite composite single point surface areas is 28 m²/g (Table 4.4) with the CRS sample being more suitable for gas separation. However, BET values are similar, and the CRS addition is possibly favourable compared to MC/PVA despite equally weighted microporous zeolite content before processing. A particulate CRS content may minimise damage to zeolite surface area compared to a continuous thin MC/PVA binder film that covers more zeolite surfaces. CRS could promote gas separation without sacrificing micro- and mesoscopic network structures due to its geometry. The MC/PVA, ES isotherms above 0.87 P/P₀ reveal N₂ cannot move freely through the exposed pore networks that are inter-connected with thin channels by the sintering of polymer binder. In this case the disparity between adsorption and desorption is relatively large which is not true for the same composite that was not extruded or sintered. When powdered straight from the cast non-sintered specimen there is no complex continuous channels formed and the Langmuir values are significantly higher compared to ES samples.

The decomposition temperature of MC/PVA is below 350 °C so it is assumed the polymers have carbonised and take up no space [32,33]. The MC/PVA binder envelopes the zeolite particles during mixing since it is dissolved which is sufficient to form a free-standing structure when dry. Conversely, the CRS is a particle that does not dissolve and therefore is distributed in the zeolite

composite affording a higher exposed zeolite surface area. CSR particles are 29 μm in diameter compared to 2 μm diameter zeolite 13X so when CRS is carbonised during sintering for improved surface area empty volumes form throughout to promote gas flow and reduce pressure drop. Spherical voids that are potentially formed due to carbonisation of the CSR particles composing the cast samples, even if only momentarily spherical before collapsing, improve rapid desorption at high P/P_0 . The same theory can be applied to extruded and sintered CSR samples that accommodate absorbing greater amounts of N_2 than the baseline and 4wt% MC/PVA at P/P_0 's below 0.97. However, the ES samples show lower efficiencies and therefore a printed lattice requires more feedstock material to separate a given gas.

4.4.5. Scanning Electron Microscopy

Imaged sintered baseline samples (Figure 4.15, E) include a single ~ 0.3 mm diameter cavity composing a more consistent surface compared to the sintered 4 wt% CSR composite (Figure 4.15, F) composed of a range of cavity sizes. CSR particles of ~ 20 μm diameter are distanced apart by ~ 50 μm at the surface (Figure 4.15, C), and similarly distributed cavities are shown after sintering and carbonisation of the CSR (Figure 4.15, D and F). The cavity diameter distribution is likely due to electrostatic agglomeration of CSR particles during mixing. It should be noted that carbonised polymer and steam is formed during sintering that escapes through pores and voids but may also build in pressure causing vapour to rupture the composite. These cavities reduce surface area but offer intracrystalline free volumes for rapid gas permeation and a lowered pressure drop for potentially faster CO_2 uptake.

Non-sintered surfaces of both the baseline and 4 wt% MC/PVA show no visible cavities, however, the non-sintered baseline composite shows a visibly rough texture that lends itself to attrition during handling. The increased binder volume composing 4 wt% MC/PVA form ripples at the surface of the specimen (Figure 4.15, G) presenting a binder content that causes excessive adhesion for casting and extruding. The 4 wt% MC/PVA paste requires post processing to achieve a smooth surface finish for minimising roughness and associated attrition. Excessive adhesion prevents DW of the paste, hence a 4 wt% PVA/MC was discontinued for rheology assessment and calliper measurements. Preliminary printing showed a 4 wt% CSR paste does not create excess adhesion and formed the intended geometry by DW.

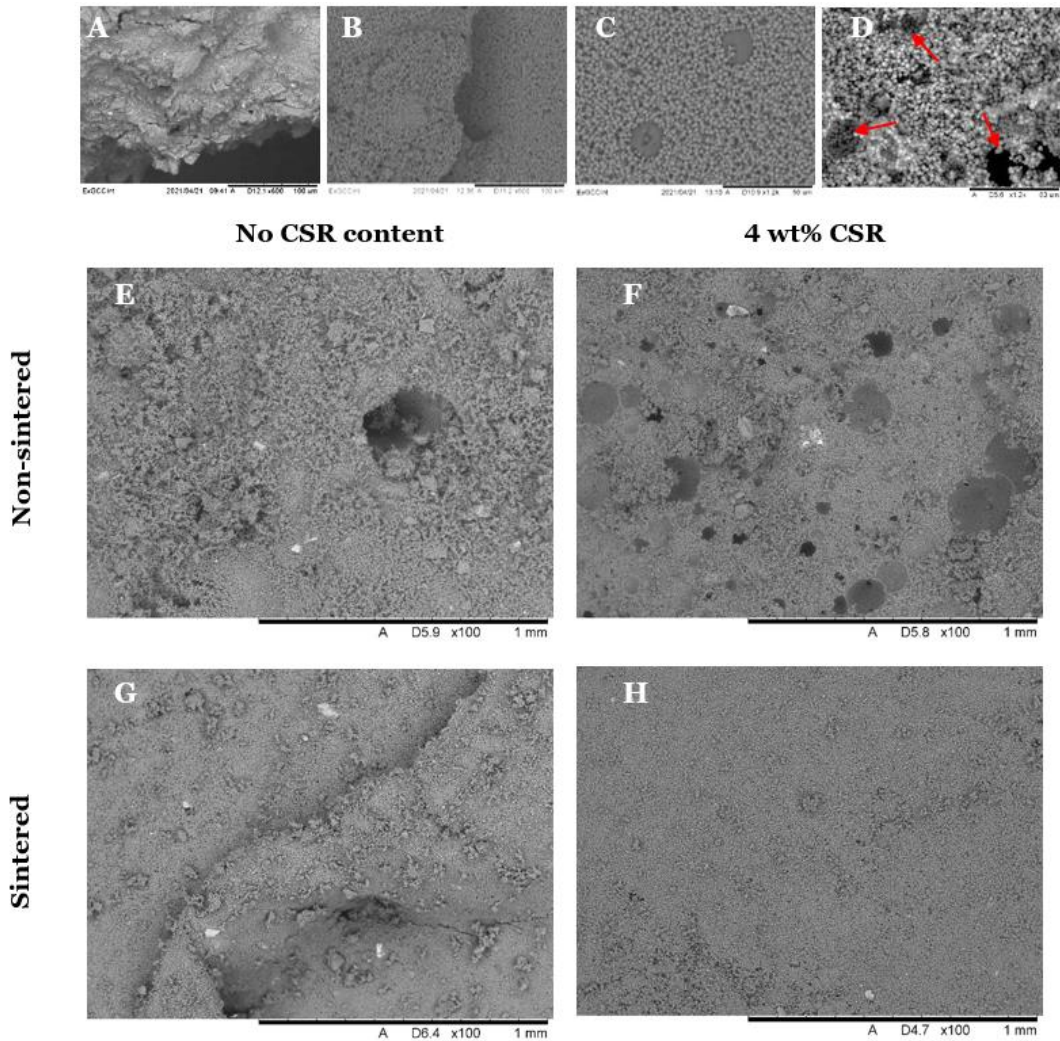


Figure 4.15. Desktop SEM images of bentonite (A), printed zeolite composite (B), 2 wt% CSR particles at the printed surface (C), and sintered 4 wt% CSR showing circular voids highlighted by red around (D), sintered composite with zero additive (E), sintered composite with 4 wt% CRS addition (F), non-sintered flat surface of with 4 wt% addition of binder mixture (G), and non-sintered surface of added 4 wt% CSR flat surface (H).

A dried bentonite cast sample was imaged using SEM showing typical binder surface texture that can aid zeolite composite printability (Figure 4.15, A). The natural bentonite clay is composed of irregular particle geometries formed from agglomerated microplatelets that provide plasticity to the printed composite (Figure 4.15, B). The composite features a ridge that formed between layers of a print, an inherent structural weak zone of DW printed parts. Bentonite particles are not visible when added to the zeolite in small amounts suggesting a thin isotropic distribution is achieved that lends to preventing crack formation. Furthermore, the effect that CSR sized cavities has

on compression strength is minimal, of 1.3 (± 0.4) and 1.1 (± 0.4) MPa for sintered baseline and sintered 4 wt% CSR composites, respectively (Table 4.2).

4.4.6. Calliper Measurements

The DW print quality was assessed by simply measuring the dimensions of the printed baseline and 4 wt% CSR samples using callipers. Results given in Table 4.5 show a difference in sample height when measured with and across the printed top lines, which is 5% reduced with the addition of 4 wt% CSR over the baseline paste composition.

Table 4.5. Calliper measured baseline and 4 wt% CSR sample length (l), width (w), thickness parallel to printed top lines (t_a) and thickness perpendicular to printed top lines (t_e) with vertical distortion provided as percentage change between t_a and t_e .

Sample	l (mm)	w (mm)	t_a (mm)	t_e (mm)	Vertical distortion (%)
Baseline	26.7 (± 0.9)	26.1 (± 1.6)	6.9 (± 0.2)	6.3 (± 0.2)	8
4 wt% CSR	27.5 (± 0.3)	27.7 (± 0.2)	6.4 (± 0.1)	6.2 (± 0.2)	3

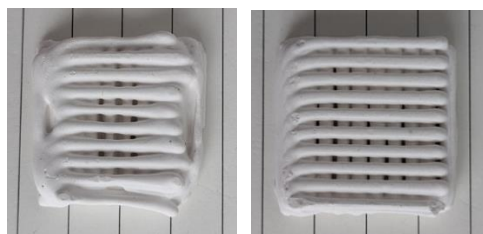


Figure 4.16. Baseline (left) and 4 wt% CSR (right) DW printed samples.

Comparing the two samples in Figure 4.16, it is clear that the geometric distortion of the baseline sample is greater than that of the 4 wt% CSR sample. The distortion of the baseline sample width is greater than the distortion measured along its length. The polymer content hardens as the structure dries that causes the perimeter to rise from the print bed and the structure shrinks towards its centre. In the case of the measured 4 wt% sample, the difference between length and width is negligible providing an improved representation of the intended woodpile structure of 25×25×6.6 mm. Print accuracy is governed by paste rheology and curing behaviour which are key to scaling of such 3D printed adsorbants. The 4 wt% CSR paste shows an improvement over

the baseline paste for satisfying regulatory requirements for reliable manufacture and commercial deployment.

4.4.7. Surface Tension Analysis

CSR content decreases baseline surface tension and wettability. Surface tension of CSR in water measured 38-41 mN/m at a 0.5 wt% addition, and 55-44 mN/m at a 1.5 wt% addition which is beneficially lower than that of water and bentonite in water [34]. The CSR will lower the effect of surface tension acting to deform the layer(s) towards the filament midpoint considering surface tension forces contribute to greater deformation shortly after deposition from a nozzle. It is because of slumping by gravity and surface tension that Barki *et.al* highlighted the importance of yield stress after deposition and capillary forces that reduce surface energy for merging layers into a strong structure [35]. Surface tension tends to decrease with time as capillary forces move fluid content from the fluid/solid interface and consequently bulk stresses overcome composite binder adhesion. These parameters must be balanced with the nozzle diameter to deposit a free-standing layer.

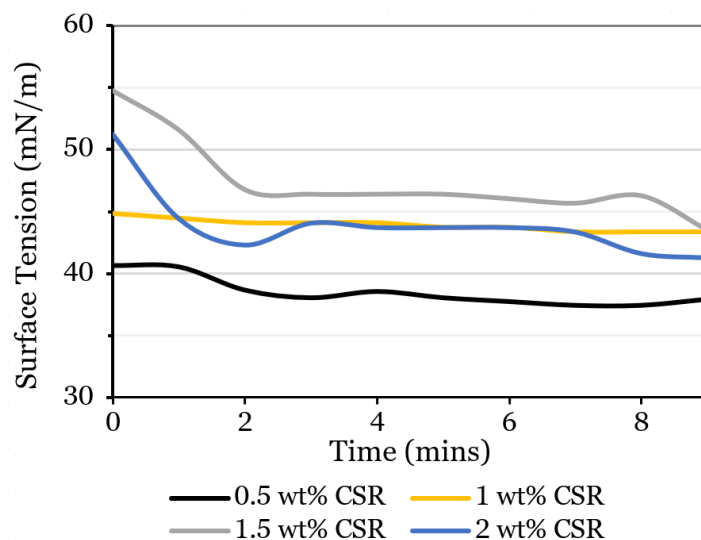


Figure 4.17. Surface Tension of 0.5, 1, 1.5, and 2 wt% CSR in DI water.

Interparticle cracks form upon drying especially when constructed on a glass substrate (Figure 4.18). These samples were equally coated and dried under the same environmental conditions and both baseline and CSR containing composites formed crazed surface tears most obvious in the CSR sample. Tensile stresses develop during drying and shrinking [36], and rubber particles

may cause residual stresses to delocalise along zeolite matrix facets and in doing so provide ‘shielding’ deformation. This renders the 4 wt% CSR composite more compliant due in part to a greater formation of crazes instead of macrocracks. It is possible that favourably positioned CSR act as craze nucleation sites upon drying, which exhaust before water evaporating from a layer reaches equilibrium with its environment causing void coalescence and crack growth.

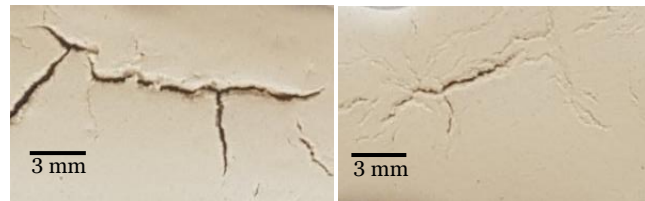


Figure 4.18. Zeolite composites with zero (left) and added 4 wt% CSR (right) showing an example of crack formation.

Lowered surface tension and increased distribution of stresses across larger volumes during drying means CSR can facilitate decreased shrinkage via transforming tensile stresses to hydrostatic stresses. Shear yielding of the plastic binders containing CSR therefore likely lowers warping during drying. This is especially noteworthy considering the importance of moisture level and first layer resolution of cementitious materials on the mechanical properties of a DW printed part [37].

4.4.8. Rheology of Zeolitic Composite Pastes

A lowered water content of baseline paste composition increases η (Figure 4.19); from 54.0, 52.5, and 51.0 wt% DI water with corresponding η of 25.1, 75.5, and 140.9 Pa·s (Table 4.6), as calculated using equations in Section 2.5.6). Pastes exhibit stability of shearing i.e., typical shear thinning with no anomalous data points or clusters that would suggest jamming of particles. An important criterion for DW is a non-zero yield typical of Bingham plastic behaviour for self-supporting structural requirements during layering, and starting measured datapoints were 0.6, 0.6, and 1.1 shear rates for 54.0, 52.5, and 51.0 wt% DI water containing pastes respectively. Considering that shear rate was programmed from 0.6 it is possible that the 54.0, 52.5 wt% DI water pastes are pseudoplastic fluids and not feasible for DW. The two baseline pastes of 51 wt% and 54 wt% may represent a pseudoplastic fluid and Bingham

plastic respectively because their viscosity values are separated by 300 to 800% when sheared up to 30 s^{-1} .

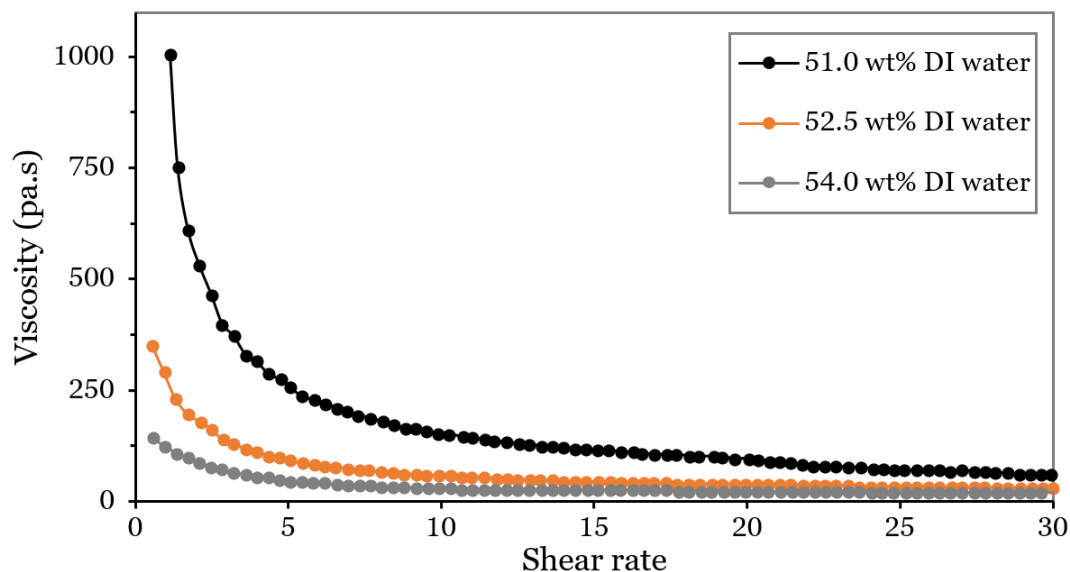


Figure 4.19. Baseline zeolite composite pastes with water content 51.0, 52.5, 54.0 wt% DI water of stable shear thinning profiles.

The baseline 52.5 wt% DI water paste was used as a denominator for relative viscosity (η_r) calculation (Figure 4.20) with baseline and CSR pastes showing a slight overall dilatant effect. All CSR pastes with 52.5 wt% DI water content yield η_r between the 51 and 54 wt% DI water baseline plots, averaging at 1.02 (± 0.05) initially and 1.14 (± 0.11) at 28.5 s^{-1} . The 2 wt% CSR presents consistently high relative viscosity and is therefore most resistant to shear, which could be due to a high compression modulus when dry. In all other cases, relative viscosity decreases up to a shear rate of $15\text{-}18 \text{ s}^{-1}$ followed by a steady increase.

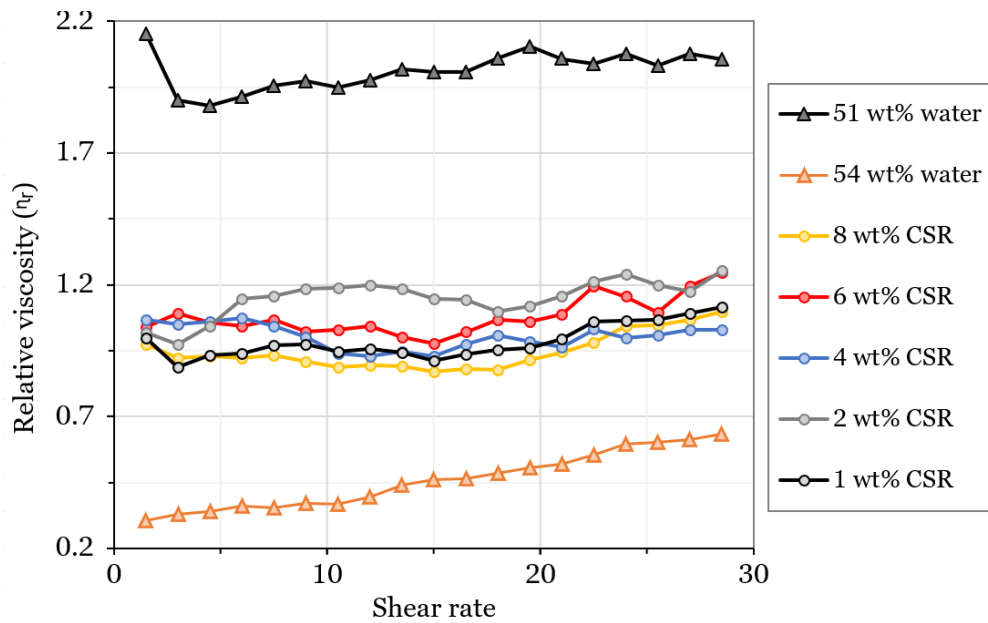


Figure 4.20. Relative viscosity of baseline and added CSR pastes calculated using 52.5 wt% DI water viscosity values as a common denominator. Each plotted value represents three averaged viscosity values implemented to reduce noise.

Shear thinning MC/PVA polymer chains dissolve in water and arrange themselves inducing anisotropy to the direction of applied shear at low shear rates below $\sim 15 \text{ s}^{-1}$, with CSR particles and small polymer agglomerates likely prolonging the physical rearrangement of paste morphology into a formation of lowest available surface energy. Viscosity begins to increase after arrangement potentially due to van-der Waals attractions between shearing layers that increase causing a relative dilatant effect above shear rates of $\sim 18 \text{ s}^{-1}$. Another consideration is evaporation of the water that increases resistance to shear. By noting these phenomena, an improved understanding of DW of zeolite adsorbent structures is made for accurate gas separation in enclosed environments.

Assessed pastes were quantified for shear thinning characteristics using the power law (n), $\log(\eta)/\log(\dot{\gamma})$ and line of best-fit (Figure 4.21). A paste sensitivity to water is highlighted by increased n with added water, jumping from 0.21 and 0.18 for 51.0 and 52.5 wt% DI water, to 0.47 in the case of 54.0 wt% DI water.

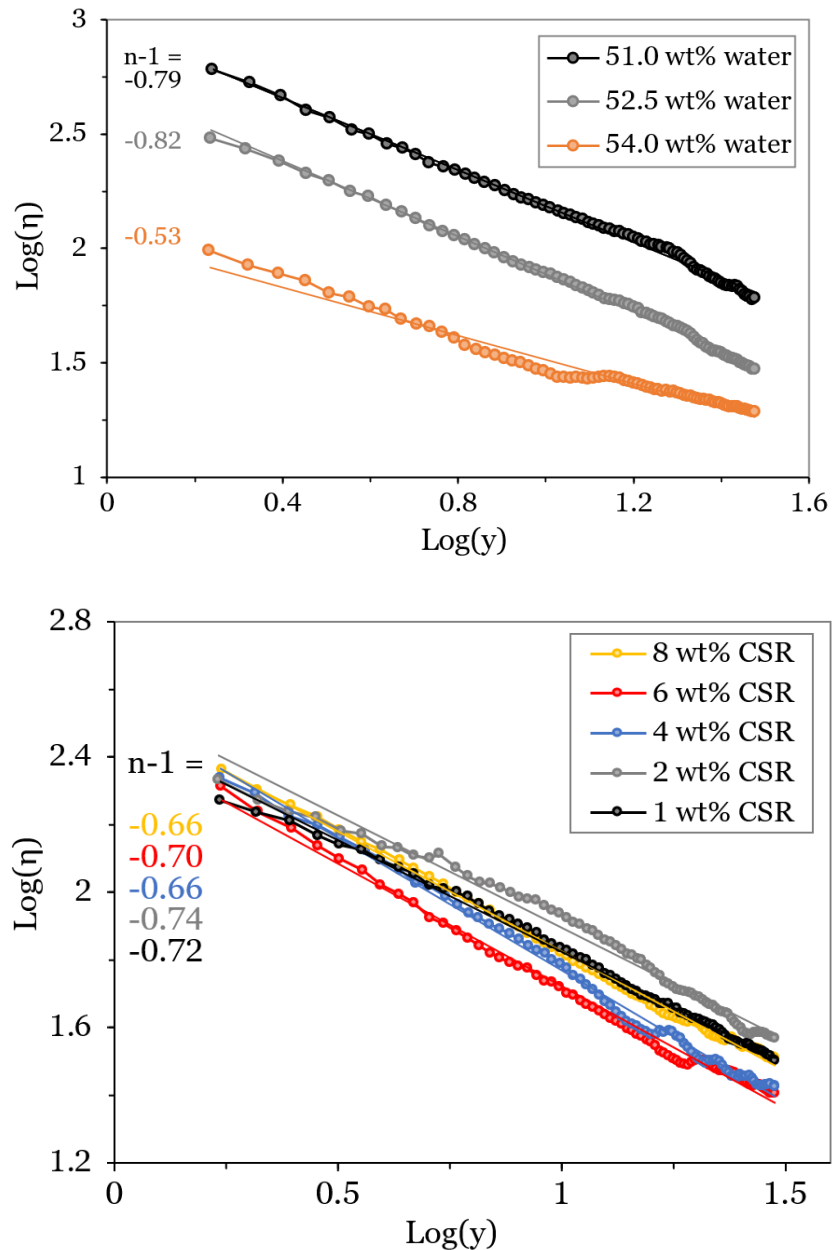


Figure 4.21. $\text{Log}(\eta)$ against $\text{log}(\dot{\gamma})$ used to calculate power law values of baseline pastes (top) and added CSR pastes (bottom).

All pastes exhibit shear thinning as all values of n are below 1, with 1 and 2 wt% CSR providing relatively high values of 0.34. A 4-8 wt% CSR content provides a relative thinning influence as values of n decrease to 0.26-0.3 but remain above the reference baseline n of 0.18. The 4 wt% CSR paste was established as the optimum CSR addition for strengthening the composite paste and is also optimum in terms of shear thinning properties due to its lowest n of all assessed CSR samples. Sheer thinning is desirable for softening during extrusion without sacrificing stiffness of layered paste.

Paste hydrostatic pressure (σ_{HP}) decreases proportionately from 1.19-1.16 when CSR content is increased from baseline to 8 wt% CSR content. A proportional increase is true with added water because the density of the CSR is 1g/cm^3 which is equal to that of water. This means that a slight but detrimental gravity assisted distortion of printed layers may occur with increased CSR content, offsetting a reduced surface tension with added CSR.

Table 4.6. Rheology parameters for DW characterisation: power law index (n), shear stress (γ), flow consistency index (K), viscosity (η), and pressure change (P) of baseline with 54, 52.5, and 51 wt% DI water and CSR pastes of 1 to 8 wt%.

Sample	n	γ (Pa)	K (Pa·sⁿ)	η (kPa·s)	ΔP (kPa)
54.0 wt% water	0.47	16.2	110	25.1	8.8
52.5 wt% water	0.18	10.3	513	75.5	26.4
51.0 wt% water	0.21	10.9	933	140.9	49.2
1 wt% CSR	0.34	13.6	302	54.0	18.9
2 wt% CSR	0.34	13.6	363	64.9	22.7
4 wt% CSR	0.26	12.0	355	56.6	19.8
6 wt% CSR	0.28	12.4	275	45.1	15.7
8 wt% CSR	0.3	12.8	339	57.0	19.9

Flow consistency index, K, is measured as the Y intercept of a $\log(\eta)/\log(\gamma)$ graph and indicates the viscosity of a paste sample to be processed via shear force. A 2 wt% CSR paste is of highest K at 363 Pa·s, and a 6 wt% CSR paste is lowest at 275 Pa·s. These figures are used with power law index n and parameters from an extruder such as flow rate and nozzle diameter to provide ΔP values. Despite a relatively high K of 355 Pa·s, the 4 wt% CSR paste provides the median ΔP value of 19.8 kPa due to beneficial shear thinning behaviour. With high K, low n, and median ΔP in respect to all CSR pastes the 4 wt% CSR paste can be expected to be highly viscous and stable at low shear, print at high speed, and generate low pressure drop i.e., resistance to extrusion is low and consequent maximum extrusion speed is high. The 6 wt% sample is similar but with a trade-off between beneficial high viscosity and low ΔP .

A 4 wt% CSR paste exhibits the lowest yield stress (γ) of the CSR samples potentially due to a morphology that requires the least shear force to initiate shearing and is therefore of lowest inertia. This may be due to an optimum CSR wt% for strong and well-defined shear layers that do not create unnecessary friction during shear as represented by low n and high η . Yield stress is particularly insightful for control of extrusion at low shear rates. Hence, a 4

wt% CSR paste will be most responsive to impulse force which promotes accurate DW. The 4 wt% CSR paste is likely reliable under intense printing conditions such as rapid extrusion velocity and acceleration, lowering the likelihood of print failure, e.g., under extrusion via plunger retraction.

Extrusion pressure measurements using the 4 and 8 wt% CSR pastes in a 5ml syringe highlights that back pressure can normalise in the first 5 mm of extrusion (Figure 4.22). Back pressure develops initially by impulse during the first ~ 1.5 mm and continues a lower positive gradient between 5 and 10 mm as the plunger displaces the isotropic paste. Paste extrudate using nozzles of 1.6- and 1.8-mm diameter show displacement with near linear pressure increase as compaction occurs in the syringe cylinder before extruding at equilibrium pressure from the nozzle. On the other hand, extrudate from a 2 mm nozzle does not compress at all and so reaches an equilibrium pressure of 0.06-0.09 MPa at 2.4 mm, which continues as a plateau for the remainder of extrusion time.

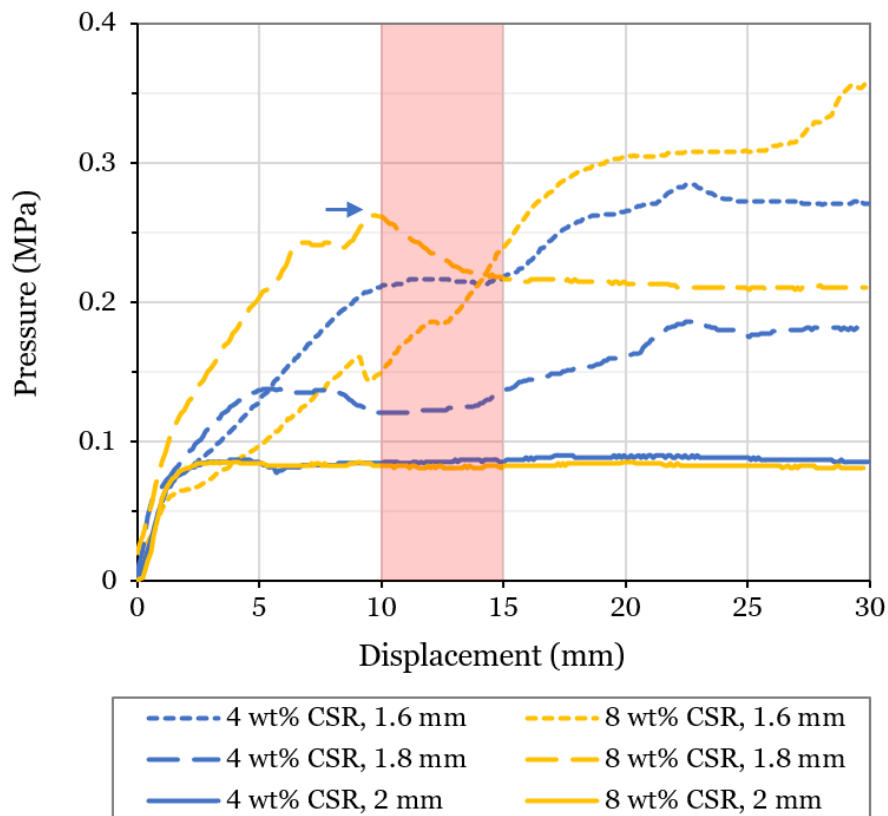


Figure 4.22. Extrusion pressure profiles using a 5 ml luer lock syringe at a plunger speed of 6 mm/s, showing the influence of using 1.6, 1.8, and 2 mm nozzle diameters for 4 wt% and 8 wt% CRS pastes. A proposed equilibrium/relaxation zone is highlighted in red, and a blue arrow highlights potential CSR decompression.

Nozzle diameters of 1.8 mm feature pressure fluctuations between 0.12-0.26 MPa due to uniform compaction of elastic zeolite with unpredictable motion of entrapped water and air pockets (Figure 4.22). However, a 1.8 mm diameter accommodates rising pressure to give relatively stable pressure plateaus at 0.18 and 0.21 MPa for 4 and 8 wt% CSR pastes, respectively. Whereas syringes fitted with 1.6 mm nozzles feature pressure change due to severe and uneven compaction whereby water content is visibly removed (paste dehydrated) from low density volumes within the syringe. As a result, 1.6 mm nozzle extrusion pressures continue rising to 0.27 and 0.36 MPa for 4 and 8 wt% CSR pastes, respectively.

A paste with 8 wt% CSR content and 1.6 mm syringe nozzle is least stable under the assessed conditions whereby friction and zeolite compression cause pressure to increase sharply effecting shear thinning and DW potential. As a critical volume of CSR particles move closer together while entering the 1.6 mm nozzle their elastic properties generate back-pressure capable of clogging the syringe.

A decrease in pressure past a peak at 10 mm displacement while extruding 8 wt% CRS with a 1.8 mm nozzle could be a decompression of CSR content as indicated by the blue arrow (Figure 4.22). This also occurred in the case of 4 wt% CSR but with a shallow peak at 9 mm. A notable stable pressure zone is apparent between 10- 15 mm as highlighted by the yellow box where all pastes feature signs of relaxation. Pressure profiles from the three most resistant pastes intersect acutely at 14.2 mm before levelling off, hence, extrusion pressures of the 1.6 mm nozzle at 4 wt% CSR, and 1.8 mm nozzle at 8 wt% CSR potentially provide operation limits for nozzle diameter and CSR content combination. Extruder set-up should account for increased pressure from reduced nozzle diameter and added CSR with an optimum observed set-up for a 6 mm/s plunger speed being a 1.8 mm nozzle and 4-8 wt% CSR or a 1.6-1.8 mm nozzle with 4 wt% CSR content.

A review by Shane Lawson *et al* highlights the challenges to scale-up for directly printed adsorbents mentioning that DW of presynthesised adsorbents is likely the most attractive prospect for scale-up because it has clearly been demonstrated to fabricate tunable and complex geometries [38]. DW adsorbent performance compared to traditional configurations manufactured via powder or cast based techniques does not show a critical drop in adsorbent or catalyst performance, and neither does the work presented in this thesis chapter. Like other works in the literature, this thesis chapter has employed a small-scale syringe with a small nozzle with the problem being that automation

has not been demonstrated without hands-on time or a skilled operator. The fabrication of scalable configurations for a wide variety of separation and reaction applications is feasible but depends on satisfying compositional and structural requirements. Lawson considers the retention of particle structure (i.e., particle crystallinity, size, and topography) the first criteria to address using mechanical, thermal, and chemical means.

In terms of shape engineering, moulding can decrease adsorption efficiency as shown by Siyu Pu et al who showed a 20% reduction of ethylene and ethane adsorption compared to the powdered counterpart [39]. Thakkar et al noted a 26% reduction of nitrogen adsorption (from 770 to 571 m²/g) between powdered zeolite 13X and a monolith with the same formulation as the baseline composite studied in this thesis chapter. In this thesis chapter, extrusion of a monolith reduced nitrogen adsorption by 30% from its powdered form. The main advantage of the 4 wt% CSR composites as a formulation for scale-up deployment is the ability to be printed into mechanically strong adsorbent structures while printing with low solvent volatility that tends to offer universal printability.

4.5. Conclusions

Gas separation systems suffer from brittle failure and one approach to improving system performance is by employing AM to fabricate the adsorbent structure that allows for complex geometric design, reduced pressure drop across the system, and increased tuneability for various applications. Zeolite 13X is typically strong in compression and to further this attractive property a baseline composite of 90 wt% zeolite was combined with a CSR particle showing UCS increase from 4.92 (± 1.22) to 7.75 (± 0.75) MPa when combined with 4 wt% CSR and tested at a strain rate of 1.67 $\cdot 10^{-3}$. The baseline and 4 wt% CSR UCS dropped to 3.74 (± 0.37) and 6.37 (± 1.01) when assessed at a 5 $\cdot 10^{-2}$ strain rate. However, it appears that the rubber content is deformed and physically activated at a strain rate of 5 $\cdot 10^{-2}$ which improves strain to failure of the 4 wt% CSR composite from 0.05 (± 0.004) at 5 $\cdot 10^{-2}$ to 0.10 (± 0.014) at 1.67 $\cdot 10^{-3}$. Improved compression strength of DW free-standing scaffolds for low pressure drop and tunable adsorbent structures can reduced particle attrition during handling, transportation, installation, and consequently their efficiency and industrial adoption.

The preparation of DW printed structures for adsorption applications typically require sintering at temperatures around 700 °C to maximise surface area. Zeolite/binder composite pastes underwent thermal degradation that increased with every additional processing step as shown from XRD spectra used to measure crystallinity. The crystallinity of a non-sintered baseline composite is 26 (± 3)%, with extruding and sintering, and annealing further lowering crystallinity to 15 (± 2)%. Heat transfer rate during heating is dependent on geometric form and therefore plays a significant role in determining final part crystallinity, FAU structure content, and gas selectivity. From the XRD and BET results it is recommended that printed zeolite 13X lattices of 1.8 mm wall thickness should be sintered at 720 °C for less than 2.5 hours and not annealed. Further work should include an assessment of dwell time and part wall thickness to establish ideal sintering times and temperatures for given DW extruded geometries to maximise preservation of FAU structures and avoid unnecessary thermal degradation of fully sintered prints. A final DW printed structure can offset sub-optimal sintering conditions, a realistic scenario for manufacture of large structures using large ovens for sintering, by ensuring high volumes of zeolite is provided as the feedstock and large prints are fabricated.

It is hypothesised that the surface area of zeolite 13X/binder composites is best determined using Langmuir and BET due to a near horizontal isotherm between 0.1 and 0.8 followed by a rise in adsorption and slow desorption rate above 0.8 P/P_0 suggesting the presence of a multilayer. Samples of lower crystallinity, including ES samples, yield lower surface areas confirming the destruction of selective FAU framework with increased thermal degradation. Baseline sintered BET surface area using N₂ as the adsorbate was 466 (± 16) cm³/g, which decreased to 332 (± 5) cm³/g when extruded and sintered. The addition of 4 wt% CSR content further decreases in BET surface area to 148 (± 17) cm³/g but increased Langmuir surface area from 390 (± 1) to 447 (± 1) cm³/g with average pore width increasing from 2.7 (± 0.2) to 5.9 (± 0.3) nm. Although, a CSR addition was slightly less detrimental to surface area compared to 4 wt% MC/PVA that showed a 131 (± 15) cm³/g BET surface area, Langmuir surface area of 389 (± 1) cm³/g, and average pore size of 6.7 (± 0.4) nm. SEM images captured CSR particles before the sintering step and CSR particle sized cavities after the sintering step suggesting a fully carbonated polymer. Cavities in a sintered printed structure may reduce pressure drop for rapid pressure cycling and molecular sieving. Spherical voids from CSR removal appear beneficial for surface area compared to thin channels that

likely form by the removal of binder during sintering which contribute to the large 4 wt% MC/PVA adsorption/desorption hysteresis loop.

All other experiments using zeolite 13X pastes in this chapter aimed to quantify the benefits that CSR provides DW printing performance. A 4 wt% CSR increases paste stability for DW as shown using IR imaging and corresponding heat maps. The perimeters of baseline and 4 wt% CSR IR maps indicate warping as quantified using a quadratic best fit curve whereby the 'a' coefficient was 2×10^{-4} for baseline and 9×10^{-5} for 4 wt% CSR. Warping is partly reduced by CSR addition due to a lowered surface tension.

The viscosity of pastes with 52.5 wt% DI water content is 75.5 and 56.6 Pa·s for baseline and 4 wt% CSR samples respectively, hence, paste preparation requires less water therefore reducing surface tension and reducing evaporation and molecular movement upon solidification. Lower necessitated water also benefits product sustainability in terms of lowered resource requirements. Print stability also improved by CSR as shown by a slight reduction in ΔP that increases the maximum print and extrusion speeds. A 4 wt% CSR addition offers shear thinning properties described by a power law index of 0.26, and yield stress of 10.0 Pa for improved control at near zero deformation during layering compared to other CSR content samples assessed.

Pastes of 4 wt% and 8 wt% CSR addition extrudes continuously between 0.8 and 2.8 MPa when extruded through 1.8 and 2 mm nozzles at a 6 mm/s plunger speed. A 4 wt% CSR shows controlled extrusion through a 1.6 mm nozzle, however an 8 wt% CSR addition does not. This suggests a compression of rubber and uncontrolled dehydration of zeolite at 8 wt% CSR that acts to limit a 5 ml syringe fitted with a 1.6 mm nozzle in manufacturing robust zeolite 13X/binder DW structures. A 4 wt% CSR benefits DW printability, compression strength, and N_2 adsorption when compared to the equivalent 4 wt% of previously established MC/PVA content.

Ideally, a gas adsorbent system does not require polymer content as it is incinerated before use, therefore further work should consider catalytic applications that do not require the removal of the rubber strengthening phase such as the CSR content. Alternatively, and more relevant to this thesis chapter should be the investigation of an open pore polymer phase that would avoid the need for binder removal, in turn avoiding FAU destruction during heat treatment. Reducing the steps required between formulation and structure implementation will reduce energy usage, streamline business operations, and further strengthen the benefits of 3D printing of adsorbents.

4.6. References

- [1] S.M. Auerbach, *et al*, Handbook of zeolite science and technology, CRC press, (2003)
- [2] C. Chen, *et al*, CO₂ capture using zeolite 13X prepared from bentonite, *Appl Surf Sci.* 292, (2014)
- [3] A. Khaleque, *et al*, Zeolite synthesis from low-cost materials and environmental applications: A review, *Environmental Advances.* 2, (2020)
- [4] K.S.W. Sing, *et al*, Reporting Physisorption Data for Gas/Solid Systems with Special Reference to the Determination of Surface Area and Porosity, *International Union of Pure and Applied Chemistry.* 50, (1985)
- [5] M. Xu, *et al*, Evaluation and optimization of VPSA processes with nanostructured zeolite NaX for post-combustion CO₂ capture, *Chemical Engineering Journal.* 371, (2019)
- [6] K. Narang, F. Akhtar, Freeze granulated zeolites X and A for biogas upgrading, *Molecules.* 25, (2020)
- [7] S. Wang, *et al*, Fabricating Mechanically Robust Binder-Free Structured Zeolites by 3D Printing Coupled with Zeolite Soldering: A Superior Configuration for CO₂ Capture, (2019)
- [8] S. Lawson, *et al*, The Effects of Cell Density and Intrinsic Porosity on Structural Properties and Adsorption Kinetics in 3D-Printed Zeolite Monoliths, (2020)
- [9] R. v. Siriwardane, *et al*, Adsorption of CO₂ on zeolites at moderate temperatures, *Energy and Fuels.* 19, (2005)
- [10] V. Garshasbi, *et al*, Equilibrium CO₂ adsorption on zeolite 13X prepared from natural clays, *Appl Surf Sci.* 393, (2017)
- [11] I.A.M. Ahmed, *et al*, Coordination of Cd²⁺ ions in the internal pore system of zeolite-X: A combined EXAFS and isotopic exchange study, *Geochim Cosmochim Acta.* 73, (2009)
- [12] C.J. Humphreys, The significance of Bragg's law in electron diffraction and microscopy, and Bragg's second law, *Acta Crystallogr A.* 69, (2013)
- [13] F. Rezaei, P. Webley, Structured adsorbents in gas separation processes, *Sep Purif Technol*, (2010)
- [14] S. Li, *et al*, Strategies to control zeolite particle morphology, *Chem Soc Rev.* 48, (2019)
- [15] Wacker, Safety Data Sheet 1907/2006/EC, GENIOPERL® P52 IMPACT MODIFIER, 11, (2021)
- [16] G. Whiting, *et al*, Heats of water sorption studies on zeolite-MgSO₄ composites as potential thermochemical heat storage materials, *Solar Energy Materials and Solar Cells.* 112, (2013)
- [17] H. Thakkar, *et al*, 3D-Printed Zeolite Monoliths for CO₂ Removal from Enclosed Environments., (2016)
- [18] O. Levinger, *Instructables Workshop - Syringe Extruder*, (2015). Available at www.instructables.com/Syringe-Extruder/
- [19] C. Duty, *et al*, What makes a material printable? A viscoelastic model for extrusion-based 3D printing of polymers, *J Manuf Process.* 35, (2018)
- [20] M.B. Pourazar, *et al*, Preparation of 13X zeolite powder and membrane: Investigation of synthesis parameters impacts using experimental design, *Mater Res Express.* 7, (2020)
- [21] A. Sowunmi, *et al*, Dataset on the comparison of synthesized and commercial zeolites for potential solar adsorption refrigerating system, *Data Brief.* 20, (2018)
- [22] A. Ojuva, *et al*, Mechanical performance and CO₂ uptake of ion-exchanged zeolite A structured by freeze-casting, *J Eur Ceram Soc.* 35, (2015)

- [23] J.P. Cecchini, *et al*, Enhancing mechanical properties of ceramic papers loaded with zeolites using borate compounds as binders, *Bioresources*. 8, (2013)
- [24] F. Akhtar, L. Bergström, Colloidal processing and thermal treatment of binderless hierarchically porous zeolite 13X monoliths for CO₂ capture, *Journal of the American Ceramic Society*. 94, (2011)
- [25] S. Chandrasekhar, P.N. Pramada, Thermal studies of low silica zeolites and their magnesium exchanged forms, *Ceram Int*. 28, (2002)
- [26] M.M.J. Treacy, Fifth E. Higgins, eds, Powder pattern identification table, in: Elsevier Science B.V. Amsterdam, (2007)
- [27] J. Rouquerol, *et al*, Adsorption by Clays, Pillared Clays, Zeolites and Aluminophosphates, In Adsorption by Powders and Porous Solids : Principles, Methodology and Applications, Academic Press, (2014)
- [28] M. Noack, *et al*, The change of the unit cell dimension of different zeolite types by heating and its influence on supported membrane layers, *Microporous and Mesoporous Materials*. 117, (2009)
- [29] W. Schwieger, *et al*, Hierarchy concepts: Classification and preparation strategies for zeolite containing materials with hierarchical porosity, *Chem Soc Rev*. 45, (2016)
- [30] H. Thakkar, *et al*, 3D-Printed Zeolite Monoliths for CO₂ Removal from Enclosed Environments, (2016)
- [31] F.J. Sotomayor, *et al*, Characterization of Micro/Mesoporous Materials by Physisorption: Concepts and Case Studies, *Acc. Mater. Surf. Res*. 3, (2018)
- [32] X.G. Li, M.R. Huang, H. Bai, Thermal decomposition of cellulose ethers, *J Appl Polym Sci*. 73, (1999)
- [33] S.H. Salh, D.A. Raswl, Thermal stability of polymer composite films based on polyvinyl alcohol doped with different fillers, *Open Access Journal of Physics*. 2, (2018)
- [34] R.K. Dadashev, *et al*, Features of isotherms of the surface tension of a bentonite water suspension, *Bulletin of the Russian Academy of Sciences: Physics*. 78, (2014)
- [35] A. M'Barki, *et al*, Linking Rheology and Printability for Dense and Strong Ceramics by Direct Ink Writing, *Sci Rep*. 7, (2017)
- [36] M. Ortiz, A continuum theory of crack shielding in ceramics, *Journal of Applied Mechanics, Transactions ASME*. 54, (1987)
- [37] J.G. Sanjayan, *et al*, Effect of surface moisture on inter-layer strength of 3D printed concrete, *Constr Build Mater*. 172, (2018)
- [38] S. Lawson, Recent Advances in 3D Printing of Structured Materials for Adsorption and Catalysis Applications, *Chem. Rev*. 121 (2021)
- [39] S. Pu, J, Performance Comparison of Metal-Organic Framework Extrudates and Commercial Zeolite for Ethylene/Ethane Separation, *Ind. Eng. Chem. Res*. 57 (2018)

Chapter 5. Upcycling of Hospital Blue Wrap Waste into Fused Deposition Modelling Filament

5.1. Chapter Summary

In this chapter, hospital blue wrap rPP is upcycled from a former waste stream into FFF filament with customisable properties through blending with SEBS copolymer. FFF filament is a relatively expensive polymer product because it facilitates the modelling of complex parts of near net shape. The proposed strategy put forward in this chapter works towards a closed loop for blue wrap to be used as a secondary material for hospital parts that are in-house manufactured at short lead times while providing profit to actors involved in its transformation from waste stream to commercial product. Filament is extruded and printed into tensile and impact specimens, and it is shown that a 13.0 wt% SEBS blend is strongest in tension. A rapid change in elongation is noted past a 16.7 wt% addition of SEBS, which is investigated using optical microscopy and ligament thickness theory for the interest of identifying the ductile/brittle transition of different rPP wraps. Thermally recycled and ground blue wrap was not extrudable on its own, and MFI values drop from 104 (± 18) g/10mins (equal to 118 g/10mins from the literature) for the ground rPP to 45 (± 2) g/10mins for the 20.0 wt% SEBS filament. A cost-benefit analysis is conducted to determine the financial viability of the novel filament that can replace virgin plastics in the marketplace and in doing so reduce associated waste and emissions of virgin plastics production.

5.2. Introduction

Medical nonwoven SMS PP sterilization wrap, known commonly as blue wrap, can be found in hospitals globally due to their chemical and thermal resistance that makes for an inert and sanitary plastic fabric [1]. Blue wrap is a layered low-density fabric that makes its storage, transportation, and recycling a challenge. Therefore, landfill and incineration at EoL are often employed leading to reduced landfill capacity and increased GHG emission, respectively. The current lack of recycling infrastructure and low cost of virgin plastic production from non-renewable polyolefins requires a multidisciplinary solution that works towards reduced environmental damage caused by plastic production and plastic waste [2].

This chapter brings to light an emerging blue wrap compaction machine used to recycle blue wrap. Once recycled into block form the uses are still limited

because the rPP is brittle and requires further processing to create products of value to validate their use as a secondary material. Polymer morphology developments include molecular weight tuning of a co-polymer blend that can reduce additive percolation threshold for a sudden increase of a desirable property (such as toughness) at low additive content [3,4]. However, recycled materials properties must be developed while bearing in mind the possibility of impurities or mixed fractions reducing the repeatability of their manufacture. Accordingly, a precise ± 0.05 mm deviation of FFF extrudate diameter is needed to ensure final printed parts pertain pre-determined mechanical properties [5].

5.3. Experimental

In this chapter, rPP/SEBS blend thermal properties were assessed using DSC, and flow rates were determined using MFI indexing. SEBS dispersion was imaged using optical microscopy and analysed for particle diameter for the calculation of interparticle distance to validate a sharp rise in toughness. Tensile testing and optical microscopy were carried out for non-annealed samples, and for annealed samples that had been left at room temperature (15-30 °C) for approximately four years to assess the effect of ageing on filament properties. It is important to recognise the value added by conversion to filament, hence a cost benefit analysis was conducted.

Blue wrap rPP was dry blended with SEBS G1657 for extrusion and spooling using a single screw extruder (Figure 5.1). This facilitated rubber toughening of brittle ground rPP for use as FFF filament and subsequent printing of mechanical specimens.

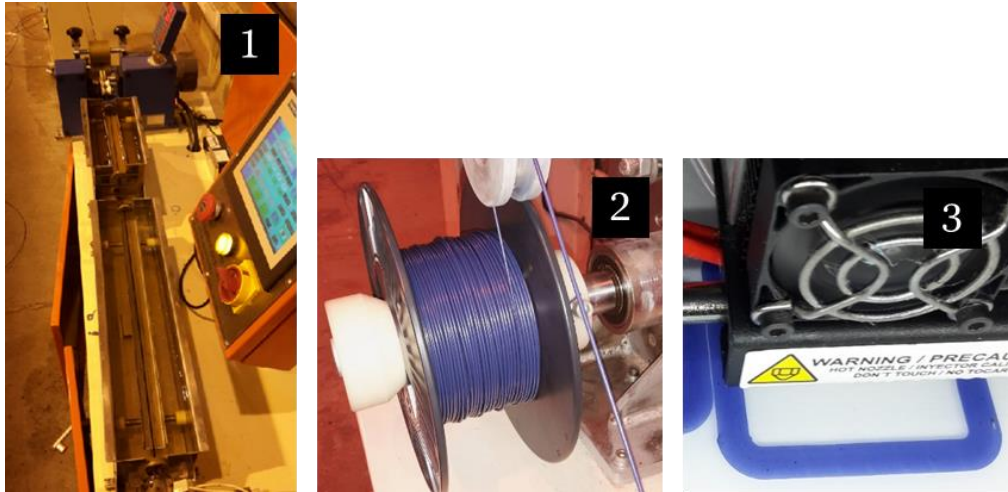


Figure 5.1. Single screw extruder showing main and tolerance displays (1), spooling of rPP/SEBS filament (2). And FFF printing with rPP/SEBS filament (3).

5.3.1. Recycled Polypropylene Blended with Styrene-Ethylene-Butylene-Styrene

Recycled hospital blue wrap polypropylene (rPP) was used to create FFF filament from a compacted block form. Granulated rPP (<5 mm diameter) produced by grinding of a recycled block of blue wrap (800 x 200 x 60 mm) in a hammer mill was supplied by an industrial partner, the Thermal Compaction Group (TCG Ltd). Compounded SEBS pellets were virgin Kraton G1675 V, and for trouser tear virgin Kraton G1643 (Kraton Polymers LLC). Both granulated rPP and SEBS were used as received and their chemical structures are presented in Figure 5.2. Spools for storing and 3D printing extruded filament made from rPP/SEBS were purchased wholesale second-hand.

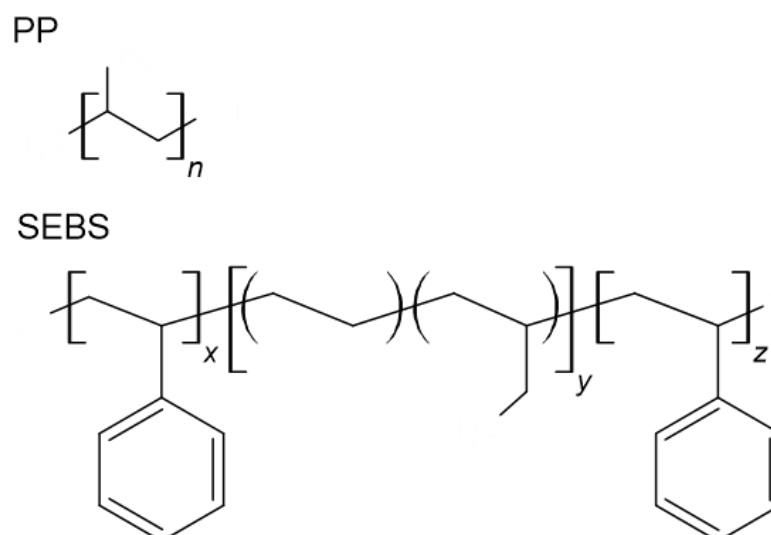


Figure 5.2. Chemical structures of isotactic PP with 'n' repeating units typically between 200-2,900, and SEBS with 'x','y', and 'z' repeating units typical between 300-1,200.

FFF printer filaments of rPP/SEBS blends were created for mechanical and financial evaluation by dry blending SEBS with rPP in the proportions indicated in Table 5.1 utilising a Songhu SHSJ-25 Mini single-screw extruder. Extruder mould temperature was set to 160 °C, cylinder temperature was 180 °C, and puller speed was 27-31 Hz and adjusted periodically to maintain 1.75 mm filament diameter.

Table 5.1. SEBS addition to rPP and wt% SEBS content in rPP/SEBS blends for analysis.

SEBS addition as % of rPP mass	wt% SEBS
10	9.1
15	13.0
20	16.7
25	20.0
30	23.1

5.3.2. Imaging of Recycled Surgical Blue Wrap Blend Morphologies

Samples for rPP and rPP/SEBS crystallite observations using visible light microscopy were made by heating filaments samples on a glass microscope

slide at 190 °C on a hot plate allowing them to melt, flow and cool to form a solid sheet. These were imaged using a Zeiss Primotech upright Reichert microscope and Matscope software, at magnifications of 100, 200 and 400x. Crystallites were observed in their spherulite formation by reflecting light from above. Spherulite diameters were measured from micrographs using ImageJ software with histograms of spherulite diameter distributions plotted for evaluation of crystallisation kinetics. Mean spherulite diameters and standard deviations are calculated for comparison from spherulite formations between samples, rPP and 9.1 wt% SEBS samples of 202 and 158 measurable spherulites, respectively.

Rubber morphologies were observed only in light transmitting mode. Samples for rubber phase observations were prepared by flattening filament 10 mm in length between two glass slides held at 190 °C for 1 minute using a HPC480 heat press machine before holding the temperature at 120 °C for 1 hour to allow the samples to crystallise. Rubber particle diameter analysis was conducted using ImageJ software from microscope images captured at 2880 x 2160 resolution using a Keyence VHX-7000. Imaged rubber particles were analysed in ImageJ with the 25 µm scale bar measured and set equivalent to 239 pixels, while ‘magnifying’ afforded the capability of measuring distance of <1 nm across pixels. This was repeated 10 times across the imaged sample surface to provide an arithmetic mean average particle diameter to calculate ligament thickness (L_c) (equation 2.12), where D_c is the critical particle diameter, β is a geometry factor close to unity, given here to be 1, and ϕ_r is the particle volume fraction [6]. Although the density of PP varies with degree of crystallinity [7], the density of G1657 SEBS and isotactic PP are both 0.9 g/cm³ so ϕ_r is 1:1.

$$L_c = D_c \{ \beta (\pi / (6\phi_r))^{1/3} - 1 \} \quad (2.12)$$

5.3.3. Differential Scanning Calorimetry

The thermal properties of rPP/SEBS blends were examined to inform on blend printability. Melting temperature (T_m), crystallisation temperature (T_c), supercooling (ΔT), and crystallinity (X_c) were measured from 10 mg filament samples by differential scanning calorimetry (DSC) using a Perkin Elmer STA6000 instrument and Pyris software. Scanning temperature was held at 30 °C for 1 minute before increasing at 10 °C/min to a maximum temperature of

250 °C, before cooling at the same rate to 30 °C. Mass change was measured by a vertical displacement balance sensor. The values for T_m and T_c were recorded as the peaks of the endotherm and exotherm plots respectively and ΔT was calculated (equation 2.10). Blend enthalpy (H_m) was compared to that of an entirely crystalline PP sample to established crystallinity (equation 2.11) where ΔH_m is the melting enthalpy of a blend sample; ΔH_m^0 is the melting enthalpy corresponding to 100 % crystalline PP (190 mW/g); and w is the weight fraction of blend rPP content [8]:

$$\Delta T = T_m - T_c \quad (2.10)$$

$$X_c = \frac{\Delta H_m}{\Delta H_m^0 * w} * 100, \% \quad (2.11)$$

5.3.4. Fused Deposition Modelling of Upcycled Polypropylene from Waste Blue Wrap

Single screw extruded rPP/SEBS filaments were printed for compression and impact testing using a Witbox 2 printer with 0.6 mm nozzle to allow for filament surface deviations. The direct extruder head design of the Witbox was selected to facilitate the printing of soft filament, e.g., higher SEBS content rPP/SEBS filament. Printing parameters for printing the rPP/SEBS filament are given in Table 5.2. A heated bed was not utilised to print the rPP/SEBS filament because the T_g of PP is around 6 °C and SEBS is around -45 °C, although packaging tape was applied to the bed to aid with bed adhesion [9,10]. The flow rate was varied between 83-87% to allow for changes in blend MFI and control extrusion rate avoiding over- or under-extrusion.

Table 5.2. Print parameters for printing rPP/SEBS filament.

Nozzle Temperature (°C)	Bed Temperature (°C)	Print speed (mm/s)	Flow Rate (%)	Infill (%)	Nozzle Diameter (mm)
190	20	30	85	100	0.6

5.3.5. Tensile Testing

A 300 Series Universal Hounsfield tensile tester was utilised for tensile testing. Three rPP/SEBS specimens of each filament blend were printed with Type 1BA dimensions for calculation of arithmetic mean and root mean square (RMS) error. Tensile testing was carried out in according to ISO 527-2:2012 using an extension speed of 5 mm/min to observe elastic and plastic regimes during elongation.

5.3.6. Impact Testing

Impact testing utilised an Instron MPX Charpy impact tester and V-notched printed samples (55×10×10 cm, with an 8 mm width at the 2 mm deep notch point). Impact energy (kJ) was calculated according to the ISO 179:2010 engineering standard. The pendulum release angle was set to 150° automatically by the machine, with the hammer striking the flat side of the samples as to observe changes to sample strength with increased SEBS content.

5.3.7. Trouser Tear for Characterisation of Interlayer Strength

Trouser tear was used as an additional strength measurement to identify the effect of rubber toughening on printed interlayer strength. Sample interlayer strength is the resistance to tearing governed by of a volume of polymer blend measured to indicate the extent of molecular diffusion between printed layers. A technique that also assesses interlayer strength is tensile testing of dog bone samples with the print orientation perpendicular to the applied force. However, the true stress is more closely measured using trouser tear due to the change in Poissons ratio associated to tensile testing of ductile materials such as PP and SEBS. The trouser tear specimen is pulled from one end while the other is stationary, creating a propagating tear originating from a pre-determined location. Hence – and unlike tensile testing – the stress field is concentrated between two printed layers directly measuring the force required to separated them.

Blends of rPP with SEBS G1643 were assessed for interlayer strength, where G1643 has a 20/80 styrene/rubber ratio that lends to higher tear strength

compared to G1657 ratio of 13/87 [11]. G1643 SEBS blends of 9.1-23.1 wt% SEBS were prepared and printed as detailed for G1657 blends in Section 2.2.3.



Figure 5.3. Trouser tear rPP/SEBS printed sample secured in a tensile machine and torn along its centreline for quantifying interlayer strength.

Extension speed was set to 180 mm/min as detailed in ISO 6383 1:2015. The sample geometry for printing and testing was 1 mm thick and 50 mm in length. A razor was used to cut the first 20 mm of the specimen down its centreline and secured in a H5KT Tinius Olsen tensile machine with a 15 mm gauge gap.

5.3.8. Flexural Testing

A 300 Series Universal Hounsfield was utilised for measuring flexural properties by three-point bending, carried out in accordance with the ISO 178:2019 standard. Bone-like samples of 80 mm length with a fixed gauge length of 64 mm were applied a negligible pre-load (>0.1 kg as indicated by the instrument) to ensure the cylindrical loading edge was touching the centreline of the sample. The speed of the crosshead was programmed to 1.5 mm/min and samples were tested to failure.

5.3.9. Melt Flow Indexing

The MFI of rPP/SEBS blends were determined using a Davenport Model 3/8I instrument with a 2.18 kg piston weight, loading 5g filament samples at a pre-heat of 140 °C before increasing and holding the temperature to 190 °C. Samples were held for five minutes in-line with ISO 1133. Melt flow index was calculated from the mass of polymer that flowed through the instrument's die (w) per minute (t) as calculated using equation (2.13) [12]. Five measurements

for each filament blend were taken with errors calculated as standard deviation (SD).

$$\text{MFI} = \frac{w \cdot 600}{t} \quad (2.13)$$

5.3.10. Cost Benefit Analysis

A cost benefit analysis was conducted in collaboration with Rhys Charles at Swansea University to gauge value added to rPP by conversion to 3D printer filament. This was done by comparison of the costs of producing the filament from granulated rPP with retail prices of commercially available PP printer filament available in the UK. The production process of surgical blue wrap rPP granulated rPP blocks upcycled into spooled FFF filament was costed: Extrusion required i) labour, ii) energy, and iii) materials costs. Spooling required: i) labour, and ii) materials costs. Labour time and energy consumption are scaled from production of 1 kg of filament to production of 15 kg/day of filament (approximately 1 block of rPP processed per day) using a 4 kW Songhu SHSJ-25mm mini single-screw extruder system with 1 kg hopper and production rate of 1 kg/hour with 1 kg of filament collected per spool for sale. All costs are converted from pound sterling (£) to US dollars (\$) using an exchange rate of 1.25 \$/£ (exchange rate on 24/03/23). Unit costs for energy, materials and labour are given (Table 5.3). CAPEX for purchase of a Songhu SHSJ-25 Mini single-screw extruder system at \$8,800 is included using a payback time of 5 years with 252 working days per year.

Table 5.3. Unit costs used in cost benefit analysis.

Cost	Description	Unit cost
rPP	15 kg block from hospitals	0.20 \$/kg
Spool	Second-hand wholesale price (300 unit order)	0.10 \$/kg
SEBS	5 kg quantities of Kraton G1675 V	2.95 \$/kg
Labour	UK average labour cost (Q3 2020) [20]	28.50 \$/hour
Energy	UK average non-domestic electricity price (Q4 2022) [13]	0.301 \$/kWh

5.4. Results

5.4.1. Thermal Analysis of Recycled Polypropylene and Styrene-Ethylene-Butylene-Styrene Blends

Results of DSC analysis present melting temperatures (T_m) of each blend that indicate thermal stability suitable for FFF (Table 5.4). A 9.1 wt% SEBS blend provides the highest T_m of 167.2 °C, with the range of 9-23 wt% SEBS blends exhibiting a narrow range of T_m (164.2-167.2 °C). These values are within a predictable range of melting temperatures for PP [14] and indicate good heat resistance and suitability to typical high temperature applications for PP where components come into contact with boiling water and steam e.g. during autoclave cycles when held at 121-131 °C [15]. Thermal properties of PP have not been compromised by the thermal recycling and polymer blending processes suggesting the rPP/SEBS blend is suitable for FFF printing of autoclavable medical products such as PPE, ventilator components, and distancing tools enabling rapid on-site production to near net shape and unique specifications by inexperienced users in hospitals during times of high demand.

Table 5.4. DSC results: thermal properties of rPP/SEBS blends.

Wt% SEBS	ΔH_m (mW/g)	X_c (%)	T_m (°C)	T_c (°C)	ΔT (°C)
9.1	50.1	23.7	167.2	126.6	40.7
13.0	36.6	16.4	165.2	128.7	36.5
16.7	30.8	13.0	164.2	126.8	37.4
20.0	28.6	11.3	165.3	128.5	36.7
23.1	35.4	13.0	165.0	126.6	38.5

A reduction in crystallinity (X_c) with increasing SEBS content is observed, with X_c more than halving when SEBS content is increased from 9 wt% to 20 wt%. Hence, increasing SEBS content results in increased amorphous structure in final printed samples most likely due to an increase in styrene groups present which disrupt the lattice structure of the non-polar PP matrix. The retention of thermal stability following SEBS addition also results from styrene which itself is of high thermal stability and enhances thermal properties of the blend via the more rigid polystyrene domains that function as nuclei and induce PP to

organise as a 3D unit at higher temperatures resulting in improved mechanical properties for tough filament [16]. A less crystalline microstructure that crystallises at a slow rate is preferred because of a low degree of warpage and lower thermal expansion [17]. Hence, increased SEBS content may reduce warpage and thermal expansion for accurately modelling end-use parts.

All filament blends underwent similar degrees of undercooling, within a 4.2 °C range when cooled at 10 °C/min, suggesting similar crystallisation rates. A small range of low T_c values across all blends results in large undercooling with mean ΔT of 38 (± 1.7) °C (Table 5.4), a substantial temperature range for controlled nucleation via annealing.

DSC of blue wrap rPP and SEBS blends show a single endotherm indicating that the blend constituents are miscible and solidify from a homogenous phase (Table 5.4). This is expected because SEBS is often used to improve the interfacial adhesion of PP blends that can feature a single endotherm at high temperatures [18,19]. However, the polar polystyrene units of SEBS results in dispersal of the SEBS from the non-polar PP phase as an amorphous microdomain upon cooling. Therefore, SEBS microdomains may be present during melting but are undetected by DSC because of their small sizes [20]. Melt phase miscibility shown by the single endotherm confirms SEBS as a promising choice of elastomer to modify thermo-mechanical properties of blue wrap rPP for FFF printing.

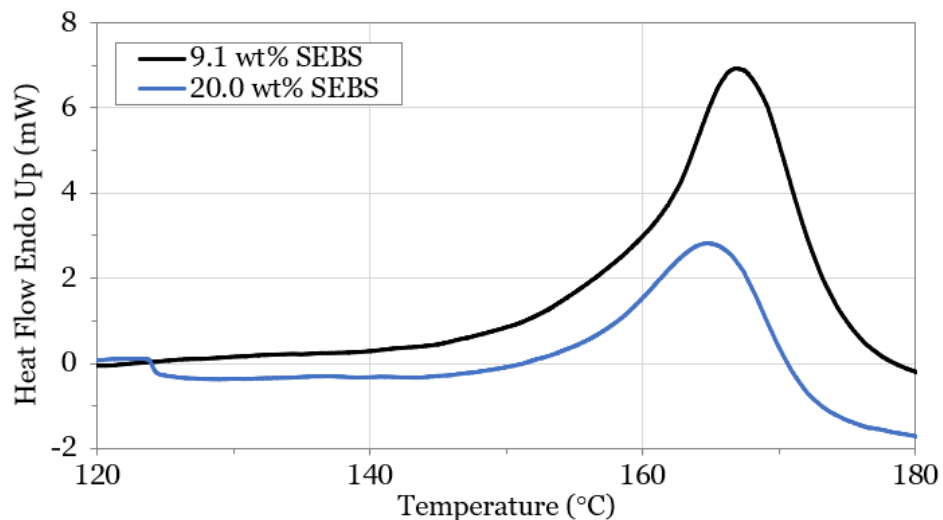


Figure 5.4. Single melting endotherms indicating miscibility of most crystalline (9.1 wt% SEBS) and least crystalline (20.0 wt% SEBS) samples held in air when heated at 10 °C/min.

Extruded polymeric material must hold a desired shape when extruded to be printed accurately. A 9.1 wt% SEBS maintains a relatively high MFI value of

103 (± 8) g/10mins, comparable to the result for granulated rPP of 104 (± 18) g/10mins (Figure 5.5), and 118 g/10mins measured from previous research by Bhat *et al* for pelletised recycled SMS fabric measured [21].

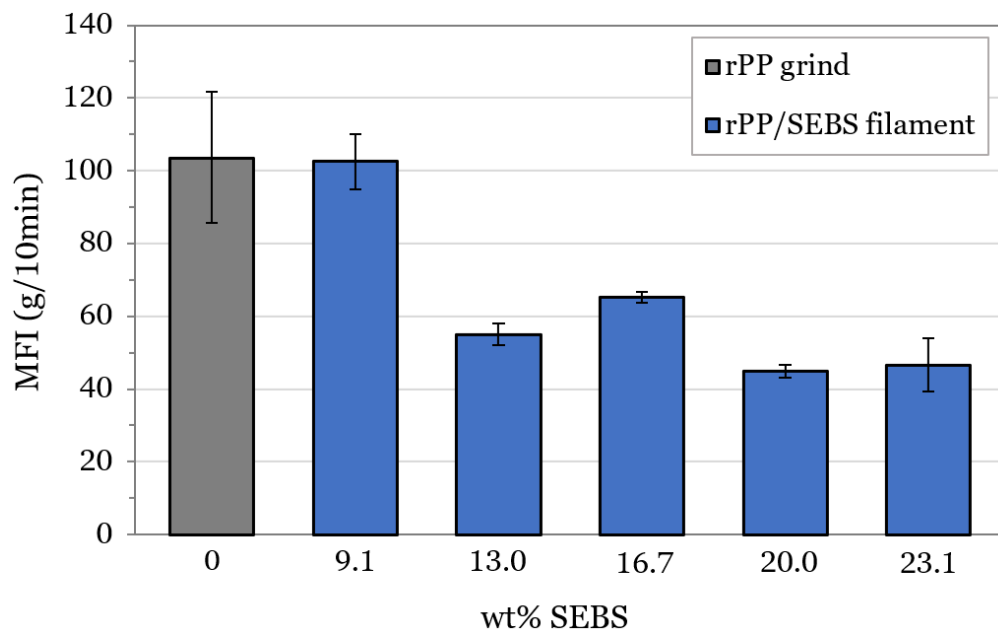


Figure 5.5. Melt Flow Indexing of rPP/SEBS blend. Error bars show standard deviation of results.

Values of MFI standard deviation from 9.1 wt% SEBS are about half those from granulated rPP, suggesting a 9.1 wt% SEBS content grants more predictable flow properties during extrusion. Although 9.1wt% blend may have a prohibitively high MFI for FFF applications, the result suggests 9.1 wt% SEBS may be a potential route to utilise rPP in injection moulding applications where MFI values of 5-100 g/10mins are suitable [22] and steady fast flow of molten plastic is important to reach far corners of a complex mould. However, injection moulding cannot achieve on site and near net shape manufacture. Further increasing SEBS content to 13-23 wt% significantly reduces MFI, ranging from 65-45 g/10mins. This confirms that blending SEBS in these quantities yields MFI more suitable for FFF printing. Such a decrease in blend MFI may be explained by an increased number of long chain SEBS molecules that when of a pure state have a MFI of only 22 g/10mins [23].

Clean rPP was incapable of maintaining a circular cross-section during single-screw extrusion so was unable to be directly FFF printed, however SEBS additions past 9.1 wt% provided extrusion control for creating filament. A minimum MFI of 45 (± 2) g/10mins is achieved at 20.0 wt% SEBS content, reducing MFI by the greatest extent, and bringing properties close to that of an ideal FFF filament. MFI standard deviation is considerably lowered in the case

of 9.1-20.0 wt% SEBS, with 16.7 wt% SEBS presenting the most reproducible flow properties and therefore enabling precise extrusion control for successful layering by FFF.

Minimising SEBS addition is important to ensure high recycled content of the filament and to minimise cost and environmental impacts from SEBS production. The observed MFI change between 9.1-13.0 wt% SEBS is a reduction from 103 (± 8) to 55 (± 3) g/10mins representing a significant drop in flow rate per mass of SEBS. A 20 wt% SEBS offered the lowest average MFI values despite 23.1 wt% SEBS containing more rubber, better offsetting rPP MFI values with less virgin content. Crystal structures and rubber particles were next observed to identify relationships between weight addition of SEBS, reduced MFI values with overall reduced MFI error, and subsequent blend printability and mechanical properties. Rubber formations were imaged paying particular attention to 20.0 wt% SEBS blend as it measured the lowest average MFI and crystallinity content. The MFI analysis demonstrates how the SMS processed wrap, once a fluid spun to make fabric, can be made compatible for stable extrusion as FFF filament.

5.4.2. Extrudate Tolerance

Figure 5.6 shows extruded filament diameter decreasing with extrusion time, peaking at a maximum diameter of 1.78 mm and a minimum diameter of 1.74 mm. The average filament diameter across 9.5 seconds of extrusion is 1.75 mm with one SD being 0.01 mm and therefore a value of four SDs is 0.4 mm which is within the generally expected industry tolerance for filament diameter of ± 0.5 mm. This indicates potential for commercial deployment of the filament, but a more complete assessment would be required using an industrial set-up with a twin-screw extruder and scaled up feed volumes.

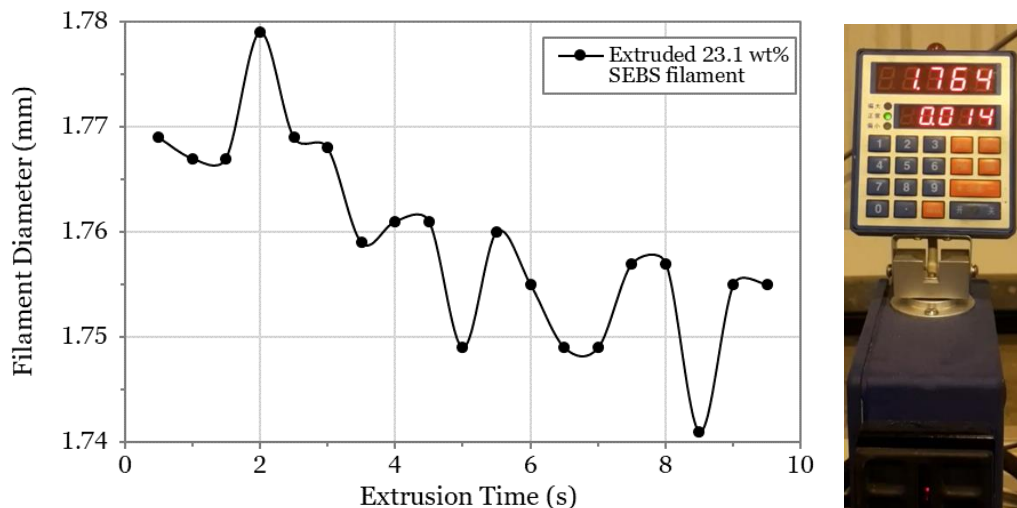


Figure 5.6. Diameter of extruded filament (left) as recorded by the laser micrometre (right).

The recycled blue wrap feedstock is not without impurities that prevented continuous 3D printing of the spool. The filament was therefore cut into 30 to 50 cm sections to be fed directly into the extruder printer head. The impurities form as lumps in the filament which can be seen in Figure 5.7. Such impurities might include dust and grit accumulated during handling, transporting, and recycling outside of the hospital. This is a problem that could dictate commercial success of the rPP/SEBS filament but has been tackled for injection moulding in the literature by using a twin-screw extruder with mesh strainer that collects impurities during processing [24].

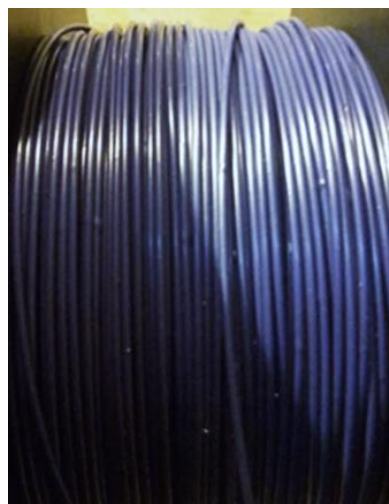


Figure 5.7. Spooled 23.1 wt% SEBS filament showing signs of recycle contamination.

5.4.3. Micrographs and Crystallinity

Spherulite size distributions measured in rPP and 9.1 wt% SEBS samples show rPP spherulite diameter range from 18.5-46.3 μm with an average of 32.8 (± 0.8) μm , while 9.1 wt% SEBS contains spherulites with wider distribution of diameters ranging from 24-53 μm and 11% larger average of 37 (± 1) μm . Once solidified, the increase in spherulite size between rPP and 9.1 wt% SEBS suggests that SEBS blends will be of lower tensile strength.

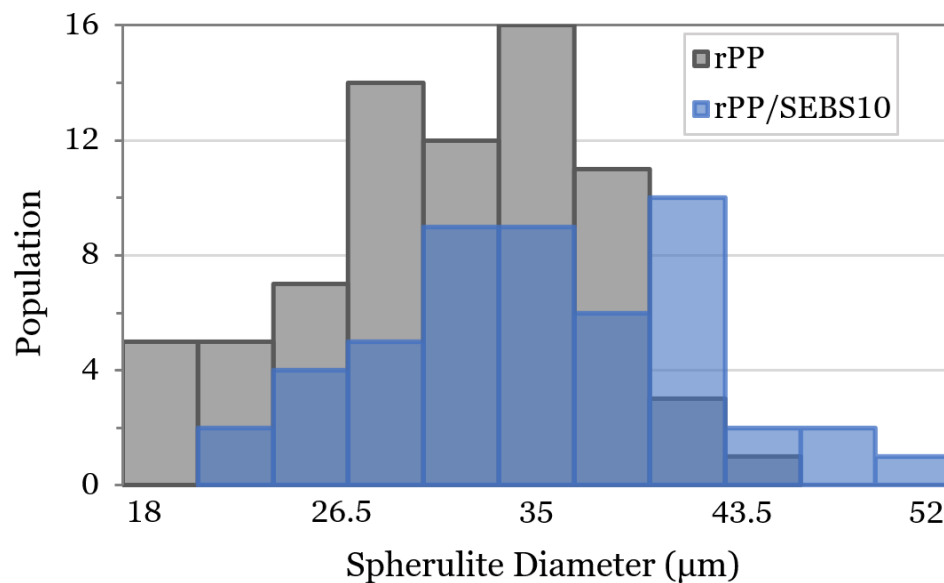
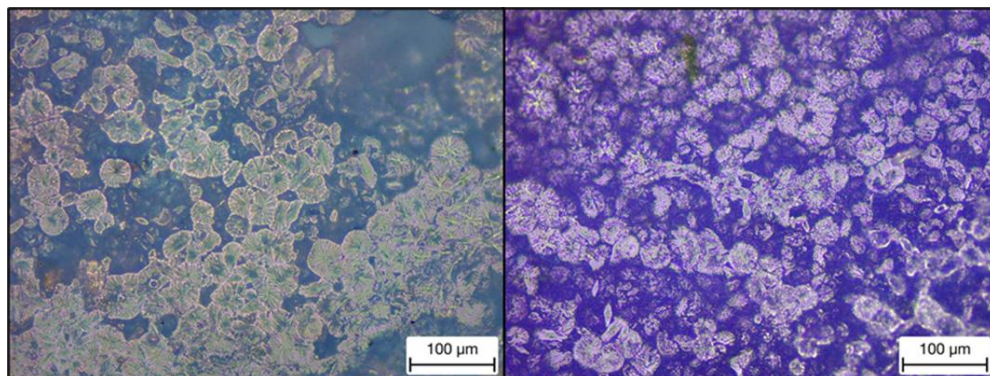


Figure 5.8. Optical micrographs of rPP and 9.1 wt% SEBS samples (top) and their spherulite diameter dispersions (bottom) measured using ImageJ.

The 9.1 wt% blend features spherulite formations with well-defined interspherulite hyperbolic boundaries where the crystallites impinge upon one-another (Figure 5.8, top). Both clean rPP and 9.1 wt% blend show birefringence typical of crystalline and amorphous material composing spherulites, suggesting the lamellae are anisotropic and contribute towards orientation of molecules. This can provide filament with ductility for spooling,

and impact toughness for wider ranging printed part utility. Differences in optical properties can be used to differentiate plastic types during automated separation processes during recycling, and so differences in refractive index may facilitate effective separation of rPP from rPP/SEBS blends in future waste management facilities.

5.4.4. Mechanical Testing and Ligament Thickness Analysis

Measured rPP/SEBS blend Charpy impact strength increased from 4.5-14.3 kJ/m² between 9.1-23.1 wt% SEBS content (Figure 5.9, bottom). Toughness only slightly increases with SEBS content up to 16.7 wt% SEBS from 4.5- 5.5 kJ/m². However, further increasing SEBS content results in more significant increases in toughness to 9.1 kJ/m² and 14.3 kJ/m² at 20.0 wt% and 23.1 wt% respectively. Blends of high amorphous content combined with the stable aromatic rings composing styrene provides high toughness. Greater relative toughness at 20.0 wt% and above may be explained by the fact that the 20.0 wt% sample is composed of closely situated SEBS phase particles that act to impede crack growth and evenly dissipate stress. The 23.1 wt% SEBS blend pertains similar impact energy to typical injection moulded commercial PP of ~12 kJ/m², from previous research of Charpy PP samples with MFI of 15 g/10min [25]. The low toughness of blue wrap rPP may be explained by the rheological requirements to create SMS blue wrap, as blue wrap was originally produced by spinning as a highly fluid PP melt, and processing often involves chain scission by mixing with pentaerythritol or peroxides [26].



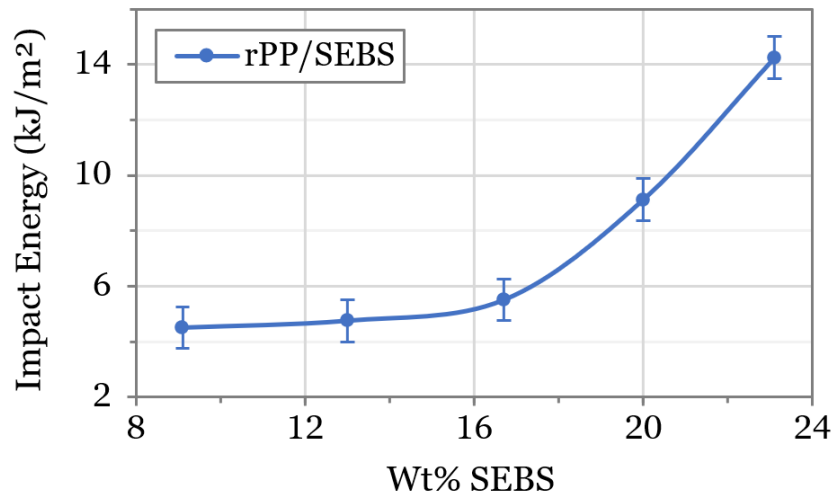


Figure 5.9. Impact energy (bottom) calculated for rPP/SEBS printed Charpy specimens of 80 mm² cross-section at the notch point (shown with fracture surface, top) with error bars given as ± 0.8 kJ machine tolerance from a blank run.

Solid fracture surfaces (Figure 5.9, top) are free of visible inclusions or cavities which confirms that printed samples form by uniform melting of interlayer boundaries, hence interlayer stress field interactions can be considered negligible. Fracture area surface roughness increases with higher SEBS content showing that SEBS increases plastic deformation of the blends. The SEBS phase may cavitate near the matrix interface that enhances impact resistance by increasing strain. Failure by matrix crazing is likely for the 9.1-16.7 wt% SEBS blends that cleave few new surfaces during fracture. However, particles that intercept cracks lead to increased matrix yielding and further delay sample bifurcation of 20.0-23.3 wt% SEBS blends.

Tensile strengths also present a brittle failure for 9.1-16.7 wt% printed rPP/SEBS blends (Figure 5.10), while a more ductile failure is achieved at 20.0-23.1 wt% SEBS (Figure 5.11).

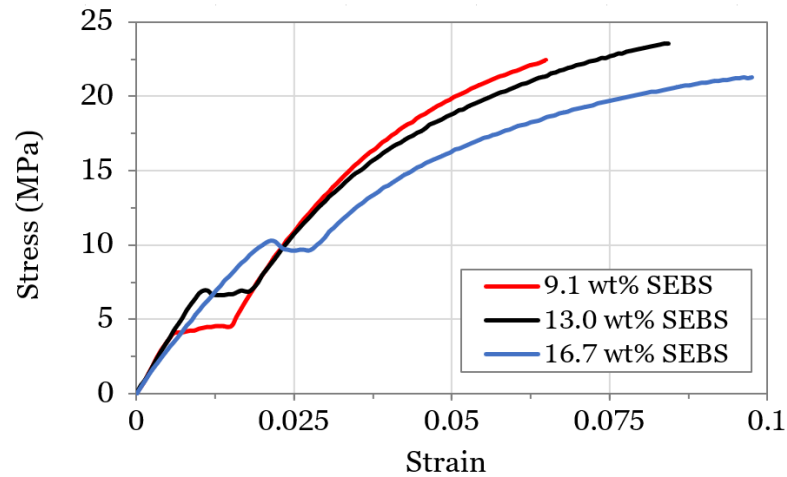


Figure 5.10. Typical brittle tensile behaviour of 9.1-16.7 wt% rPP/SEBS.

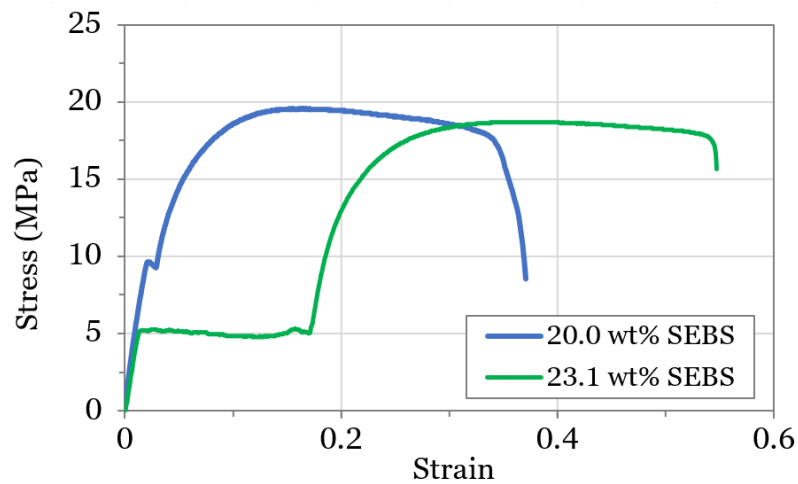


Figure 5.11. Typical ductile tensile behaviour of 20.0 and 23.1 wt% rPP/SEBS.

UTS of 9.1-13 wt% SEBS blends is similar, increasing slightly from 21.4 (± 1.1) to 22.5 (± 1.2) MPa (Figure 5.12). Further SEBS content reduces UTS to its minimum value across all samples at 23.1 wt% SEBS of 17.5 (± 1.6) MPa. The 9.1 wt% SEBS blend tensile strength is comparably low, at 19.6 (± 2.8) MPa considering the superior tensile strength of PP. This might be explained by 9.1 wt% SEBS high MFI and large MFI standard deviation causing printed samples to feature surface imperfections. Irregular viscosity causes uneven deposition of printed layers in tensile specimens that leads to local stress field formations at irregular surfaces prone to warping. Such weak points can cause premature crack formation and propagation limiting 9.1 wt% SEBS UTS. Degraded plastic from thermal recycling can be recovered through modification with elastomers such as SEBS [27], and at 13.0 wt% SEBS the highest UTS value of 22.5 (± 1.2) MPa is observed. This strength closely matches results obtained by Zander *et al* for blends of PP and polyethylene terephthalate (PET) compatibilized with

SEBS, of 23.1 (± 1) MPa [28]. Generally, an increase in both strength and toughness is atypical when toughened with an elastomer. The 9.1-16.7 wt% SEBS blends can be categorised as strong and brittle considering their reasonable UTS values with low elasticity (0.05- 0.10 strain). These lower SEBS addition blends would find use as pellets for injection moulding prioritising strength-to-weight ratio products that benefit from the high compaction and smooth surface finish.

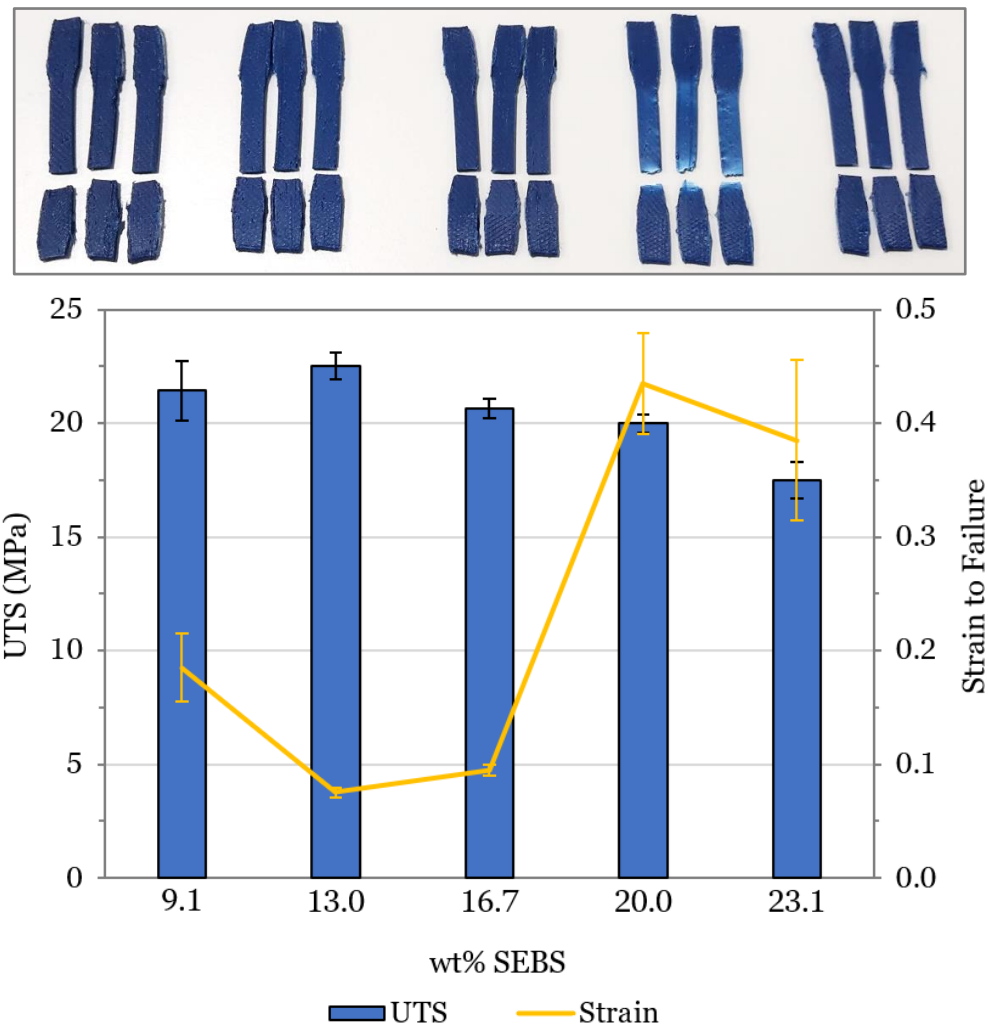


Figure 5.12. Printed and tested rPP/SEBS tensile samples (top) with stress whitened 20.0 wt% SEBS, and their measured UTS and strain to failure (bottom).

Measured 23.1 wt% SEBS samples featured a plateau after exceeding the elastic limit, at 3.3 (± 1.3) MPa, they extended 4.0 (± 0.1) mm when deforming in a state of flow stress (Figure 5.11). These early plateaus represent non-uniform strain along the sample length. Here, elastic deformation of the gauge length occurs as the sample ends undergo necking, similar to profiles shown by Setz *et al* [29]. Although all samples failed at the neck (Figure 5.12) it is only the 20.0 and 23.1 wt% samples that are ductile enough to distribute the stress

across the gauge length and significantly delay bifurcation at the neck. The 23.1 wt% SEBS blend likely undergoes a natural state of flow due to small interparticle distances capable of dispersing stress along the sample while strain hardening at the neck. As an engineering strain plateau represents hardening in the instance of true strain, the samples true strain harden during the stress plateaus. Recycled polymers do not usually display stress discontinuity due to thermal or chemical degradation during reprocessing. However, here necking provides toughness that opens potential engineering applications subject to cyclic forces, and ones that require crack termination before catastrophic and potentially costly product failure occurs.

All measured 20 wt% SEBS tensile samples featured stress whitening along their sample gauge lengths, which is visible due to incident light being diffracted by nanoscopic cracks occurring at crazed surfaces. Samples stress whitened around voids perpendicular to the axis of strain (Figure 5.13, A), and parallel to the axis of strain (Figure 5.13, B) but with two regions of layers that strain whitened to a lesser degree than neighbouring layers. All 20 wt% SEBS samples featured considerable stress whitening at their failure surfaces (Figure 5.13, C). Stress whitening pattern variations may be due inclusions in the post-consumer rPP.

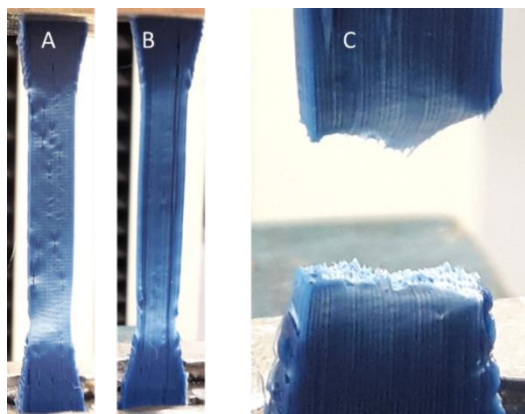


Figure 5.13. 20 wt% SEBS blend showing visible perpendicular whitening (A), predominantly parallel stress whitening (B), and ductile fracture surface (C).

Room temperature annealed (aged) 9.1-23.1 wt% SEBS blends were also assessed for tensile strength and strain to failure (Figure 5.14). Annealing is possible due to a lower than room temperature T_g of both polymers that facilitates the formation of crystalline regions from amorphous regions. The strain to failure of 9.1 wt% SEBS was 0.19 (± 0.03) which shows no noticeable change to non-annealed samples. However, annealed 13.0 wt% SEBS was 2.5 (± 0.9) which is a 33 \times increase over non annealed. Annealing of 16.7-23.1 wt%

SEBS filament caused further pronounced increases in strain to failure of 5.1 (2.7) to 17.8 (± 1.8) of $<54\times$ increase over non annealed strain to failure. The organised annealed morphology allows for drawing to a greater extent than was observed for non-annealed 20.0 and 23.1 wt% SEBS samples.

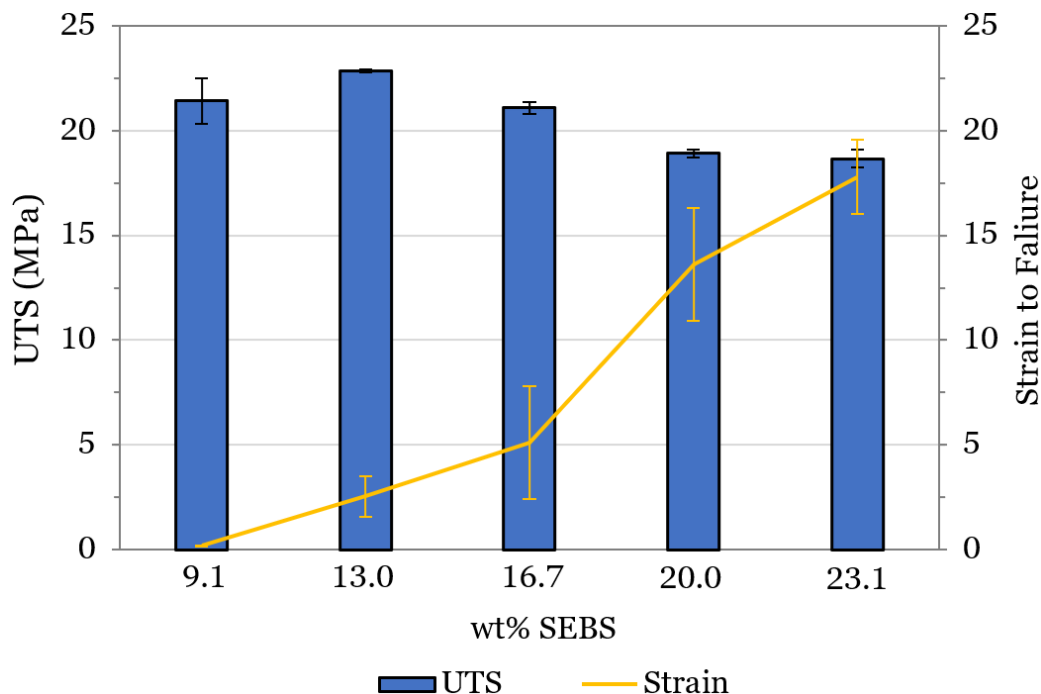


Figure 5.14. Printed annealed rPP/SEBS tensile UTS and strain to failure.

Annealed samples show similar UTS values compared to non-annealed samples, between 18.7 (± 0.1) and 22.9 (± 0.4) MPa. An increase in strain to failure and negligible change in UTS is expected when annealing thermoplastics that can lead to increased peel (interlayer) strengths [30]. UTS standard deviation error decreased for annealed 13.0-23.1 wt% SEBS blends relative to non-annealed blends suggesting more uniform morphologies developed that facilitated more accurately printed samples.

Cold drawing plateaus at 15 MPa occurred in the case of 16.7, 20.0, and 23.1 wt% SEBS samples while the 23.1 wt% gradually strain hardened (Figure 5.15). Drawing at 15 MPa s achieves a continuously aligning PP matrix, from isotropic lamella with styrene domains transferring force via sliding to a formation of thin microfibrils. A coalescence of spherical particles into microfibrils during cold drawing has been known to occur when above the T_g of the reinforcing component [31]. This can allow for improved rubber toughening compared to non-annealed samples, opening new potential added-value applications that require toughness. Final part FFF filament, or other rPP/SEBS products made using pellets, can be annealed without sacrificing

UTS. These include common load bearing applications such as handles and fixtures, and shatter proof items from medical trays to phone cases. This would be made more reliable with further work investigating annealing at elevated temperatures to replicate room temperature aging at faster annealing rates.

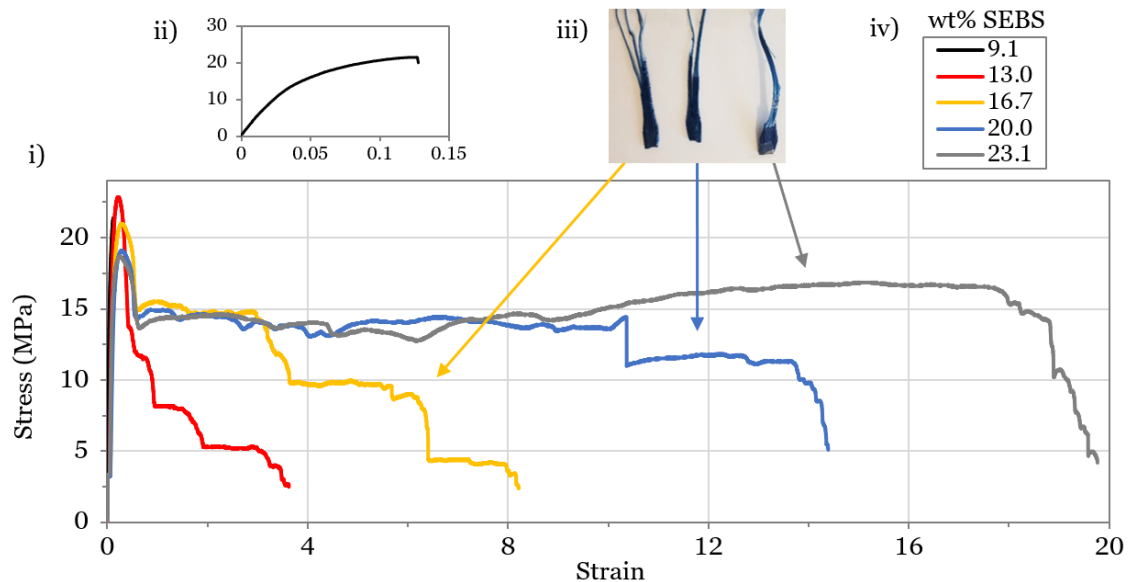


Figure 5.15. Typical drawing behaviour of measured annealed 9.1-23.1 wt% SEBS samples (i), close-up of 9.1 wt% SEBS for clarity (ii), samples showing parallel interlayer failure of tensile 16.7, 20.0, and 23.1 wt% SEBS samples (iii), and key for graphs (iv).

Grouped printed rPP/SEBS tensile sample layers split from one-another during elongation that caused sharp dips in stress (Figure 5.15). Elongation caused a significant reduction of annealed sample thickness when extending to lengths of up to 20× the original sample length. Lower contact areas between intact layers reduces interlayer bonding strength that eventually, depending on the SEBS addition, separates into multiple strands that continue to draw molecules to the direction of force. Therefore, weak regions of 13.0, 16.7, and 20.0 wt% SEBS samples failed but did not cause catastrophic failure of the whole sample, which kept extending. Only the 9.1 and 23.1 wt% SEBS did not split and failed as one gauge length indicating that SEBS could increase interlayer strength but is influenced by its ratio.

The trouser tear method used to separate printed layers and quantify interlayer bond strength of annealed blends show an increase from 2.9 (± 1.3)-5.3 (± 1.4) N/mm with SEBS addition (Figure 5.16). Two SEBS grades were assessed to observe any change in tear strength with styrene/rubber ratio, of which the G1643 of 20/80 is stronger than the G1657 of 13/87 ratio. Blends with SEBS G1643 content show between 8.2 (± 1.8) and 10.0 (± 3.7) N/mm tear

resistance that is a 1.9 and 2.8× increase in force over G1657 SEBS content. Therefore it is a 7% increase in styrene that provides significant added resistance to interlayer failure, which is a typical failure point for 3D printed parts. A stonger bond between rPP/SEBS G1643 printed layers extends not only the possible applications of the final filament product but also life-in-service potentially minimising associated lifecycle GHG emissions.

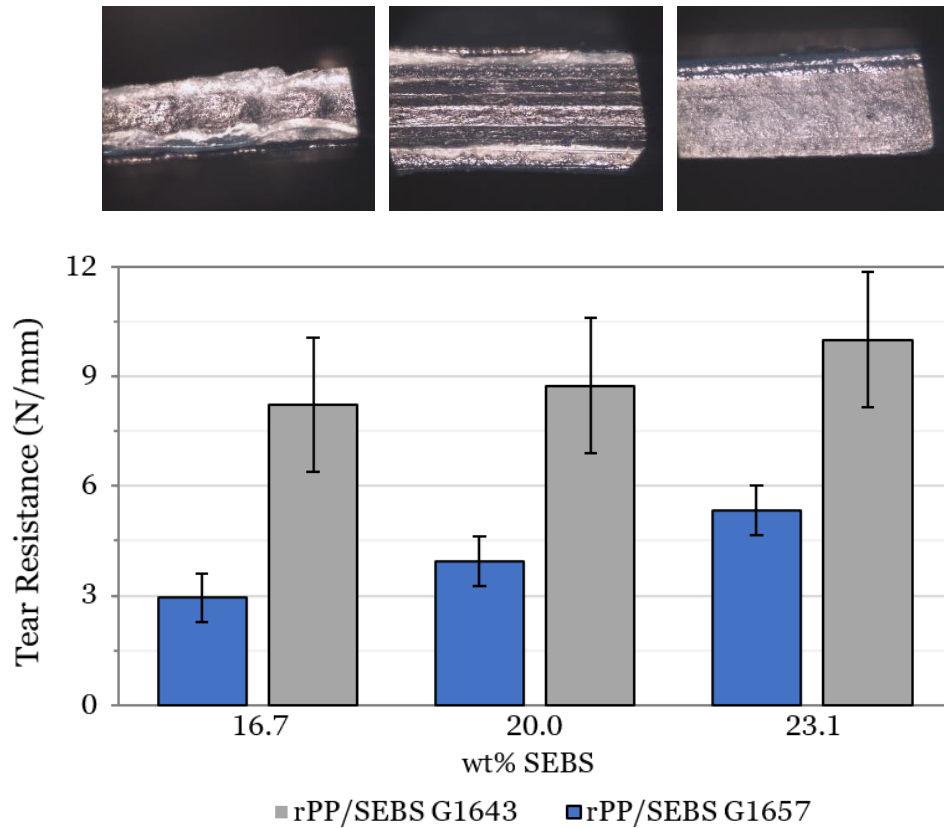


Figure 5.16. Trouser tear failure surfaces of the annealed 16.7, 20.0, and 23.1 wt% G1657 SEBS samples (top), and tear resistance of both G1657 and SEBS grades (bottom) with error bar height given as 1 SD.

Tear resistance increases with wt% SEBS content peaking at the highest assessed blend of 23.1 wt% SEBS possibly owing to a morphology of increasingly overlapping SEBS particle stress volumes that increase plastic deformation. Trouser tear failure surfaces show an uneven surface at 16.7 wt% and possible signs of thin films peeling at the perimeter compared to a more even and flat profile at 23.1 wt% SEBS. Note that the 16.7 wt% sample shows the most reflective surface and appears to feature bands perpendicular to the direction of tearing that may indicate intermittent crack growth. Whereas the 23.1 wt% sample is a flat surface and the SEBS content may have facilitated greater strain and a more continuous applied force to a blunted crack tip.

Enhanced ductility observed from impact, tensile, and tear resistance testing potentially derives from increased SEBS phase cavitation, and increased matrix deformation via stress volume sphere coalescence. Heat pressed annealed and non-annealed rPP/SEBS (G1657, G1643 was only investigated for tear resistance) morphologies of 16.7-23.1 wt% SEBS films were assessed using optical microscopy showing particle distributed from single screw extrusion, printing, and heat pressing (Figure 5.17). Images of non-annealed films show at least some agglomeration whereas annealed samples are of a more uniform SEBS spherical particle distribution.

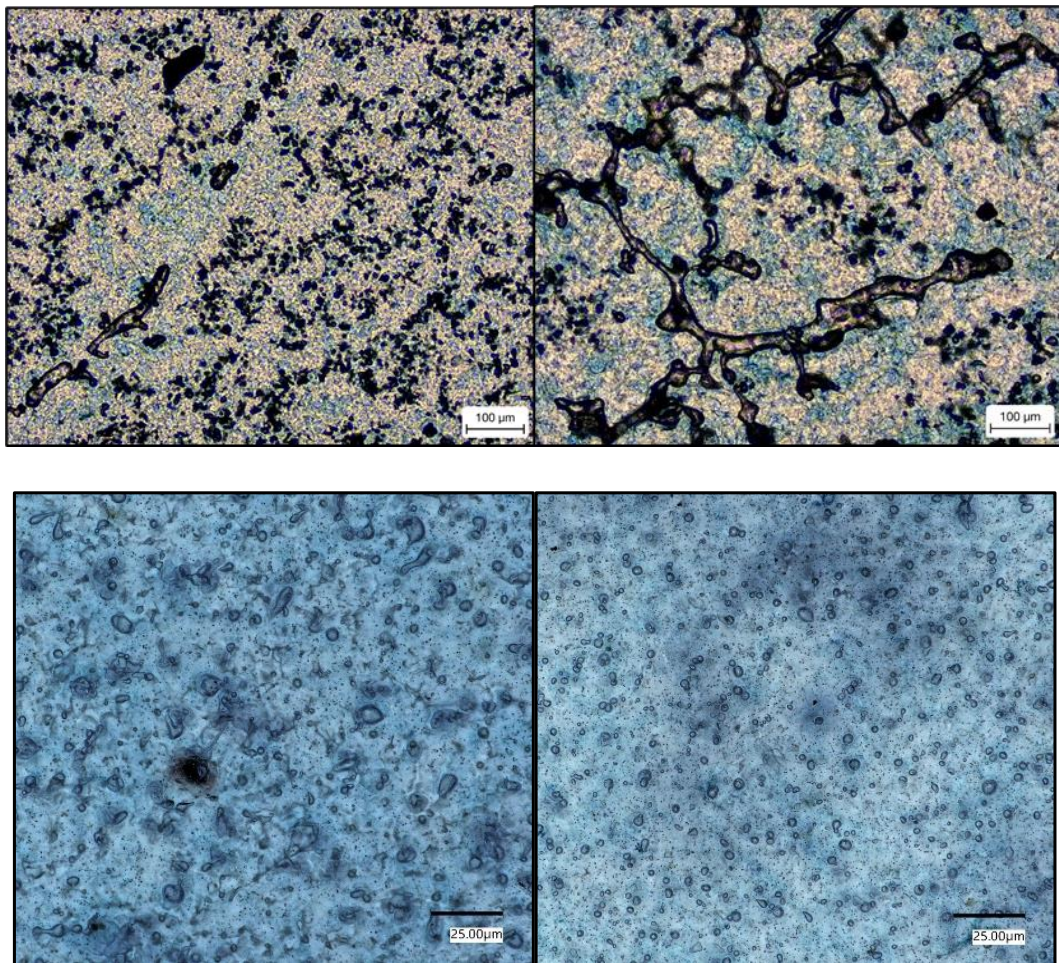


Figure 5.17. Rubber particles composing 20.0 wt% (top left) and 23.1 wt% (top right) non-annealed rPP/SEBS blends. Annealed 16.7 wt.% SEBS (bottom left) and annealed 20.0 wt% SEBS (bottom right).

Matrix ligament thicknesses of the SEBS blends were calculated using ImageJ measured particle diameters to quantitatively rationalise differences in rPP/SEBS morphology and explain a significant elastic yield increase observed from 0.1 (± 0.01) at 16.7 wt% SEBS to 0.43 (± 0.05) strain at 20.0 wt% SEBS content. The matrix ligament thickness decreased as SEBS additions increased

from 16.7 to 23.1 wt% SEBS (Table 5.5). SEBS particles across blends peaked in size in the case of 16.7 wt% blend, and a finer dispersion of SEBS particles composed 23.1 wt% samples. Values of particle diameter measured between 10-20 μm dropped from 13.2 (± 2.7) to 11.8 (± 1.6) μm potentially due to the van-der Waals attractions between SEBS microphase particles growing in number and increasing the surface-tension of the matrix with increased SEBS addition. The measured critical ligament (L_c) thickness for rPP/SEBS blends is 4.7 (± 0.6) μm , if the interparticle distance between a 10-20 μm SEBS diameter range is higher than L_c then the blend is brittle, and below L_c the blend is ductile.

Table 5.5. SEBS particle diameters and calculated ligament thicknesses of rPP/SEBS blends using a lower particle diameter limit of 10 μm and upper diameter limit of 20 μm for not annealed samples (NA), and a lower particle diameter limit of 2.5 μm for annealed (A) samples, error given in brackets is SD.

Wt% SEBS	Annealed (A) or not (NA)	Particle diameter (μm)	Matrix ligament thickness (μm)
16.7	NA	13.2 (± 2.7)	6.1 (± 1.2)
20.0	NA	12.4 (± 1.6)	4.7 (± 0.6)
23.1	NA	11.8 (± 1.6)	3.7 (± 0.5)
9.1	A	4.7 (± 1.6)	3.8 (± 0.7)
13.0	A	4.1 (± 0.9)	2.4 (± 0.5)
16.7	A	4.9 (± 1.5)	2.3 (± 0.7)
20.0	A	4.0 (± 0.9)	1.5 (± 0.5)
23.1	A	3.5 (± 0.5)	1.1 (± 0.3)

The rPP/SEBS matrix ligament thickness reduces with added SEBS, from 6.1 (± 1.2)-3.7 (± 0.5) μm between 16.7-23.1 wt% SEBS, showing thicker ligaments than Stricker *et al's* value of 0.27 μm due to the imaging method used [23]. Stricker *et al* measured L_c using transmitting electron microscopy (TEM) to observe SEBS particles of 10-20 vol% in a PP matrix of ≤ 20.5 MFI and showed that L_c decreases with increased SEBS addition, and increases with lowered MFI. The ligament thickness decreasing with SEBS further validates its use in blending with the rPP from blue wrap and can assist in offsetting the production of virgin PP that often does not require toughening. The rPP/SEBS

blend can be quickly assessed for matrix ligament thickness using optical microscopy to determine toughness for a given application.

As mentioned earlier, annealed 13.0-23.1 wt% SEBS blends feature notable cold drawing in tension, hence a value of L_c can be taken from annealed 13.0 wt%. The ligament thickness of these blends is below L_c due to aging, a slow relaxation of the morphology and distribution of SEBS. The L_c of annealed and non-annealed samples is the same value; however, it is represented here using particle diameter limits that change according to image resolution. It is recommended that the range of particle diameter limits is given if a strategy of identifying a brittle to ductile failure mode using optical microscopy for L_c calculation is to be employed in further work. The actual L_c is lower than either $4.7 (\pm 0.6) \mu\text{m}$ or $2.4 (\pm 0.5)$ and is typically identified using higher resolution imaging.

Cold drawing in tension is the most intuitive example of the mechanical data presented in this chapter to discuss the influence of ligament thickness. At the elastic limit, plastic deformation via spherulite destruction occurs, with molecules orientating along the axis of strain, increasingly re-aligning from a spherulite structure to a more ordered fibrous one. Plastic deformation of the new structure then develops by fracture of the lamella and formation of microfibrils [32]. The fibre structure then undergoes continual collapse via sliding. Here, depending on blend ligament thickness, the duration of sliding of short chain lengths of rPP is significant due to a greater quantity of ductile and well dispersed SEBS molecules that delocalises stresses across spherulites. Interfibrillar tie molecules, that is elongated amorphous material between crystals, limit longitudinal sliding that leads to cavitation, critically sized cracks, and catastrophic failure. Hence the presence of SEBS of ligament thickness $<4.7 (\pm 0.6) \mu\text{m}$ measured between a $10\text{-}20 \mu\text{m}$ likely delays morphology transformation by elongation to a position of maximum compliance.

rPP/SEBS blends cannot be separated back into the original counterparts as they have become intimately mixed and van-der Waals interactions bond the PP to the alkyl portion of the SEBS polymer [33]. Therefore, by blending these two polymers the newly formed material must be critiqued as to not reduce the utility of the highly recyclable rPP granules. SEBS is a TPE that can be polymerised at a variety of molecular weights and MFIs, and like PP it generally pertains a low glass transition and high melting temperature, meaning SEBS will not significantly subtract from the recyclability of rPP. Furthermore, SEBS is known to act as a thermoset at room temperature due to

the styrene block forming hard domains that resemble physical crosslinks. In this context, non-annealed 20 wt% SEBS or annealed 13.0 wt% SEBS represent optimal blends as they can be considered ductile with reasonable UTS, with low MFI and crystallinity for enhanced utility as FFF printer filament.

5.4.5. Cost Benefit Analysis

The costs of production of rPP/SEBS filament ranges from 14.10-14.48 \$/kg depending on SEBS content when 15 kg/day are produced at a rate of 1 kg/hour (Figure 5.18). A breakdown of these costs is given (Table 5.6). Sale of this filament in 1 kg quantities would result in an approximate cost-benefit of ~30 \$/kg if sold at the lowest price identified for commercially available PP filament at this time (~45 \$/kg), accepting that costs of grinding rPP are yet to be factored into the overall cost benefit. This indicates that production of rPP/SEBS filament would generate significant added value over the hospital produced block rPP.

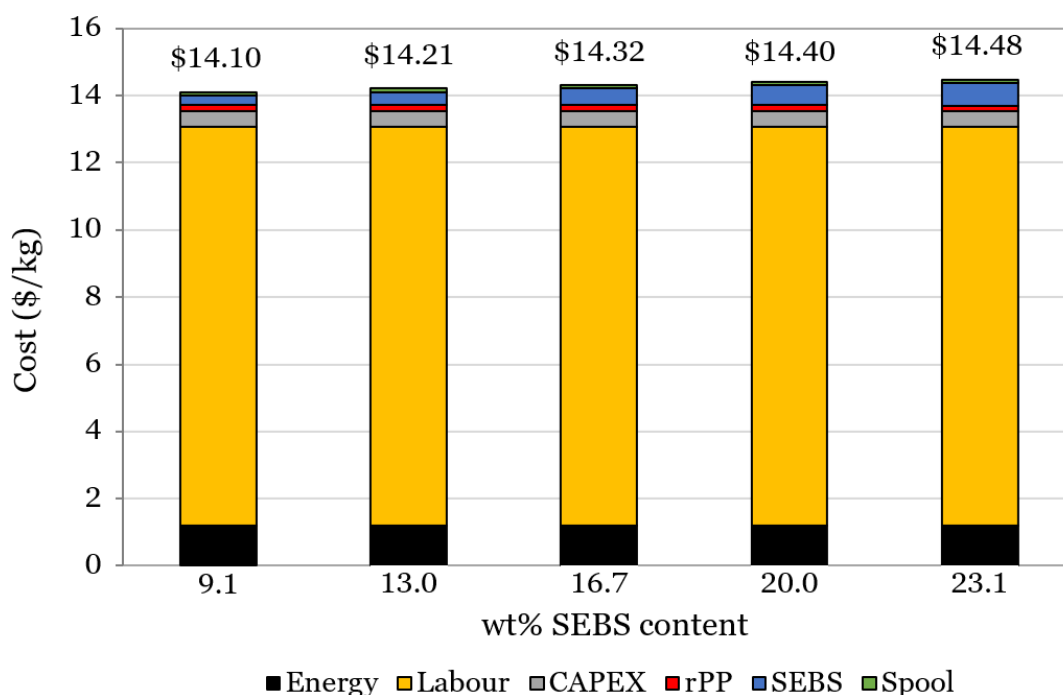


Figure 5.18. Per kg costs of producing rPP/SEBS filament at a rate of 1 kg/hour.

Labour accounts for most of the cost (82-84%), with materials accounting for 4-6%, and energy and CAPEX accounting for 8-9% and 3%, respectively. Materials costs increase with SEBS content, with SEBS accounting for 49-73% of materials costs, and 2-5% of overall costs.

Table 5.6. Cost breakdown for production of 15 kg per day of 1.75 mm rPP/SEBS filament at a rate of 1 kg/hour with a Songhu SHSJ-25mm extrusion system.

SEBS content (wt%)	Cost (\$/kg) (% of total)							Total
	Energy	Labour	CAPEX	Materials				
				rPP	SEBS	Spool	Total materials	
9.1	1.21 (9%)	11.87 (84%)	0.47 (3%)	0.18 (1%)	0.27 (2%)	0.10 (1%)	0.55 (4%)	14.10
13.0	1.21 (9%)	11.87 (84%)	0.47 (3%)	0.17 (1%)	0.39 (3%)	0.10 (1%)	0.66 (5%)	14.21
16.7	1.21 (8%)	11.87 (83%)	0.47 (3%)	0.17 (1%)	0.50 (4%)	0.10 (1%)	0.77 (5%)	14.32
20.0	1.21 (8%)	11.87 (83%)	0.47 (3%)	0.16 (1%)	0.59 (4%)	0.10 (1%)	0.85 (6%)	14.40
23.1	1.21 (8%)	11.87 (82%)	0.47 (3%)	0.15 (1%)	0.68 (5%)	0.10 (1%)	0.93 (6%)	14.48

The UK cost of labour is relatively high compared to OECD average so potential exists to increase the viability of processing in other countries with lower labour costs [34]. The labour intensity of the process is mainly attributed to time spent monitoring the process and adjusting parameters to ensure product remains on spec (40% of total labour time), and weighing and mixing materials to refill the hopper on the system (39% of total labour time). It was necessary to fill the hopper in 500 g quantities to maintain a homogenous product due to the high quantity of fines in the ground rPP received which migrate to the bottom of the hopper during extrusion. This necessitates two batches of rPP/SEBS to be weighed, mixed, and fed to hopper per kg of filament produced. Better control of particle size during grinding of the brittle rPP blocks could potentially eliminate the problem of fines. Automated blending of materials to produce greater quantities of homogenous rPP/SEBS to fill the 1 kg hopper on the Songhu SHSJ-25mm extruder could considerably reduce labour costs associated with weighing and mixing materials, and half the number of times the hopper needs re-filling. Savings at higher throughput are associated with reduced labour time spent at the system monitoring and maintaining spec per kg produced and greater energy efficiency at higher throughput. The SHSL-25mm system has a maximum throughput of 2 kg/hour so potential exists to double production rate. Larger systems capable of 20 kg/hour are also available which may be considerably more energy efficient, increase output with little increase in labour cost and reduce CAPEX per kg of filament produced considerably.

Hospitals utilise SMS PP globally for sterilisation wrap and items such as face masks, curtains, and clothing. The proposed approach to upcycling is an opportunity to keep such PP in the economy while improving polymer properties for applications demanding toughness. Such an approach will enable health services to provide a continuous local supply of secondary material from their waste plastics. This has yet to be achieved nationally because low density fabrics are not readily recycled by traditional methods. Furthermore, by creating FFF filament from granulated blocks via the 'Sterimelt' it is feasible to manufacture customisable and intricate parts printed on-site at low cost while at the same time generating environmental benefit through waste prevention. Applications for the filament range from hobbyist modelling, to shatter proof customisable (customer specific ergonomics) phone casing, to more industrious ones such as car interior parts, and military repairs such as drone casings that require remote and quick replacement.

Most NHS hospitals still implement a linear waste economy where low density wrap that is often contaminated is placed into bags and transported for disposal despite there being a profitable alternative. Contamination, cost of collection and sterilisation, and minimal recoverable value are likely barriers to recycle such waste, however, the alternative method utilising a 'Sterimelt' compacts uncontaminated blue-wrap and other PP items on-site.

5.5. Conclusions

Hospital blue wraps made of PP are used globally for sterilisation measures but are disposed of after a single use, creating waste emission when burned or sent to landfills. This thesis chapter presents a method to convert the former waste stream blue wrap into added value FFF filament through toughening with SEBS. Here, mechanical and rheological properties of blue wrap rPP have been established for application as FFF filament. The rPP granules are insufficient to create FFF filament from directly, however UTS values for 13 wt% SEBS as-printed tensile samples measure 22.5 (± 1.2) MPa suggesting accurate printed layers and sufficient interlayer adhesion. Interlayer strength is drastically owed to the styrene content of the 16.7-23.1 wt% SEBS with values of tear resistance reaching 10.0 (± 3.7) N/mm. A 13 wt% SEBS blend represents a lightweight and strong blend while elongation of non-annealed blends is minimal up to 20 wt% SEBS content whereby a sudden increase to

43 % elongation occurs that correlates to a representative critical ligament thickness of $4.7 \pm 0.5 \mu\text{m}$. Ligament thickness is determined using optical light microscopy and ImageJ analysis and calculated using particle diameter limits that depend on resolution.

The equivalent elongation of 20.0 wt% SEBS when annealed at room temperature for about four years shows a $<54\times$ increase over non annealed strain to failure. Negligible change of printed sample UTS was observed between annealed and non-annealed filaments. Impact toughness increases with SEBS addition and the non-annealed 23.1 wt% SEBS blend measures $14 (\pm 0.8) \text{kJ/m}$ which matches that of virgin PP with literature values for PP being 12kJ/m . Comparing the rPP granules and 9.1 wt% SEBS spherulite diameters shows an increase from $32.8 (\pm 0.8)$ to $37.0 (\pm 1.0) \mu\text{m}$ which works to toughen the material during deformation. Optical properties are also influenced by crystallinity that can benefit sorting and recovery of rPP grades at designated facilities.

Considerable thermodynamic miscibility occurred at a molecular level as shown by a single melting exotherm measured using DSC. Large undercoolings of $38 (\pm 1.7) ^\circ\text{C}$ are achieved between all rPP/SEBS blends, which is useful for controlled nucleation, minimised part shrinkage, and tuning of mechanical properties during cooling. MFI values suggest a blue wrap rPP/SEBS blend is best fitted for injection moulding. However, MFI is reduced from $103 (\pm 8)$, which is unstable extrusion, to $45 (\pm 2) \text{g}/10\text{mins}$ between 9.1 wt% and 20 wt% SEBS. From observing all SEBS stabilised blends, a recommended MFI for rPP used as FFF filament is $\leq 65 \text{g}/10\text{mins}$.

Blending rPP recycle from blue wrap with SEBS costs between 14.10 to 14.48 \$/kg to convert to FFF filament showing a promising avenue to generate potentially high profit margin given the cost to granulate and extrude filament. The cost of producing the filament will depend significantly on the price of labour and throughput rate, while the cost of spooling and secondary material is less significant. Hospitals globally can transition to circular practices of remanufacturing their blue wrap as a secondary raw material printer filament feedstock, which in turn can go on to be printed into various on-site tools and fixtures that saves money (or generates a profit), avoids environmental emissions, and creates collaborative job opportunities along the new products value stream. Wider impacts may be considered for further work by the simple conversion of rPP/SEBS extrudate conversion into pellets for injection moulding of sterilisable day-to-day objects.

5.6. References

- [1] H.K. Shinn, *et al*, Segregation for reduction of regulated medical waste in the operating room: A case report, *Korean J Anesthesiol.* (2017).
- [2] S.M. Al-Salem, *et al*, Recycling and recovery routes of plastic solid waste (PSW): A review, *Waste Management.* 29, (2009)
- [3] X.R. Sun, *et al*, Effect of phase coarsening under melt annealing on the electrical performance of polymer composites with a double percolation structure, *Physical Chemistry Chemical Physics.* 20, (2017)
- [4] P. Wang, *et al*, Sandwich-structure styrene-butadiene-styrene block copolymer (SBS)/polypropylene (PP) blends: The role of PP molecular weight, *J Mater Res.* 34, (2019)
- [5] M. Iqbal Mohammed, *et al*, A Low Carbon Footprint Approach to the Reconstitution of Plastics into 3D-Printer Filament for Enhanced Waste Reduction, (2017)
- [6] P. Wersin *et al*, Modelling bentonite-water interactions at high solid/liquid ratios: Swelling and diffuse double layer effects, *Appl Clay Sci.* 26, (2004)
- [7] K.E. N'Tsoukpoe *et al*, A review on the use of calcium chloride in applied thermal engineering, *Appl Therm Eng.* 75, (2015)
- [8] A. Charles *et al*, Down-facing surfaces in laser powder bed fusion of Ti6Al4V: Effect of dross formation on dimensional accuracy and surface texture, *Addit Manuf.* 46, (2021)
- [9] D. Mäder, *et al*, Glass Transition Temperature Depression of Elastomers Blended with Poly(propene)s of Different Stereoregularities, *Macromolecules.* 32, (1999)
- [10] L. Wang, J. *et al*, Thermal properties of spray-dried cellulose nanofibril-reinforced polypropylene composites from extrusion-based additive manufacturing, *J Therm Anal Calorim.* 136, (2019)
- [11] H. Veenstra, *et al*, Co-continuous morphologies in polymer blends with SEBS block copolymers, *Polymer (Guildf).* 40 (1999)
- [12] L.T. Sin, *et al*, *Overview of Poly(lactic Acid)*, Elsevier, (2013)
- [13] BEIS, Quarterly Energy Prices UK October to December 2022 and annual data for 2022, (2023).
- [14] P. Mishra, *A Text Book of Fibre Science and Technology*, 2000.
- [15] M.S. Hossain, *et al*, Treatment of Clinical Solid Waste Using a Steam Autoclave as a Possible Alternative Technology to Incineration, *Int J Environ Res Public Health.* 9, (2012)
- [16] F.O.M.S. Abreu, *et al*, SBS and SEBS block copolymers as impact modifiers for polypropylene compounds, *J Appl Polym Sci.* 95, (2005)
- [17] M. Spoerk, *et al*, Material extrusion-based additive manufacturing of polypropylene: A review on how to improve dimensional inaccuracy and warpage, *J Appl Polym Sci.* (2020)
- [18] H. Veenstra, *et al*, Co-continuous morphologies in polymer blends with SEBS block copolymers, *Polymer (Guildf).* 40, (1999)
- [19] S. Samsudin, *et al*, Effect of SEBS on the Mechanical Properties and Miscibility of Polystyrene Rich Polystyrene/ Polypropylene Blends, *Progress in Rubber, Plastics and Recycling Technology.* 21, (2005)

- [20] A. Saffar, *et al*, Phase behavior of binary blends of PP/PP-g-AA: Limitations of the conventional characterization techniques, *Polym Int.* 65, (2016)
- [21] G. Bhat, *et al*, Conversion of Recycled Polymers/Fibers Into Melt-Blown Nonwovens, *Polym Plast Technol Eng.* 38, (1999)
- [22] BAE Systems plc, Material for 3D Printing and a 3D Printed Device Ep 3 459 995 a1, (2019)
- [23] KRATON G1657 V Polymer - Data Document K630DDb17A, (2018)
- [24] B. van Straten, *et al*, Surgical waste reprocessing: Injection molding using recycled blue wrapping paper from the operating room, *J Clean Prod.* 322 (2021)
- [25] B. Ozcelik, Optimization of injection parameters for mechanical properties of specimens with weld line of polypropylene using Taguchi method, *International Communications in Heat and Mass Transfer.* 38, (2011)
- [26] Q. Ni, *et al*, Microstructure and properties of polypropylene/glass fiber composites grafted with poly(pentaerythritol triacrylate), *Journal of Polymer Research.* 18, (2011)
- [27] E. Matei, *et al*, Predescu, C. Pantilimon, A. Pica, C. Predescu, Recycled Polypropylene Improved with Thermoplastic Elastomers, *Int J Polym Sci.* (2017)
- [28] N.E. Zander, *et al*, Recycled polypropylene blends as novel 3D printing materials, *Addit Manuf.* 25, (2019)
- [29] S. Setz, *et al*, Morphology and mechanical properties of blends of isotactic or syndiotactic polypropylene with SEBS block copolymers, *J Appl Polym Sci.* 59, (1996)
- [30] S. Fakirov, *et al*, Contribution of coalescence to microfibril formation in polymer blends during cold drawing, *Journal of Macromolecular Science, Part B: Physics.* 46, (2007)
- [31] F. Stricker, *et al*, Influence of rubber particle size on mechanical properties of polypropylene-SEBS blends, *J Appl Polym Sci.* 68, (1998)
- [32] A. Peterlin, Molecular Model of Drawing Polyethylene and Polypropylene, *J Mater Sci.* 6, (1971)
- [33] K. Ragaert, L. Delva, K. Van Geem, Mechanical and chemical recycling of solid plastic waste, *Waste Management.* 69, (2017)
- [34] OECD, Unit labour costs (indicator), (2022)

**Chapter 6. Lightweight and
Bone-Like Epoxy Matrix
Composites Characterized
using Drilling and
Mechanical Testing**

6.1. Chapter Summary

This chapter is concerned with the application of thermosetting polymer composites for sustainable applications that justify their often resource intensive manufacture and challenging recyclability. The aim is to develop customisable bone-like epoxy composites for surgical training and education. Additives selected for biomimicking include polyethylene (PE) fibres, glass (GF) fibres, Jasmonite AC730 gypsum (GY, i.e, calcium sulphate, CaSO_4), and hydroxyapatite (HA). The composites are developed by quantitative analysis of drill force, compression, and flexural tests. Two drill rigs were designed and used for drilling, one utilises a tensile machine and the other utilises a pillar drill. Images are captured for qualitative analysis of sharp and blunted surgical drill bit cutting edges, and drilled hole and swarf formations of bone-like samples. Pig tibia bone is used as a reference for drilled and imaged phantoms. Results show composite porosity, additive combination, drill bit sharpness, and drill spindle speed and feed rates effect biomimicking potential. A proof-of-concept bone model for surgical training and education is manufactured using FFF and moulding of the most bone-like composite.

6.2. Introduction

A growing concern to surgical care is that graduates do not consistently achieve the required skill set to transition from resident surgeon training to surgical practice, which threatens to increase rates of surgical error [1–3]. One well proven approach that maximises technical skill acquisition is simulation based surgical education [3]. Pre-operative surgical planning and patient education often employs 2D images from computed tomography (CT) scans that limit pathology identification by visual estimation, which represents another source of surgical error [4]. Tactile training options include cadavers that are challenging to source and cause ethical implications [5]. Cadaveric bones are impractical due to storage time deterioration causing a risk of infection. Collagen degrades post-mortem that increases bone stiffness and decreases bone toughness as compounded by water loss [6]. Conversely, haptic bone models are made from inert polymers that offer a reliable substitute for cadavers in the operating theatre, particularly when models are composed of biomimicking materials [7].

Haptic bone models can be used for augmented reality simulations that enhance touch and visual feedback. Practice procedures that use augmented haptic models can be stopped, sped up or slowed down to maximise the acquisition of knowledge. CT and x-ray scanning is used to create patient specific 3D models that can be 3D printed [8]. Printed models are anatomically accurate due to recent progress in computation, slicer software and meshing parameters, and in addition can be printed onsite with short lead times [8–10]. 3D printing haptic bone models aims to mimic bone, which is a natural composite having evolved its complex hierarchical cortical and trabecular morphology over millions of years.

Cortical bone strength is anisotropic due to a hierarchical pore and mineral composed structure (Figure 6.1) of relatively high resistance to compression force but low resistance to shear [11]. Bone tensile strength is typically between 95-117 MPa, and modulus of elasticity is between 1.2-2.8 GPa which is about 60% of bones compression strength [12,13]. Cortical bone flexural strength ranges from 30-330 MPa that decreases with porosity of <15% and correlates with age [14,15].

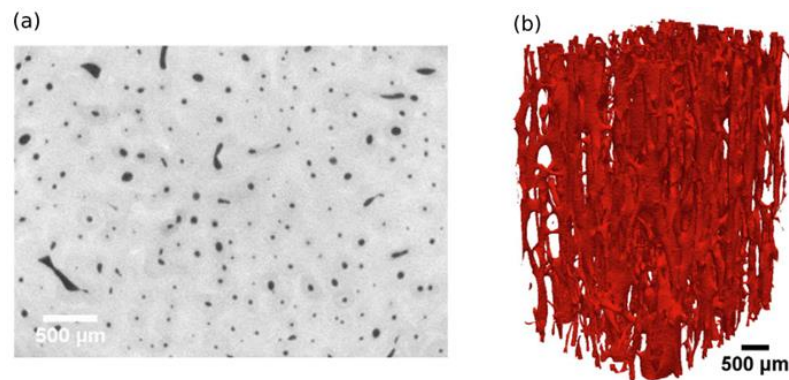


Figure 6.1. Cross section of cortical bone scanned using synchrotron radiation μ CT showing a distributed pore and mineral network (a), and a 3D rendering of the network after binarization of the volume (b) [16].

Drilled chip characteristics are influenced by the mechanical properties and thermal conductivity of bone, with inadequate drill parameters capable of causing localised cell death. R. Pandey *et al* showed that minimal bone damage occurs at 40 mm/min feed rate and 500 rpm spindle speed by using multi-response process optimization [17]. M. Akhbar *et al* proposed a 0.175 mm/rev feed rate and 50 rpm spindle speed for thermal osteonecrosis prevention that reduced maximum temperatures by >19% over previous bone drilling parameter investigations [18].

Human bone exhibits time dependant ductile and brittle behaviour [19]. Drilled bone thrust and cutting forces are well covered in the literature [13,15,20–25] but analysis of drilled force profiles often does not include the study of failure mode with respect to time dependency (viscoplasticity and viscoelasticity). Considering bone is quasi-ductile and exhibits viscoelasticity, it is important to analyse at a range of deformation rates to understand bones full range of mechanical properties [26]. Furthermore, there has been no clear research contributions involving the design of a range of bone-like epoxy composites for distributed manufacture using FFF.

A study was conducted by Brown et al who examined high strain rates of three leading bone phantoms using quasi-static compression and a split-Hopkinson pressure bar system for biomechanical, forensic, and clinical research [27]. The authors showed that the higher density Bonesim sample was best at recreating the transverse compressive properties of cranial bone. All but the densest porous phantom samples underwent a linear elastic response under compression followed by stress drop-off, plateauing from cell collapse, and a sharp rise from densification (Figure 6.2). All composites assessed by Brown et al show strain rate dependant behaviour that was most pertinent at a strain rate of 10^3 s^{-1} .

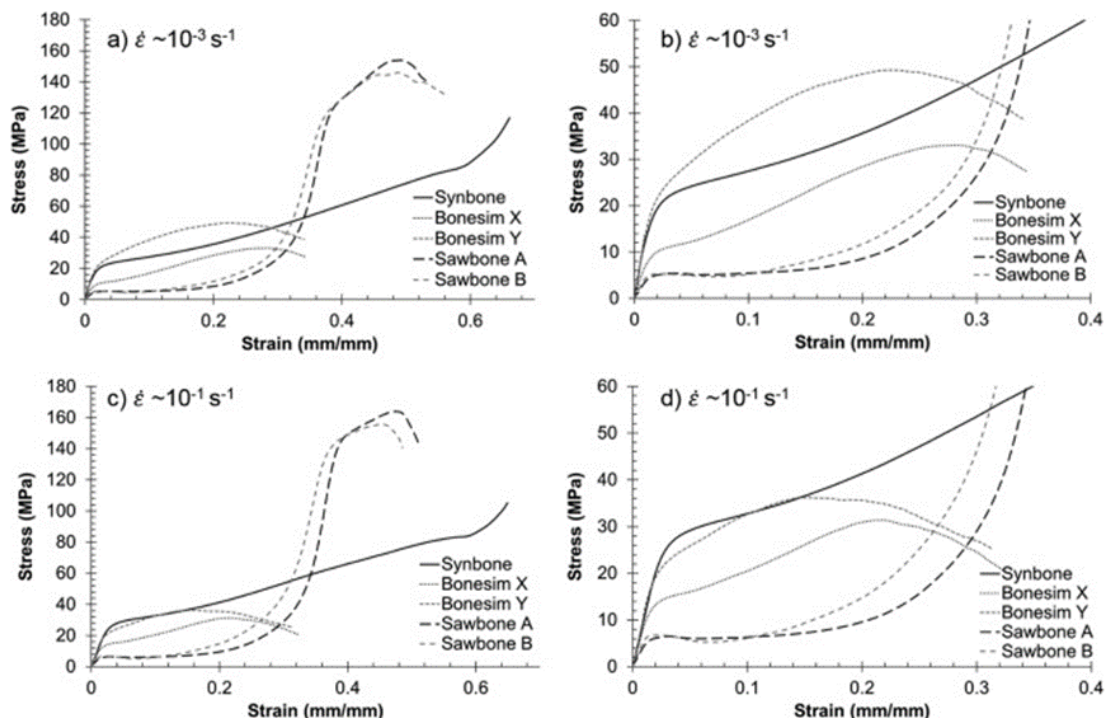


Figure 6.2. Compression stress/strain graphs of five commercial bone phantom materials at strain rates of a) 10^{-3} s^{-1} and c) 10^{-1} s^{-1} , close-up presented b) and d), respectively [27].

Customisable bone-like properties afford patient specific surgical preparation and can pertain synchronous tactility to a given patients bone [28]. Biomimicking bone often involves epoxy mixed with glass fibre reinforcement as established by Sawbones® who are current market leaders in orthopaedic training model manufacture [29]. HA is also frequently employed as it is a close approximation of mineral content of bone [30]. The molecular structure of HA and bone is mostly composed of calcium phosphate (Figure 6.3).

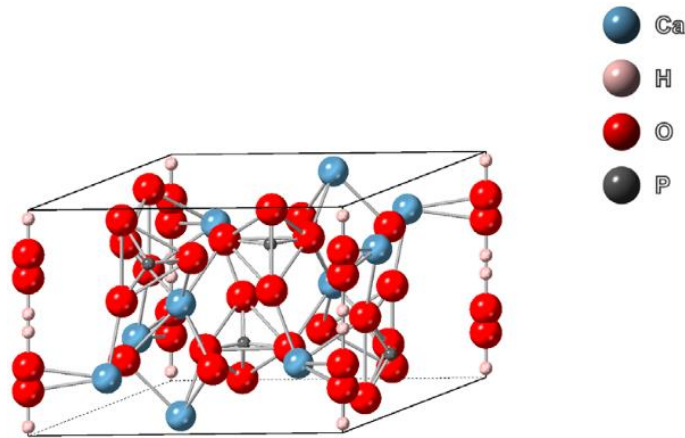


Figure 6.3. Molecular structure of HA of hexagonal crystal structure [31].

The annual supply chain of rubber polymers including epoxy resin accounts for 480 PJ of energy consumption and 16 MMT CO₂ equivalent of GHG emissions [32]. This chapter aims to contribute bone-like epoxy-based phantoms for improved medical training and reduced iatrogenic error as an example of active sustainability.

6.3. Experimental

Epoxy samples of single additive composition were prepared to understand their effect on drilling properties: 1 wt% PE, 2 wt% PE, 1 wt% GF, 2 wt% GF, 5 wt% HA, 20 wt% HA, 5 wt% GY, and 20 wt% GY as added to 100 wt% epoxy. A PE fibre was selected and tested as a viscoelastic additive to replicate the complex machinability of bone and provide an alternative to established glass fibre. PE and GF were acquired from MBFibreglass® and used as received. HA is a close approximation of bone mineral content and the selected powder of product number GL1661PHA/-45 was used as received from MO-SCI Healthcare®. Jasmonite AC730 is a commercially available gypsum-based

powder and was selected to provide an alternative to HA for bone phantom manufacture. Samples were prepared as explained in Section 2.2.4.

Single additive composite drilling employed only method 1, with spindle speed measured using a PCE-DT 50 optical tachometer. Bone-like multiple additive composites employed method 1. Bone drilling utilised methods 1 and 2 employing a feed rate of 1.3 mm/s and spindle speed of 800 rpm or 1750 rpm, respectively. Rotation and feed of the drill was stopped after breakthrough and the drill bit was lifted back through the machined hole. Drill bits were replaced every 25 holes for method 1, and for each sample for method 2 to maintain a sharp leading edge.



Figure 6.4. Method 1 drilling rig with tensile machine actuator shown drilling pig tibia bone secured in vice (left). Method 2 drilling rig with load cell drill force transducer and pillar drill actuator for drilling epoxy composites secured by machine screws.

Single additive drilling was carried out using one drill bit, with the order of drilling being HA, GF, GY, and PE. Images captured drill bit blunting and drilled sample surfaces using SEM and infinite focus microscopy. Drilled sample stiffness is calculated as the linear portion of the drill thrust force gradient that occurs up to the bite point and represents elastic deformation. Work done was calculated as the total area under the thrust force curve and represents toughness. Composite thrust force was referenced against those of pig tibia bone. Single additive composites were analysed for maximum thrust force, stiffness, and work done with the most bone-like single addition composites combined and abbreviated from Cb1 to Cb5. Cb6 is a sample made for high flexural strength application.

Drilling of multiple additive composites was carried out using one new drill bit per sample. The mechanical testing procedure employed for multiple additive

composites is given in Table 6.1, and the manufacture of a foot and ankle model for surgical training was completed using the most bone-like composite.

*Table 6.1. Composition of iterated bone mimicking epoxy composites and associated abbreviations, *numbers are wt% additions.*

Bone-like composite	Composition (%)					Abbreviation*
	PE	GF	GY	HA	Epoxy	
Cb1	1.68	1.68	12.61	-	84.03	2/2/15/0
Cb2	0.97	1.94	-	-	97.09	1/2/0/0
Cb3	0.68	-	3.42	27.40	68.50	1/0/5/40
Cb4	0.68	-	27.40	3.42	68.50	1/0/40/5
Cb5	-	-	4	16	80.00	0/0/5/20
Cb6	-	1.87	4.67	-	93.46	0/2/5/0

6.3.1. Epoxy Matrix Composite Preparation for the Development of Bone Phantoms

Virgin Epon 828 Epoxy was selected as the bone phantom matrix material to be combined with additives of either low embedded energy or well-established bone-like properties. Epon 828 has a viscosity ideal for dispersing particle additions and is routinely used for standard resin formulation and fabrication [33].

Bone sample female moulds of 60×30×3 mm were made using tin-cured silicone and laser cut acrylic male moulds secured in a glass petri-dish using a glue gun. The mould was cured for 24 hours at 60 °C before casting the epoxy samples. Low temperature epoxy release was then sprayed onto the dish and left to dry for 5 minutes to minimise adhesion of the epoxy to the petri dish. A cast thickness of 3 mm aimed to replicate cortical thickness for the comparison of measured composite compression and flexural force values with those of bone from previous research.

Composites were made in 200 g batches using two-part epoxy 828 with parts A and B combined with the intended additives. Each prepared resin composite was added to a 500 ml glass beaker and thoroughly mixed with a spatula by hand for 5 minutes before degassing for 1 minute and then left to rest and degassed again for 1 minute. Samples were left to cure at room temperature for 72 hours once cast from the beaker into the silicone mould.

Fresh tibia bone was drilled as a reference to epoxy composite bone mimicking materials to iterate drilling and mechanical properties to achieve bone-like properties. Pig bone offers a human-like alternative to human bone [34], and was acquired locally with each bone drilled within 3 days of the time of slaughter. Pig tibia bone cortical thickness was measured at 3 mm via preliminary drilling, as observed from the distance between drill bit bite-point and breakthrough. The tibia bone was selected for its geometry which is ideal for repeatable drilling of its most flat region termed the posterior or medial surface. Sourced bones were refrigerated at 5 °C before equilibrating at room temperature for 1 hour and drilled at room temperature. Pig bones along with other samples examined using drilling method 1 were fixed in a vice with the flat region faced perpendicular to the drilling axis.

6.3.2. Foot and Ankle CAD Modelling and Printing

A bone model of a human right foot by IReVans was sourced from Sketchfab and modified in Autodesk Meshmixer to be printed [35]. Tubes of 4 mm diameter were added to connect bones that compose the foot and ankle as to visually distinguish each bone while minimising the amount of filament needed to print (Figure 6.5). Tube placement was selected according to ease of printing while affording a robust design, i.e, avoiding overhands and external connections. The final watertight STL model for printing was composed of 89,000 polygons. Individual foot and ankle bones were printed to be used as male moulds for bone-like composite casting.

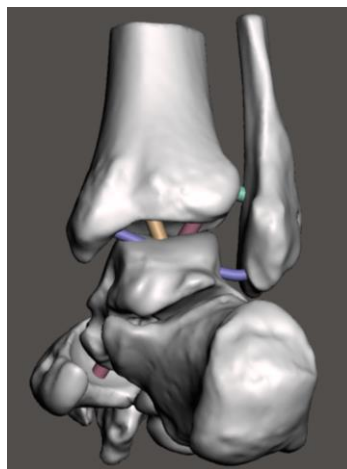


Figure 6.5. Ankle model for surgical communication modified in Meshmixer by adding coloured tubes for enhanced aesthetic and ease of 3D printing.

An Ultimaker 3 Extended was used to print anatomical models in PLA for subsequent manufacture of silicone moulds. A model of the lower foot composed of five parts was printed with a 0.15 mm layer height taking 9 hrs to print (Figure 6.6). Tin-cure silicone was poured over the PLA prints in paperboard walled moulds that once cured was filled with polymer composite resin to create bone-like anatomical models. An optimum iterated bone-like composite was cast into the shape of an upper foot (all bones above two of the five tarsal bones that represent the midfoot).

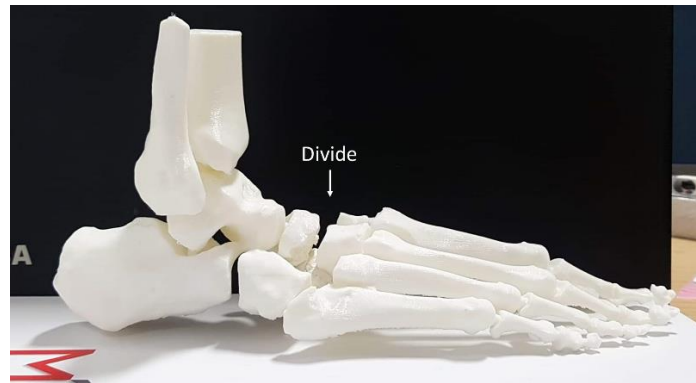


Figure 6.6. Foot and ankle model printed in PLA for 1) manufacture of female mould, and 2) visual comparison with bone-like epoxy composites.

6.3.3. Optical Microscopy of Drilled Bone-like Sample Surfaces and the Drill Bits

An Alicona infinite focus microscope in light reflecting mode was used to image drilled hole perimeters of epoxy composite samples and categorise roughness severity at 5 and 10 x magnification. Composite samples were placed horizontally with images captured and stitched at a Z-step interval of 200 nm over a total height of $\leq 300 \mu\text{m}$. Composite swarf formation is the visual chip accumulation and distribution from machining which was assessed using a digital camera. Images compared composite surfaces to those of fresh pig tibia bone swarf.

A Hitachi TM4000 benchtop instrument was used to image drill bits that had worn down by machining composite samples to describe any differences in thrust forces observed.

6.3.4. Bone-Like Composite Density Calculation

Sample density was calculated by mass and volume. Mass was measured using analytical scales, and volume was measured using callipers where length, l, width, w, and thickness, t, were measured from the centre of the sample. Void fraction was calculated by considering the theoretical density, as calculated from the collected data sheets of each additive suppliers. Void fraction is given by equation 2.14:

Table 6.2. Additive materials with quoted density from supplier data sheet.

Material	ρ_t	Ref.
Epoxy	1.6	[36]
Glass fibre	2.6	[37]
PE fibre	1.0	[38]
Gypsum	2.8	[39]
HA	3.2	[40]

$$V_f = [(\rho_t - \rho_m) / \rho_t] \quad (2.14)$$

Where ρ_t is the theoretical density and ρ_m is the measured density.

6.3.5. Drilling Procedure and Data Interpretation

2 mm diameter drill bits with 2 cutting flutes were supplied by Photon Surgical Systems (SKU: VETO-0807) and used to drill three holes (method 1) or five holes (method 2) to record standard deviation (SD) of thrust forces. Method 1 used each drill bit for 25 holes and method 2 employed a new drill bit for each sample. Pig tibia bone drilled data was recorded using method 1, and multiple additive bone-like samples were measured using method 1 and method 2 for cross comparison.

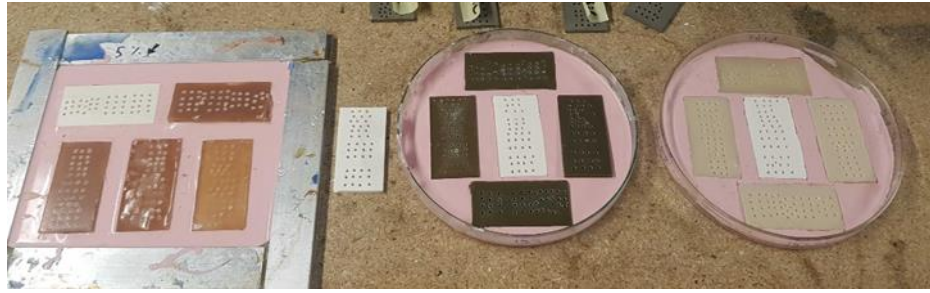


Figure 6.7. Preliminary method 1 drilling to establish toughening mechanisms and identify most and least resistant materials to drilling.

Method 1 drilling utilised a Mac Allister MSHD600 hammer drill secured in a tensile machine using two jubilee cables and an equal L-shaped angle bar. Two Jubilee cables were positioned for supporting the weight of the drill below the handle and reducing vibrations above the chuck. The bar was held in a mechanical wedge action tensile machine grip and lowered towards the sample, and the chucks slack was minimised by removing a pre-load spring and spanning the disengaged clutch with a stainless-steel washer. Method 1 facilitated bone and synthetic sample drilling because the adjustable vice width facilitated holding the uneven geometry of bone. Method 1 chip loading of composites was 2.9×10^{-4} and 3.6×10^{-4} , and between 1.4×10^{-4} and 7.1×10^{-4} for pig bone as calculated via equation 2.15:

$$\text{Chip loading} = \frac{\text{feed rate}}{(\text{RPM} \times \text{number of flutes})} \quad (2.15)$$

Where feed rate is of mm/s, spindle speed is of rpm, and number of flutes is 2.

Physico-mechanical properties were determined to iterate haptic feedback of the developed composites to become bone-like; elastic deformation was measured as the gradient of an initial linear portion of drilling curves which describes sample stiffness. Stiffness was measured via drill bit specimen contact causing a displacement of ~ 0.5 mm into the surface leading up to bite point and consequent plastic deformation.

Method 2 drill rig set-up (Figure 6.8) utilised a Bridgeport Series I 2HP pillar drill for direct measurement of thrust force, i.e., force did not transfer through the drill shaft to the transducer to quantify drilling characteristics of composites of combined additive composition. Two 5 kg load cells were fixed to an experimental aluminium module used to measure drilling thrust forces. Load cell threads were removed on their fixed sides to promote a flush contact with the aluminium module, and two 4 mm holes were drilled into each sample to secure flat sample surfaces to that of the load cells using machine bolts.

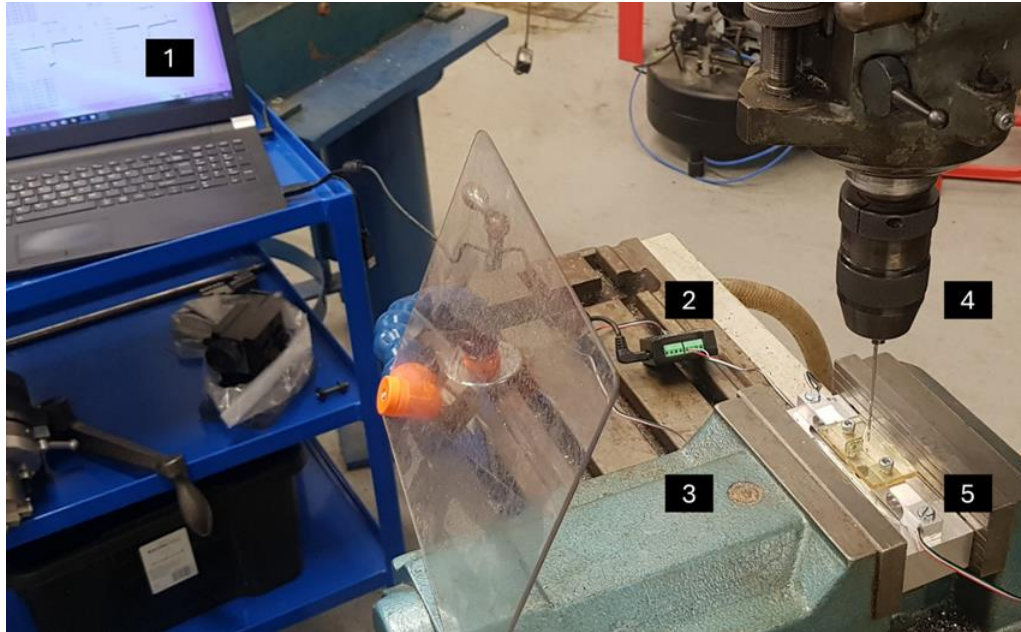


Figure 6.8. Method 2 drill rig set-up to measure thrust force from bone-like samples: data gathered (1), Arduino mini microcontroller (2), vice used to hold the aluminium module (3), pillar drill chuck (4), sample on compression load cells (5).

Bone drilling was not investigated utilising method 2 drilling due to the machining of bone that may compromise the natural geometry and hydration level of fresh bone and in turn its hoop and hydrostatic stresses. Thrust forces were relayed via a Phidget22 control panel. Force and displacement were zeroed when fitting samples to avoid error arising from vice tightening.

6.3.6. Compression Testing

A 300 Series Universal Hounsfield was utilised for compression testing according to ISO 604:2003. Bone-like composites were compression tested with an applied pre-load of $<10^{-2}$ of the peak stress, and a crosshead speed was set to 5 mm/min for compression strength and 1 mm/min for compression modulus testing. Compression samples were of 4 mm height and modulus samples were of 50 mm high, respectively. The crosshead was programmed to compress modulus samples to 0.9 peak stress after an initial test that identified peak stress. Compression strength samples were displaced by the crosshead that travelled 3 mm vertically.

6.4. Results

6.4.1. Drilling of Bone and Epoxy Composites

Single additive epoxy matrix composites were drilled at 1 mm/s feed and 1750 rpm spindle speed for the comparison of thrust force to bone which is of relatively low stiffness and work done of 16.2 (± 1.5) N/mm and 26.8 (± 2.2) N.mm, respectively (Figure 6.9). Single additive composite stiffness is between 17.7 (± 0.4) and 53.6 (± 1.2) N/mm for 5 wt% HA and 2 wt% PE, respectively, which is the gradient of the thrust force curves leading up to the bite point that occurs between 0.5-1 mm displacement. Work done drilling these samples is between 36.2 (± 1.5) and 77.0 (± 3.2) N.mm for 5 wt% GY and 2 wt% PE, respectively. All single additive polymer composites show high strength compared to bone, with 5 wt% HA and 20 wt% HA presenting the most bone-like thrust forces.

Of all samples the PE fibre epoxy composite is most resistant to drilling, which could be due to the strength of aligned PE molecules as has found application in ballistic armour [41,42]. It can be theorised that a randomly arranged PE fibre causes intermittent in-plane force loading of the PE backbone. Drilled PE work done values reach 121.6 (± 3.0) N.mm which is twice that of clean epoxy of 62.3 (± 2.2) N.mm. However, it is likely that the drill bit was most blunted when drilling PE samples as these were the last to be assessed.

GFs provides similar work done values of 101.0 (± 7.7) to GY of 96.2 (± 0.9) N.mm and since GF is harder than epoxy when machined the fibres either fracture or deform the matrix. HA is the additive least resistant to drilling and was the first assessed, hence the drill bit was least worn. The Mohs hardness of HA is 5 which is greater than that of GY of 2 further confirming that work done during drilling is dependent on shear strength as contributed by the additive, as opposed to a direct dependence on additive hardness [43].

When feed rate is increased from 1 mm/s to 1.5 mm/s work done increases more so than stiffness (Figure 6.9) which suggests chip formation by plastic deformation is more time dependant than initial elastic deformation. Work done during drilling depends on covalent bond rupture, therefore a 1.5 mm/s feed rate results in disproportionate change to plastic and elastically deformation. It should be noted that an increase to displacement before the bite-point will lead to a build-up of flexural resistance against the drill bit that propagates more quickly once the surface is penetrated.

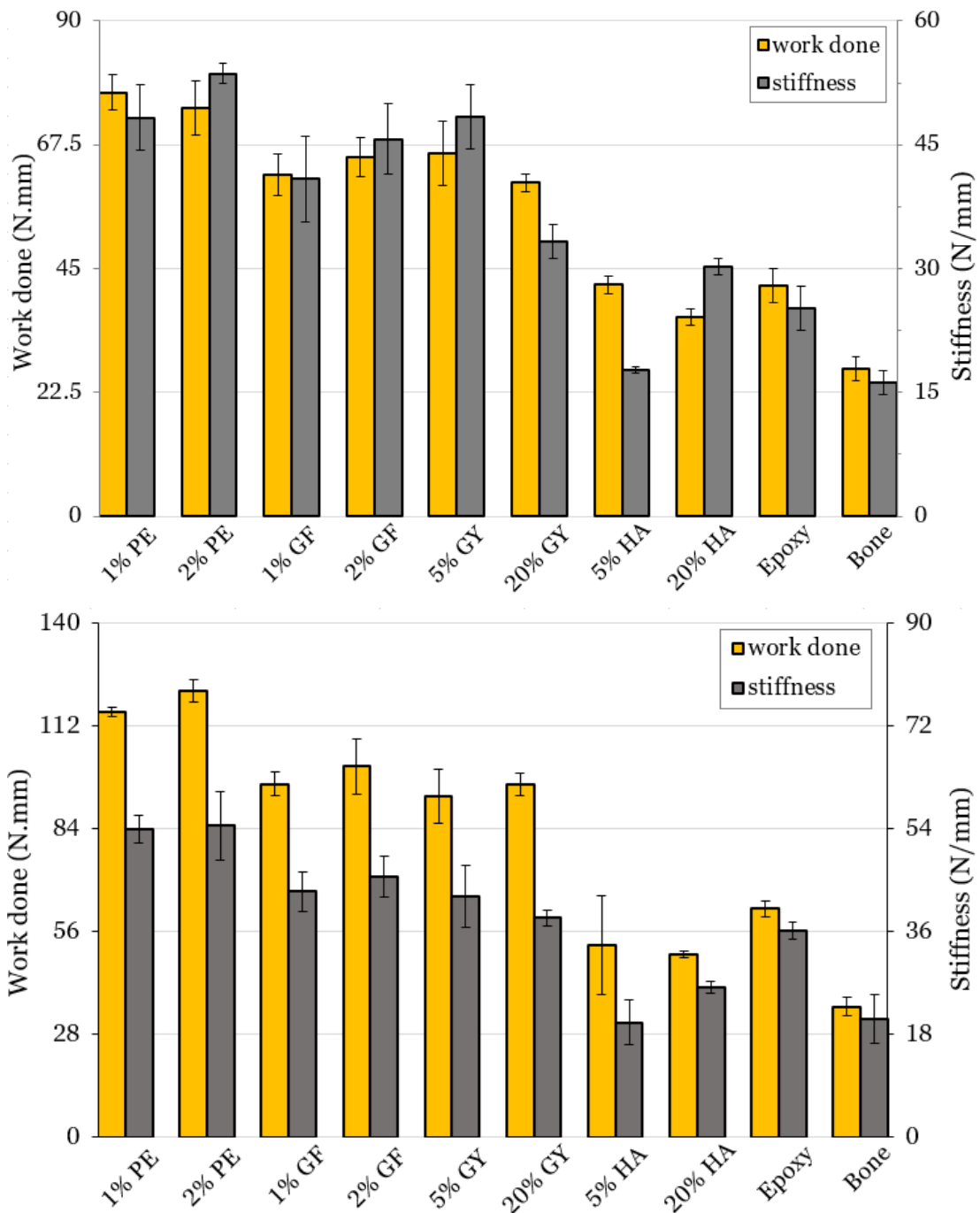


Figure 6.9. Stiffness and work done required to drill each fibre or powder containing epoxy composite presented with SD error bars, drilled at 1750 rpm and a 1 mm/s feed rate (top) and 1750 rpm at 1.5 mm/s feed rate (bottom).

All single additive samples stiffen under increased drill bit feed rate other than 20 wt% HA and 5 wt% GY that feature stiffness values of 30.2 (± 1.0) and 48.4 (± 3.9) N/mm at a 1 mm/s feed rate and 26.2 (± 1.0) and 42.2 ± 5.5 N/mm at a 1.5 mm/s feed rate (Figure 6.9). This is significant because bone is a quasi-ductile material that fractures under compression at similar stress values to its yield point, which in the case of a 1.5 mm/s feed rate was at 4.0 (± 0.2) MPa

and 4.8 (± 0.8) MPa, respectively. Yield point, fracture point, and UCS data (Table 6.3) can help inform bone tissue engineers to aid their design of related products such as bone scaffolds. Changes to stress measured between yield point and fracture point shows that all selected additives other than 20 wt% HA achieve complete stress retention under at least one feed rate. This is despite the lack of hierarchical structure that provides typical cortical bone with strain hardening potential as previously quantified using stress-strain data from uniaxial tensile testing [44].

Table 6.3. Yield point, ultimate compression strength (UCS), and fracture point data for drilled composites and pig bone drilled with a 1750 rpm spindle speed and 1 mm/s and 1.5 mm/s feed rates. SD error is given in brackets.

	Yield (Mpa)		UCS (mpa)		Fracture (MPa)		Fracture (mm)	
	1 mm/s	1.5 mm/s	1 mm/s	1.5 mm/s	1 mm/s	1.5 mm/s	1 mm/s	1.5 mm/s
1% PE	10.0 (0.8)	12.3 (0.8)	11.1 (0.7)	17.2 (0.3)	9.6 (0.9)	15.4 (0.7)	2.5 (0.1)	2.6 (0.1)
2% PE	8.3 (0.5)	15.1 (0.4)	11.0 (1.6)	16.5 (0.5)	8.4 (0.3)	15.1 (0.4)	2.7 (0.1)	2.8 (0.1)
1% GF	7.8 (0.7)	13.7 (0.4)	7.8 (0.6)	14.1 (0.1)	6.2 (0.6)	13.1 (0.2)	2.8 (0.1)	3.0 (0.1)
2% GF	7.6 (0.2)	10.1 (0.6)	8.1 (0.4)	13.7 (1.2)	7.0 (0.5)	11.5 (1.2)	2.9 (0.1)	3.0 (0.1)
5% GY	8.2 (0.3)	11.2 (1.2)	9.1 (0.8)	14.2 (1.1)	8.4 (0.7)	13.2 (0.6)	2.3 (0.1)	2.5 (0.1)
20% GY	6.5 (0.1)	11.5 (0.1)	8.1 (0.3)	13.6 (0.2)	7.2 (0.4)	13.0 (0.3)	2.7 (0.1)	2.6 (0.1)
5% HA	4.2 (0.1)	5.8 (0.9)	5.7 (0.2)	7.6 (0.4)	4.9 (0.2)	6.9 (0.2)	3.0 (0.1)	3.1 (0.1)
20% HA	4.7 (0.3)	5.8 (0.3)	4.7 (0.2)	6.5 (0.4)	3.5 (0.2)	5.5 (0.3)	3.2 (0.1)	3.3 (0.1)
Epoxy	4.8 (0.3)	7.2 (0.2)	5.7 (0.3)	8.1 (0.3)	4.2 (0.3)	6.8 (0.5)	2.8 (0.1)	2.9 (0.1)
Bone 1	2.9 (0.5)	4.0 (0.2)	3.6 (0.2)	4.9 (0.6)	3.6 (0.2)	4.8 (0.8)	2.9 (0.3)	2.9 (0.3)

All single additive sample thrust forces from 1 mm/s and 1.5 mm/s feed rates and 1750 spindle speed show similar yield and fracture stresses (Table 6.3). The highest stress retention and therefore least brittle composite is 1 wt% PE of yield point 12.3 (± 0.8) and fracture point 15.4 (± 0.7) MPa at a feed rate of 1.5 mm/s. A 20 wt% HA addition provides lowest stress retention at 1.5 mm/s, yielding at 5.8 (± 0.3) MPa and fracturing at 5.5 (± 0.3) MPa. HA lowers epoxy yield, UCS and work done values providing more bone-like properties.

The brittleness coefficient reflects a materials ability to withstand strain between the elastic limit and yield strain points [12]. However, brittleness coefficient is calculated from compression and tensile data that both employ a constant loaded area. The loaded area during drilling is only constant when the drill bit has entered the material such that it forms a circle where the drill bit diameter corresponds to the sample area under compression, hence, yield point is the correct point along the drilled curve to calculate a brittleness coefficient for thrust force curves. Brittleness coefficient cannot be obtained for thrust force curves because its calculation also requires strain corresponding to elastic limit and failure point which is derived from sample deformation – a continuous phenomenon unlike machining that requires removal of material. For this reason, resilience, hardening, and tangent modulus parameters cannot be calculated.

To improve bone-like behaviour and mimic the complex structure of bone, HA was incorporated into three composites containing multiple additives: Cb3, Cb4 and Cb5. Cb1 and Cb2 composites are intended to be lightweight and tough for potential weight saving applications. Strength remains high in the case of PE containing composites with the Cb4 showing equal work done and stiffness to the Cb1 composite despite a 40 wt% addition of GY further confirming the similar shear strengthening effects provided by GF and GY.

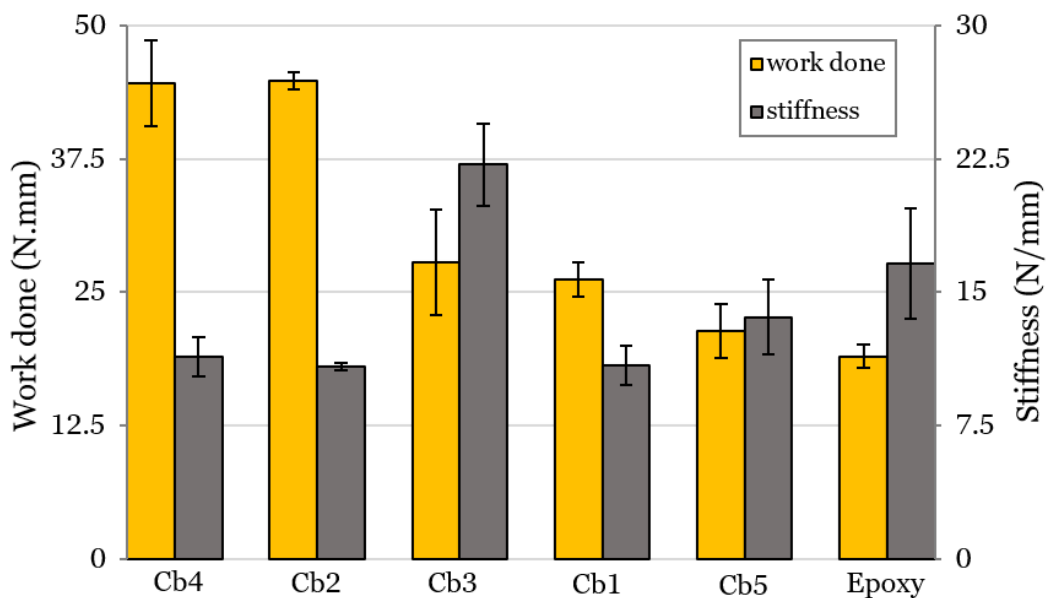


Figure 6.10. Method 2 drilled composites of multiple additive content showing work done and stiffness for each 3 mm thick sample with content formatted as PE/GF/GY/HA wt%.

Drilling using a pillar drill (method 2) employed one new drill bit per sample, drilled at a spindle speed of 800 rpm which likely caused stiffness of drilled epoxy samples to decrease by around 30% relative to work done. Yield and fracture stresses (Table 6.4) from method 2 drilling reveals clean epoxy yield and failure at 2.2 (± 0.2) MPa which is a greater stress retention than all samples except Cb2 which yielded at 4.3 (± 0.3) MPa and fractured at 4.6 (± 0.1) MPa. The multiple additive composite stress retention is low compared to those single additive composite results that could be due to sharpness of drill bit or composite structure complexity.

Table 6.4. Yield, UCS, and fracture data of method 2 drilled multiple additive Cb1-Cb5 samples. SD error is given in brackets.

	Yield (MPa)	UCS (MPa)	Fracture (MPa)	Fracture (mm)
Epoxy	2.2 (0.2)	2.6 (0.1)	2.2 (0.2)	2.6 (0.1)
Cb1	3.8 (0.7)	4.0 (0.7)	3.5 (0.4)	2.5 (0.1)
Cb2	4.3 (0.3)	6.0 (0.2)	4.6 (0.1)	2.9 (0.1)
Cb3	3.3 (0.1)	3.7 (0.2)	2.4 (0.2)	2.9 (0.1)
Cb4	6.2 (0.4)	6.5 (0.5)	4.8 (0.2)	3.0 (0.1)
Cb5	2.7 (0.4)	2.7 (0.3)	2.3 (0.2)	2.7 (0.1)

A clean epoxy sample is a reference between drilling methods 1 and 2 that shows stress retention is between 0.4 and 0.6 MPa higher when drilled using method 2 which suggests an elastic response is facilitated to a greater extent when cutting larger chips. This might explain how multiple additive samples containing GF of highest elastic modulus provides the highest stress retention.

Slipping of the drill bit during drilling is more common at increased spindle speeds and lowered chip loadings whereby heat generated can influence the mechanical properties of the additives, which also causes bone damaged during surgery. Surgical drilling spindle speed is usually set between 40 rpm and 3000 rpm with new drill bits employed for reasons not limited to ensured minimal slip and accurate cutting that generate thrust forces between 9 and 125 N [22].

Pig tibia bone was assessment using a blunt drill bit (at least 25 runs) and a new drill bit to understand whether a drop in thrust force occurring between

drilling methods is caused by drill bit blunting or a reduced spindle speed. Thrust forces from chip loadings between 2.9×10^{-4} and 4.3×10^{-4} show increased thrust force with chip size (Figure 6.11). Drill bit cutting edges are clearly rounded after ≥ 25 runs (Figure 6.12).

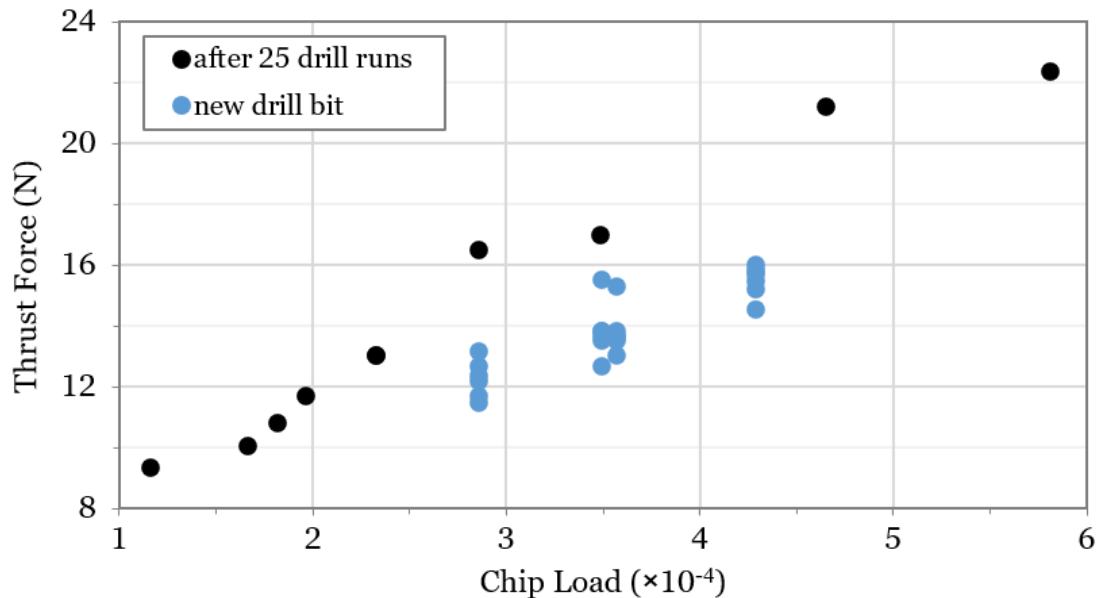


Figure 6.11. Method 1 drilled pig bone thrust forces at three chip loadings show a positive gradient and time dependence (viscoelasticity), with force between two sets of data of similar y axis intercept (zero machine rate).

Six measurements using a new drill bit provide SD error ± 0.8 N indicate an efficient machining process with minimal energy lost as friction. The grouped data from a new drill bit provides drilled UCS values of $3.9 (\pm 0.2)$ MPa, $4.4 (\pm 0.2)$ MPa, and $4.9 (\pm 0.2)$ MPa at 2.9 , 3.6 , and 4.3×10^{-4} chip loadings, respectively. Bone was drilled using a 1.3 mm/s feed rate under method 1 drilling to have comparable chip loading to method 2 drilling. A linear relationship between peak thrust force against chip loading would indicate that bone acts as plastic solid when drilled. Deviation from a theoretical linear trend is energy lost, likely as heat, which is most clear above a chip loading of 2.9×10^{-4} due to increase slip and friction. Extrapolating blunt and new drill bit trends to the Y-axis at zero chip load reveals a similar intercept (of 5.9 N if linear) where the theoretical zero machining occurs, which suggests that drill bit rounding does not affect the yield point of bone.

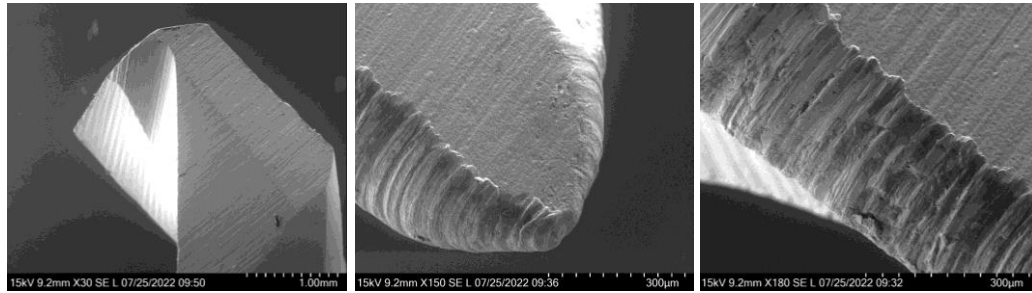


Figure 6.12. SEM of drill bit cutting edges; of unused 3.5 mm diameter bit (left) and used bit having drilled at least 25 times showing rounded tip (middle), and irregular wear of cutting edge (right).

Plastic deformation of a drill bit during cutting ≥ 25 runs shows an uneven blunt cutting edge with damage caused by hard composite additives (Figure 6.12) resulting in 10 to 30% thrust force increase (Figure 6.11). This will have increased measured single additive thrust forces compounded for PE compared to earlier drilled samples, hence PE UCS of ~ 17 MPa may be closer to that of GY and GF of ~ 14 MPa.

6.4.2. Thrust Force Profiles of Bone and Multiple Additive Composites

Pig tibia bone measured here produce thrust forces between 9-39 N when drilled at a 0.5-2.5 mm/s feed rate and spindle speeds between 3000-1350 rpm (Figure 6.13). Stress accumulation due to a compressed layered cortical bone structure causes a delay in yield point from 0.3-1 mm with increased feed rate. Drill bit break-through (sample failure) occurred between 2.3-3.7 mm displacement from the top surface and increased with feed rate. The drilled profiles show dips in force of 1-3 N that represent low density volumes where fluid content is high or mineral density is low. Free space was mimicked using particle additions for improving fidelity of bone phantoms.

Thrust forces from pig tibia bone decreased from 16-10 N with increasing spindle speeds of 1750-3000 rpm having a less severe effect on bone thrust force than feed rate (Figure 6.13). The 1350 rpm spindle speed caused a large step-up in thrust force to 49.5 N that suggests cut chips fail to exit the flute faster than they are cut, hence bone compacts in the flutes leading to clogging that increases rates of cell death failed surgical procedures [22].

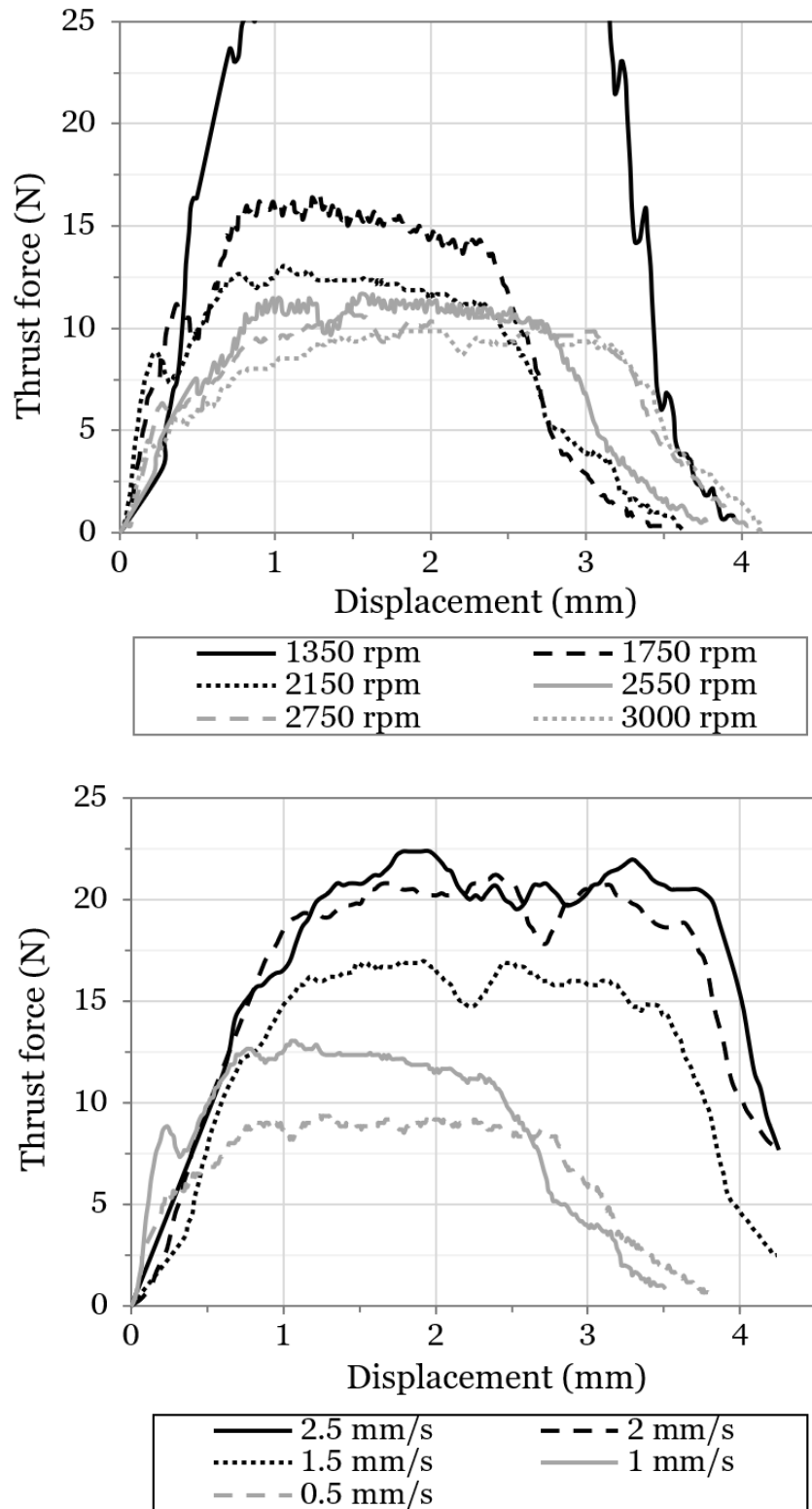


Figure 6.13. Measured pig tibia bone drilled thrust forces from 1350-3000 rpm spindle speed at 1mm/s feed rate (top), and 0.5 to 2.5 mm/s feed rate (bottom) at 1750 rpm.

Drill thrust force profiles from method 2 drilling are like those from method 1 (Figure 6.14), hence thrust forces measured using spindle speed between 800-1750 rpm can be compared across drilling methods 1 and 2.

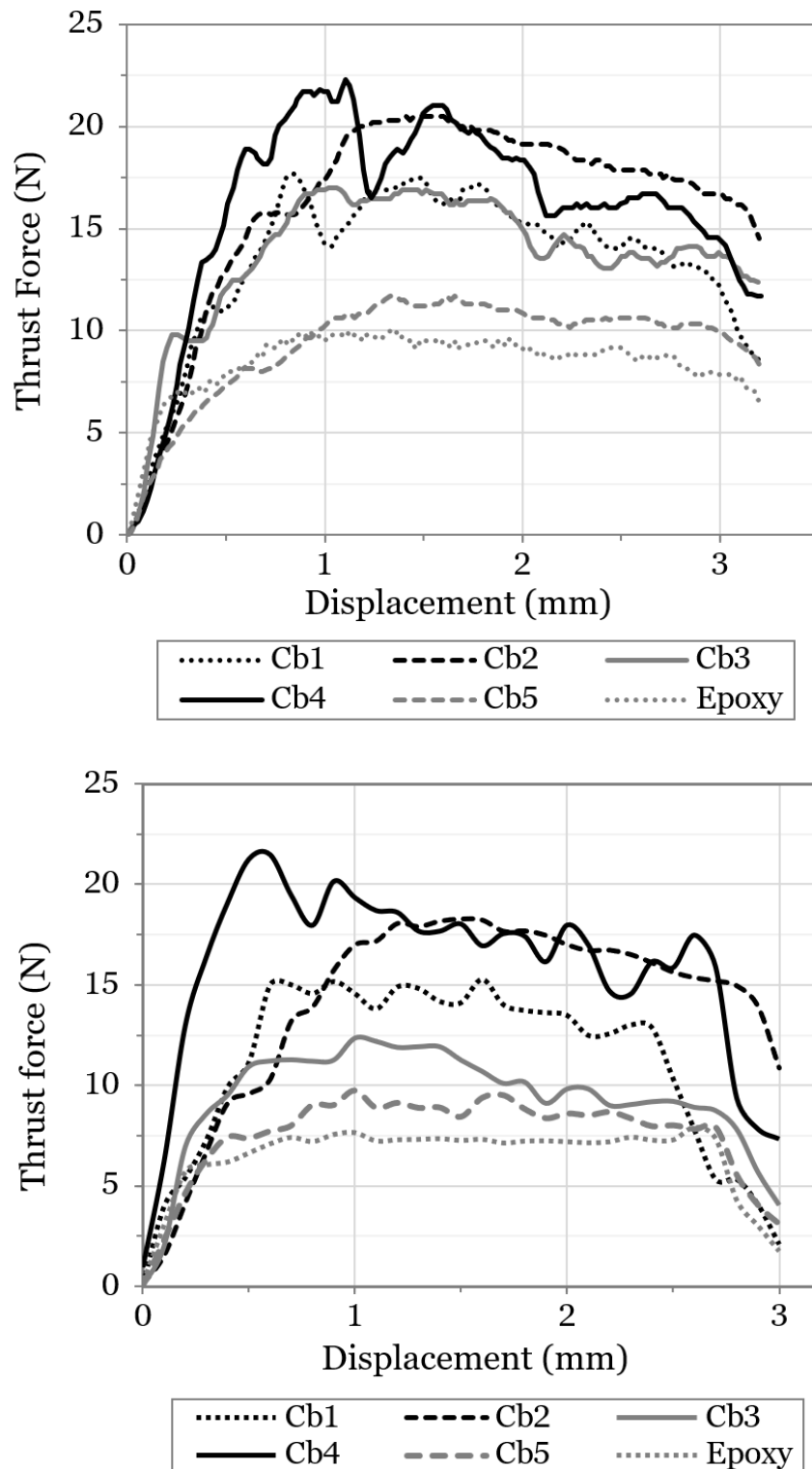


Figure 6.14. Measured drilling thrust force curves when drilling composite samples at 1.3 mm/s feed rate and 1750 rpm (method 1, top) and 1.3 mm/s and 800 rpm (method, bottom).

The range of thrust forces produced by drilling multiple additive composites lie between 10- 22 N and fits pig tibia thrust forces that measured between 9-22 N (Figure 6.14) and previous research values reported by D.L Brisman of 12-24 N who utilized a 2 mm diameter drill bit to drill bovine femur bone [44]. Pig tibia and multiple additive composites produce comparable results to commercial bone simulation materials of similar thrust force profiles studied by A Feldmann *et al* of thrust forces between 5-30 N [45]. The drilled samples using method 2 (Figure 6.14) show well distributed increases in peak force that is potentially advantageous to bone phantom design whereby surgeons can refer to a spectrum of thrust forces that replicate patient specific bone criteria.

All multiple additive composites other than Cb2 have fibre and mineral loadings that possibly mimics the fibre and mineral composition of bone. As with clean epoxy, the powderless Cb2 sample has a smooth thrust force profile that lacks peak and dip features that mimic low and high density cavities composing bone. All assessed multiple additive composites can find application as bone-like phantoms considering their similar thrust force profiles to those of bone. For example, Cb1 and Cb2 may be applied as strong adult bones while Cb5 may resemble weak bone of low bone mineral density. The Cb1 composite was selected to be cast as a foot and ankle model (Figure 6.15) based on its thrust force profile similarities with bone. The Cb5 thrust force curves are within 3 N of clean epoxy profiles so the only practical advantage might come from realistic swarf formation which is later assessed in Section 6.4.4.

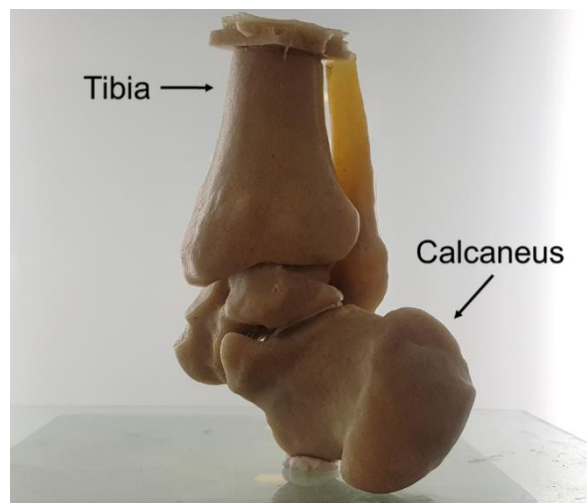


Figure 6.15. Ankle joint medical model cast using Cb1 composite.

Tunable biomimicking phantoms might benefit from adjusting the Cb3 and Cb4 GY/HA ratios to offer a spectrum of thrust forces between 8-22 N when

machined at the assessed drill parameters. HA is the most bone-like chemical structure which requires resource demanding wet chemistry and hydrothermal techniques to produce unlike GY that is naturally occurring and available at low cost [46]. However, HA offers low thrust forces at no cost in cavity and stress retention offering unique bone-like properties.

6.4.3. Density and Mechanical Testing of Epoxy Composites

As cortical bone density is 1.9 g/cm³, composite density is increased and becomes more bone-like with the addition of HA of density 3.2 g/cm³ and GY of density 3.0 g/cm³ (Table 6.5) [13,47,48]. Increased particulate content increases theoretical density but also increases porosity caused by trapped air during mixing. Pores are gaseous artifacts most noticeable with the Cb4 composite that contains differently shaped particles clustered with PE fibres that thickens epoxy. However, porosity does not significantly offset compression strength particularly in the case of Cb4 that contains a 40 wt% addition of gypsum, a 15.8% porosity, and is of 135 (±15) MPa compression strength. It is possible that gypsum particles interact by interlocking during compression, promoting particle to particle surface area and an increased compression strength. Typically, cortical bone elasticity decreases with intracortical porosity that increases risk of fracture as seen with osteoporosis [49]. By performing cavity examination using x-ray CT modelling, and soon potentially ultrasonic scanning, patient specific bone porosity can be realised for use in designing specific additive combinations for bone phantom based training and surgical preparation.

Table 6.5. Density, porosity, flexural and compressive properties of developed composites. Standard deviation is given in brackets.

Phantom Composite	Density (g/cm³)	Theoretical Density (g/cm³)	Porosity (%)
Cb1	1.09	1.21	9.5
Cb2	1.09	1.11	1.8
Cb3	1.09	1.27	14.8
Cb4	1.17	1.39	15.8
Cb5	1.10	1.28	13.8
Cb6	1.13	1.15	1.9

Phantom Composite	Flexural Strength (MPa)	Flexural Modulus (GPa)	Compressive Strength (MPa)	Compressive Modulus (GPa)
Cb1	45 (3)	2.1 (0.1)	93 (8)	1.4 (0.1)
Cb2	47 (2)	1.7 (0.1)	77 (4)	1.4 (0.1)
Cb4	39 (3)	1.1 (0.1)	135 (15)	1.5 (0.1)
Cb6	72 (3)	2.7 (0.2)	101 (2)	1.5 (0.2)

Cb2 provides the lowest measured compression strength of 77 (± 4) MPa due to a lack of hard particles (Table 6.5). Compression modulus of the samples corresponds to particle addition than to fibre addition, whereas flexural strength and flexural modulus corresponds to fibre additions. Glass content facilitates considerable flexion of Cb6 of flexural modulus 2.7 (± 0.2) GPa and flexural strength 72 (± 3) MPa. The mechanical strength in compression and flexion suggest that the epoxy samples fully cured and that molecules drawn to the direction of stress between additives are representative of the compositions [23]. The mechanical properties measured here can be used for continuum mechanics and simulations, and input for machine learning programs that advance the structure-property knowledge of bone and bone-like materials [50].

6.4.4. Images of Machined Composites

Drilled bone shows a build-up of debris surrounding the perimeter of a drilled hole once the bit is removed from the sample (Figure 6.16). This is swarf that requires replication to create a realistic bone phantom aesthetic, but also a

realistic surgical practice procedure. Clean epoxy samples show non-bone-like chip formations that are long continuous chips spiralling and catching the drill bit flutes. Epoxy surfaces that become electrostatically attracted to one another during drilling conduct electrons to the metal drill bit. The developed multiple additive composites visually mimic bone swarf with various success where Cb1 and Cb4 are visually the most bone-like due to the drill flutes holding the least amount of machined material. This might be because powders discharge an electrostatic attraction between the epoxy and drill bit.



Figure 6.16. Method 2 drilled multiple additive composites and reference materials (from left to right): clean epoxy, Cb2, Cb4, Cb1, and bone.

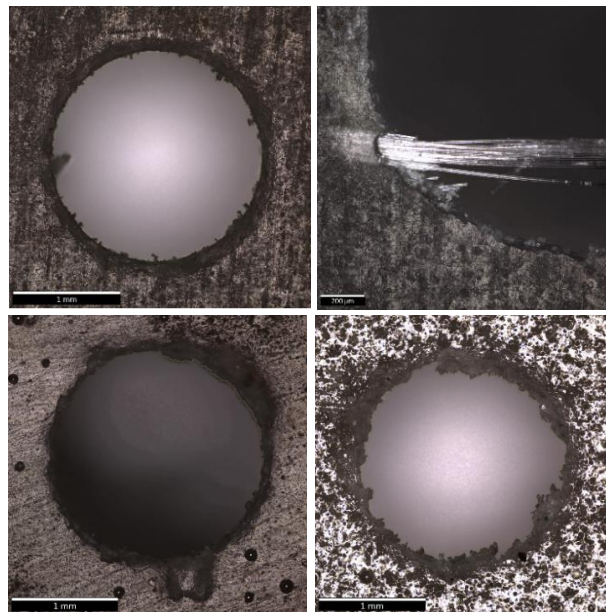


Figure 6.17. Infinite focus micrographs of Cb1 (top) and Cb4 (bottom).

Bone that typically pertains a flat and even perimeter that is mimicked by Cb1 (Figure 6.17) [51]. In contrast, Cb4 drilled holes forms a rough exit hole, and an uneven entry hole perhaps caused by a high particle loading that weakens the tensile strength of the samples. An exposed glass fibre strand in Cb1 may be considered not visually compromising having observed bone-like swarf formations from Cb1.

6.5. Conclusions

Bone phantom models are used by surgeons to interpret a patient specific surgery but the options for bone-like performance during practice surgery are limited. Sawbones® among a few other companies sell bone-like phantoms that facilitate practice surgery with machinable properties resembling bone. However, these are not patient specific properties that this thesis chapter aims to develop. Phantom bone manufacture typically employs HA as a component which is synthesised with the approximate properties of the mineral content of bone but is of high embedded energy due to highly resource intensive processing. Four additives were selected, PE, GF, GY, and HA for creating bone-like epoxy composites in-part to justify the energy intensive production of epoxy resin and minimise the use of HA. Bone phantom composites developed aim to reduce orthopaedic iatrogenic error by offering a range of bone-like properties for patient specific model manufacture with FFF and moulding. Drilled thrust forces, compression and flexural strengths, and images of multiple additive composites were referenced against pig tibia bone samples.

Bone was drilled at a range of feed rates between 1-1.5 mm/s, and spindle speeds between 800-3000 rpm, with drill bit blunting after 25 drilled holes observed using SEM imaging. Pig tibia cortical bone thickness was shown as 2.3-3.7 mm using drill bit break through point. Bone drill forces show feed rate between 0.5-2.5 mm/s at 1750 rpm can influence thrust force by 14 N, spindle speed between 1350-3000 rpm at 1 mm/s can influence by 11 N, and drill bit flutes can clog at a spindle speed of 1350 and 1 mm/s feed rate. Drill bit cutting edge rounding causes a 3-5 N increase to pig tibia bone peak thrust force. Measured bone provided the third lowest drill strengths, after clean epoxy, and a 5 wt% GY and 20 wt% HA (Cb5) composite yielding stiffness and work done values of 16.2 (± 1.5) N/mm and 26.8 (± 2.2) N.mm (error is SD), respectively. The strongest measured epoxy composite when drilled is 1 wt% PE, reaching 17.2 (± 0.7) when drilled at 1.5 mm/s feed rate. PE was drilled after the other additives studied and therefore was assessed utilising the most worn drill bit. HA and GY in epoxy cause dips in drill thrust force profiles that recreate the dips of naturally porous bone. HA is the least drill, compression and bend strengthening additive in epoxy, however drilled strength could be lowest due to measurement with a new drill bit.

Multiple additive composites were drilled using a pillar drill with a new drill bit per sample. A range of bone-like properties were developed with the 5 wt% GY

and 20 wt% HA composite (Cb5) showing the lowest drilled UCS of 2.7 (± 0.3) MPa, and the 1 wt% PE, 40 wt% GY and 5wt% HA composite (Cb4) showing highest drilled UCS of 6.5 (± 0.5) MPa. Bone was compared across drill rig methods using calculated chip loadings. Pig tibia bone provided a drilled UCS of between 3.9 (± 0.2)-4.9 (± 0.2) MPa at 2.9×10^{-4} and 4.3×10^{-4} chip loading, respectively. The most bone-like multiple additive composite contains 2 wt% PE, 2 wt% GF, and 15 wt% GY (Cb1) as observed when drilled and imaged for swarf formation. A Cb1 composed foot and ankle bone phantom was manufactured using FFF and moulding to demonstrate a final bone-like phantom for surgical preparation.

The range of developed bone-like properties offer a simple three step modelling, FFF printing, and epoxy matrix casting method to manufacturing patient specific bone phantoms for surgical practice and patient communication. The wider aim and impact of this work is to reduce iatrogenic error in the operating theatre. For future work, all developed models presented should be qualitatively assessed using a questionnaire matrix for surgeon feedback.

The most bone-like composite developed (Cb1) avoids the use of resource intensive and financially costly HA and in doing so lowers the embodied energy of bone modelling for surgical use, which should be quantified in further work for commercial incentivisation. The resulting patient specific phantoms can potentially be manufactured with legions which would best be achieved by directly 3D printing the models that also eliminated a process step for shorter lead times.

6.6. References

- [1] M.A. Makary, M. Daniel, Medical error-the third leading cause of death in the US, *BMJ (Online)*. 353, (2016)
- [2] J. Fryer, *et al*, A. Meier, R. Williams, B. George, Identifying and Addressing High Priority Issues in General Surgery Training and Education, *J Surg Educ.* 76, (2019)
- [3] A.K. Sachdeva, *et al*, Interventions to address challenges associated with the transition from residency training to independent surgical practice, *Surgery (United States)*. 155, (2014)
- [4] M. Suzuki, *et al*, Rapid prototyping of temporal bone for surgical training and medical education, in: *Acta Otolaryngol*, (2004)
- [5] B.L. Tai, *et al*, 3D Printed composite for simulating thermal and mechanical responses of the cortical bone in orthopaedic surgery, *Med Eng Phys.* 61, (2018)

- [6] D.J. Wescott, Postmortem Change in Bone Biomechanical Properties: Loss of Plasticity, *Forensic Sci Int.* (2019)
- [7] F. O'Neill, *et al*, Validity of synthetic bone as a substitute for osteoporotic cadaveric femoral heads in mechanical testing, *Bone Joint Res.* (2012)
- [8] F. Rengier, *et al*, 3D printing based on imaging data: Review of medical applications, *Int J Comput Assist Radiol Surg.* 5, (2010)
- [9] J. Elfar, *et al*, Composite bone models in orthopaedic surgery research and education, *Journal of the American Academy of Orthopaedic Surgeons.* 22, (2014)
- [10] P.S. Corona, M. Vicente, K. Tetsworth, V. Glatt, Preliminary results using patient-specific 3d printed models to improve preoperative planning for correction of post-traumatic tibial deformities with circular frames, *Injury.* 49, (2018)
- [11] K. Schmidt-Nielsen, S.-N. Knut, *Scaling: why is animal size so important?*, Cambridge university press, (1984)
- [12] C.Y. Lin, J.H. Kang, Mechanical properties of compact bone defined by the stress-strain curve measured using uniaxial tensile test: A concise review and practical guide, *Materials.* 14, (2021)
- [13] A.K.S. S. N. Khan, R. M. Warkhedkar, Human bone strength evaluation through different mechanical tests, *International Journal of Current Engineering and Technology*, (2014)
- [14] E. Seeman, Bone quality: The material and structural basis of bone strength, *J Bone Miner Metab.* 26, (2008)
- [15] J.D. Currey, What determines the bending strength of compact bone?, *Journal of Experimental Biology.* 202, (1999)
- [16] X. Cai, H. Follet, L. Peralta, M. Gardegaront, D. Farlay, R. Gauthier, B. Yu, E. Gineyts, C. Olivier, M. Langer, A. Gourrier, D. Mitton, F. Peyrin, Q. Grimal, P. Laugier, Anisotropic elastic properties of human femoral cortical bone and relationships with composition and microstructure in elderly, *Acta Biomater.* (2019)
- [17] R.K. Pandey, S.S. Panda, Optimization of bone drilling parameters using grey-based fuzzy algorithm, *Measurement (Lond).* (2014)
- [18] M.F.A. Akhbar, A.R. Yusoff, Fast & Injurious: Reducing thermal osteonecrosis regions in the drilling of human bone with multi-objective optimization, *Measurement (Lond).* 152, (2020)
- [19] H. Kirchner, Ductility and brittleness of bone, in: *Int J Fract.* (2006)
- [20] R.K. Pandey, S.S. Panda, Drilling of bone: A comprehensive review, *J Clin Orthop Trauma.* 4, (2013)
- [21] D.B. Burr, Changes in bone matrix properties with aging, *Bone.* 120, (2019)
- [22] F.R. Ong, Analysis of bone drilling characteristics for the enhancement of safety and the evaluation of bone strength, (2014)
- [23] H. Peterlik, *et al*, From brittle to ductile fracture of bone, *Nat Mater.* 5, (2006)
- [24] J. Lee, B *et al*, Modeling and experimentation of bone drilling forces, *J Biomech.* 45, (2012)
- [25] M. Aghvami, *et al*, A Thermal and Biological Analysis of Bone Drilling, *J Biomech Eng.* (2018)
- [26] S. Bandyopadyay-Ghosh, Bone as a collagen-hydroxyapatite composite and its repair, *Trends Biomater Artif Organs.* 22, (2008)
- [27] A.D. Brown, *et al*, Escobedo-Diaz, P.J. Hazell, The mechanical response of commercially available bone simulants for quasi-static and dynamic loading, *J Mech Behav Biomed Mater.* (2019)
- [28] J. Hao, *et al*, Material characterization and selection for 3D-printed spine models, *3D Print Med.* 4, (2018)
- [29] MatWeb Material Property Data. Sawbones Third-Generation Simulated Cortical Bone. Available at: www.matweb.com/search/DataSheet. Accessed January 13th, 2023

- [30] F. Scalera, *et al*, A. Maffezzoli, Development and characterization of UV curable epoxy/hydroxyapatite suspensions for stereolithography applied to bone tissue engineering, *Ceram Int.* 40, (2014)
- [31] D.G. Filip, *et al*, Current Development in Biomaterials—Hydroxyapatite and Bioglass for Applications in Biomedical Field: A Review, *J Funct Biomater.* 13, (2022)
- [32] S.R. Nicholson, *et al*, Manufacturing energy and greenhouse gas emissions associated with plastics consumption, *Joule.* 5, (2021)
- [33] Y. Ganesan, *et al*, Interface toughness of carbon nanotube reinforced epoxy composites, *ACS Appl Mater Interfaces.* 3, (2011)
- [34] A.I. Pearce, *et al*, Animal models for implant biomaterial research in bone: A review, *Eur Cell Mater.* 13, (2007)
- [35] IReVans, Right Foot Bones, Attribution 4.0 International (CC BY 4.0), (2018). Available at www.sketchfab.com/3d-models/right-foot-bones
- [36] Hexion, RP: 3075 EPON Resin 828 Technical Data Bulletin, 8, (2005)
- [37] Jushi Group, MSDS Q/JS J0520-2012, 10, (2012)
- [38] Polytek, PolyfiberII SDS, 2, (2011)
- [39] Jesmonite, FB730NSB - AC730 Natural Stone Base / Gel Coat, 9, (2019)
- [40] Mo-sci, DATA SHEET – GL1661PHA, 1, (2020)
- [41] N. Gupta, M. Doddamani, Polymer Matrix Composites, *Jom.* 70, (2018)
- [42] Peijs, 1.5 High Performance Polyethylene Fibers., in: *Comprehensive Composite Materials II*, (2018)
- [43] D. Tabor, Mohs's hardness scale - A physical interpretation, *Proceedings of the Physical Society. Section B.* 67, (1954)
- [44] D.L. Brisman, The Effect of Speed, Pressure, and Time on Bone Temperature during the Drilling of Implant Sites, *International Journal of Oral and Maxillofacial Implants.* (1996)
- [45] A. Feldmann, *et al*, Experimental evaluation of cortical bone substitute materials for tool development, surgical training and drill bit wear investigations, *Med Eng Phys.* 66, (2019)
- [46] M. Akram, *et al*, Extracting hydroxyapatite and its precursors from natural resources, *J Mater Sci.* 49, (2014)
- [47] S.M. Snyder, E. Schneider, Estimation of mechanical properties of cortical bone by computed tomography, *Journal of Orthopaedic Research.* 9, (1991)
- [48] J.C. Lotz, *et al*, Mechanical properties of metaphyseal bone in the proximal femur., *J Biomech.* 24, (1991)
- [49] Q. Grimal, P. Laugier, Quantitative Ultrasound Assessment of Cortical Bone Properties Beyond Bone Mineral Density, *Irbm.* 40, (2019)
- [50] C.T. Chen, G.X. Gu, Machine learning for composite materials, *MRS Commun.* 9, (2019)
- [51] Y. Akiba, *et al*, Biological Evaluation of Implant Drill Made from Zirconium Dioxide, *Clin Implant Dent Relat Res.* 19, (2017)

Chapter 7. Conclusions and Future Work

The manufacturing method of AM has yet to reach its full potential in creating engineering products using polymer composites, where the polymer content forms a continuous matrix phase. This thesis focusses on engineering products that aid a transition towards a circular economy. It furthers the understanding of AM as a tool for advancing polymer science enabled sustainability and works to improve selected systems efficiencies.

In this thesis, secondary research presented in the introduction highlights the need for a holistic approach in addressing current and potential environmental, social, and economic innovations within the field of sustainable polymer composites. It is described how energy usage and GHG emissions pose a significant portion of pollution produced by the plastics industry. Experimental work in this thesis includes the development of composites for thermochemical energy storage, and gas separation with microporous sieves. Common waste blue wrap PP was sourced from NHS hospitals and received in a compacted and ground rPP form to be blended with SEBS for upcycling as recyclable FFF filament. Hospital plastics contaminated in the operating theatre are often single use plastics and their unsustainable landfill or incineration EoL options may be justified by considering an overall increase to quality of life and human capital. Epoxy bone-phantoms were developed using a range of additives to improve their biomimicking properties for improved orthopaedic surgeon training and communication. Each chapter describes underlying polymer science for each measured materials property, often drawing upon the phenomena of degradation, molecular mobility, bond formation, reaction energy, and fracture/failure mode.

This thesis set out with a key consideration of consumption and resource management as to maximise the value derived from all research materials utilised. The project successfully achieved its aim of contributing towards sustainable manufacture of PP that when recycled from blue wrap into filament using thermal compaction and extrusion can challenge the properties of virgin PP FFF filament and reduce the corresponding virgin production rates. A recommended MFI limit of 65 g/10 mins for FFF indicates the rPP of 103 (± 8) g/10mins is best suited to pellet manufacture for injection moulding that could unlock mass reductions in virgin PP demand. Another accomplishment was the use of low cost, abundant, and locally acquirable materials where possible. This included the selection of blue wrap PP waste from hospitals, natural clay instead of processed vermiculite or a synthetic microporous polymer/ceramic used to house energy storing salt hydrates, and epoxy additives such as glass fibre and gypsum as employed to replace resource intensive HA in bone phantom manufacture.

Deploying products and strategies of improved sustainability to a commercial level was prioritised by considering potential scalability. This was largely achieved for each developed and assessed product by incorporating AM as a common production method. Key examples of where scaling potential is highlighted include: a consideration of single-screw extruder size and rPP FMD filament production rates of 1-20 kg/hr, the rapid manufacture time of 25 min per under-extruded FFF scaffold that were coated in abundant and easily prepared bentonite/CaCl₂ used for twice rechargeable THS, measuring DW adsorption scaffold compression strengths of ≥ 7.75 (± 0.75) MPa in-part to help understand attrition and longevity, and utilising desktop FFF printed moulds for distributed bone phantom manufacture. It was shown that AM is a versatile means of local manufacture due in-part to low set-up and modification costs, a wide variety of compatible materials, and the possible resolution of printed customisable and cloud manageable end-use parts.

This thesis consists of one main contribution per chapter as planned for but features several contributions that evolved through research and write-up. The main contributions are: i). A previously costly low density and single use PP waste was sourced from NHS hospitals and transformed into FFF filament of ≥ 22.5 (± 1.2) MPa UTS and 14 kJ/m² impact strength with the potential to be a profitable closed loop solution for hospitals. ii). Common THS reactor design was reconceptualised and developed to overcome the common performance and efficiency bottleneck issues of pressure drop, uneven vapour sorption, and uncontrolled deliquescence. Tailorable TPMS scaffolds were manufactured in PC using FFF then coated with a bentonite/CaCl₂ plastic solid that to the authors knowledge is the first of its kind. iii). Printable zeolite 13X formulations that are capable of CO₂ capture were optimised by for compression strength by the novel addition of 4 wt% CSR that showed to benefit printability in-part by lowering viscosity from baseline figure of 75.5 to 56.6 Pa·s. The CSR did not compromise N₂ adsorption when compared to the equivalent 4 wt% of typical MC/PVA binder, of 148 (± 17) cm³/g and 131 (± 15) cm³/g BET surface area, respectively. iv). An increase to known additive loading combinations using readily available materials (glass fibre, PE fibre, and gypsum), as optimised when containing 2 wt% additions of glass and PE fibres and 15 wt% gypsum that produce life-like mechanical and drilled properties for patient specific surgeon training and communications.

Further contributions to the field of Materials Science include: the use of optical microscopy and image analysis to identify a critical ligament thickness of 4.7 (± 0.5) μm for the future determination of SEBS toughened PP failure mode. Recycled blue wrap blended and extruded at incremental SEBS wt%

achieved reliable printed specimens used to measure impact energy, tear resistance, and tensile strength. The use of a hospital integrated Sterimelt machine that thermally compacts large quantities (~20 kg/cycle) of SMS fabrics for conversion to FFF filament. Two custom drill rigs were constructed for the comparison of fresh bone thrust force to polymer composites thrust force which enhanced the reliability of measured bone-like properties. Porosity calculations of between 1.8-15.8% furthered the understanding of each bone-like materials tactility and swarf formation under machining for realistic use in operating theatres.

The roughness of bentonite/CaCl₂ composites for THS was measured from a 1.65 mm² area providing Sq values between 80 (±40) and 40 (±10) µm using infinite focus microscopy contributing an original interpretation of sorption potential. Novel TPMS structures employed FEA simulations for benchmarking against baffle and fin heat transfer units. Printed experimental TPMS scaffolds were coated with two quantities (7.5-7.2 and 6.2-5.3 g) of bentonite/CaCl₂ which led to identifying a thinner walled structure as more energy efficient despite containing more salt hydrate. This thesis contributes furthered knowledge on customisable part design and function achieved when AM is combined with polymer composites. Gas separation studies show that CSR containing pastes were successfully printed into customisable log-pile structures having assessed print resolution using calliper measurements. There has been no clear previous research effort to quantify warping of a DW printed zeolitic structure using calliper measurements. The work on calcified zeolite structures contributed a study of the effect of geometry on XRD measured crystallinity and BET surface area. It was found that a change to polymer additive type effected crystallinity of the calcinated samples by 6 wt% with the geometry of calcined samples showing negligible effect. However, surface areas of as-printed baseline structures showed a significant drop from the cast and ground value of 466 (±16) m²/g to 332 (±5) m²/g of adsorbed N₂. Another contribution to the future development of printed gas separation structures is the utilisation and modification of low cost and readily available printer hardware as adapted for DW using an open source FFF printed paste extruder model.

This thesis is potentially limited by the design of methods whereby the field of sustainable polymer composites was explored according to emerging AM processable products. It is a product driven thesis presenting research conducted to impact the sector by developing unique solutions to sustainability bottlenecks. Throughout this thesis there occurred changes in direction of study as to create as large a positive impact on the plastics sector and address

problems with AM through analytical methods. Initially, single-use plastics were prioritized but with further work and a complete change of industrial partnership came the pursuit of limiting atmospheric pollution to reduce lifecycle emissions from plastics. Further work will address this potential limitation by propagating the recommended strategies that benefit each products performance, efficiency, and sustainability. For example, many single use PLA and PE nonwoven fabrics may be thermally compacted, dry blended and extruded for upcycling into FFF filament. PLA is well suited to AM, showing that recycling of previous waste stream low density wraps using the proposed strategy can act as just the start of a globally adopted closed loop economy for these materials. Likewise, the redesigned THS using an AM scaffold can be optimised using a more conductive scaffold and higher surface area aluminosilicate perhaps capable of use in hostile environments that yield higher efficiencies. Hence, the work in this thesis can acts as the starting point for customisable clay/salt embedded AM scaffolds for unlocking new THS performance.

Other further work includes utilising powerful FEA simulations for models that include a heating gradient to simulate the effect of salt embedded bentonite reacting with water vapour. Many different TPMS geometries such as neovius, lipnoid, and fischer-koch geometries can be studied for improved heat transfer. Powerful FEA simulations use expensive specialist software that involve millions of elements and are time consuming, often require days to run. Hence, FEA simulations in this thesis involved tens of thousands of elements that limits the work to small surface area models simulated for heat transfer under non-extreme environmental conditions.

Further work should also aim to directly print multiple types of epoxy and corresponding composite bone phantom formulations using static mixer nozzles and commercially available clay printers. This will enable distributed patient-specific production by connecting surgeons/pathology specialists with hospital 3D printing and modelling engineers online. A similar strategy could be pursued for industrial printing of the developed zeolite 13X gas separation scaffolds as customised for each individual industrial flue gas. The developed bone phantom formulations would also benefit from qualitative evaluation by orthopaedic surgeons, which was not feasible during this project due to the coronavirus pandemic and a limited availability of experienced surgeons. However, as with all chapters, continued progress towards early adoption in situ requires industrial research and analysis into new materials including those presented in this thesis.